

THE UNIVERSITY OF CHICAGO

DEVELOPMENT OF MULTIFUNCTIONAL METAL-ORGANIC FRAMEWORKS
FOR CATALYTIC APPLICATIONS

A DISSERTATION SUBMITTED TO
THE FACULTY OF THE DIVISION OF THE PHYSICAL SCIENCES
IN CANDIDACY FOR THE DEGREE OF
DOCTOR OF PHILOSOPHY

DEPARTMENT OF CHEMISTRY

BY
YANG SONG

CHICAGO, ILLINOIS

AUGUST 2021

© 2021

YANG SONG

ALL RIGHTS RESERVED

Table of Contents

List of Figures	vii
List of Tables	xiii
List of Schemes	xiv
List of Abbreviations	xv
Abstract	xix
Acknowledgement	xxi
Chapter 1. Introduction.....	1
1.1 Metal-Organic Frameworks (MOFs).....	1
1.2 Post-Synthetic Modification (PSM) on MOFs	3
1.2.1 Functionalization at MOF linkers/ligands	4
1.2.2 Functionalization at MOF Nodes.....	5
1.2.3 Functionalization in MOF Cavities.....	6
1.3 MOFs for Catalytic Applications.....	7
1.3.1 Reductive Reactions.....	8
1.3.2 Lewis Acid Promoted Reactions.....	9
1.3.3 Photocatalytic Reactions	10
1.4 References.....	11
Chapter 2. Metal-Organic Framework Nodes Support Single-Site Nickel (II)-Hydride Catalysts for the Hydrogenolysis of Aryl Ethers.....	20
2.1 Introduction.....	20
2.2 Results and Discussion	21
2.2.1 Synthesis and Characterization of Ti ₈ -BDC-NiBr	21
2.2.2 Synthesis and Characterization of Ti ₈ -BDC-NiH	24
2.2.3 Ti ^{III} ₂ Ti ^{IV} ₆ -BDC-NiH Catalyzed Hydrogenolysis of Benzyl Phenyl Ether.....	29
2.2.4 Ti ^{III} ₂ Ti ^{IV} ₆ -BDC-NiH Catalyzed Hydrogenolysis of Other Benzyl Phenyl Ethers	31
2.3 Conclusion	34
2.4 Experimental.....	35
2.4.1 Material and Methods	35
2.4.2 Synthesis of Ti ₈ -BDC	36
2.4.3 Synthesis of Ti ₈ -BDC-NiBr	37

2.4.4 Thermogravimetric Analysis (TGA) of Ti ₈ -BDC-NiBr	37
2.4.5 EXAFS Analysis	38
2.4.6 Typical Procedure for Ti ^{III} ₂ Ti ^{IV} ₆ -BDC-NiH Catalyzed Hydrogenolysis	39
2.5 References.....	40
Chapter 3. Multistep Engineering of Synergistic Catalysts in a Metal-Organic Framework for Tandem C-O Bond Cleavage	44
3.1 Introduction.....	44
3.2 Results and Discussion	48
3.2.1 Synthesis of Mixed-Ligand MOF 1 and Removal of pdac Ligands via Ozonolysis ...	48
3.2.2 Triflation of 1-OH and Lewis Acidity Determination for 1-OTf.....	57
3.2.3 Synthesis and Characterization of 1-OTf-PdCl ₂ and 1-OTf-Pd ^{NP}	60
3.2.4 1-OTf-PdCl ₂ Catalyzed Tandem Ether/alcohol C-O Bond Cleavage	66
3.2.5 1-OTf-PdCl ₂ Catalyzed Tandem Ester C-O Bond Cleavage.....	70
3.2.6 Heterogeneity of 1-OTf-Pd ^{NP}	72
3.2.7 Proposed Tandem Pathway.....	76
3.3 Conclusion	77
3.4 Experimental.....	78
3.4.1 Material and Methods	78
3.4.2 Synthesis and Characterization of MOF 1	79
3.4.3 Synthesis and Characterization of 1-OH.....	80
3.4.4 Synthesis and Characterization of 1-OTf.....	81
3.4.5 Synthesis and Characterization of 1-OTf-PdCl ₂	81
3.4.6 X-ray Absorption Study	81
3.4.7 Quantification of Lewis Acidity by N-methylacridone Fluorescence	82
3.4.8 A typical procedure for 1-OTf-PdCl ₂ catalyzed tandem ether/alcohol C-O bond cleavage	83
3.4.9 Condition optimization for 1-OTf-PdCl ₂ catalyzed tandem ester C-O bond cleavage	84
3.4.10 Condition optimization for 1-OTf-PdCl ₂	85
3.4.11 Background reactions and control experiments	86
3.4.12 Synthesis and Characterization of 1-OTf-Pd ^{NP}	89

3.4.13 Recycle and reuse experiments in 1-OTf-PdCl ₂ catalyzed tandem C-O bond cleavage	89
3.5 References.....	90
Chapter 4. Metal-Organic Framework with Dual Active Sites in Engineered Mesopores for Bioinspired Synergistic Catalysis	95
4.1 Introduction.....	95
4.2 Results and Discussion	97
4.2.1 Synthesis and Characterization of 1-OTf-Ir.....	97
4.2.2 1-OTf-Ir Catalyzed Reductive Cross-Coupling Reactions	102
4.2.3 Mechanistic Studies	106
4.3 Conclusion	113
4.4 Experimental.....	113
4.4.1 Material and Methods	113
4.4.2 Synthesis of 1-OTf-Ir.....	114
4.4.3 X-ray Absorption Study.....	115
4.4.4 Synergistic Catalytic Reactions	116
4.4.5 Time-dependent Experiment.....	125
4.4.6 Synthesis of 1-OTf-Ir-high and 1-OTf-Ir-low	126
4.4.7 Synthesis of 1-Ir and 1-OH-Ir	128
4.4.8 Control Experiment.....	130
4.4.9 NMR Spectra	131
4.5 References.....	132
Chapter 5. Titanium Hydroxide Secondary Building Units in Metal-Organic Frameworks Catalyze Hydrogen Evolution under Visible Light	136
5.1 Introduction.....	136
5.2 Results and Discussion	138
5.2.1 Synthesis of Ti ₃ -BPDC-Ir and Ti ₃ -BPDC-Ru.....	138
5.2.2 ¹ H NMR Analysis	141
5.2.3 Thermogravimetric Analysis	142
5.2.4 Visible Light-Driven Hydrogen Evolution Reaction (HER)	144
5.2.5 Photophysical Studies	146

5.2.6 Electrochemical Studies.....	149
5.2.7 Proposed Reaction Mechanism.....	153
5.3 Conclusion	156
5.4 Experimental.....	157
5.4.1 Material and Methods	157
5.4.2 Synthesis of Me ₂ L ₁	158
5.4.3 Synthesis of H ₂ L ₁	160
5.4.4 Synthesis of H ₂ L ₂	161
5.4.5 Synthesis of Ti ₃ -BPDC-Ir and Ti ₃ -BPDC-Ru.....	162
5.4.6 Fitting of Luminescence Quenching by BIH.....	163
5.4.7 Apparent Quantum Yield Determinations	163
5.5 References.....	165
Chapter 6. Cerium-Based Metal-Organic Layers Catalyze Hydrogen Evolution Reaction through Dual Photoexcitation	168
6.1 Introduction.....	168
6.2 Results and Discussion	170
6.2.1 Synthesis and Characterization of Ce ₆ -BTB MOL.....	170
6.2.2 Synthesis and Characterization of Ce ₆ -BTB-Ir and Ce ₆ -BTB-Ru	175
6.2.3 Photocatalytic Hydrogen Evolution Reaction.....	179
6.2.4 Photophysical Studies	181
6.2.5 Electrochemical Studies.....	187
6.2.6 Proposed Reaction Mechanism.....	192
6.3 Conclusion	194
6.4 Experimental.....	195
6.4.1 Material and Methods	195
6.4.2 Synthesis of [(HMBA)Ir(ppy) ₂]Cl and [(HMBA)Ru(bpy) ₂]Cl ₂	196
6.4.3 X-ray Absorption Spectroscopy.....	204
6.4.4 Fitting of Luminescence Quenching.....	205
6.5. References.....	206

List of Figures

Figure 1-1. Examples of commonly used MOFs in various applications.....	3
Figure 1-2. Schematic showing different strategies toward MOF functionalization: functionalization at organic linkers (left); functionalization at SBUs (middle), entrapment of catalytic active species (right).....	4
Figure 1-3. Examples of well-studied PSMs on MOF ligands.	5
Figure 1-4. Examples of well-studied PSMs on MOF nodes.	6
Figure 1-5. Examples of well-developed PSM in MOF cavities.	7
Figure 1-6. MOF-catalyzed reductive reactions.	9
Figure 1-7. MOFs with Lewis acidic sites catalyzed liquid phase organic transformations.	10
Figure 1-8. MOFs promoted artificial photosynthesis.	11
Figure 2-1. Ti ₈ node-supported Ni ^{II} -H catalyzes hydrogenolysis of lignin model compounds. Titanium, nickel, oxygen, carbon and hydrogen atoms are shown in blue, green, red, gray and white, respectively.	21
Figure 2-2. Structure of Ti ₈ -BDC and its metalation with NiBr ₂ to form Ti ₈ -BDC-NiBr.....	22
Figure 2-3. (a) PXRD patterns of Ti ₈ -BDC (red) and Ti ₈ -BDC-NiBr (green) in comparison to the PXRD pattern simulated from the CIF file of Ti-BDC (black). (b) TEM image of Ti ₈ -BDC-NiBr. (c) Nitrogen sorption isotherms of Ti ₈ -BDC (black) and Ti ₈ -BDC-NiBr (blue).....	22
Figure 2-4. (a) Optimized structure and (b) measured bond distances of Ti ₈ -BDC-NiBr.	23
Figure 2-5. EXAFS spectra (black circles) and fit (gray solid line) in R-space at the Ni K-edge adsorption of Ti ₈ -BDC-NiBr.....	24
Figure 2-6. (a) EPR spectra of Ti ^{III} ₂ Ti ^{IV} ₆ -BDC-NiH (red), and Ti ^{IV} ₈ -BDC-NiH (blue). (b) Ti K-edge XANES spectra of Ti ₈ -BDC-NiBr (red), Ti ^{III} ₂ Ti ^{IV} ₆ -BDC-NiH (blue), and Ti ^{IV} ₈ -BDC-NiH (black).	25
Figure 2-7. Ni K-edge XANES spectra of Ti ₈ -BDC-NiBr (red), Ti ^{III} ₂ Ti ^{IV} ₆ -BDC-NiH (blue), and Ti ^{IV} ₈ -BDC-NiH (pink) in comparison to Ni(NO ₃) ₂ (black).....	26
Figure 2-8. (a) Oxidation of Ti ^{III} to Ti ^{IV} with FcPF ₆ through electron transfer reaction. (b) EXAFS spectra (black circles) and fit (gray line) in R space at the Ni K-edge adsorption of Ti ^{IV} ₈ -BDC-NiH. The scattering paths of Ni to THF-oxygen (pink), axial oxo (orange), equatorial oxo (blue) hydride (green), and titanium (purple) were shown.....	27
Figure 2-9. (a) Optimized structure and (b) measured bond distances of Ti ^{III} ₂ Ti ^{IV} ₆ -BDC-NiH..	28
Figure 2-10. EXAFS spectra (black circles) and fits (gray solid line) in R-space at the Ni K-edge adsorption of Ti ^{III} ₂ Ti ^{IV} ₆ -BDC-NiH.	28
Figure 2-11. Recycle experiments for the Ti ^{III} ₂ Ti ^{IV} ₆ -BDC-NiH catalyzed hydrogenolysis of benzyl phenyl ether.....	31
Figure 2-12. Proposed mechanism for the hydrogenolysis of benzyl phenyl ether (α -O-4) by the Ti ^{III} ₂ Ti ^{IV} ₆ -BDC-NiH. The activation energies for key-bond metathesis are shown.	34
Figure 2-13. (a) PXRD pattern of freshly prepared Ti ₈ -BDC MOF. (b) TEM image of the Ti ₈ -BDC MOF, showing thick-plate morphology. Scale bar is 1 μ m.....	36
Figure 2-14. TGA curve of freshly prepared Ti ₈ -BDC-NiBr in the 25-800 $^{\circ}$ C range.	38
Figure 2-15. GC-MS traces for the hydrogenolysis of benzyl phenyl ether to afford toluene and cyclohexanol as the sole products at complete conversion.....	40
Figure 3-1. Schematic representation of sequential post-synthetic engineering of MOF 1	47
Figure 3-2. ¹ H NMR spectrum of digested 1 in DMSO- <i>d</i> ₆ . Red and blue circles correspond to dcbpy and pdac ligands, respectively.....	48

Figure 3-3. TGA curve of freshly prepared 1 in the 25-800 °C range.	49
Figure 3-4. (a) SEM and (b) TEM images of as synthesized MOF 1	50
Figure 3-5. PXRD pattern of the freshly prepared MOF 1 (red) compared to that of DUT-5 (black).	50
Figure 3-6. N ₂ sorption isotherm of MOF 1	51
Figure 3-7. ¹ H NMR spectrum of digested 1 -OH in DMSO- <i>d</i> ₆ . Red circles correspond to dcbpy ligands. No signals corresponding to pdac ligand are seen in the ¹ H NMR spectrum, indicating complete removal of pdac ligands during ozonolysis.	53
Figure 3-8. TGA curve of 1 -OH in the 25-800 °C temperature range.	54
Figure 3-9. The similarity of PXRD patterns of 1 (red) and 1 -OH (blue) to the simulated pattern of DUT-5.	55
Figure 3-10. TEM image of 1 -OH.	55
Figure 3-11. Comparison of N ₂ sorption isotherms of 1 (black) and 1 -OH (blue).	56
Figure 3-12. Pore size distributions of (a) 1 and (b) 1 -OH.	56
Figure 3-13. ¹ H NMR spectrum of the supernatant from 1 -OH activation with Me ₃ SiOTf. The amount of (Me ₃ Si) ₂ O was determined to be 1.93 equiv. w.r.t. to the Al ₂ (OH)(OH ₂) sites.	58
Figure 3-14. (a) DRIFT spectra of 1 (blue), 1 -OH (red), and 1 -OTf (black). (b) Zoomed-in view of the DRIFT spectra show a significant red shift of ν(μ ₂ -OH) from 3708 cm ⁻¹ in 1 (blue) and 1 -OH (red) to 3687 cm ⁻¹ in 1 -OTf (black).	59
Figure 3-15. Fluorescence spectra of 1 -OTf (black), 1 -OH (red), and free NMA (dashed).	60
Figure 3-16. TGA curve of 1 -OTf-PdCl ₂ in the 25-800 °C range.	61
Figure 3-17. TEM image of 1 -OTf-PdCl ₂	62
Figure 3-18. The similarity of PXRD patterns of 1 (red), 1 -OH (blue), 1 -OTf (green), 1 -OTf-PdCl ₂ (purple), and 1 -OTf-Pd ^{NP} (khaki) to the simulated pattern of DUT-5 (black) indicates the crystallinity of the MOF was maintained after multi-step post-synthetic manipulations.	62
Figure 3-19. EXAFS spectrum (gray solid line) and fit (black circles) in R-space at the Pd K-edge adsorption of 1 -OTf-PdCl ₂ , with the fragment structure of (bpy)PdCl ₂ for EXAFS fitting of the Pd coordination environment in 1 -OTf-PdCl ₂ . H atoms were omitted for clarity.	63
Figure 3-20. TEM image of 1 -OTf-Pd ^{NP} shows evenly distributed Pd NPs in the MOF matrix after <i>in situ</i> reduction in catalytic reactions.	64
Figure 3-21. XANES Spectra of 1 -OTf-PdCl ₂ , 1 -OTf-Pd ^{NP} , Pd foil, and PdCl ₂	65
Figure 3-22. Linear combination fitting of 1 -OTf-Pd ^{NP} XANES feature using those of Pd foil and PdCl ₂ as the basis functions.	66
Figure 3-23. NMA fluorescence spectra upon binding to 1 -OTf (black) and 1 -OTf-Pd ^{NP} recovered from C-O bond cleavage of 1-methylcyclohexanol (red).	73
Figure 3-24. ¹⁹ F NMR spectra of the supernatant (maroon) and the digested MOF (green).	74
Figure 3-25. The “hot filtration” test of 1 -OTf-PdCl ₂ catalyzed tandem C-O bond cleavage reaction.	75
Figure 3-26. Recycle experiments for 1 -OTf-PdCl ₂ catalyzed C-O bond cleavage of 1-methylcyclohexanol. Plots of methylcyclohexane yields (%) in six consecutive runs with 3 h of reaction time.	76
Figure 3-27. Proposed tandem pathway for 1 -OTf-PdCl ₂ -mediated C-O bond cleavage.	77
Figure 3-28. GC-MS spectrum of 1 -OTf-PdCl ₂ catalyzed tandem ether/alcohol C-O bond cleavage of 1,8-cineole (The two MS spectra correspond to the cis/trans isomer of menthane).	84
Figure 3-29. GC-MS spectra of 1 -OTf-PdCl ₂ catalyzed tandem ester C-O bond cleavage of terpinyl acetate (The two MS spectra correspond to the cis/trans isomers of menthane).	85

Figure 4-1. Comparison between an enzyme active site with binding center and catalytic center (left) and an engineered mesopore in 1 -OTf-Ir with Lewis acid as binding center and Ir-photosensitizer as catalytic center (right).	97
Figure 4-2. ¹ H NMR spectrum of digested 1 -OTf-Ir in DMSO- <i>d</i> ₆ . Red circles correspond to dcbpy ligands, while blue circles correspond to L ₁ ligands.....	99
Figure 4-3. ¹ H NMR spectrum of digested 1 -OTf-Ir-high in DMSO- <i>d</i> ₆ . Red circles correspond to dcbpy ligands, while blue circles correspond to L ₁ ligands.....	100
Figure 4-4. PXRD patterns of 1 (red), and 1 -OTf-Ir (blue) in comparison to the simulated pattern for DUT-5.	101
Figure 4-5. Normalized UV-vis spectra and emission spectra (with 368 nm excitation) of 1 -OTf-Ir in comparison to Me ₂ L ₁ ligands in DMF with a concentration of 20 μM based on Ir.	101
Figure 4-6. EXAFS spectrum (gray solid line) and fit (black circles) in R-space at the Ir L ₃ -edge adsorption of 1 -OTf-Ir, with the fragment structure of Ir(bpy) ₃ for EXAFS fitting of the Ir coordination environment in 1 -OTf-Ir. H atoms were omitted for clarity.....	102
Figure 4-7. PXRD patterns of 1 (red), 1 -OTf-Ir (blue), and 1 -OTf-Ir (after reaction) (pink) in comparison to the simulated pattern for DUT-5.	107
Figure 4-8. Yields of 1c with recovered MOF 1 -OTf-Ir in five consecutive runs.....	108
Figure 4-9. Time-dependent yields of 1c with different catalysts.	109
Figure 4-10. Emission spectra of 1 -OTf-Ir (10 μM based on Ir component, CH ₃ CN) after the addition of different amounts of HEH (left) or 1a (right) with 365 nm excitation. Insets show the plots of <i>I</i> ₀ / <i>I</i> of 1 -OTf-Ir as a function of equivalents of HEH (left) or 1a (right).	110
Figure 4-11. Proposed reaction mechanism for 1 -OTf-Ir catalyzed reductive cross-coupling of azaarenes with esters.....	112
Figure 4-12. ¹ H NMR spectrum of digested 1 -OTf-Ir-high in DMSO- <i>d</i> ₆ . Red circles correspond to dcbpy ligands, while blue circles correspond to L ₁ ligands.....	126
Figure 4-13. ¹ H NMR spectrum of digested 1 -OTf-Ir-low in DMSO- <i>d</i> ₆ . Red circles correspond to dcbpy ligands, while blue circles correspond to L ₁ ligands.....	127
Figure 4-14. PXRD patterns of 1 -Ir and 1 -OH-Ir in comparison to the simulated pattern for DUT-5.....	128
Figure 4-15. ¹ H NMR spectrum of digested 1 -OH-Ir in DMSO- <i>d</i> ₆ . Red circles correspond to dcbpy ligands, while blue circles correspond to L ₁ ligands.....	129
Figure 4-16. ¹ H NMR spectrum of digested 1 -Ir in DMSO- <i>d</i> ₆ . Red circles correspond to dcbpy ligands and blue circles correspond to pdac ligands. Only negligible peaks of L ₁ ligands are observed.	130
Figure 5-1. Schematic showing photocatalytic HER by Ti ₃ -BPDC-Ir via electron injection from photo-reduced [Ir ^{III} (ppy) ₂ (dcbpy ^{•-})] ⁰ ligands into Ti ₃ (OH) ₂ SBUs. Ti, Ir, O, and N atoms are shown in blue, gold, red, and mazarine, respectively.....	138
Figure 5-2. Optical photographs of (a) Ti ₃ -BPDC-Ir and (b) Ti ₃ -BPDC-Ru. Scale bar is 50 μm.	139
Figure 5-3. SEM image of (a) Ti ₃ -BPDC-Ir and (b) Ti ₃ -BPDC-Ru.	140
Figure 5-4. PXRD patterns of synthesized Ti ₃ -BPDC-Ir (red) and Ti ₃ -BPDC-Ru (blue) in comparison to the simulated Ti ₃ -BPDC pattern.....	140
Figure 5-5. ¹ H NMR spectra of digested Ti ₃ -BPDC-Ir in DMSO- <i>d</i> ₆ . Red, blue and green circles correspond to BPDC, L ₁ and acetates, respectively.....	141
Figure 5-6. ¹ H NMR spectra of digested Ti ₃ -BPDC-Ru in DMSO- <i>d</i> ₆ . Red, pink, and green circles correspond to BPDC, L ₂ and acetates, respectively.....	142

Figure 5-7. TGA curve of freshly prepared Ti ₃ -BPDC-Ir in 25~600 °C range.	143
Figure 5-8. TGA curve of freshly prepared Ti ₃ -BPDC-Ru in 25~600 °C range.	144
Figure 5-9. Time-dependent HER TONs of Ti ₃ -BPDC-Ir and Ti ₃ -BPDC-Ru along with homogenous controls.	145
Figure 5-10. PXRD patterns of Ti ₃ -BPDC-Ir and Ti ₃ -BPDC-Ru after photocatalysis in comparison to the simulated pattern of Ti ₃ -BPDC.	146
Figure 5-11. Normalized UV-vis spectra of (a) Ti ₃ -BPDC-Ir and (b) Ti ₃ -BPDC-Ru in comparison to their homogenous photosensitizing ligands in DMF with a concentration of 20 μM based on Ir/Ru.	146
Figure 5-12. Emission spectra of (a) Ti ₃ -BPDC-Ir and (b) Ti ₃ -BPDC-Ru (20 μM based on Ir/Ru) after the addition of different equivalents of BIH with 365 or 450 nm excitation, respectively.	147
Figure 5-13. Emission spectra of Me ₂ L ₁ (30 μmol) after the addition of different amounts of BIH (a) and Ti ₆ cluster (b) in 2 mL of MeCN with 365 nm excitation.	148
Figure 5-14. Emission Spectra of Me ₂ L ₂ (30 μM) after addition of different amount of BIH (a) and different amount Ti ₆ cluster (b) in 2 ml of CH ₃ CN under 450 nm excitation.	148
Figure 5-15. Plots of I ₀ /I of Me ₂ L ₁ and Me ₂ L ₂ as a function of the concentration of BIH (mM).	149
Figure 5-16. CVs of 0.5 mg Ti ₃ -BPDC coated on electrode surface and 5mM Ti ₆ cluster in a 20 mL 0.1 M TBAH/CH ₃ CN solution with or without 250 μL H ₂ O and 250 μL TFA. TBAH = Tetrabutylammonium hexafluorophosphate.	150
Figure 5-17. EPR spectra of Ti ₃ -BPDC-Ir in the dark or under light irradiation.	151
Figure 5-18. EPR spectra of Ti ₃ -BPDC-Ru in the dark or under light irradiation.	151
Figure 5-19. XANES analysis demonstrated the generation of Ti ^{III} species after photoirradiation.	152
Figure 5-20. CV of Me ₂ L ₁ in 0.1 M TBAH/CH ₃ CN (Tetrabutylammonium hexafluorophosphate). Potential sweep rate was 100 mV/s.	154
Figure 5-21. CV of Me ₂ L ₁ in 0.1 M TBAH/CH ₃ CN (Tetrabutylammonium hexafluorophosphate). Potential sweep rate was 100 mV/s.	155
Figure 5-22. ¹ H NMR spectrum of Me ₂ L ₁ (500 MHz) in CDCl ₃	159
Figure 5-23. ¹³ C NMR spectrum of Me ₂ L ₁ (500 MHz) in CDCl ₃	159
Figure 5-24. ¹ H NMR spectrum of H ₂ L ₁ (500 MHz) in DMSO- <i>d</i> ₆	161
Figure 5-25. ¹ H NMR spectrum of H ₂ L ₂ (500 MHz) in DMSO- <i>d</i> ₆	162
Figure 6-1. Schematic showing the synthesis of Ce ₆ -BTB and Ce ₆ -BTB-Ru MOLs and photocatalytic HER by Ce ₆ -BTB-Ru through dual photoexcitation. Ce, Ru, N and O atoms are shown in orange, pink, blue and red, respectively.	169
Figure 6-2. Views of Ce ₆ -BTB (a) and Ce ₆ SBU (b) along the vertical direction. Views of Ce ₆ -BTB (c) Ce ₆ SBU (d) along the lateral direction.	170
Figure 6-3. PXRD pattern of Ce ₆ -BTB MOL in comparison to the simulated pattern of Hf ₆ -BTB MOL.	171
Figure 6-4. ¹ H NMR spectra of digested Ce ₆ -BTB.	172
Figure 6-5. TGA curve of freshly prepared Ce ₆ -BTB in the 25 - 600 °C range.	173
Figure 6-6. TEM (a) and HRTEM (b) of Ce ₆ -BTB.	174
Figure 6-7. AFM topography and height profile of Ce ₆ -BTB.	174
Figure 6-8. Schematic showing a Ce ₆ SBU with an estimated height of ~1.2 nm.	175
Figure 6-9. TGA curve of freshly prepared Ce ₆ -BTB-Ir in the 25 - 600 °C range.	176
Figure 6-10. TGA curve of freshly prepared Ce ₆ -BTB-Ru in the 25 - 600 °C range.	177

Figure 6-11. TEM (a) and HRTEM images (b) of Ce ₆ -BTB-Ir.	178
Figure 6-12. TEM (a) and HRTEM images (b) of Ce ₆ -BTB-Ru.	178
Figure 6-13. PXRD patterns of Ce ₆ -BTB-Ir and Ce ₆ -BTB-Ru in comparison to Ce ₆ -BTB pattern.	179
Figure 6-14. Time-dependent HER TONs of Ce ₆ -BTB-Ir and Ce ₆ -BTB-Ru along with homogenous controls.	180
Figure 6-15. PXRD pattern of Ce ₆ -BTB-Ir (after reaction), and Ce ₆ -BTB-Ru (after reaction) in comparison to the Ce ₆ -BTB pattern.	181
Figure 6-16. UV-vis spectra of (a) Ce ₆ -BTB-Ru and (b) Ce ₆ -BTB-Ir in comparison to their homogeneous photosensitizing ligands in DMF with a concentration of 20 μM based on Ir/Ru.	182
Figure 6-17. Emission spectra of Ce ₆ -BTB-Ru (a) and Ce ₆ -BTB-Ir (b) after the addition of different equivalents of BIH with 365 or 450 nm excitation, respectively.	182
Figure 6-18. Emission Spectra of [(MeMBA)Ir(ppy) ₂]Cl (30 μM) after addition of different amounts of BIH (a) and different amounts Ce ₆ cluster (b) in 2 ml of MeCN under 365 nm excitation.	183
Figure 6-19. Emission Spectra of [(MeMBA)Ru(bpy) ₂]Cl ₂ (30 μM) after addition of different amounts of BIH (a) and different amounts Ce ₆ cluster (b) in 2 ml of MeCN under 450 nm excitation.	184
Figure 6-20. Plots of <i>I</i> ₀ / <i>I</i> of [(MeMBA)Ir(ppy) ₂]Cl and [(MeMBA)Ru(bpy) ₂]Cl ₂ as a function of BIH concentration (mM).	185
Figure 6-21. XANES spectra of Ce ₆ -BTB-Ir and Ce ₆ -BTB-Ru before and after photoirradiation.	186
Figure 6-22. XANES fitting of (a) Ce ₆ -BTB-Ir and (b) Ce ₆ -BTB-Ru.	187
Figure 6-23. CVs of 5 mM Ce ₆ cluster and 0.5 mg Ce ₆ -BTB MOL coated on electrode surface under photocatalytic HER condition (20 mL 0.1 M TBAH/CH ₃ CN solution with 0.5 ml AcOH. TBAH = Tetrabutylammonium hexafluorophosphate).	188
Figure 6-24. CVs of [(MeMBA)Ir(ppy) ₂]Cl in 0.1 M TBAH/MeCN (TBAH = Tetrabutylammonium hexafluorophosphate). Potential sweep rate was 100 mV/s.	189
Figure 6-25. CVs of [(MeMBA)Ru(bpy) ₂]Cl ₂ in 0.1 M TBAH/MeCN (TBAH = Tetrabutylammonium hexafluorophosphate). Potential sweep rate was 100 mV/s.	189
Figure 6-26. CV of Ce ₆ cluster in 0.1 M TBAH/MeCN (TBAH = Tetrabutylammonium hexafluorophosphate). Potential sweep rate was 100 mV/s.	190
Figure 6-27. Absorption (solid line) and emission (dashed line) spectra of a Ce ^{III} -MOF-808 suspension in MeCN.	191
Figure 6-28. Photocatalytic activities of Ce ₆ -BTB-Ru under 450 nm irradiation and Ce ₆ -BTB and Ce ₆ -BTB-Ru under 350 – 700 nm irradiation for 24h.	192
Figure 6-29. Proposed photocatalytic cycle for the hydrogen production catalyzed by Ce ₆ -BTB-Ru through a dual photoexcitation pathway.	193
Figure 6-30. (a) Proposed photocatalytic HER pathway on the Ce site. (b) Shut down of photocatalytic HER on the Ce site with TEMPO as a radical scavenger.	194
Figure 6-31. ¹ H NMR spectrum of MeMBA (500 MHz) in CDCl ₃ .	197
Figure 6-32. ¹³ C NMR spectrum of MeMBA (500 MHz) in CDCl ₃ .	198
Figure 6-33. ¹ H NMR spectrum of [(MeMBA)Ir(ppy) ₂]Cl (500 MHz) in CDCl ₃ .	199
Figure 6-34. ¹³ C NMR spectrum of [(MeMBA)Ir(ppy) ₂]Cl (500 MHz) in CDCl ₃ .	200
Figure 6-35. ¹ H NMR spectrum of [(HMBA)Ir(ppy) ₂]Cl (500 MHz) in DMSO- <i>d</i> ₆ .	201

Figure 6-36. ^1H NMR spectrum of $[(\text{MeMBA})\text{Ru}(\text{bpy})_2]\text{Cl}_2$ (500 MHz) in CD_3OD	202
Figure 6-37. ^{13}C NMR spectrum of $[(\text{MeMBA})\text{Ru}(\text{bpy})_2]\text{Cl}_2$ (500 MHz) in CD_3OD	203
Figure 6-38. ^1H NMR spectrum of $[(\text{HMBA})\text{Ru}(\text{bpy})_2]\text{Cl}_2$ (500 MHz) in $\text{DMSO-}d_6$	204

List of Tables

Table 2-1. Optimization of $\text{Ti}^{\text{III}}_2\text{Ti}^{\text{IV}}_6\text{-BDC-NiH}$ Catalyzed Hydrogenolysis of Benzyl Phenyl Ether. ^a	30
Table 2-2. Hydrogenolysis of Various Benzyl Ethers. ^a	32
Table 2-3. Hydrogenolysis of Other Lignin Model Compounds. ^a	33
Table 3-1. Screening of reaction conditions for 1-OTf-PdCl₂ Catalyzed Tandem Etheric/Alcohol C-O Bond Cleavage. ^a	68
Table 3-2. Substrate Scope for 1-OTf-PdCl₂ Catalyzed Tandem Etheric/Alcoholic C-O Bond Cleavage. ^a	70
Table 3-3. Substrate Scope for 1-OTf-PdCl₂ Catalyzed Ester C-O Bond Cleavage. ^a	72
Table 3-4. Condition optimization for 1-OTf-PdCl₂ catalyzed tandem ether/alcohol C-O bond cleavage of 1,8-cineole	86
Table 3-5. Background and control experiments for 1-OTf-PdCl₂ catalyzed tandem ether/alcohol C-O bond cleavage of 1,8-cineole. ^a	88
Table 4-1. Optimization of reaction conditions. ^a	103
Table 4-2. 1-OTf-Ir catalyzed reductive cross-coupling of vinylazarenes with NHP esters. ^a .	104
Table 4-3. 1-OTf-Ir catalyzed reductive cross-coupling of alkynylazaarenes with NHP esters. ^a	105
Table 4-4. 1-OTf-Ir catalyzed reductive cross-coupling of aryl bromomethyl ketones. ^a	105
Table 4-5. 1-OTf-Ir catalyzed the synthesis of marketed drug molecules.	106

List of Schemes

Scheme 2-1. Hydrogenolysis of Benzyl Phenyl Ether.	39
Scheme 3-1. Schematic representation of ozonolysis treatment for the removal of pdac ligands.	52
Scheme 3-2. Chemical equation showing ozonolysis of 1 to afford 1-OH with $\text{Al}_2(\text{OH})(\text{OH}_2)$ defect sites.....	52
Scheme 3-3. Chemical equation showing triflation of 1-OH to afford 1-OTf	57
Scheme 3-4. Chemical equation showing metalation of 1-OTf with $\text{Pd}(\text{MeCN})_2\text{Cl}_2$ to afford 1- OTf-PdCl₂ and <i>in situ</i> reduction of 1-OTf-PdCl₂ to generate 1-OTf-Pd^{NP}	61
Scheme 3-5. Synthetic procedure for MOF 1	80
Scheme 3-6. 1-OTf-PdCl₂ catalyzed 1,8 cineole C-O bond cleavage.	83
Scheme 3-7. 1-OTf-PdCl₂ catalyzed terpinyl acetate C-O bond cleavage.	84
Scheme 4-1. Synthetic route to 1-OTf-Ir	98
Scheme 4-2. Control reaction catalyzed by 1-OTf and 1-OH-Ir	109
Scheme 4-3. Radical capture experiment with TEMPO.	111
Scheme 4-4. Radical capture experiment with 1,1-diphenylethene.	111
Scheme 4-5. Homogeneous control with $\text{Ir}(\text{Me}_2\text{dcby})(\text{ppy})_2\text{Cl}$ and $\text{Al}(\text{OTf})_3$	131
Scheme 4-6. Control reaction catalyzed by 1-OTf and 1-OH-Ir	131
Scheme 5-1. Schematic showing the synthesis of Ti₃-BPDC-Ir and Ti₃-BPDC-Ru	139
Scheme 5-2. Proposed catalytic cycle for the visible-light-driven HER catalyzed by Ti₃-BPDC-Ir	154
Scheme 5-3. Detailed catalytic mechanism on the Ti site via the $\text{Ti}^{\text{IV+}}/\text{Ti}^{\text{III}}$ cycle.	156
Scheme 5-4. Schematic representation of the synthetic procedure for Me₂L₁	158
Scheme 5-5. Schematic representation of the synthetic procedure for H₂L₁	160
Scheme 5-6. Schematic representation of the synthetic procedure for H₂L₂	161
Scheme 6-1. Schematic representation of the synthesis of MeMBA	196
Scheme 6-2. Schematic representation of the synthesis of [(HMBA)Ir(ppy)₂]Cl	199
Scheme 6-3. Schematic representation of the synthesis of [(HMBA)Ru(bpy)]Cl₂	202

List of Abbreviations

2D	2-dimensional
3D	3-dimensional
°C	degree Celsius
Å	angstrom
ΔR	change in scattering half-path length
σ^2	mean standard relative deviation of a scatter
λ_{\max}	emission maximum
AcOH	acetic acid
AFM	atomic force microscopy
ANL	Argonne National Laboratory
APS	Advanced Photon Source
B ₃ LYP	Becke 3-parameter, Lee-Yang-Parr (hybrid DFT functional)
BDC	1,4-benzenedicarboxylate
BET	Brunauer-Emmett-Teller
BPDC	biphenyl-4,4'-dicarboxylate
bpy	2,2'-bipyridine
BTB	1,3,5-benzenetricarboxylate
BIH	1,3-dimethyl-2-phenyl-2,3-dihydro-1H-benzo[d]imidazole
CCDC	Cambridge crystallographic data centre
CO ₂ RR	carbon dioxide reduction reaction
CV	cyclic voltammogram

D ₂ O	deuterium oxide
dcbpy	2,2'-bipyridine-5,5'-dicarboxylate
DCE	1,2-dichloroethane
DCM	dichloromethane
DFT	density functional theory
DME	dimethoxyethane
DMF	<i>N,N</i> -dimethylformamide
DMSO	dimethyl sulfoxide
DUT	Dresden University of Technology
E ₀	energy shift of the photoelectron
EPR	electron paramagnetic resonance
ESI	electrospray ionization
EXAFS	extended X-ray absorption fine structure
GC	gas chromatography
GC-MS	gas chromatography-mass spectroscopy
HER	hydrogen evolution reaction
HKUST	Hongkong University of Science and Technology
HRTEM	high resolution transmission electron microscopy
HRMS	high resolution mass spectroscopy
HOMO	highest occupied molecular orbital
ICP-MS	inductively coupled plasma mass spectroscopy
I ₀	incident beam density
I _t	transmitted beam density

I_{ref}	reference beam intensity
IFEFFIT	software used for fitting EXAFS spectra
IR	infrared spectroscopy
K_{sv}	Stern-Völmer constant
LUMO	Lowest occupied molecular orbital
MeCN	acetonitrile
MeOH	methanol
MeMBA	methyl 2-(5'-methyl-[2,2'-bipyridin]-5-yl)acetate
MIL	Matériaux de l'Institut Lavoisier
MOF	metal-organic framework
MOL	metal-organic layer
NBO	natural bond orbital
NHE	normal hydrogen electrode
NMA	N-methylacridone
NMR	nuclear magnetic resonance
NP	nanoparticle
NU	Northwestern University
pdac	1,4-benzenediacrylate
PEG	polyethylene glycol
POM	polyoxometalate
ppy	2-phenylpyridine
PXRD	Powder X-ray diffraction
PSM	post-synthetic modification

QE	quantum yield
R ²	Goodness-of-fit metric
S ₀ ²	Passive electron reduction factor
SBU	secondary building unit
SEM	scanning electron microscopy
TCD	thermal conductivity detector
TEA	triethylamine
TEM	transmission electron microscopy
TEMPO	2,2,6,6-tetramethyl-1-piperidinyloxy
TFA	trifluoroacetic acid
TGA	thermogravimetric analysis
THF	tetrahydrofuran
TON	turnover number
UiO	University of Oslo
UV-vis	ultraviolet and visible
XANES	X-ray absorption near-edge structure
XAS	X-ray absorption spectroscopy
ZIF	zeolitic imidazolate framework

Abstract

Yang Song: Development of Multifunctional Metal-Organic Frameworks for Catalytic Applications

Under the Direction of Professor Wenbin Lin

Metal-organic frameworks (MOFs) have emerged as a highly versatile and tunable platform for the design of structurally uniform solid catalysts. Highly active multifunctional MOF catalysts have been developed via a number of novel post-synthetic strategies, including functionalization at MOF linkers/ligands, functionalization at MOF SBUs, and entrapment of catalytically active species (e.g. metal nanoparticles, metal complexes, and organic molecules) in MOF pores, channels, and cavities. The resultant multifunctional MOF catalysts have been used to catalyze a broad scope of reactions. This dissertation focuses on the design and synthesis of multifunctional MOFs for several catalytic reactions, including reductive reactions, Lewis acid promoted reactions, and photocatalysis.

The first part of this dissertation (Chapter 2 and Chapter 3) discusses MOF-promoted C-O bond cleavage. In Chapter 2, we showed that Ti₈-BDC works as an excellent platform to support a single-site Ni-H catalyst for aryl ether hydrogenolysis. The C-O bond linkages of the model compounds for typical bonds in lignin were selectively cleaved by the Ni-H catalyst to produce aromatic molecules as well as cyclohexanol under mild conditions. In Chapter 3, we further developed a multifunctional aluminum MOF-based catalytic system (**1**-OTf-Pd^{NP}) for one-pot tandem C-O bond cleavage. This tandem catalysis overcomes the strong C-O binding energy and transforms biomass into valuable hydrocarbon fuels. The synergistic Lewis acids and Pd NPs in the MOF showed outstanding catalytic activities in the C-O bond cleavage of a broad scope of

ethers, alcohols, and esters to exclusively generate deoxygenated saturated alkanes under relatively mild conditions.

The second part of this dissertation (Chapter 4) focuses on photocatalytic organic synthesis. While the multifunctional catalytic system in Chapter 3 showed outstanding performance in tandem catalysis for C-O bond cleavage, we further utilized the same MOF platform to incorporate Ir-based photosensitizers (Ir-PSs) to construct a bioinspired MOF-based photocatalytic system. Strongly Lewis acidic sites and Ir-PSs sites were installed in **1-OTf-Ir** for reductive cross-coupling reactions between *N*-hydroxyphthalimide (NHP) esters or aryl bromomethyl ketones with vinyl- or alkynyl-azaarenes to afford functionalized azaarene derivatives.

The third part of this dissertation (Chapter 5 and Chapter 6) further discusses photocatalysis with MOFs, specifically photocatalytic hydrogen evolution reaction (HER), an important half reaction of water splitting. In Chapter 5, we hierarchically assembled photosensitizers and catalytic sites in Ti₃-BPDC. The proximity of multiple photosensitizers to the catalytic Ti₃(OH)₂ SBU facilitates multielectron transfer upon photoexcitation, leading to 80-fold enhancement in HER activity over the corresponding homogeneous controls. In Chapter 6, we developed a two-dimensional Ce-based MOF in order to overcome the shortcomings of MOF materials in photocatalysis. The reduction of one dimension reduces light scattering and allows free diffusion of reactive species throughout the framework. The proximity of PSs to the catalytic Ce₆ SBUs facilitated electron transfer upon photoexcitation, leading to 8.7- to 9.3-fold enhancement in HER activity over their homogeneous controls.

Acknowledgement

It has been a long and incredible journey to bring me here to write my dissertation. I feel so fortunate to be surrounded by many talented and ardent people over the past five years. Without their help, this dissertation would not have been possible.

First and foremost, I would like to express my deepest appreciation to my advisor, Professor Wenbin Lin. I could not have asked for a better research mentor than him. I am grateful for the opportunity he provided for me to work on metal-organic framework (MOF)-based catalysis in his lab. He brought me into the door of scientific research, and trained me to dig deeply into experimental results rather than simply accept other's conclusions. His fearlessness to the unknown and adventurous fields of science and passion to push the boundaries of chemical research touched me most. I also appreciate his sincere trust and constant support when I felt trapped and lost in research directions. I have learned from my own experience about the hard work going into training a budding graduate student to become an independent researcher. Prof. Lin's dedication, encouragement, and guidance make what I am now and will continue to impact me in the future.

I would also like to thank the other committee members: Professor Bozhi Tian and Professor John Anderson, for their kind help in reviewing my dissertation. I am honored to have them review my research and provide valuable suggestions.

There are so many senior collaborators I must acknowledge. Dr. Yu-Sheng Chen from ChemMatCARS helped me a lot in collecting single-crystal datasets at Argonne National Laboratory. I will miss many meals he treated us there. I would like to thank Dr. Tianpin Wu, Dr. Lu Ma, Dr. Joshua Wright, and Dr. Yujia Ding for their kind help in X-ray absorption experiments

at Argonne National Laboratory. I am also grateful to Professor Cheng (Wave) Wang, and Professor Zhi-Ming Zhang for their valuable suggestions in my research projects.

I am so fortunate to have many talented and supportive senior lab collaborators. First, I would like to thank Dr. Zekai Lin and Dr. Pengfei Ji, who guided me at the beginning of my graduate study. I want to thank Zekai for teaching me EXAFS fitting techniques. He brought me to Argonne National Laboratory and taught me how to do X-ray diffraction and X-ray absorption experiments. Pengfei is passionate about science. From him I learned a lot of skills in synthesis and characterizations of MOFs. I would like to thank Dr. Yunayuan Zhu and Dr. Yangjian Quan. We collaborated on many projects, and I learned a lot from each discussion we had about both academics and life in general. I would also like to thank Dr. Ruoyu Xu, Dr. Kaiyuan Ni, Dr. Guangxu Lan, and Dr. Wenbo Han for their collaborations and constructive advices on my projects. Finally, I want to express my special thanks to Dr. Yunhong Pi, a former visiting student in the Lin lab. Yunhong is an ardent person and is always willing to help others selflessly. I am grateful for her contributions to the projects we worked on.

I am most fortunate to have Xuanyu (Jeff) Feng as a trusted and closest colleague. We collaborated on more than ten projects. He is a gifted person who is creative in coming up with new ideas. Meanwhile, he enjoys sharing good chemistry. His competence and personality make our collaborations very efficient. I will also miss many dinners we had in Chinatown and countless hiking around Chicago we had over the past five years. I also want to thank another great collaborator, Zhe Li, another visiting student in the Lin Lab. Zhe is skillful in theoretical calculations, and I am grateful for his theoretical supports to many of my projects. Besides research, Zhe is also a good person to talk with. I enjoyed the experiences of his kind and professional guidance in opening new credit card accounts. I want to thank many other lab members, including

Ziwan Xu, Xiaomin Jiang, Taokun Luo, Geoffrey Nash, Yingjie Fan, and other current and former group members for their support and friendship. Finally, I am also happy to work with two outstanding UChicago undergraduates, Justin Chen, and Michael Kaufmann. They demonstrated persistence, intelligence, and diligence in each project they participated. I have no doubt about the bright future ahead of them.

Finally, I want to thank my parents, Qin Shi, and Chengyu Song. It is extremely difficult for me to be away from them for such a long time. I could always feel their loneliness and missing their only child every time I called them. It is their constant and unconditional love, support, and encouragement that make me survive and thrive in graduate school. I am looking forward to the days when I can be close to them again.

Chapter 1. Introduction

1.1 Metal-Organic Frameworks (MOFs)

As a novel class of highly porous crystalline materials that are constructed from metal ions or clusters and organic linkers, metal-organic frameworks (MOFs), also called porous coordination polymers (PCPs), have attracted significant attention from a broad spectrum of scientists and engineers in the past two decades.¹⁻⁴ MOFs are crystalline, organic-inorganic hybrid molecular materials constructed by coordinative bonds between metal nodes, or secondary building units (SBUs) and organic multidentate ligands. Dependent on the sizes of inorganic nodes and organic ligands as well as the topologies of the structures, MOFs can have pores and channels with sizes ranging from several Ångstroms to several nanometers.⁵⁻⁶ MOFs thus bridge the gap between zeolites possessing Ångstrom-sized pores and mesoporous silica materials with nanometer-sized pores.⁷ The flexibility with which the constituents' geometry, size, and functionality can be varied has made MOFs a much more fertile research field than zeolites and mesoporous silica materials.

The idea of MOFs can be traced back the discovery of Prussian Blue which was first synthesized by the German paint maker Johann Jacob Diesbach in 1706.⁸ Although many papers on coordination polymers have sporadically appeared in the literature over the past few decades,⁹ the seminal work by Richard Robson in 1980's established the foundation of coordination polymers and coordination networks.¹⁰ Professor Omar Yaghi first coined the term of metal-organic frameworks in 1995,⁹ generalized the synthesis of MOFs, and introduced many key concepts such as secondary building units and isorecticular synthesis. As a result of pioneering research by Yaghi, Kitagawa, Ferey, Zaworotko, Lin, Kim, and many others, the field of MOF research has witnessed exponential growth over the past two decades. One notable example is

MOF-5 constructed from simple terephthalate linkers and Zn_4O tetrahedral SBUs, first reported by Yaghi in 1999. MOF-5 showed a much higher apparent surface area than most zeolites.¹ To date, tens of thousands of MOFs have been reported. The unique features of MOFs, including structural diversity and tunability, high surface areas, and functionalities, have rendered MOFs highly versatile materials with potential applications in many fields, including gas adsorption and separation,¹¹⁻¹³ chemical sensing,¹⁴ nanomedicine,¹⁵⁻¹⁶ catalysis,¹⁷⁻²¹ and many others.²²⁻²³ Several types of MOFs have been widely used for the study of these applications (**Figure 1-1**), including the MOF-5 family and the ZIF-8 family with Zn-based SBUs,²⁴⁻²⁷ HKUST-1 with Cu_2 paddle-wheel SBUs,²⁸⁻²⁹ the MIL-53 series with Al, Fe, or Cr-based SBUs,³⁰⁻³¹ MIL-125 with Ti-based SBUs,³²⁻³⁴ the UiO series,³⁵⁻³⁶ MOF-808,³⁷ and NU-1000³⁸ with Zr and Hf SBUs. Some of these MOF families possess high stability, porosity, and tunability, making them prime candidates for MOF catalysis.

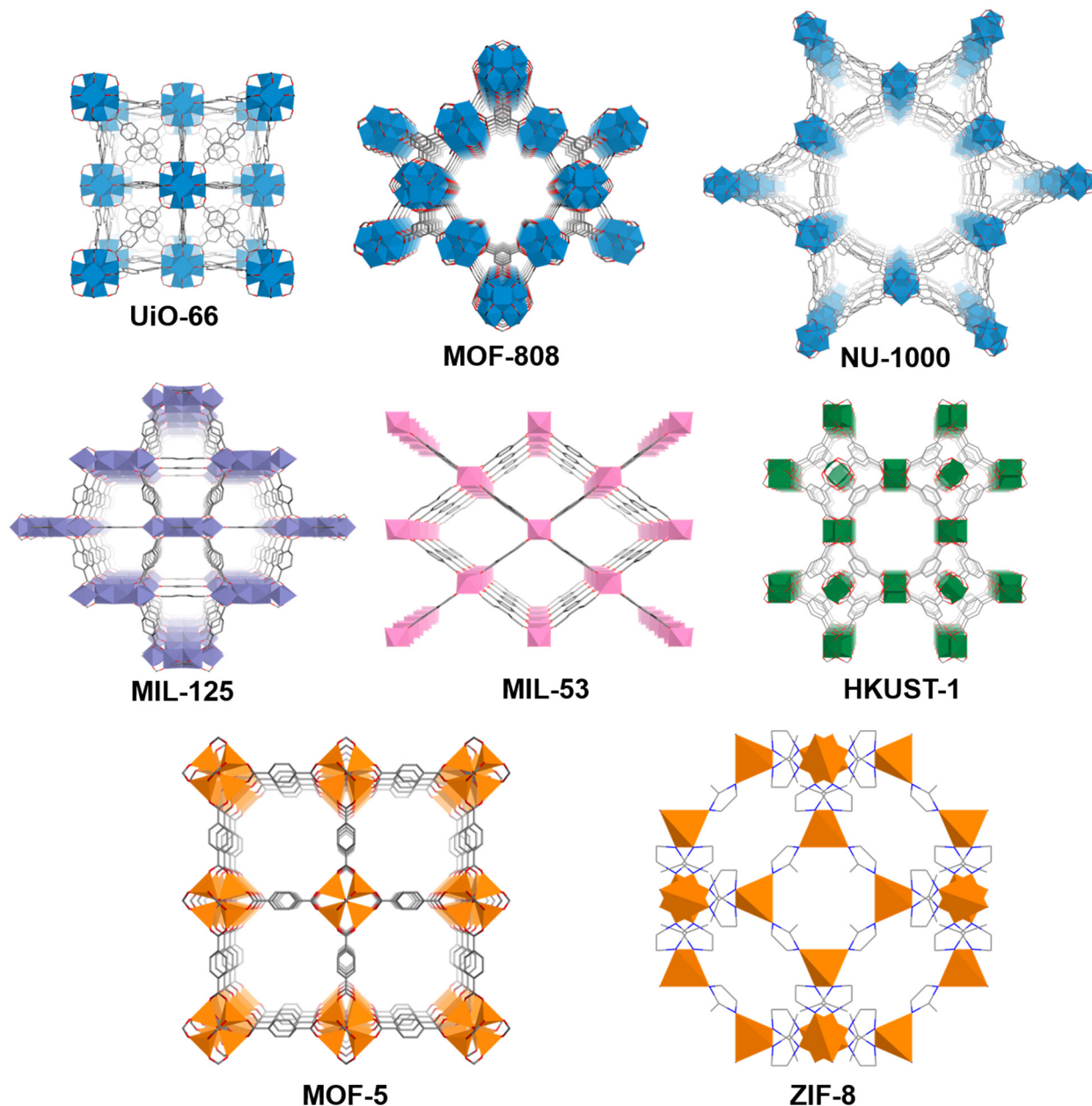


Figure 1-1. Examples of commonly used MOFs in various applications.

1.2 Post-Synthetic Modification (PSM) on MOFs

In the past two decades, the research of MOF catalysis has witnessed significant progress.³⁹⁻⁴² The initial efforts on MOF catalysis focused on the use of coordinatively unsaturated sites on metal ions or clusters as Lewis acidic sites and modifications of organic linkers to install

Brønsted acid sites (such as sulfonic acids) and basic sites (such as amino groups).⁴³⁻⁴⁴ However, the reaction scope catalyzed by the simple acid/base sites are quite limited. To unleash the potential of MOF catalysis, a number of novel synthetic strategies have been developed in the past fifteen years to construct highly active MOF catalysts. These synthetic strategies can be broadly classified into three categories: (a) functionalization at MOF linkers/ligands; (b) functionalization at MOF SBUs; (c) entrapment of catalytically active species (e.g. metal nanoparticles, metal complexes, and organic molecules) in MOF pores, channels, and cavities (**Figure 1-2**). These synthetic strategies can be implemented via either direct synthesis or post-synthetic modification (PSM).⁴⁵⁻⁴⁸ Different methods could also be combined to afford multifunctional sites for more complicated tandem, cooperative, and synergistic catalysis.

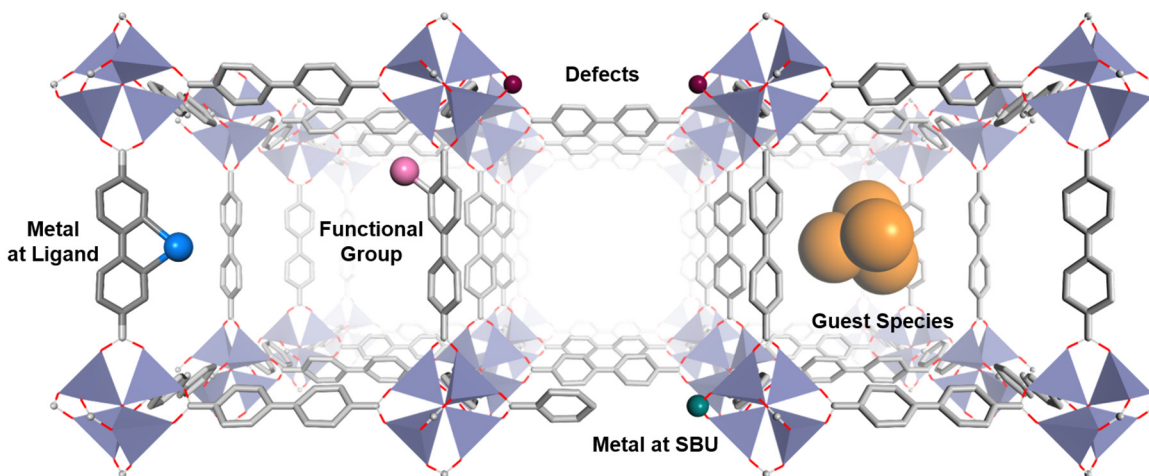


Figure 1-2. Schematic showing different strategies toward MOF functionalization: functionalization at organic linkers (left); functionalization at SBUs (middle), entrapment of catalytic active species (right).

1.2.1 Functionalization at MOF linkers/ligands

This is the most studied type of MOF functionalization that involves covalent modification of the organic linker, coordination of a metal center to the organic linker, or other methods of modifying the organic linker (**Figure 1-3**).⁴⁹ Functional groups on organic linkers can be tailored

for heterogeneous catalysis. There are a variety of functional groups serving as active sites for catalysis, such as amino,⁵⁰⁻⁵² azide,⁵³⁻⁵⁴ aldehyde,⁵⁵ and others.⁵⁶⁻⁵⁸ Furthermore, the functional groups on MOF linkers (either neutral or anionic) can be immobilized with metal ions through dative functionalization.⁵⁹⁻⁶⁴ In general, the active functional groups can be linked to the MOF ligands, thereby resulting in a stable catalytic system.

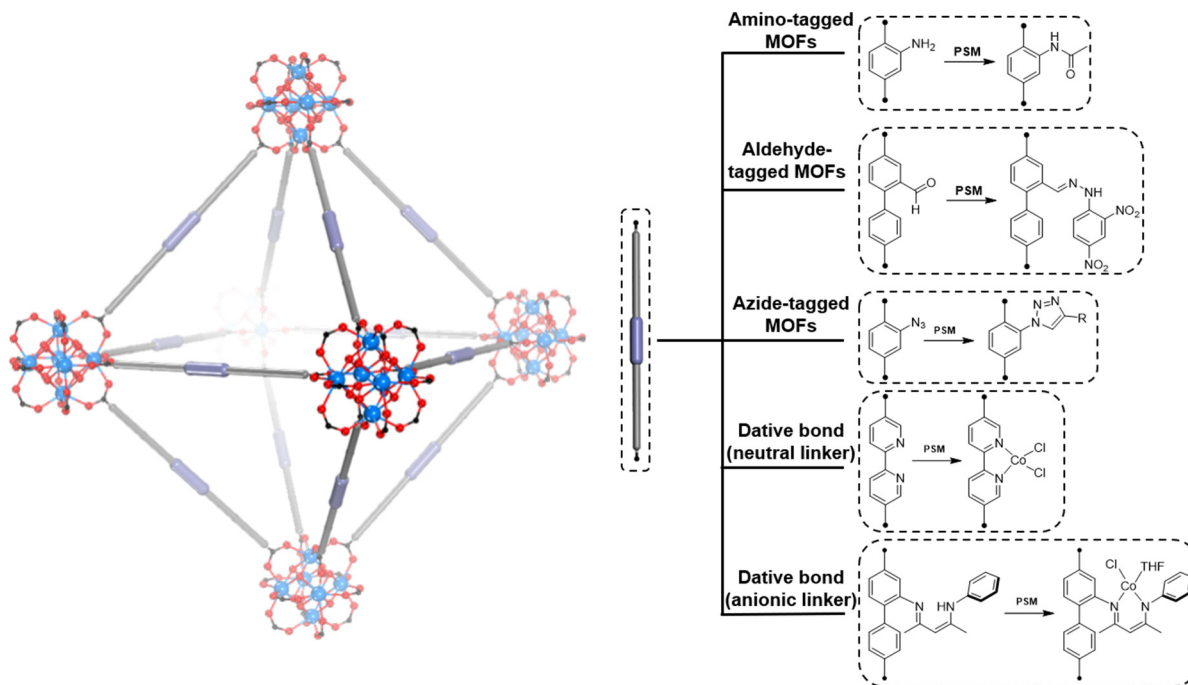


Figure 1-3. Examples of well-studied PSMs on MOF ligands.

1.2.2 Functionalization at MOF Nodes

This method allows the functionalization of SBUs to afford the catalytic centers (**Figure 1-4**): hydroxyl groups on the SBUs can be used as anchoring sites,⁶⁵⁻⁶⁶ SBUs can be grafted with pendant ligands,⁶⁷⁻⁶⁸ native metals in SBUs can be substituted with catalytically active metals,⁶⁹⁻⁷⁰ and framework metal centers can be reduced or oxidized to turn on catalytic activities.⁷¹

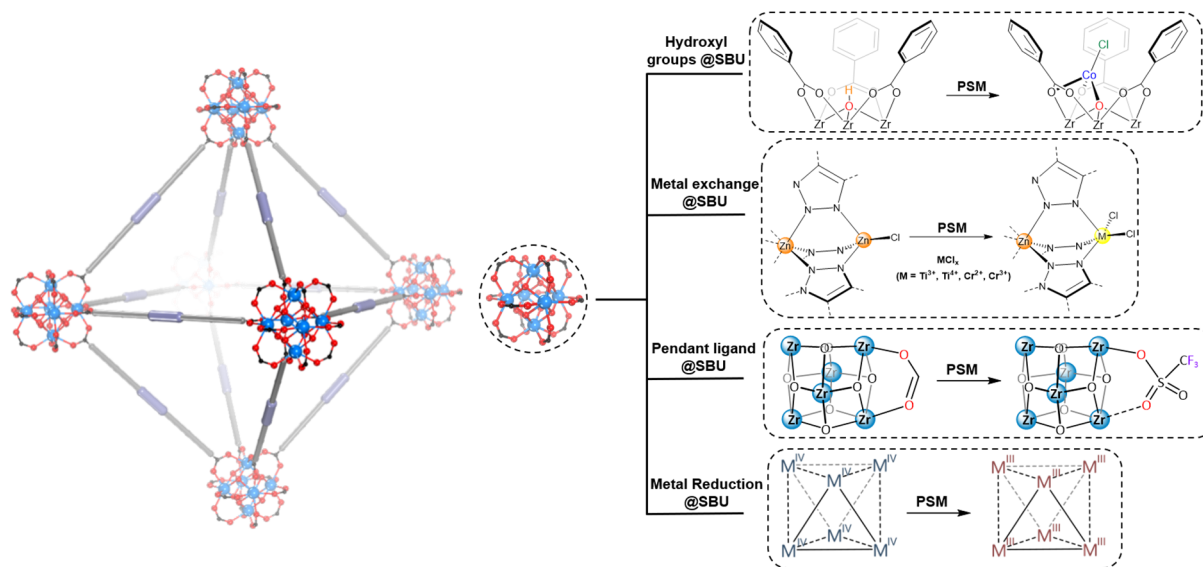


Figure 1-4. Examples of well-studied PSMs on MOF nodes.

1.2.3 Functionalization in MOF Cavities

This method refers to the functionalization by confining catalytic species such as metal nanoparticles in MOF cavities via electrostatic interactions or through cage/channel confinement (**Figure 1-5**). Metal nanoparticles,⁷²⁻⁷⁴ metal complexes,⁷⁵⁻⁷⁶ and polyoxometalates (POMs)⁷⁷⁻⁷⁸ have all been encapsulated in MOFs for catalytic applications. As highly porous materials, MOFs provide an ideal platform to encapsulate guest species (e.g. metal nanoparticles, metal complexes, and polyoxometalates) in their pores via noncovalent interactions. Such guest@MOF composites combine the advantages of MOF hosts—porous structure, chemical versatility, and structural tailorability—with those of functional guests to afford new catalytic materials.

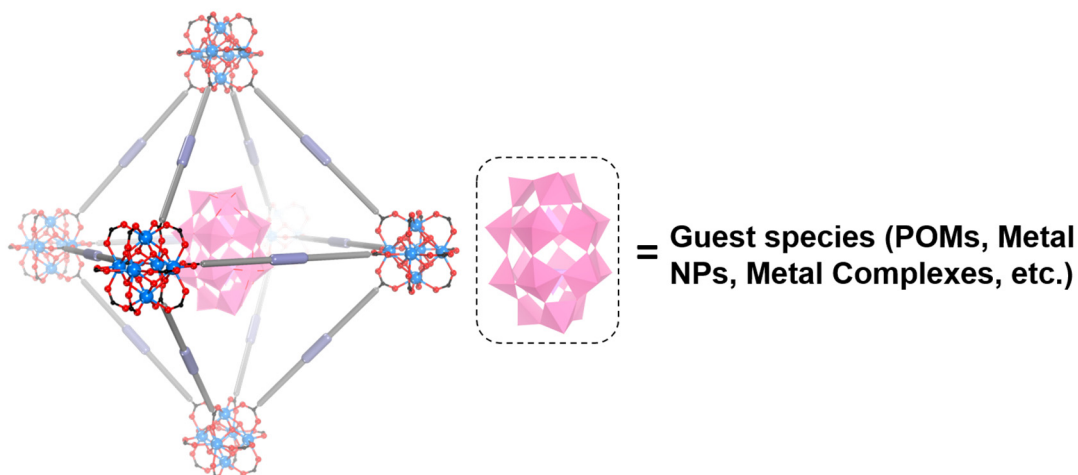


Figure 1-5. Examples of well-developed PSM in MOF cavities.

1.3 MOFs for Catalytic Applications

MOFs have drawn great attention for their catalytic applications as they offer a high density of catalytic sites in a highly porous solid, and often with good stability at high temperatures.³⁹ MOFs have many properties that endow them unique properties as catalysts. MOF catalysts share structural similarity to homogeneous catalysts, but the catalytic sites are isolated from each other in the infinite networks of MOFs. The periodic structures of MOFs ensure that all of active sites are the same and dispersed uniformly throughout the structures. These active sites are accessible to substrates via the pores and channels that are on the order of several Ångstroms to several nanometers in dimensions. These channels and pores also allow the transport of the products away from the catalytic sites to avoid poisoning and inhibition of active sites. As a result, MOF catalysts possess the advantages conferred by a homogeneous catalyst.⁷⁹ Meanwhile, one major advantage of MOF catalysts over homogeneous catalysts is their recyclability, a property that is common to heterogeneous catalysts. Therefore, MOFs nicely combine the merits and advantages of homogeneous metal complex catalysts (high density and uniformity of catalytic sites) and heterogeneous catalysts (rigidity, stability, and recyclability).⁸⁰ Besides, one additional distinct

feature of MOFs is their very high surface areas (BET surface areas ranging from 1000 m²/g to 10000 m²/g), making MOF materials superior to traditional porous materials (e.g. zeolite, silica).⁸¹ The high surface area enables the adsorption and enrichment of substrates around active sites, further facilitating reactant activation and catalytic conversion. More importantly, the well-defined structures throughout the infinite crystalline MOF frameworks are of great importance to study the reaction mechanisms, which can be very difficult to achieve in other systems. This feature of MOF catalysts facilitates the identification of the relationships between structures and catalytic performances.⁸² Therefore, MOF provides a versatile platform for the construction of well-defined solid catalysts for the study of fundamental catalysis.

Over the past two decades, MOFs have been developed to catalyze a broad scope of organic reactions. In this chapter, I would like to focus on MOF-catalyzed reductive-type reactions, Lewis acid promoted reactions, and photocatalytic reactions, as these type reactions will be the subjects of this Ph.D. thesis.

1.3.1 Reductive Reactions

The active metal sites in MOFs have been extensively used as highly active catalysts in reductive reactions (**Figure 1-6**), such as unsaturated bond hydrogenation,^{62, 83-85} hydroborylation,^{65, 86} and more recently, hydrogenolysis of lignocellulosic C-O bonds.⁸⁷⁻⁸⁸ As hydrogenation and hydrofunctionalization reactions are widely used to convert unsaturated feedstocks into valuable compounds in the chemistry industry, MOF catalysts have the potential to replace some currently used precious metal catalysts in reductive reactions. Active site isolation allows MOF catalysts to operate at elevated temperatures which is employed for large scale processes for engineering reasons.

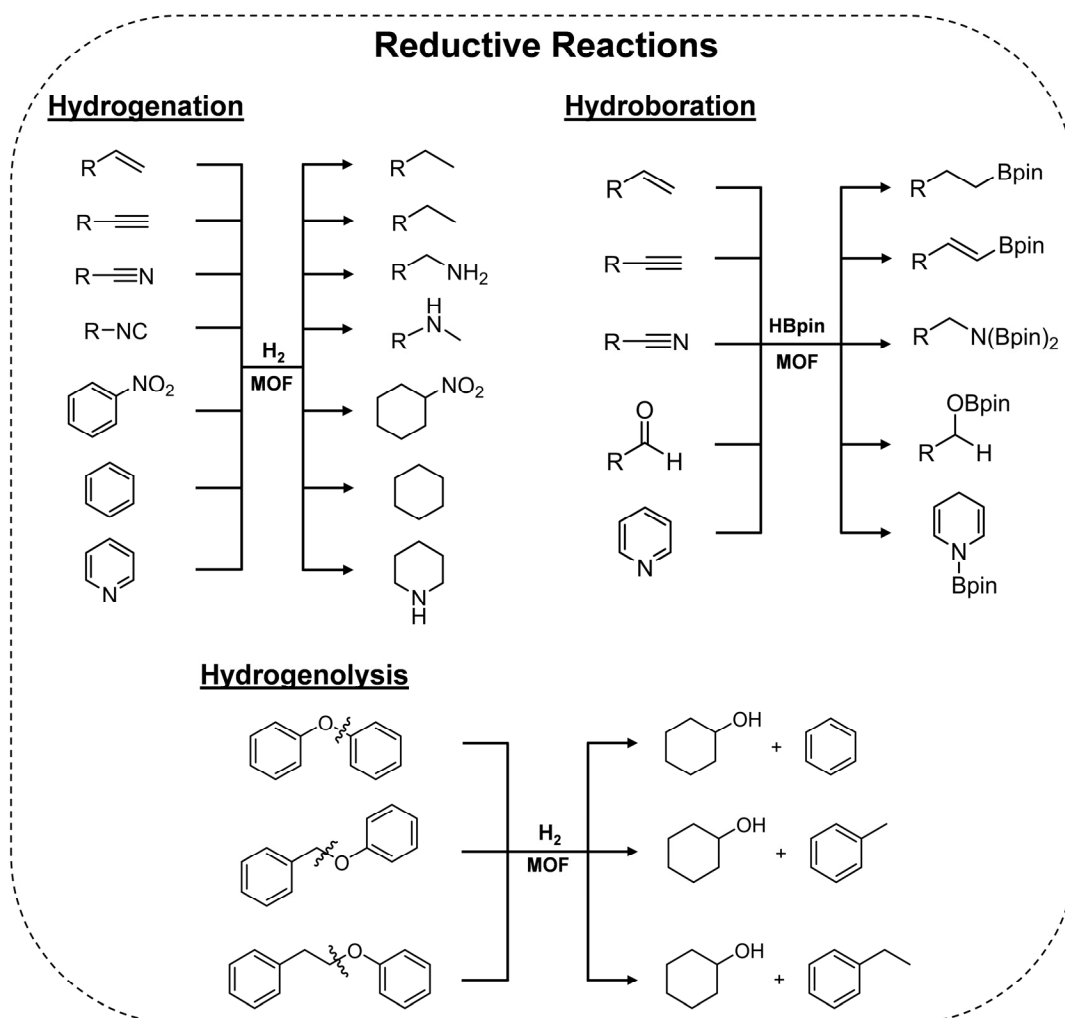


Figure 1-6. MOF-catalyzed reductive reactions.

1.3.2 Lewis Acid Promoted Reactions

As metal nodes of many MOFs have moderate Lewis acidity, MOFs have been extensively explored as Lewis acid catalysts for a variety of organic reactions since the report by Fujita and coworkers on the cyanosilylation reaction between benzaldehyde and cyanotrimethylsilane promoted by Lewis acidic Cd-centers in a Cd coordination polymer.⁸⁹ In most cases, Lewis acidity of MOF materials comes from coordinatively unsaturated metal/metal-oxo SBUs. A wide scope of organic transformations has been catalyzed by Lewis acidic MOFs (**Figure 1-7**), including

epoxide ring-opening reaction,^{68, 90} Diels-alder reaction,^{68, 91-92} Friedel-Craft acylation,^{68, 93} and multicomponent Povarov reactions.⁹⁴

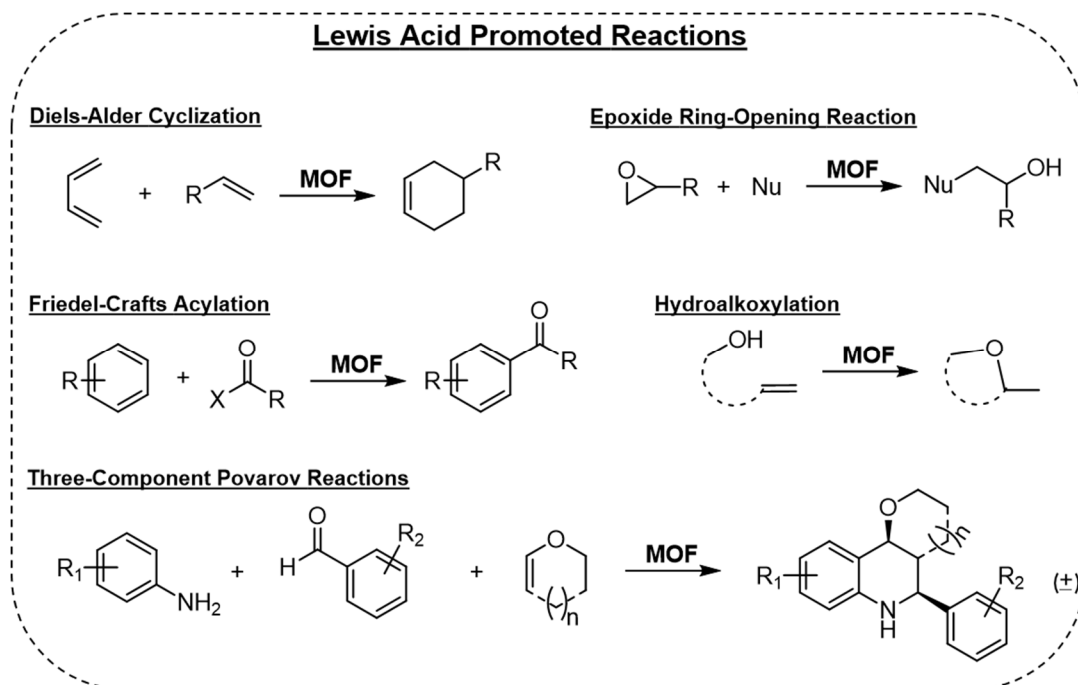


Figure 1-7. MOFs with Lewis acidic sites catalyzed liquid phase organic transformations.

1.3.3 Photocatalytic Reactions

The ever-increasing global demand for energy has spurred extensive research activities on the efficient utilization of solar energy.^{19, 95} As a unique type of heterogeneous catalysis, photocatalysis can transform solar energy to chemical energy and therefore has attracted extensive research interest during the past several decades. As a novel platform, MOF can hierarchically assemble different components to achieve photoresponse for artificial photosynthesis. Compared to traditional photocatalysts, MOFs have some advantages benefiting from their structure diversity and tailorability. First, the crystalline and porous structures enable unrestricted diffusion of both substrates and products. Second, proximity between photosensitizers and catalytic sites significantly improves reaction efficiency. Moreover, the rigid and robust structures provide high

stability of the resultant MOF-based photocatalysts, allowing for recycling and reuse of MOF photocatalysts. The most important advantage of MOFs with respect to other inorganic materials is their well-defined structure. The uniformity of the active sites allows the elucidation of the photocatalytic pathway. MOF-based photocatalysts have been examined for many photocatalytic reactions (**Figure 1-8**), including hydrogen evolution reaction (HER),⁹⁶⁻⁹⁷ CO₂ reduction reaction (CO₂RR),⁹⁸⁻⁹⁹ water oxidation,^{96, 100} and organic transformations.¹⁰¹⁻¹⁰³

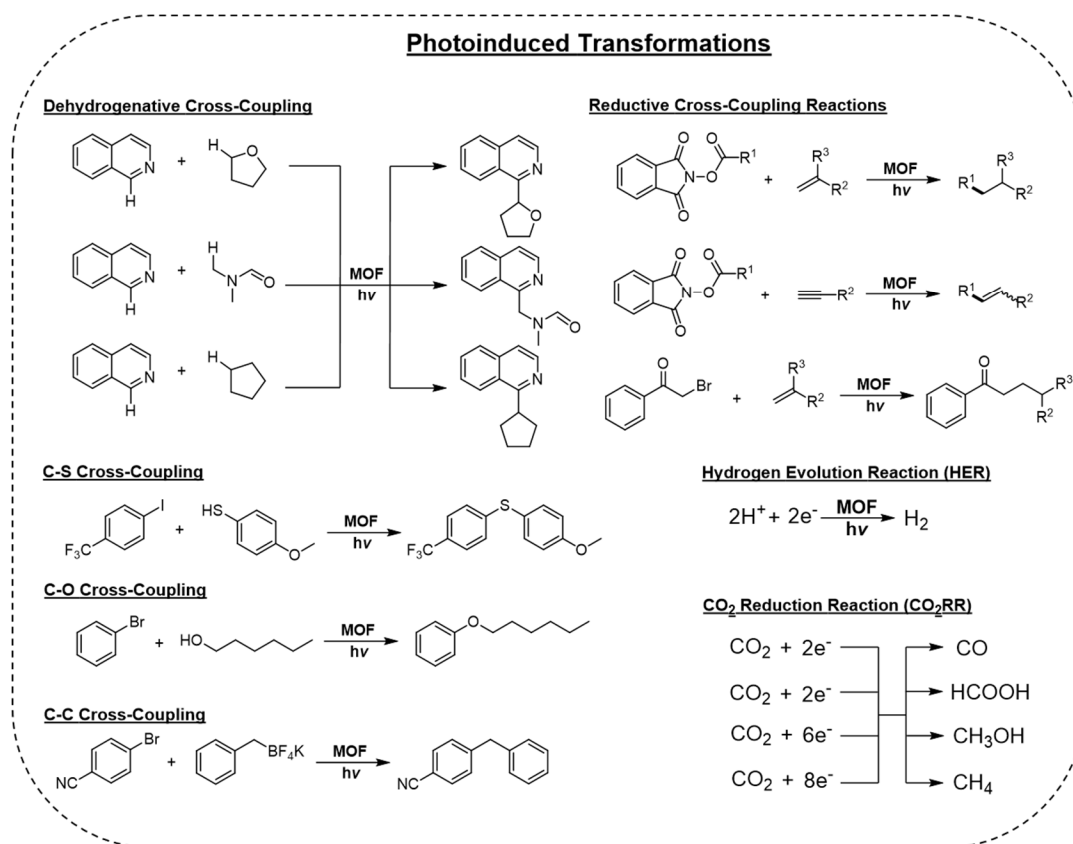


Figure 1-8. MOFs promoted artificial photosynthesis.

1.4 References

- (1) Li, H.; Eddaoudi, M.; O’Keeffe, M.; Yaghi, O. M., Design and synthesis of an exceptionally stable and highly porous metal-organic framework. *Nature* **1999**, *402* (6759), 276-279.
- (2) Tranchemontagne, D. J.; Mendoza-Cortés, J. L.; O’Keeffe, M.; Yaghi, O. M., Secondary building units, nets and bonding in the chemistry of metal-organic frameworks. *Chemical Society Reviews* **2009**, *38* (5), 1257-1283.

- (3) Introduction to Metal–Organic Frameworks. *Chemical Reviews* **2012**, *112* (2), 673-674.
- (4) Zhou, H.-C. J.; Kitagawa, S., Metal–Organic Frameworks (MOFs). *Chemical Society Reviews* **2014**, *43* (16), 5415-5418.
- (5) Marshall, C. R.; Staudhammer, S. A.; Brozek, C. K., Size control over metal–organic framework porous nanocrystals. *Chemical Science* **2019**, *10* (41), 9396-9408.
- (6) Usman, K. A. S.; Maina, J. W.; Seyedin, S.; Conato, M. T.; Payawan, L. M.; Dumée, L. F.; Razal, J. M., Downsizing metal–organic frameworks by bottom-up and top-down methods. *NPG Asia Materials* **2020**, *12* (1), 58.
- (7) Jiao, L.; Wang, Y.; Jiang, H.-L.; Xu, Q., Metal–Organic Frameworks as Platforms for Catalytic Applications. *Advanced Materials* **2018**, *30* (37), 1703663.
- (8) Bartoll, J. In *The early use of Prussian blue in paintings*, Proceedings of the 9th International Conference on NDT of Art, 2008.
- (9) Charpin, P.; Nierlich, M.; Vigner, D.; Lance, M.; Baudry, D., Structure of the second crystalline form of uranium(IV) tetrahydroborate. *Acta Crystallographica Section C* **1987**, *43* (8), 1465-1467.
- (10) Hoskins, B. F.; Robson, R., Infinite polymeric frameworks consisting of three dimensionally linked rod-like segments. *Journal of the American Chemical Society* **1989**, *111* (15), 5962-5964.
- (11) Li, J.-R.; Sculley, J.; Zhou, H.-C., Metal–Organic Frameworks for Separations. *Chemical Reviews* **2012**, *112* (2), 869-932.
- (12) Sumida, K.; Rogow, D. L.; Mason, J. A.; McDonald, T. M.; Bloch, E. D.; Herm, Z. R.; Bae, T.-H.; Long, J. R., Carbon Dioxide Capture in Metal–Organic Frameworks. *Chemical Reviews* **2012**, *112* (2), 724-781.
- (13) Murray, L. J.; Dincă, M.; Long, J. R., Hydrogen storage in metal–organic frameworks. *Chemical Society Reviews* **2009**, *38* (5), 1294-1314.
- (14) Hu, Z.; Deibert, B. J.; Li, J., Luminescent metal–organic frameworks for chemical sensing and explosive detection. *Chemical Society Reviews* **2014**, *43* (16), 5815-5840.
- (15) Giménez-Marqués, M.; Hidalgo, T.; Serre, C.; Horcajada, P., Nanostructured metal–organic frameworks and their bio-related applications. *Coordination Chemistry Reviews* **2016**, *307*, 342-360.
- (16) Della Rocca, J.; Liu, D.; Lin, W., Nanoscale Metal–Organic Frameworks for Biomedical Imaging and Drug Delivery. *Accounts of Chemical Research* **2011**, *44* (10), 957-968.
- (17) Liu, J.; Chen, L.; Cui, H.; Zhang, J.; Zhang, L.; Su, C.-Y., Applications of metal–organic frameworks in heterogeneous supramolecular catalysis. *Chemical Society Reviews* **2014**, *43* (16), 6011-6061.

- (18) Dhakshinamoorthy, A.; Asiri, A. M.; Garcia, H., Metal–organic frameworks catalyzed C–C and C–heteroatom coupling reactions. *Chemical Society Reviews* **2015**, *44* (7), 1922-1947.
- (19) Zhang, T.; Lin, W., Metal–organic frameworks for artificial photosynthesis and photocatalysis. *Chemical Society Reviews* **2014**, *43* (16), 5982-5993.
- (20) Chughtai, A. H.; Ahmad, N.; Younus, H. A.; Laypkov, A.; Verpoort, F., Metal–organic frameworks: versatile heterogeneous catalysts for efficient catalytic organic transformations. *Chemical Society Reviews* **2015**, *44* (19), 6804-6849.
- (21) Ma, L.; Abney, C.; Lin, W., Enantioselective catalysis with homochiral metal–organic frameworks. *Chemical Society Reviews* **2009**, *38* (5), 1248-1256.
- (22) Cui, Y.; Yue, Y.; Qian, G.; Chen, B., Luminescent Functional Metal–Organic Frameworks. *Chemical Reviews* **2012**, *112* (2), 1126-1162.
- (23) Mínguez Espallargas, G.; Coronado, E., Magnetic functionalities in MOFs: from the framework to the pore. *Chemical Society Reviews* **2018**, *47* (2), 533-557.
- (24) Rosi, N. L.; Eckert, J.; Eddaoudi, M.; Vodak, D. T.; Kim, J.; Keeffe, M.; Yaghi, O. M., Hydrogen Storage in Microporous Metal-Organic Frameworks. *Science* **2003**, *300* (5622), 1127.
- (25) Park, K. S.; Ni, Z.; Côté, A. P.; Choi, J. Y.; Huang, R.; Uribe-Romo, F. J.; Chae, H. K.; O’Keeffe, M.; Yaghi, O. M., Exceptional chemical and thermal stability of zeolitic imidazolate frameworks. *Proceedings of the National Academy of Sciences* **2006**, *103* (27), 10186.
- (26) Karagiari, O.; Lalonde, M. B.; Bury, W.; Sarjeant, A. A.; Farha, O. K.; Hupp, J. T., Opening ZIF-8: A Catalytically Active Zeolitic Imidazolate Framework of Sodalite Topology with Unsubstituted Linkers. *Journal of the American Chemical Society* **2012**, *134* (45), 18790-18796.
- (27) Kuo, C.-H.; Tang, Y.; Chou, L.-Y.; Sneed, B. T.; Brodsky, C. N.; Zhao, Z.; Tsung, C.-K., Yolk–Shell Nanocrystal@ZIF-8 Nanostructures for Gas-Phase Heterogeneous Catalysis with Selectivity Control. *Journal of the American Chemical Society* **2012**, *134* (35), 14345-14348.
- (28) Chui, S. S. Y.; Lo, S. M. F.; Charmant, J. P. H.; Orpen, A. G.; Williams, I. D., A Chemically Functionalizable Nanoporous Material [Cu₃(TMA)₂(H₂O)₃]_n. *Science* **1999**, *283* (5405), 1148.
- (29) Fan, S.; Dong, W.; Huang, X.; Gao, H.; Wang, J.; Jin, Z.; Tang, J.; Wang, G., In Situ-Induced Synthesis of Magnetic Cu-CuFe₂O₄@HKUST-1 Heterostructures with Enhanced Catalytic Performance for Selective Aerobic Benzylic C–H Oxidation. *ACS Catalysis* **2017**, *7* (1), 243-249.
- (30) Millange, F.; Serre, C.; Férey, G., Synthesis, structure determination and properties of MIL-53as and MIL-53ht: the first C₃ hybrid inorganic–organic microporous solids: C₃(OH)·{O₂C–C₆H₄–CO₂}·{HO₂C–C₆H₄–CO₂H}_x. *Chemical Communications* **2002**, (8), 822-823.

- (31) Ai, L.; Li, L.; Zhang, C.; Fu, J.; Jiang, J., MIL-53(Fe): A Metal–Organic Framework with Intrinsic Peroxidase-Like Catalytic Activity for Colorimetric Biosensing. *Chemistry – A European Journal* **2013**, *19* (45), 15105-15108.
- (32) Dan-Hardi, M.; Serre, C.; Frot, T.; Rozes, L.; Maurin, G.; Sanchez, C.; Férey, G., A New Photoactive Crystalline Highly Porous Titanium(IV) Dicarboxylate. *Journal of the American Chemical Society* **2009**, *131* (31), 10857-10859.
- (33) Sun, D.; Ye, L.; Li, Z., Visible-light-assisted aerobic photocatalytic oxidation of amines to imines over NH₂-MIL-125(Ti). *Applied Catalysis B: Environmental* **2015**, *164*, 428-432.
- (34) Fu, Y.; Sun, D.; Chen, Y.; Huang, R.; Ding, Z.; Fu, X.; Li, Z., An Amine-Functionalized Titanium Metal–Organic Framework Photocatalyst with Visible-Light-Induced Activity for CO₂ Reduction. *Angewandte Chemie International Edition* **2012**, *51* (14), 3364-3367.
- (35) Cavka, J. H.; Jakobsen, S.; Olsbye, U.; Guillou, N.; Lamberti, C.; Bordiga, S.; Lillerud, K. P., A New Zirconium Inorganic Building Brick Forming Metal Organic Frameworks with Exceptional Stability. *Journal of the American Chemical Society* **2008**, *130* (42), 13850-13851.
- (36) Waitschat, S.; Fröhlich, D.; Reinsch, H.; Terraschke, H.; Lomachenko, K. A.; Lamberti, C.; Kummer, H.; Helling, T.; Baumgartner, M.; Henninger, S.; Stock, N., Synthesis of M-Uio-66 (M = Zr, Ce or Hf) employing 2,5-pyridinedicarboxylic acid as a linker: defect chemistry, framework hydrophilisation and sorption properties. *Dalton Transactions* **2018**, *47* (4), 1062-1070.
- (37) Furukawa, H.; Gándara, F.; Zhang, Y.-B.; Jiang, J.; Queen, W. L.; Hudson, M. R.; Yaghi, O. M., Water Adsorption in Porous Metal–Organic Frameworks and Related Materials. *Journal of the American Chemical Society* **2014**, *136* (11), 4369-4381.
- (38) Mondloch, J. E.; Bury, W.; Fairen-Jimenez, D.; Kwon, S.; DeMarco, E. J.; Weston, M. H.; Sarjeant, A. A.; Nguyen, S. T.; Stair, P. C.; Snurr, R. Q.; Farha, O. K.; Hupp, J. T., Vapor-Phase Metalation by Atomic Layer Deposition in a Metal–Organic Framework. *Journal of the American Chemical Society* **2013**, *135* (28), 10294-10297.
- (39) Wei, Y.-S.; Zhang, M.; Zou, R.; Xu, Q., Metal–Organic Framework-Based Catalysts with Single Metal Sites. *Chemical Reviews* **2020**, *120* (21), 12089-12174.
- (40) Feng, X.; Song, Y.; Lin, W., Transforming Hydroxide-Containing Metal–Organic Framework Nodes for Transition Metal Catalysis. *Trends in Chemistry* **2020**, *2* (11), 965-979.
- (41) Guo, J.; Qin, Y.; Zhu, Y.; Zhang, X.; Long, C.; Zhao, M.; Tang, Z., Metal–organic frameworks as catalytic selectivity regulators for organic transformations. *Chemical Society Reviews* **2021**, *50* (9), 5366-5396.
- (42) Whelan, É.; Steuber, F. W.; Gunnlaugsson, T.; Schmitt, W., Tuning photoactive metal–organic frameworks for luminescence and photocatalytic applications. *Coordination Chemistry Reviews* **2021**, *437*, 213757.

- (43) Jiang, J.; Yaghi, O. M., Brønsted Acidity in Metal–Organic Frameworks. *Chemical Reviews* **2015**, *115* (14), 6966-6997.
- (44) Zhu, L.; Liu, X.-Q.; Jiang, H.-L.; Sun, L.-B., Metal–Organic Frameworks for Heterogeneous Basic Catalysis. *Chemical Reviews* **2017**, *117* (12), 8129-8176.
- (45) Seo, J. S.; Whang, D.; Lee, H.; Jun, S. I.; Oh, J.; Jeon, Y. J.; Kim, K., A homochiral metal–organic porous material for enantioselective separation and catalysis. *Nature* **2000**, *404* (6781), 982-986.
- (46) Wu, C.-D.; Hu, A.; Zhang, L.; Lin, W., A Homochiral Porous Metal–Organic Framework for Highly Enantioselective Heterogeneous Asymmetric Catalysis. *Journal of the American Chemical Society* **2005**, *127* (25), 8940-8941.
- (47) Cohen, S. M., The Postsynthetic Renaissance in Porous Solids. *Journal of the American Chemical Society* **2017**, *139* (8), 2855-2863.
- (48) Venkataraman, D.; Gardner, G. B.; Lee, S.; Moore, J. S., Zeolite-like Behavior of a Coordination Network. *Journal of the American Chemical Society* **1995**, *117* (46), 11600-11601.
- (49) Cohen, S. M., Postsynthetic Methods for the Functionalization of Metal–Organic Frameworks. *Chemical Reviews* **2012**, *112* (2), 970-1000.
- (50) Wang, Z.; Cohen, S. M., Postsynthetic Covalent Modification of a Neutral Metal–Organic Framework. *Journal of the American Chemical Society* **2007**, *129* (41), 12368-12369.
- (51) Wang, Z.; Tanabe, K. K.; Cohen, S. M., Accessing Postsynthetic Modification in a Series of Metal–Organic Frameworks and the Influence of Framework Topology on Reactivity. *Inorganic Chemistry* **2009**, *48* (1), 296-306.
- (52) Garibay, S. J.; Wang, Z.; Cohen, S. M., Evaluation of Heterogeneous Metal–Organic Framework Organocatalysts Prepared by Postsynthetic Modification. *Inorganic Chemistry* **2010**, *49* (17), 8086-8091.
- (53) Goto, Y.; Sato, H.; Shinkai, S.; Sada, K., “Clickable” Metal–Organic Framework. *Journal of the American Chemical Society* **2008**, *130* (44), 14354-14355.
- (54) Savonnet, M.; Bazer-Bachi, D.; Bats, N.; Perez-Pellitero, J.; Jeanneau, E.; Lecocq, V.; Pinel, C.; Farrusseng, D., Generic Postfunctionalization Route from Amino-Derived Metal–Organic Frameworks. *Journal of the American Chemical Society* **2010**, *132* (13), 4518-4519.
- (55) Morris, W.; Doonan, C. J.; Furukawa, H.; Banerjee, R.; Yaghi, O. M., Crystals as Molecules: Postsynthesis Covalent Functionalization of Zeolitic Imidazolate Frameworks. *Journal of the American Chemical Society* **2008**, *130* (38), 12626-12627.
- (56) Jones, S. C.; Bauer, C. A., Diastereoselective Heterogeneous Bromination of Stilbene in a Porous Metal–Organic Framework. *Journal of the American Chemical Society* **2009**, *131* (35), 12516-12517.

- (57) Garibay, S. J.; Cohen, S. M., Isorecticular synthesis and modification of frameworks with the UiO-66 topology. *Chemical Communications* **2010**, 46 (41), 7700-7702.
- (58) Burrows, A. D.; Frost, C. G.; Mahon, M. F.; Richardson, C., Sulfur-tagged metal–organic frameworks and their post-synthetic oxidation. *Chemical Communications* **2009**, (28), 4218-4220.
- (59) Kaye, S. S.; Long, J. R., Matrix Isolation Chemistry in a Porous Metal–Organic Framework: Photochemical Substitutions of N₂ and H₂ in Zn₄O[(η⁶-1,4-Benzenedicarboxylate)Cr(CO)₃]₃. *Journal of the American Chemical Society* **2008**, 130 (3), 806-807.
- (60) Sawano, T.; Ji, P.; McIsaac, A. R.; Lin, Z.; Abney, C. W.; Lin, W., The first chiral diene-based metal–organic frameworks for highly enantioselective carbon–carbon bond formation reactions. *Chemical Science* **2015**, 6 (12), 7163-7168.
- (61) Manna, K.; Zhang, T.; Lin, W., Postsynthetic Metalation of Bipyridyl-Containing Metal–Organic Frameworks for Highly Efficient Catalytic Organic Transformations. *Journal of the American Chemical Society* **2014**, 136 (18), 6566-6569.
- (62) Zhang, T.; Manna, K.; Lin, W., Metal–Organic Frameworks Stabilize Solution-Inaccessible Cobalt Catalysts for Highly Efficient Broad-Scope Organic Transformations. *Journal of the American Chemical Society* **2016**, 138 (9), 3241-3249.
- (63) Manna, K.; Zhang, T.; Carboni, M.; Abney, C. W.; Lin, W., Salicylaldimine-Based Metal–Organic Framework Enabling Highly Active Olefin Hydrogenation with Iron and Cobalt Catalysts. *Journal of the American Chemical Society* **2014**, 136 (38), 13182-13185.
- (64) Thacker, N. C.; Lin, Z.; Zhang, T.; Gilhula, J. C.; Abney, C. W.; Lin, W., Robust and Porous β-Diketiminato-Functionalized Metal–Organic Frameworks for Earth-Abundant-Metal-Catalyzed C–H Amination and Hydrogenation. *Journal of the American Chemical Society* **2016**, 138 (10), 3501-3509.
- (65) Manna, K.; Ji, P.; Lin, Z.; Greene, F. X.; Urban, A.; Thacker, N. C.; Lin, W., Chemoselective single-site Earth-abundant metal catalysts at metal–organic framework nodes. *Nature Communications* **2016**, 7 (1), 12610.
- (66) Nguyen, H. G. T.; Schweitzer, N. M.; Chang, C.-Y.; Drake, T. L.; So, M. C.; Stair, P. C.; Farha, O. K.; Hupp, J. T.; Nguyen, S. T., Vanadium-Node-Functionalized UiO-66: A Thermally Stable MOF-Supported Catalyst for the Gas-Phase Oxidative Dehydrogenation of Cyclohexene. *ACS Catalysis* **2014**, 4 (8), 2496-2500.
- (67) Madrahimov, S. T.; Gallagher, J. R.; Zhang, G.; Meinhart, Z.; Garibay, S. J.; Delferro, M.; Miller, J. T.; Farha, O. K.; Hupp, J. T.; Nguyen, S. T., Gas-Phase Dimerization of Ethylene under Mild Conditions Catalyzed by MOF Materials Containing (bpy)Ni^{II} Complexes. *ACS Catalysis* **2015**, 5 (11), 6713-6718.
- (68) Ji, P.; Feng, X.; Oliveres, P.; Li, Z.; Murakami, A.; Wang, C.; Lin, W., Strongly Lewis Acidic Metal–Organic Frameworks for Continuous Flow Catalysis. *Journal of the American Chemical Society* **2019**, 141 (37), 14878-14888.

- (69) Brozek, C. K.; Dincă, M., Cation exchange at the secondary building units of metal–organic frameworks. *Chemical Society Reviews* **2014**, *43* (16), 5456-5467.
- (70) Comito, R. J.; Fritzsche, K. J.; Sundell, B. J.; Schmidt-Rohr, K.; Dincă, M., Single-Site Heterogeneous Catalysts for Olefin Polymerization Enabled by Cation Exchange in a Metal–Organic Framework. *Journal of the American Chemical Society* **2016**, *138* (32), 10232-10237.
- (71) Ji, P.; Feng, X.; Veroneau, S. S.; Song, Y.; Lin, W., Trivalent Zirconium and Hafnium Metal–Organic Frameworks for Catalytic 1,4-De-aromatic Additions of Pyridines and Quinolines. *Journal of the American Chemical Society* **2017**, *139* (44), 15600-15603.
- (72) Hermes, S.; Schröter, M.-K.; Schmid, R.; Khodeir, L.; Muhler, M.; Tissler, A.; Fischer, R. W.; Fischer, R. A., Metal@MOF: Loading of Highly Porous Coordination Polymers Host Lattices by Metal Organic Chemical Vapor Deposition. *Angewandte Chemie International Edition* **2005**, *44* (38), 6237-6241.
- (73) Lu, G.; Li, S.; Guo, Z.; Farha, O. K.; Hauser, B. G.; Qi, X.; Wang, Y.; Wang, X.; Han, S.; Liu, X.; DuChene, J. S.; Zhang, H.; Zhang, Q.; Chen, X.; Ma, J.; Loo, S. C. J.; Wei, W. D.; Yang, Y.; Hupp, J. T.; Huo, F., Imparting functionality to a metal–organic framework material by controlled nanoparticle encapsulation. *Nature Chemistry* **2012**, *4* (4), 310-316.
- (74) Wang, S.; Fan, Y.; Teng, J.; Fan, Y.-Z.; Jiang, J.-J.; Wang, H.-P.; Grützmacher, H.; Wang, D.; Su, C.-Y., Nanoreactor Based on Macroporous Single Crystals of Metal–Organic Framework. *Small* **2016**, *12* (41), 5702-5709.
- (75) Alkordi, M. H.; Liu, Y.; Larsen, R. W.; Eubank, J. F.; Eddaoudi, M., Zeolite-like Metal–Organic Frameworks as Platforms for Applications: On Metalloporphyrin-Based Catalysts. *Journal of the American Chemical Society* **2008**, *130* (38), 12639-12641.
- (76) Li, B.; Zhang, Y.; Ma, D.; Ma, T.; Shi, Z.; Ma, S., Metal-Cation-Directed de Novo Assembly of a Functionalized Guest Molecule in the Nanospace of a Metal–Organic Framework. *Journal of the American Chemical Society* **2014**, *136* (4), 1202-1205.
- (77) Zhang, Z.-M.; Zhang, T.; Wang, C.; Lin, Z.; Long, L.-S.; Lin, W., Photosensitizing Metal–Organic Framework Enabling Visible-Light-Driven Proton Reduction by a Wells–Dawson-Type Polyoxometalate. *Journal of the American Chemical Society* **2015**, *137* (9), 3197-3200.
- (78) Kong, X.-J.; Lin, Z.; Zhang, Z.-M.; Zhang, T.; Lin, W., Hierarchical Integration of Photosensitizing Metal–Organic Frameworks and Nickel-Containing Polyoxometalates for Efficient Visible-Light-Driven Hydrogen Evolution. *Angewandte Chemie International Edition* **2016**, *55* (22), 6411-6416.
- (79) Kang, Y.-S.; Lu, Y.; Chen, K.; Zhao, Y.; Wang, P.; Sun, W.-Y., Metal–organic frameworks with catalytic centers: From synthesis to catalytic application. *Coordination Chemistry Reviews* **2019**, *378*, 262-280.
- (80) Chen, K.; Wu, C.-D., Designed fabrication of biomimetic metal–organic frameworks for catalytic applications. *Coordination Chemistry Reviews* **2019**, *378*, 445-465.

- (81) Opanasenko, M.; Dhakshinamoorthy, A.; Hwang, Y. K.; Chang, J.-S.; Garcia, H.; Čejka, J., Superior Performance of Metal–Organic Frameworks over Zeolites as Solid Acid Catalysts in the Prins Reaction: Green Synthesis of Nopol. *ChemSusChem* **2013**, *6* (5), 865-871.
- (82) Colón, Y. J.; Snurr, R. Q., High-throughput computational screening of metal–organic frameworks. *Chemical Society Reviews* **2014**, *43* (16), 5735-5749.
- (83) Ji, P.; Manna, K.; Lin, Z.; Urban, A.; Greene, F. X.; Lan, G.; Lin, W., Single-Site Cobalt Catalysts at New $Zr_8(\mu_2-O)_8(\mu_2-OH)_4$ Metal–Organic Framework Nodes for Highly Active Hydrogenation of Alkenes, Imines, Carbonyls, and Heterocycles. *Journal of the American Chemical Society* **2016**, *138* (37), 12234-12242.
- (84) Ji, P.; Manna, K.; Lin, Z.; Feng, X.; Urban, A.; Song, Y.; Lin, W., Single-Site Cobalt Catalysts at New $Zr_{12}(\mu_3-O)_8(\mu_3-OH)_8(\mu_2-OH)_6$ Metal–Organic Framework Nodes for Highly Active Hydrogenation of Nitroarenes, Nitriles, and Isocyanides. *Journal of the American Chemical Society* **2017**, *139* (20), 7004-7011.
- (85) Ji, P.; Song, Y.; Drake, T.; Veroneau, S. S.; Lin, Z.; Pan, X.; Lin, W., Titanium(III)-Oxo Clusters in a Metal–Organic Framework Support Single-Site Co(II)-Hydride Catalysts for Arene Hydrogenation. *Journal of the American Chemical Society* **2018**, *140* (1), 433-440.
- (86) Feng, X.; Ji, P.; Li, Z.; Drake, T.; Oliveres, P.; Chen, E. Y.; Song, Y.; Wang, C.; Lin, W., Aluminum Hydroxide Secondary Building Units in a Metal–Organic Framework Support Earth-Abundant Metal Catalysts for Broad-Scope Organic Transformations. *ACS Catalysis* **2019**, *9* (4), 3327-3337.
- (87) Song, Y.; Li, Z.; Ji, P.; Kaufmann, M.; Feng, X.; Chen, J. S.; Wang, C.; Lin, W., Metal–Organic Framework Nodes Support Single-Site Nickel(II) Hydride Catalysts for the Hydrogenolysis of Aryl Ethers. *ACS Catalysis* **2019**, *9* (2), 1578-1583.
- (88) Song, Y.; Feng, X.; Chen, J. S.; Brzezinski, C.; Xu, Z.; Lin, W., Multistep Engineering of Synergistic Catalysts in a Metal–Organic Framework for Tandem C–O Bond Cleavage. *Journal of the American Chemical Society* **2020**, *142* (10), 4872-4882.
- (89) Fujita, M.; Kwon, Y. J.; Washizu, S.; Ogura, K., Preparation, Clathration Ability, and Catalysis of a Two-Dimensional Square Network Material Composed of Cadmium(II) and 4,4'-Bipyridine. *Journal of the American Chemical Society* **1994**, *116* (3), 1151-1152.
- (90) Hu, Z.; Zhao, D., Metal–organic frameworks with Lewis acidity: synthesis, characterization, and catalytic applications. *CrystEngComm* **2017**, *19* (29), 4066-4081.
- (91) Ji, P.; Drake, T.; Murakami, A.; Oliveres, P.; Skone, J. H.; Lin, W., Tuning Lewis Acidity of Metal–Organic Frameworks via Perfluorination of Bridging Ligands: Spectroscopic, Theoretical, and Catalytic Studies. *Journal of the American Chemical Society* **2018**, *140* (33), 10553-10561.
- (92) Gole, B.; Bar, A. K.; Mallick, A.; Banerjee, R.; Mukherjee, P. S., An electron rich porous extended framework as a heterogeneous catalyst for Diels–Alder reactions. *Chemical Communications* **2013**, *49* (67), 7439-7441.

- (93) Rahmani, E.; Rahmani, M., Al-Based MIL-53 Metal Organic Framework (MOF) as the New Catalyst for Friedel–Crafts Alkylation of Benzene. *Industrial & Engineering Chemistry Research* **2018**, *57* (1), 169-178.
- (94) Feng, X.; Song, Y.; Lin, W., Dimensional Reduction of Lewis Acidic Metal–Organic Frameworks for Multicomponent Reactions. *Journal of the American Chemical Society* **2021**, *143* (21), 8184-8192.
- (95) Dhakshinamoorthy, A.; Li, Z.; Garcia, H., Catalysis and photocatalysis by metal organic frameworks. *Chemical Society Reviews* **2018**, *47* (22), 8134-8172.
- (96) Meyer, K.; Ranocchiari, M.; van Bokhoven, J. A., Metal organic frameworks for photocatalytic water splitting. *Energy & Environmental Science* **2015**, *8* (7), 1923-1937.
- (97) Liu, S.; Zhang, C.; Sun, Y.; Chen, Q.; He, L.; Zhang, K.; Zhang, J.; Liu, B.; Chen, L.-F., Design of metal-organic framework-based photocatalysts for hydrogen generation. *Coordination Chemistry Reviews* **2020**, *413*, 213266.
- (98) Alkhatib, I. I.; Garlisi, C.; Pagliaro, M.; Al-Ali, K.; Palmisano, G., Metal-organic frameworks for photocatalytic CO₂ reduction under visible radiation: A review of strategies and applications. *Catalysis Today* **2020**, *340*, 209-224.
- (99) M.S, R.; Shanmuga Priya, S.; Freudenberg, N. C.; Sudhakar, K.; Tahir, M., Metal-organic framework-based photocatalysts for carbon dioxide reduction to methanol: A review on progress and application. *Journal of CO₂ Utilization* **2021**, *43*, 101374.
- (100) Wang, C.; Xie, Z.; deKrafft, K. E.; Lin, W., Doping Metal–Organic Frameworks for Water Oxidation, Carbon Dioxide Reduction, and Organic Photocatalysis. *Journal of the American Chemical Society* **2011**, *133* (34), 13445-13454.
- (101) Yu, X.; Wang, L.; Cohen, S. M., Photocatalytic metal–organic frameworks for organic transformations. *CrystEngComm* **2017**, *19* (29), 4126-4136.
- (102) Zhu, Y.-Y.; Lan, G.; Fan, Y.; Veroneau, S. S.; Song, Y.; Micheroni, D.; Lin, W., Merging Photoredox and Organometallic Catalysts in a Metal–Organic Framework Significantly Boosts Photocatalytic Activities. *Angewandte Chemie International Edition* **2018**, *57* (43), 14090-14094.
- (103) Quan, Y.; Song, Y.; Shi, W.; Xu, Z.; Chen, J. S.; Jiang, X.; Wang, C.; Lin, W., Metal–Organic Framework with Dual Active Sites in Engineered Mesopores for Bioinspired Synergistic Catalysis. *Journal of the American Chemical Society* **2020**, *142* (19), 8602-8607.

Chapter 2. Metal-Organic Framework Nodes Support Single-Site Nickel (II)-Hydride Catalysts for the Hydrogenolysis of Aryl Ethers

2.1 Introduction

The rising concerns about global climate change and the depletion of fossil fuels have stimulated the pursuit of energy and commodity chemicals from renewable sources. Lignin, composing 15-30 wt % of lignocellulosic biomass and carrying 40% of its energy,¹ has the potential to supplement or replace traditional crude oil or coal as a source of arenes. However, due to the high strength and stability of its aryl ether bonds, selective depolymerization of lignin into small molecules is a great challenge.²⁻³ To date, hydrogenolysis has been examined as one route to depolymerize lignin,⁴ but most lignin hydrogenolysis reactions require non-sustainable catalysts based on Pd, Ru, Rh, and Pt and harsh reaction conditions.⁵⁻⁷ Nickel (Ni)-based catalysts are highly effective for hydrogenolysis reaction, and have been explored by several research groups for lignin hydrogenolysis reactions due high earth abundance and low price of Ni compared to other transition metals. Recently, Hartwig's group reported an exciting protocol for the cleavage of aryl ethers under mild conditions based on homogenous Ni catalysts.⁸⁻⁹ Heterogeneous catalysts with Ni nanoparticles stabilized on various supports have also been examined for reductive cleavage of aryl ethers.¹⁰⁻¹⁵ However, incomplete utilization of Ni centers on nanoparticles has compromised the overall reaction efficiency, and nonuniformity of the catalytic centers complicated the delineation of active catalysts and reaction mechanisms. Thus, it is highly desirable to construct a truly single-site solid catalyst to improve the catalytic efficiency and illuminate the corresponding C-O cleavage mechanism.

Metal-organic frameworks (MOFs) have emerged as a highly tunable material platform for the construction of single-site solid catalysts.¹⁶⁻²⁰ In this chapter, we used Ti-oxo/hydroxo

secondary building units (SBUs) of MIL-125 ($\text{Ti}_8\text{-BDC}$, BDC is 1,4-benzenedicarboxylate) to support Ni^{II} -H catalyst for highly effective and selective hydrogenolysis of aryl ethers commonly found in lignin (**Figure 2-1**). We further demonstrated that reduction of Ti_8 SBUs tuned the electronic properties of Ni^{II} -H catalyst to affect the reactivity towards the hydrogenolysis of aryl ethers.

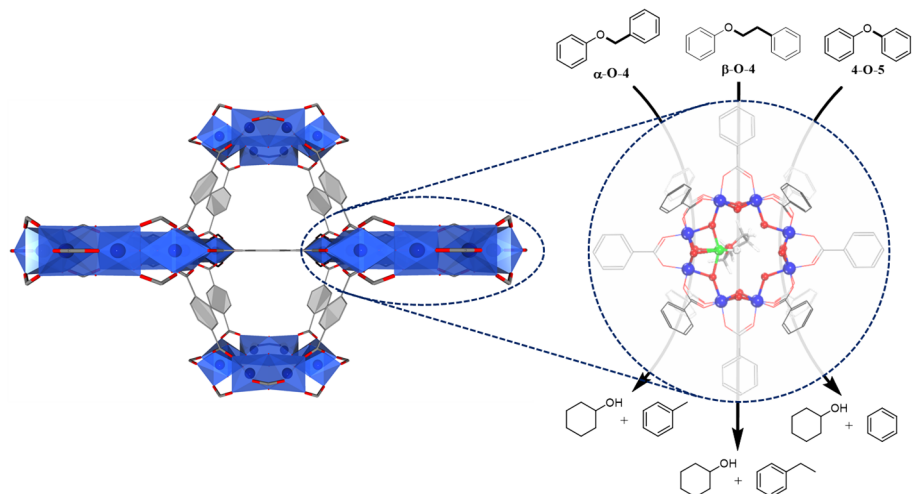


Figure 2-1. Ti_8 node-supported Ni^{II} -H catalyzes hydrogenolysis of lignin model compounds. Titanium, nickel, oxygen, carbon and hydrogen atoms are shown in blue, green, red, gray and white, respectively. Reprinted with permission from *ACS Catalysis*, **2019**, 9, 1578-1583. Copyright 2019 American Chemical Society.

2.2 Results and Discussion

2.2.1 Synthesis and Characterization of $\text{Ti}_8\text{-BDC-NiBr}$

The $\text{Ti}_8\text{-BDC}$ MOF, with the formula $\text{Ti}_8\text{O}_8(\text{OH})_4(\text{BDC})_6$ was prepared solvothermally from $\text{Ti}(\text{OiPr})_4$, H_2BDC , methanol, and dimethylformamide (DMF) according to the literature procedure.¹⁶ This MOF was metalated via first deprotonation with $\text{LiCH}_2\text{SiMe}_3$ to generate the $\text{Ti}_8\text{O}_8(\text{OLi})_4(\text{BDC})_6$ intermediate, and then treated with 1 equiv. of NiBr_2 to generate $\text{Ti}_8\text{-BDC-NiBr}$ as a light-yellow solid. The Ni content in the metalated MOF was determined to be 0.37 Ni per Ti_8 cluster by inductively coupled plasma-mass spectroscopy (ICP-MS).

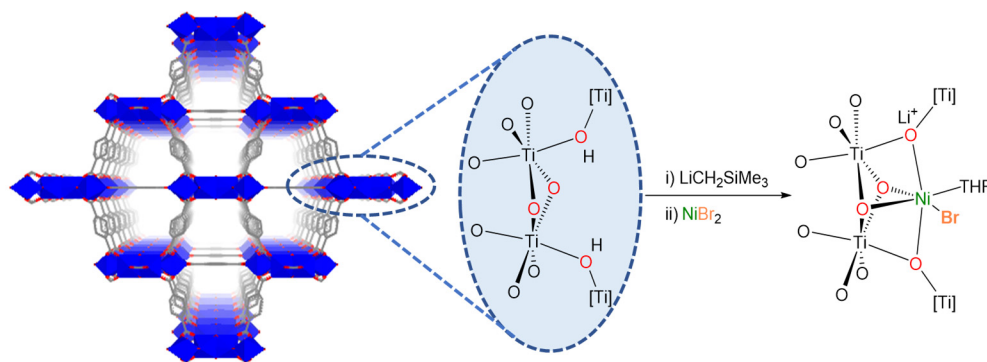


Figure 2-2. Structure of $\text{Ti}_8\text{-BDC}$ and its metalation with NiBr_2 to form $\text{Ti}_8\text{-BDC-NiBr}$. Reprinted with permission from *ACS Catalysis*, **2019**, 9, 1578-1583. Copyright 2019 American Chemical Society.

The $\text{Ti}_8\text{-BDC-NiBr}$ MOF maintained the crystallinity of pristine $\text{Ti}_8\text{-BDC}$ MOF, shown by powder X-ray diffraction (PXRD) patterns (**Figure 2-3a**). Transmission electron microscopy (TEM) imaging showed that $\text{Ti}_8\text{-BDC-NiBr}$ particles maintained the plate-like morphology of $\text{Ti}_8\text{-BDC}$ (**Figure 2-3b**). Nitrogen sorption isotherms of $\text{Ti}_8\text{-BDC-NiBr}$ indicated highly a porous structure with a Brunauer-Emmett-Teller (BET) surface area of $1280 \text{ m}^2/\text{g}$, which is slightly lower than that of $\text{Ti}_8\text{-BDC}$ ($1552 \text{ m}^2/\text{g}$, **Figure 2-3c**).

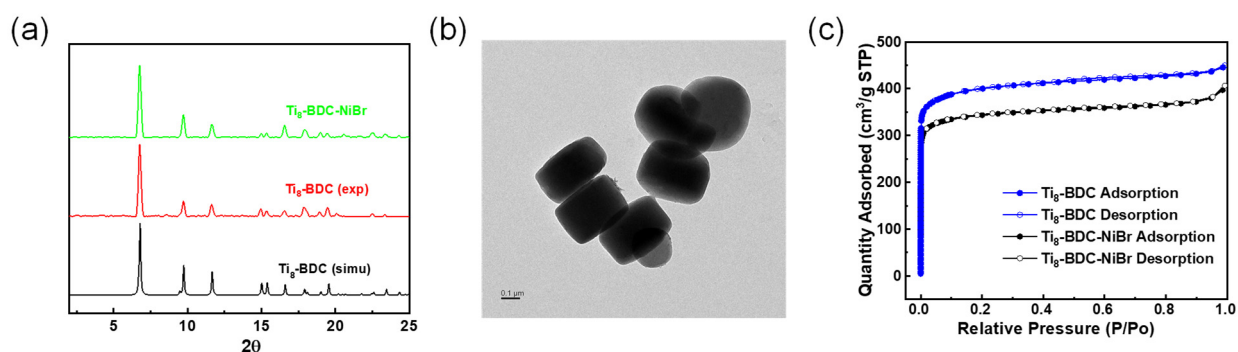


Figure 2-3. (a) PXRD patterns of $\text{Ti}_8\text{-BDC}$ (red) and $\text{Ti}_8\text{-BDC-NiBr}$ (green) in comparison to the PXRD pattern simulated from the CIF file of $\text{Ti}_8\text{-BDC}$ (black). (b) TEM image of $\text{Ti}_8\text{-BDC-NiBr}$. (c) Nitrogen sorption isotherms of $\text{Ti}_8\text{-BDC}$ (black) and $\text{Ti}_8\text{-BDC-NiBr}$ (blue). Adapted with permission from *ACS Catalysis*, **2019**, 9, 1578-1583. Copyright 2019 American Chemical Society.

The Ni coordination environment of Ti₈-BDC-NiBr was optimized by density functional theory (DFT) calculation using the B3LYP functional.²¹⁻²³ DFT optimization converged at a geometry with the octahedral Ni ion sitting in the Ti₈ octagonal plane and coordinated to two anionic bridging-oxo ($\mu_2\text{-O}^-$) groups in the axial positions and two neutral bridging-oxo ($\mu_2\text{-O}$) groups at lateral positions (**Figure 2-4**).

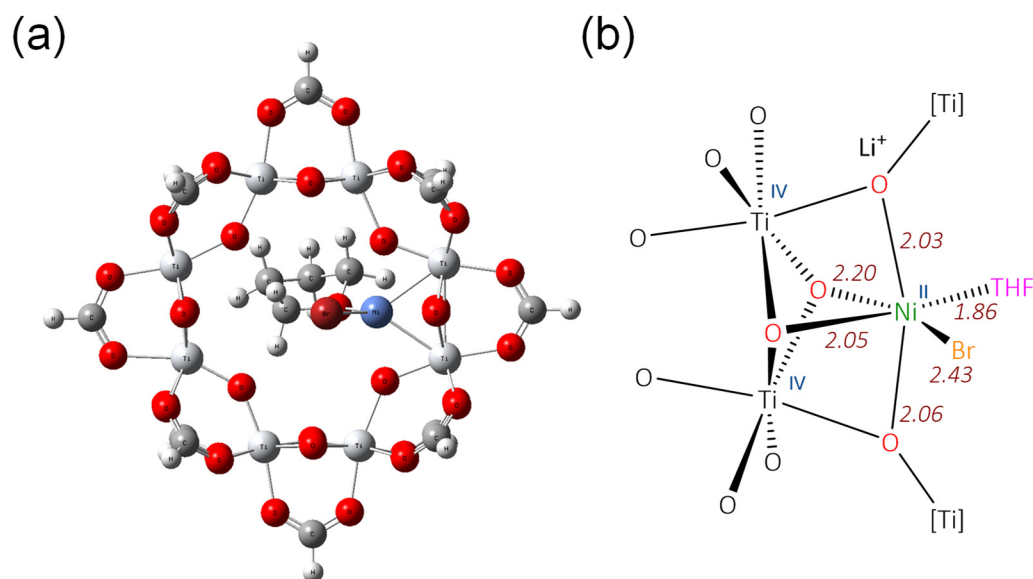


Figure 2-4. (a) Optimized structure and (b) measured bond distances of Ti₈-BDC-NiBr. Adapted with permission from *ACS Catalysis*, **2019**, 9, 1578-1583. Copyright 2019 American Chemical Society.

The calculated structural model fitted well to the extended X-ray fine structure (EXAFS) data of Ni in Ti₈-BDC-NiBr, with experimental average Ni-($\mu_2\text{-O}^-$) distance and Ni-($\mu_2\text{-O}$) distance of 1.98, and 2.11 Å, respectively, which corresponded well with the DFT calculated bond distances (**Figure 2-5**).

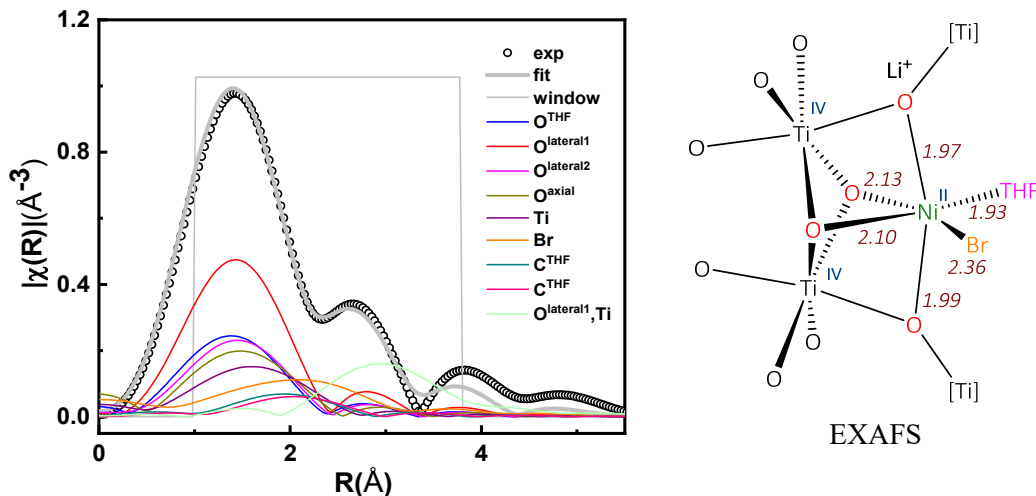


Figure 2-5. EXAFS spectra (black circles) and fit (gray solid line) in R-space at the Ni K-edge adsorption of $\text{Ti}_8\text{-BDC-NiBr}$. Adapted with permission from *ACS Catalysis*, **2019**, *9*, 1578-1583. Copyright 2019 American Chemical Society.

2.2.2 Synthesis and Characterization of $\text{Ti}_8\text{-BDC-NiH}$

Upon treatment with NaBEt_3H , the color of the $\text{Ti}_8\text{-BDC-NiBr}$ MOF immediately changed from light-yellow to black, while vigorously evolving H_2 , suggesting Ni-mediated electron transfer from the hydride to the $\text{Ti}_8\text{-Ni}$ system via reductive elimination of H_2 . Several reactivity and spectroscopic studies were performed to validate the structure and electronic properties of the proposed $\text{Ti}^{\text{III}}_2\text{Ti}^{\text{IV}}_6\text{-BDC-NiH}$ species.

The electron paramagnetic resonance (EPR) spectra of the reduced sample in toluene displayed one set of intense isotropic signal with a g-value of 1.93, which is consistent with the EPR signals of reported Ti^{III} species in the literature.²⁴⁻²⁵ This assignment is supported by the disappearance of the isotropic EPR signal when $\text{Ti}_8\text{-BDC-NiH}$ was oxidized by ferrocenium hexafluorophosphate (FcPF_6) to afford $\text{Ti}^{\text{IV}}_8\text{-BDC-NiH}$ (**Figure 2-6a**). The lack of any other signals in the EPR spectrum is consistent with the EPR silent nature of Ni^{II} species.²⁶ Besides, the Ti X-ray absorption near-edge spectroscopy (XANES) pre-edge region of $\text{Ti}^{\text{III}}_2\text{Ti}^{\text{IV}}_6\text{-BDC-NiH}$

showed an overall 0.45 eV shift to lower energy compared to those of $\text{Ti}^{\text{IV}}_8\text{-BDC-NiBr}$ and $\text{Ti}^{\text{IV}}_8\text{-BDC-NiH}$, because filling one electron to the d orbital lowers its energy and decreases the energy of the $1s \rightarrow 3d$ transition. Furthermore, the pre-edge region of $\text{Ti}_8\text{-BDC-NiH}$ has higher overall intensity than that of $\text{Ti}_8\text{-BDC-NiBr}$, presumably due to the distortion of $[\text{Ti}^{\text{III}}\text{O}_6]^{3-}$ or $[\text{Ti}^{\text{IV}}\text{O}_6]^{2-}$ octahedra caused by partial reduction, which leads to higher probability of spin-forbidden $1s \rightarrow 3d$ transitions (**Figure 2-6b**).

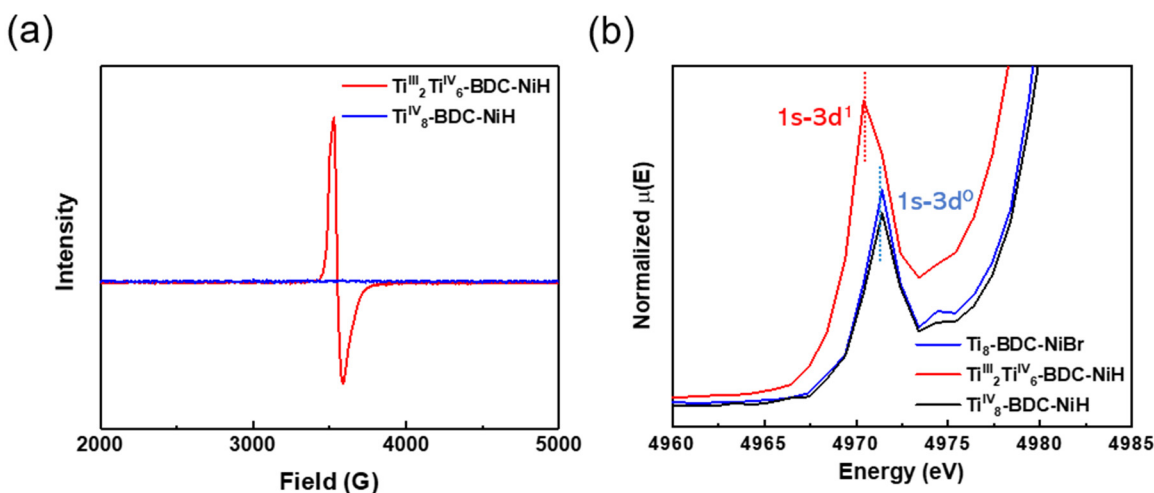


Figure 2-6. (a) EPR spectra of $\text{Ti}^{\text{III}}_2\text{Ti}^{\text{IV}}_6\text{-BDC-NiH}$ (red), and $\text{Ti}^{\text{IV}}_8\text{-BDC-NiH}$ (blue). (b) Ti K-edge XANES spectra of $\text{Ti}_8\text{-BDC-NiBr}$ (red), $\text{Ti}^{\text{III}}_2\text{Ti}^{\text{IV}}_6\text{-BDC-NiH}$ (blue), and $\text{Ti}^{\text{IV}}_8\text{-BDC-NiH}$ (black). Adapted with permission from *ACS Catalysis*, **2019**, 9, 1578-1583. Copyright 2019 American Chemical Society.

Moreover, Ni K-edge XANES spectra of $\text{Ti}_8\text{-BDC-NiBr}$, $\text{Ti}^{\text{III}}_2\text{Ti}^{\text{IV}}_6\text{-BDC-NiH}$, and $\text{Ti}^{\text{IV}}_8\text{-BDC-NiH}$ were compared against $\text{Ni}(\text{NO}_3)_2$, where the pre-edge of the three MOFs aligned well to that of $\text{Ni}(\text{NO}_3)_2$, indicating Ni^{II} centers in all three MOFs (**Figure 2-7**).

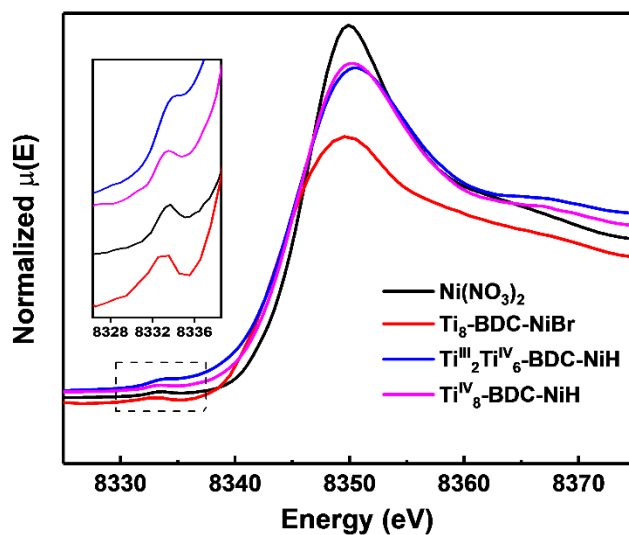


Figure 2-7. Ni K-edge XANES spectra of $\text{Ti}_8\text{-BDC-NiBr}$ (red), $\text{Ti}^{\text{III}}_2\text{Ti}^{\text{IV}}_6\text{-BDC-NiH}$ (blue), and $\text{Ti}^{\text{IV}}_8\text{-BDC-NiH}$ (pink) in comparison to $\text{Ni}(\text{NO}_3)_2$ (black). Reprinted with permission from *ACS Catalysis*, **2019**, 9, 1578-1583. Copyright 2019 American Chemical Society.

To determine the amount of Ti^{III} per $\text{Ti}_8\text{-BDC-NiH}$ cluster, the reduced MOF was titrated with ferrocenium hexafluorophosphate (FcPF_6) (5 mM in CH_2Cl_2), in which each Ti^{III} ion can reduce one FcPF_6 molecule to form a neutral ferrocene. Through this titration, 2.13 ± 0.08 equiv. of ferrocene was generated with respect to Ni as determined by gas chromatography (GC) (**Figure 2-8a**). Since the Ni centers maintained the Ni^{II} oxidation state in both reduced and oxidized MOFs as indicated by Ni K-edge XANES analysis (**Figure 2-7**) and the hydrides of first-row metals (Co, Ni, etc) are known to be poorly reducing agents through electron transfer reactions.²⁷⁻²⁸ Fc^+ ions must be reduced by the Ti^{III} centers. This analysis indicates the $\text{Ti}^{\text{III}}_2\text{Ti}^{\text{IV}}_6$ composition in each reduced $\text{Ti}_8\text{-BDC-NiH}$ cluster. In addition, EAXFS fitting revealed that the Ni coordination environment in $\text{Ti}^{\text{IV}}_8\text{-BDC-NiH}$ is similar to that of $\text{Ti}^{\text{III}}_2\text{Ti}^{\text{IV}}_6\text{-BDC-NiH}$ (**Figure 2-8b**).

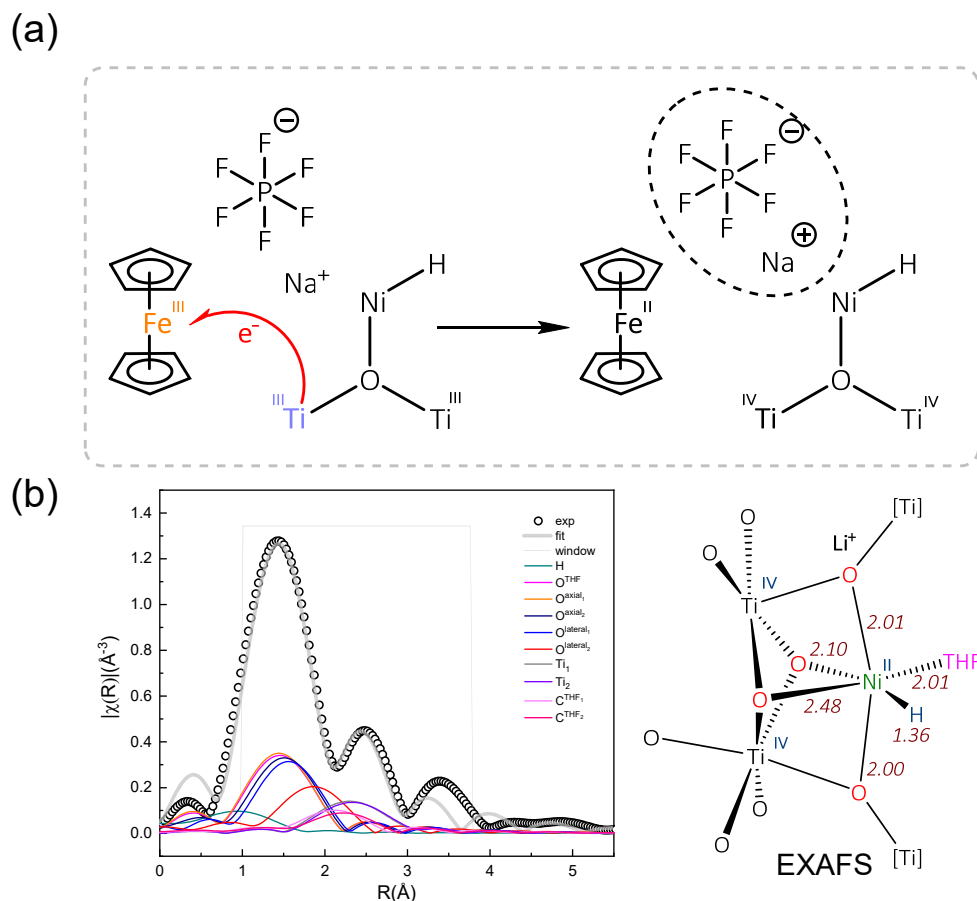


Figure 2-8. (a) Oxidation of Ti^{III} to Ti^{IV} with FcPF_6 through electron transfer reaction. (b) EXAFS spectra (black circles) and fit (gray line) in R space at the Ni K-edge adsorption of $\text{Ti}^{\text{IV}}_8\text{-BDC-NiH}$. The scattering paths of Ni to THF-oxygen (pink), axial oxo (orange), equatorial oxo (blue) hydride (green), and titanium (purple) were shown. Adapted with permission from *ACS Catalysis*, **2019**, 9, 1578-1583. Copyright 2019 American Chemical Society.

The Ni coordination environment and electronic structure in $\text{Ti}^{\text{III}}_2\text{Ti}^{\text{IV}}_6\text{-BDC-NiH}$ were studied by DFT calculation using the B3LYP functional (**Figure 2-9**). The Ni center in $\text{Ti}^{\text{III}}_2\text{Ti}^{\text{IV}}_6\text{-BDC-NiH}$ maintained a similar coordination geometry to that in $\text{Ti}_8\text{-BDC-NiBr}$, with an average calculated Ni- $(\mu_2\text{-O}^-)$ and Ni- $(\mu_2\text{-O})$ distances of 2.13 Å and 2.39 Å, respectively.

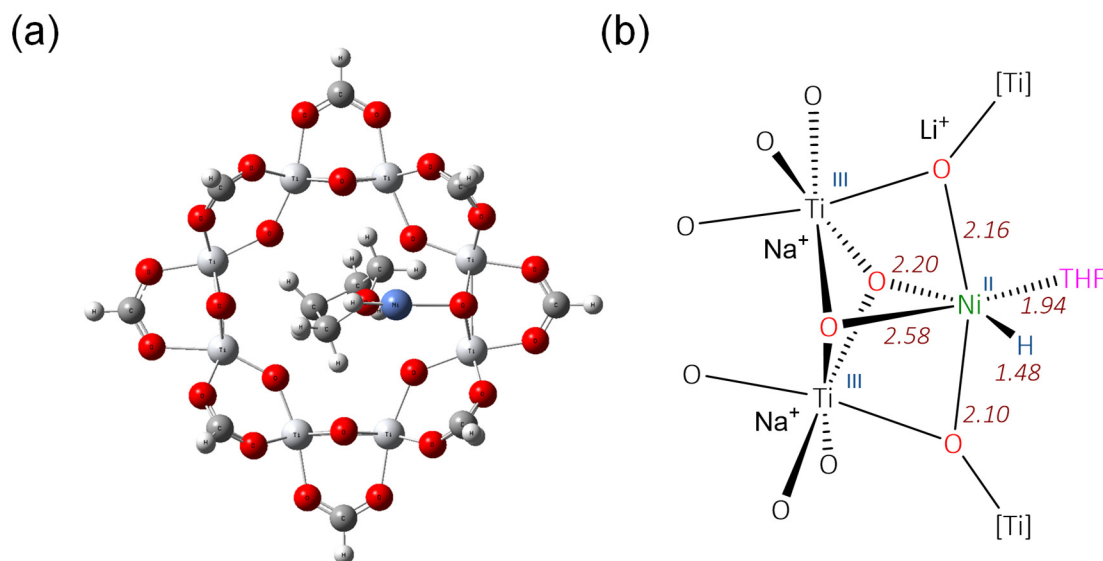


Figure 2-9. (a) Optimized structure and (b) measured bond distances of $\text{Ti}^{\text{III}}_2\text{Ti}^{\text{IV}}_6\text{-BDC-NiH}$. Adapted with permission from *ACS Catalysis*, **2019**, 9, 1578-1583. Copyright 2019 American Chemical Society.

The calculated structural model was used to fit the Ni K-edge EXAFS data, affording the experimental average Ni-($\mu_2\text{-O}^-$) and Ni-($\mu_2\text{-O}$) distances of 2.03 Å, and 2.29 Å, respectively. The bond distances from the EXAFS fitting are given in **Figure 2-10**.

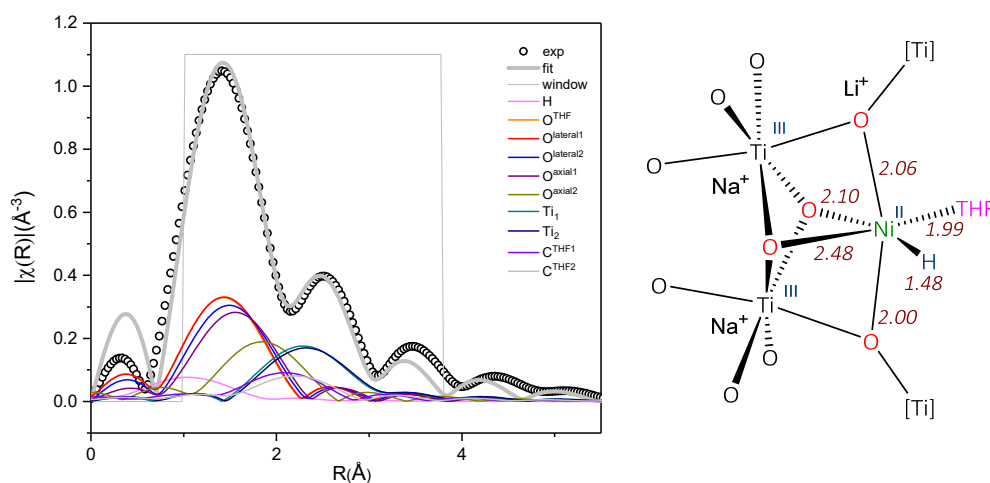


Figure 2-10. EXAFS spectra (black circles) and fits (gray solid line) in R-space at the Ni K-edge adsorption of $\text{Ti}^{\text{III}}_2\text{Ti}^{\text{IV}}_6\text{-BDC-NiH}$. Adapted with permission from *ACS Catalysis*, **2019**, 9, 1578-1583. Copyright 2019 American Chemical Society.

2.2.3 $\text{Ti}^{\text{III}}_2\text{Ti}^{\text{IV}}_6\text{-BDC-NiH}$ Catalyzed Hydrogenolysis of Benzyl Phenyl Ether

In order to evaluate the catalytic activity of the obtained materials, we first focused our attention on model molecules that contain the most common aryl ether linkages found in lignin. Hydrogenolysis of benzyl phenyl ether as a model for α -O-4 linkage in lignin has been studied to optimize the reaction conditions. At 140 °C and 1 bar of H_2 and in the absence of any base, 1 mol % loading of $\text{Ti}^{\text{III}}_2\text{Ti}^{\text{IV}}_6\text{-BDC-NiH}$ (based on Ni) completely cleaved benzyl phenyl ether in 6 h, affording toluene and cyclohexanol as the only products (**Table 2-1**). Decreasing the temperature to 120 °C lowered the conversion to 86%, giving toluene (86% yield) and cyclohexanol (82% yield) as major products. While phenol was nearly completely hydrogenated to afford cyclohexanol, no competing hydrogenation of toluene was observed under these conditions. In contrast, Ni nanoparticles gave no reactivity towards the hydrogenolysis of benzyl phenyl ether, ruling out the possibility of Ni nanoparticle catalysis in the $\text{Ti}^{\text{III}}_2\text{Ti}^{\text{IV}}_6\text{-BDC-NiH}$ system. We also investigated the impact of Ti oxidation states of the Ti_8 cluster on the catalyst performance of $\text{Ni}^{\text{II}}\text{-H}$. $\text{Ti}^{\text{IV}}_8\text{-BDC-NiH}$, generated from FcPF_6 oxidation of $\text{Ti}^{\text{III}}_2\text{Ti}^{\text{IV}}_6\text{-BDC-NiH}$, displayed no catalytic activity under the same conditions. This experiment showed that the reduction of the Ti_8 cluster to $\text{Ti}^{\text{III}}_2\text{Ti}^{\text{IV}}_6$ is essential for the catalytic activity, likely as a result of the fact that $\text{Ti}^{\text{III}}_2\text{Ti}^{\text{IV}}_6$ provides a more electron-rich Ni^{II} center to facilitate the activation of H_2 for hydrogenolysis of benzyl phenyl ether.

Table 2-1. Optimization of $\text{Ti}^{\text{III}}_2\text{Ti}^{\text{IV}}_6\text{-BDC-NiH}$ Catalyzed Hydrogenolysis of Benzyl Phenyl Ether.^a

Entry	Cat / (Ni loading)	Conv. (%)	GC Yield			
			1 %	2 %	3 %	4 %
1 ^b	$\text{Ti}^{\text{III}}_2\text{Ti}^{\text{IV}}_6\text{-NiH}$ (1 mol %)	55	55	0	0	55
2	$\text{Ti}^{\text{III}}_2\text{Ti}^{\text{IV}}_6\text{-NiH}$ (1 mol %)	100	100	0	0	100
3	$\text{Ti}^{\text{III}}_2\text{Ti}^{\text{IV}}_6\text{-NiH}$ (0.5 mol %)	34	34	22	0	12
4 ^c	$\text{Ti}^{\text{III}}_2\text{Ti}^{\text{IV}}_6\text{-NiH}$ (1 mol %)	86	86	4	0	82
5	Ni NPs (2 mol %)	0	0	0	0	0
6	$\text{Ti}^{\text{IV}}_8\text{-NiH}$ (1 mol %)	0	0	0	0	0

^aReaction conditions: Parr high-pressure reactor, freshly prepared catalyst (0.5-2 mol %), benzyl phenyl ether, 1 bar H_2 , 140 °C unless specified, heptane, 6 h unless specified. ^bThe reaction time was 1h. ^cThe reaction temperature was 120 °C.

$\text{Ti}^{\text{III}}_2\text{Ti}^{\text{IV}}_6\text{BDC-NiH}$ was reused for at least 5 times for the hydrogenolysis of benzyl phenyl ether without significant drop in yields, highlighting the robustness and recyclability of this catalyst (**Figure 2-11**).

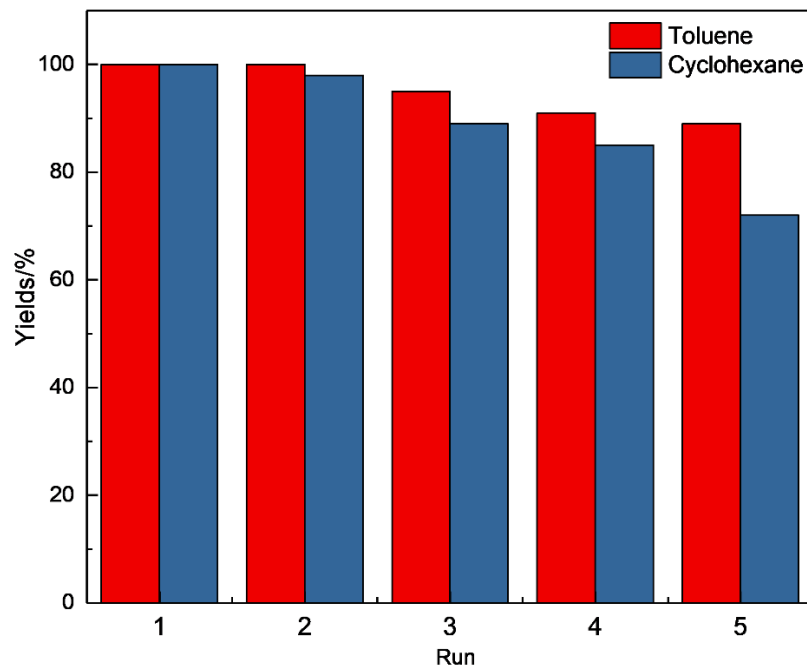
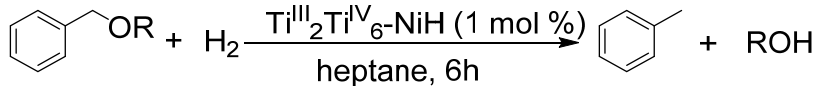
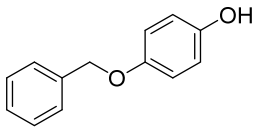
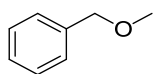
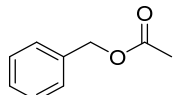


Figure 2-11. Recycle experiments for the $\text{Ti}^{\text{III}}_2\text{Ti}^{\text{IV}}_6\text{-BDC-NiH}$ catalyzed hydrogenolysis of benzyl phenyl ether. Reprinted with permission from *ACS Catalysis*, **2019**, 9, 1578-1583. Copyright 2019 American Chemical Society.

2.2.4 $\text{Ti}^{\text{III}}_2\text{Ti}^{\text{IV}}_6\text{-BDC-NiH}$ Catalyzed Hydrogenolysis of Other Benzyl Phenyl Ethers

We then tested the hydrogenolysis of other benzyl ethers including benzyl aryl and benzyl methyl ethers, which are also present in lignin linkages. Benzyl (*p*-hydroxyphenyl) ether was converted to toluene and 1,4-dihydroxycyclohexane in quantitative yields (**Table 2-2**). At 140 °C and 1 bar of H_2 , 1 mol % catalyst only gave 11% conversion for the hydrogenolysis of benzyl methyl ether. Increasing the temperature to 160 °C gave almost complete conversion without hydrogenating toluene. Under the same condition, benzyl acetate underwent complete hydrogenolysis to give toluene and acetic acid in quantitative yields.

Table 2-2. Hydrogenolysis of Various Benzyl Ethers.^a

					
Entry	Benzyl Ether	T (°C)	Conv. (%)	Toluene (%)	ROH ^b (%)
1		140	100	99	99
2		140	11	9	9
3		160	99	98	93
4		160	100	100	96 ^c

^aReaction conditions: Parr high-pressure reactor, freshly prepared $\text{Ti}^{\text{III}}_2\text{Ti}^{\text{IV}}_6\text{-BDC-NiH}$ (1 mol %), benzyl ethers, 1 bar H_2 , heptane, 6 h. ^bROH represents 1,4-cyclohexanediol for entry 1, methanol for entries 2 and 3, and acetic acid for entry 4. ^cThe yield was determined by HPLC.

We further tested $\text{Ti}^{\text{III}}_2\text{Ti}^{\text{IV}}_6\text{-BDC-NiH}$ in the hydrogenolysis of more challenging lignin model compounds, including phenylethyl phenyl ether as a model for the β -O-4 linkage and diphenyl ether as a model for the 4-O-5 linkage in lignin (**Table 2-3**). At 160 °C and 1 bar H_2 , 1 mol % catalyst converted phenylethyl phenyl ether to give cyclohexanol in 100% yield, ethyl benzene in 92% yield, and ethylcyclohexane in 8% yield. In order to improve the selectivity, we lowered the catalyst loading and the reaction temperature to avoid the hydrogenation of ethyl benzene generated from the hydrogenolysis process. At 140 °C, 1 bar H_2 , and 1 mol % catalyst loading, phenylethyl ether was selectively cleaved to give the cyclohexanol and ethylbenzene as the sole products. The 4-O-5 bond is one of the strongest ether bonds in lignin,²⁹ and its hydrogenolysis was modeled using diphenyl ether. At 140 °C and 1 bar H_2 , 1 mol % catalyst converted only 19% diphenyl ether to form cyclohexanol and benzene. Increasing the temperature

to 160 °C achieved 97% conversion and produced benzene in 80% yield and cyclohexanol 84% yield. We also observed 4% of cyclohexane resulting from hydrogenation of diphenyl ether under this condition. In general, $\text{Ti}^{\text{III}}_2\text{Ti}^{\text{IV}}_6\text{-BDC-NiH}$ showed high reactivity and excellent selectivity in cleaving aryl ethers to give saturated hydrocarbons and hydrogenated phenols. Furthermore, $\text{Ti}^{\text{III}}_2\text{Ti}^{\text{IV}}_6\text{-BDC-NiH}$ catalytic activity towards the three model linkages in lignin agrees with the trend of bond dissociation energies: 4-O-5 ($314 \text{ kJ}\cdot\text{mol}^{-1}$) > β -O-4 ($289 \text{ kJ}\cdot\text{mol}^{-1}$) > α -O-4 ($218 \text{ kJ}\cdot\text{mol}^{-1}$).

Table 2-3. Hydrogenolysis of Other Lignin Model Compounds.^a

Entry	Substrate	T (°C)	Conv. (%)	GC Yield			
				3 %	4 %	5 %	6 %
1	1	160	100	92	-	0	100
2 ^b	1	160	100	88	-	8	80
3	1	140	96	96	-	0	96
4	2	140	19	-	19	0	19
5	2	160	97	-	80	0	84

^aReaction conditions: Parr high-pressure reactor, freshly prepared $\text{Ti}^{\text{III}}_2\text{Ti}^{\text{IV}}_6\text{-BDC-NiH}$ (1 mol %), aryl ether, 1 bar H_2 , heptane, 6 h. ^b $\text{Ti}^{\text{III}}_2\text{Ti}^{\text{IV}}_6\text{-BDC-NiH}$ (0.5 mol%).

Based on the catalytic results, we proposed a plausible reaction pathway for $\text{Ti}^{\text{III}}_2\text{Ti}^{\text{IV}}_6\text{-BDC-NiH}$ catalyzed hydrogenolysis of benzyl phenyl ether (α -O-4) (**Figure 2-12**). The [Ni]-H catalyst first reacts with benzyl phenyl ether via four-centered transition state involving a $[2\sigma-2\sigma]$ cycloaddition of the [Ni]-H bond with the 'PhO-CH₂Ph' bond to furnish [Ni]-OPh and toluene. [Ni]-OPh then undergoes σ -bond metathesis with H_2 through four-centered transition state to afford phenol while regenerating the [Ni]-H to finish the catalytic cycle. DFT calculations revealed

that the transition states of four-centered Ni-H/substrate (TS1) and four-centered H₂/[Ni]-OPh (TS2) have activation energies of $E_{a1} = 21.28 \text{ kJ}\cdot\text{mol}^{-1}$ and $E_{a2} = 58.01 \text{ kJ}\cdot\text{mol}^{-1}$, respectively. DFT calculations thus show that σ -bond metathesis between [Ni]-OPh and H₂ to form [Ni]-H and phenol is the rate-determining step (RDS).

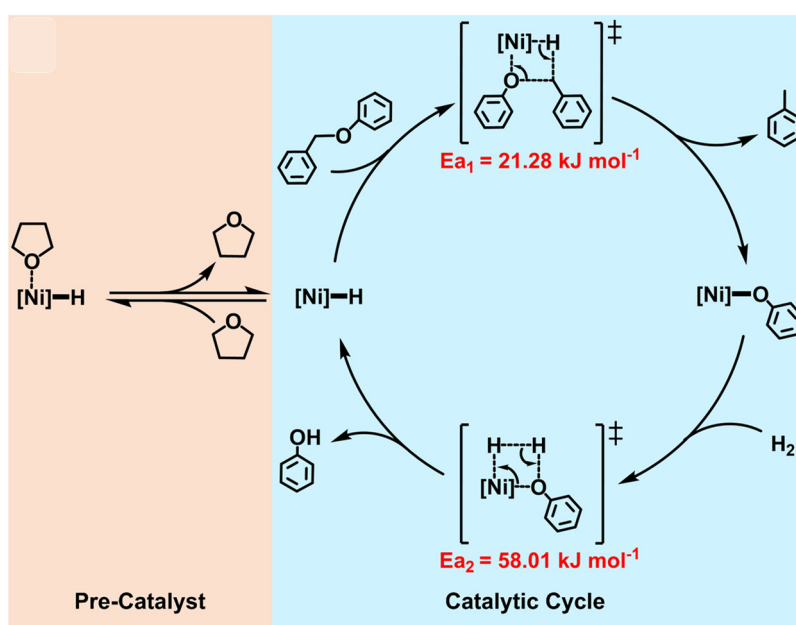


Figure 2-12. Proposed mechanism for the hydrogenolysis of benzyl phenyl ether (α -O-4) by the $\text{Ti}^{\text{III}}_2\text{Ti}^{\text{IV}}_6\text{-BDC-NiH}$. The activation energies for key-bond metathesis are shown. Reprinted with permission from *ACS Catalysis*, **2019**, 9, 1578-1583. Copyright 2019 American Chemical Society.

2.3 Conclusion

In this chapter, we reported that $\text{Ti}_8(\mu_2\text{-O})_8(\mu_2\text{-OH})_4$ SBU of $\text{Ti}_8\text{-BDC}$ (MIL-125) provided as an excellent platform to support a single-site Ni-H catalyst for aryl ether hydrogenolysis. The C-O bond linkages of α -O-4, β -O-4, and 4-O-5 model compounds representing typical bonds in lignin were selectively cleaved by the Ni-H catalyst to produce aromatic molecules as well as cyclohexanol under relatively mild conditions (140 °C, 1 bar H₂). A significant advantage of our MOF-based catalyst is its high activity without the addition of a base (such as NaO^tBu). Interestingly, upon treatment with NaBEt₃H, the Ti-oxo node of $\text{Ti}_8\text{-BDC-NiBr}$ was partially

reduced via reductive elimination of H₂ and the electron spillover from Ni to Ti. The resultant Ti^{III}₂Ti^{IV}₆-BDC-Ni^{II}-H is highly reactive towards the hydrogenolysis reactions. The corresponding oxidized Ti^{IV}₈-BDC-Ni^{II}-H is completely inactive, proving the crucial role of Ti-oxo cluster reduction on the catalytic property of the supported Ni^{II}-H species. Thus, the high stability, low cost, and exceptional activity of metal-node supported MOF catalysts make them promising candidates for potential application in the sustainable synthesis of commodity chemicals, pharmaceuticals, and agrochemicals.

2.4 Experimental

2.4.1 Material and Methods

All of the reactions and manipulations were carried out under N₂ with the use of standard inert atmosphere and Schlenk technique unless otherwise indicated. All solvents used were dry and oxygen-free. Toluene and tetrahydrofuran were degassed by sparging with N₂, filtered through activated alumina columns, and stored under N₂.

Powder X-ray diffraction (PXRD) data was collected on a Bruker D8 Venture diffractometer using a Cu K α radiation source ($\lambda = 1.54178 \text{ \AA}$). Transmission electron microscopy (TEM) images were taken on a TECNAI F30 HRTEM. N₂ sorption experiments were performed on a Micromeritics TriStar II 3020 instrument. Thermogravimetric analysis (TGA) was performed in air using a Shimadzu TGA-50 equipped with a platinum pan and heated at a rate of 1.5 °C per min. Electron paramagnetic resonance (EPR) spectra were collected with a Bruker Elexsys 500 X-band EPR spectrometer at 20 K. ICP-MS data was obtained with an Agilent 7700x ICP-MS and analyzed using ICP-MS MassHunter version B01.03. Samples were diluted in a 2% HNO₃ matrix and analyzed with a ¹⁵⁹Tb internal standard against a 12-point standard curve over the range from 0.1 ppb to 500 ppb. The correlation was >0.9997 for all analyses of interest. Data collection was

performed in Spectrum Mode with five replicates per sample and 100 sweeps per replicate. A Shimadzu GC-2010 Plus gas chromatograph equipped with a flame ionization detector (FID) was used for gas chromatographic analysis (GC). Column: SH-Rxi-5Sil MS column, 30.0 m in length, 0.25 mm in diameter, 0.25 μm in thickness. GC conditions: Injection temperature, 220 $^{\circ}\text{C}$; Column temperature program, 30 $^{\circ}\text{C}$ hold for 5 min, followed by a ramp of 5 $^{\circ}\text{C}/\text{min}$ to 60 $^{\circ}\text{C}$ then a ramp of 10 $^{\circ}\text{C}/\text{min}$ to 300 $^{\circ}\text{C}$; Column flow, 1.21 mL/min.

2.4.2 Synthesis of $\text{Ti}_8\text{-BDC}$

$\text{Ti}_8\text{-BDC}$ was synthesized using a modified literature procedure. 1,4-Benzenedicarboxylic acid (500 mg, 3.0 mmol) and titanium isopropoxide (0.6 ml, 2 mmol) were charged to a solution of 9.0 ml of dry dimethylformamide and 1.0 ml of dry methanol. The mixture was stirred gently for 5 minutes at room temperature and then transferred to a Teflon liner and put into a Stainless Steel Parr bomb at 150 $^{\circ}\text{C}$ for 24 hours. After cooling to room temperature, the white solid was recovered by centrifugation.

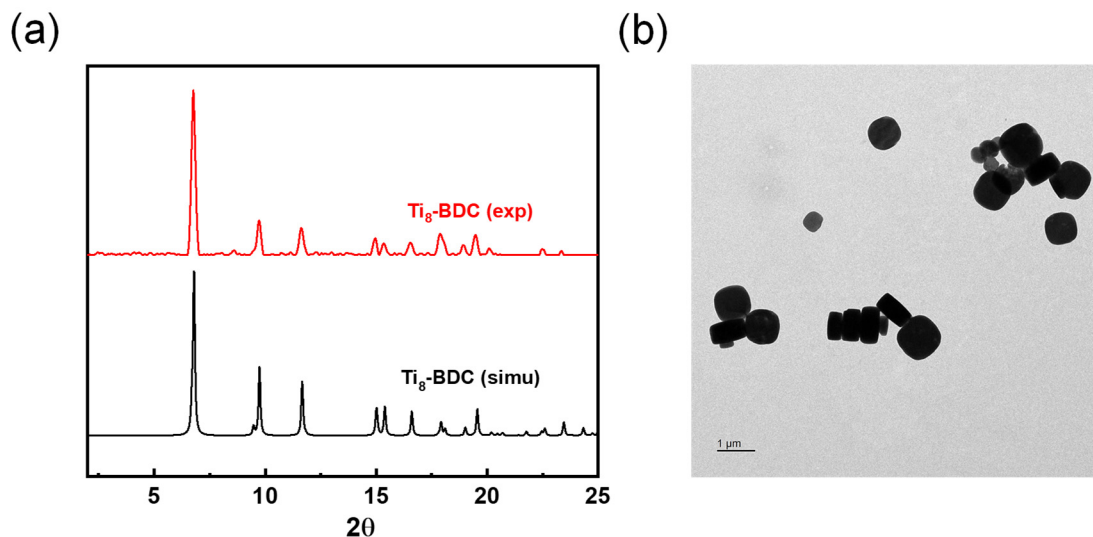


Figure 2-13. (a) PXRD pattern of freshly prepared $\text{Ti}_8\text{-BDC}$ MOF. (b) TEM image of the $\text{Ti}_8\text{-BDC}$ MOF, showing thick-plate morphology. Scale bar is 1 μm .

2.4.3 Synthesis of Ti₈-BDC-NiBr

In a N₂-filled glovebox, LiCH₂SiMe₃ (1.0 M in pentane, 2.3 mL, 10 equiv. relative to per Ti₈) was added dropwise to a suspension of Ti₈-BDC (500 mg, 29% channel solvent by TGA, 0.23 mmol Ti₈ node) in 20 mL hexanes, and the resultant light-yellow mixture was reacted for 6 h at 25 °C. The resulting light-yellow solid was collected through centrifugation and washed with hexanes six times. ICP-MS analysis showed a Ti/Li ratio of 2.07, indicating complete lithiation after treatment with LiCH₂SiMe₃. The lithiated Ti₈-BDC was then transferred to a vial containing 15.6 mL of NiBr₂ solution in DMF (20 mM). This mixture was stirred for 12 h at 25 °C and the light-yellow solid was then centrifuged and washed with DMF five times, with THF three times, and with benzene three times. Ti₈-BDC-NiBr was then freeze-dried in benzene and stored in the glovebox for further use. ICP-MS analysis showed a Ti/Ni ratio of 21.60, indicating 0.37 Ni per Ti₈ node.

2.4.4 Thermogravimetric Analysis (TGA) of Ti₈-BDC-NiBr

As shown in **Figure 2-14**, the first weight loss (26.8%) in the 25 to 270 °C temperature range corresponds to the removal of adsorbed solvents in the pores of the MOF. The second weight loss (57.2%) in the 270-550 °C temperature range corresponds to decomposition of the MOF to metal oxides, consistent with a calculated weight loss of 57.0% based on the conversion of Ti₈(μ₂-O)₈(μ₂-OLi)_{3.26}[(μ₂-O)₂NiBr(THF)Li]_{0.37}(BDC)₆ to (TiO₂)₈(NiO)_{0.35}(Li₂O)_{1.65}.

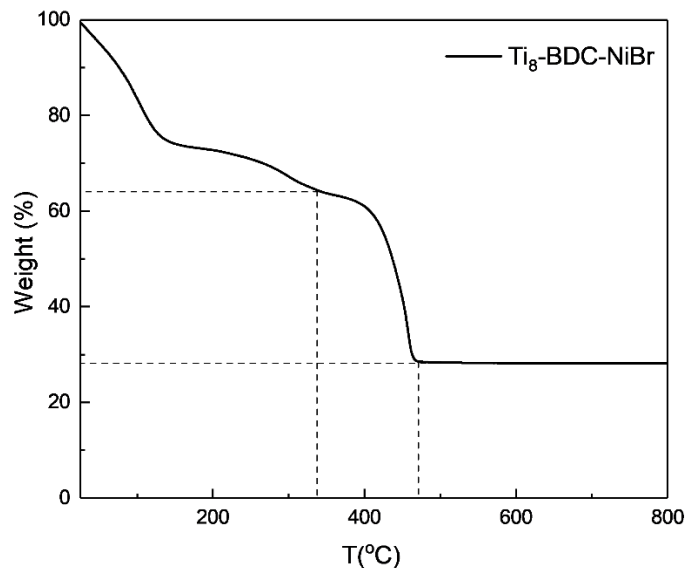


Figure 2-14. TGA curve of freshly prepared Ti₈-BDC-NiBr in the 25-800 °C range. Reprinted with permission from *ACS Catalysis*, **2019**, 9, 1578-1583. Copyright 2019 American Chemical Society.

2.4.5 EXAFS Analysis

X-ray absorption data were collected at Beamline 10-BM-A, B at the Advanced Photon Source (APS) at Argonne National Laboratory. Spectra were collected at the nickel K-edge (8333 eV) in the transmission mode. The X-ray beam was monochromatized by a Si (111) monochromator and detuned by 50% to reduce the contribution of higher-order harmonics below the level of noise. A metallic nickel foil standard was used as a reference for energy calibration and was measured simultaneously with experimental samples. The incident beam intensity (I_0), transmitted beam intensity (I_t), and reference (I_r) were measured by 20 cm ionization chambers with gas compositions of 93% N₂ and 7% Ar, 66% N₂ and 34% Ar, and 100% N₂, respectively. Data were collected over six regions: -250 to -30 eV (10 eV step size, dwell time of 0.25 s), -30 to -12 eV (5 eV step size, dwell time of 0.5 s), -12 to 30 eV (1.1 eV step size, dwell time of 1 s), 30 eV to 6 Å⁻¹, (0.05 Å⁻¹ step size, dwell time of 2 s), 6 Å⁻¹ to 12 Å⁻¹, (0.05 Å⁻¹ step size, dwell time

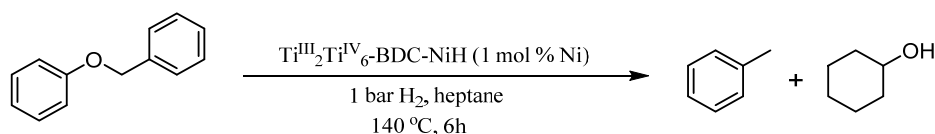
of 2 s), 12 Å⁻¹ to 15 Å⁻¹, (0.05 Å⁻¹ step size, dwell time of 4 s). Multiple X-ray absorption spectra were collected at room temperature for each sample. Samples were ground and mixed with polyethyleneglycol (PEG) and packed in a 6-shooter sample holder to achieve adequate absorption length.

Data was processed using the Athena and Artemis programs of the IFEFFIT package based on FEFF 6.³⁰⁻³¹ Prior to merging, spectra were calibrated against the reference spectra and aligned to the first peak in the smoothed first derivative of the absorption spectrum, the background noise was removed, and the spectra were processed to obtain a normalized unit edge step.

Fitting of the EXAFS region was performed using the Artemis program of the IFEFFIT package. Fitting was performed in R space, with a *k*-weight of 2 for Ni samples. Refinement was performed by optimizing an amplitude factor S_0^2 and energy shift ΔE_0 which are common to all paths, in addition to parameters for bond length (ΔR) and Debye-Waller factor (σ^2).

2.4.6 Typical Procedure for Ti^{III}₂Ti^{IV}₆-BDC-NiH Catalyzed Hydrogenolysis

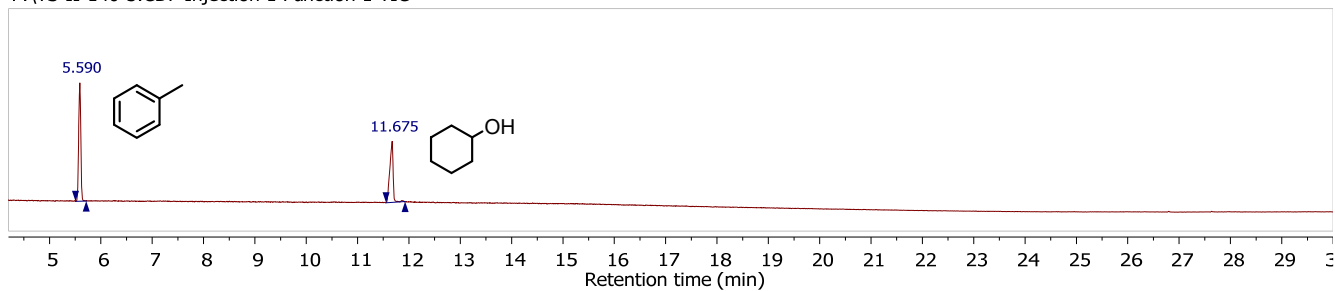
Scheme 2-1. Hydrogenolysis of Benzyl Phenyl Ether.



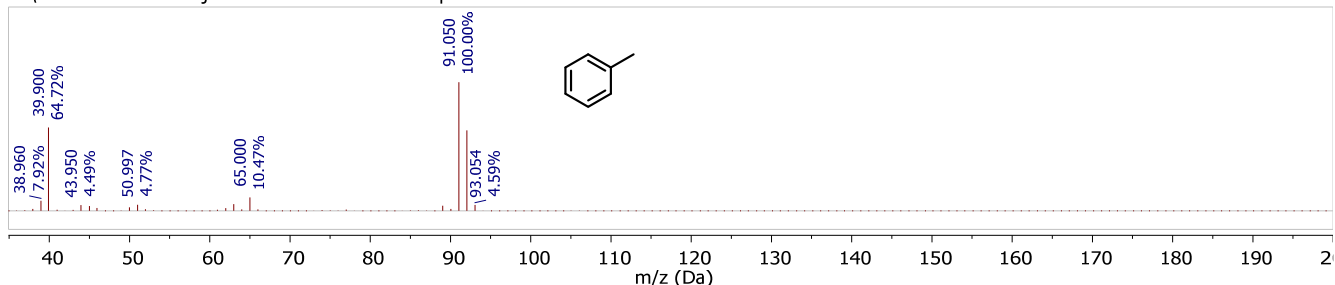
In a N₂-filled glove box, Ti₈-BDC-NiBr (3 μmol of Ni) in 1.0 mL heptane was charged into a plastic tube. NaBEt₃H (10 equiv. to Ni, 30 μL, 1.0 M in THF) was then added to the tube and the mixture was reacted for 2 h. The solid was then centrifuged, washed with heptane three times, and transferred to a Parr reactor with a glass liner using 1 mL heptane, followed by adding benzyl phenyl ether (110.5 mg, 0.6 mmol). The reactor was sealed in the glovebox, and then charged with hydrogen to 1 bar. After stirring at 140 °C temperature for 6 h, the pressure was released, and the MOF catalyst was removed from the reaction mixture via centrifugation. The supernatant was then

analyzed by GC-MS, revealing a 100% conversion of benzyl phenyl ether, and cyclohexanol and toluene as the sole reaction products. ICP-MS analysis of the supernatant showed <0.1% leaching of Ni from the $\text{Ti}^{\text{III}}_2\text{Ti}^{\text{IV}}_6\text{-BDC-NiH}$ catalyst.

F:\YS-II-140-3.CDF Injection 1 Function 1 TIC



F:\YS-II-140-3.CDF Injection 1 Function 1 MS + spectrum 5.53..5.67



F:\YS-II-140-3.CDF Injection 1 Function 1 MS + spectrum 11.56..11.79

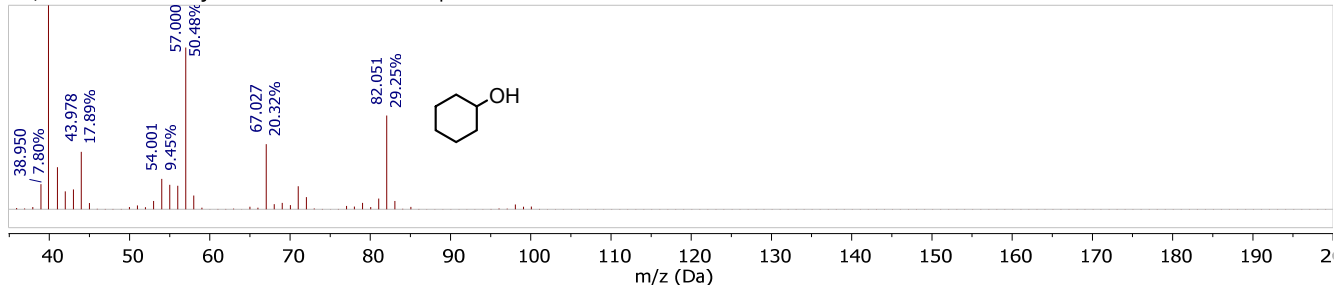


Figure 2-15. GC-MS traces for the hydrogenolysis of benzyl phenyl ether to afford toluene and cyclohexanol as the sole products at complete conversion. Reprinted with permission from *ACS Catalysis*, **2019**, 9, 1578-1583. Copyright 2019 American Chemical Society.

2.5 References

- (1) Zakzeski, J.; Bruijninx, P. C. A.; Jongerius, A. L.; Weckhuysen, B. M., The Catalytic Valorization of Lignin for the Production of Renewable Chemicals. *Chemical Reviews* **2010**, 110 (6), 3552-3599.
- (2) Ragauskas, A. J.; Williams, C. K.; Davison, B. H.; Britovsek, G.; Cairney, J.; Eckert, C. A.; Frederick, W. J.; Hallett, J. P.; Leak, D. J.; Liotta, C. L.; Mielenz, J. R.; Murphy, R.; Templer, R.; Tschaplinski, T., The Path Forward for Biofuels and Biomaterials. *Science* **2006**, 311 (5760), 484.

- (3) Sanderson, K., Lignocellulose: A chewy problem. *Nature* **2011**, *474* (7352), S12-S14.
- (4) Zaheer, M.; Kempe, R., Catalytic hydrogenolysis of aryl ethers: A key step in lignin valorization to valuable chemicals. *ACS Catalysis* **2015**, *5* (3), 1675-1684.
- (5) Yan, N.; Zhao, C.; Dyson, P. J.; Wang, C.; Liu, L. t.; Kou, Y., Selective degradation of wood lignin over noble - metal catalysts in a two - step process. *ChemSusChem: Chemistry & Sustainability Energy & Materials* **2008**, *1* (7), 626-629.
- (6) Ye, Y.; Zhang, Y.; Fan, J.; Chang, J., Selective production of 4-ethylphenolics from lignin via mild hydrogenolysis. *Bioresource technology* **2012**, *118*, 648-651.
- (7) Pepper, J.; Lee, Y., Lignin and related compounds. I. A comparative study of catalysts for lignin hydrogenolysis. *Canadian Journal of Chemistry* **1969**, *47* (5), 723-727.
- (8) Sergeev, A. G.; Hartwig, J. F., Selective, nickel-catalyzed hydrogenolysis of aryl ethers. *Science* **2011**, *332* (6028), 439-443.
- (9) Sergeev, A. G.; Webb, J. D.; Hartwig, J. F., A heterogeneous nickel catalyst for the hydrogenolysis of aryl ethers without arene hydrogenation. *Journal of the American Chemical Society* **2012**, *134* (50), 20226-20229.
- (10) Song, Q.; Wang, F.; Xu, J., Hydrogenolysis of lignosulfonate into phenols over heterogeneous nickel catalysts. *Chemical Communications* **2012**, *48* (56), 7019-7021.
- (11) He, J.; Zhao, C.; Lercher, J. A., Ni-catalyzed cleavage of aryl ethers in the aqueous phase. *Journal of the American Chemical Society* **2012**, *134* (51), 20768-20775.
- (12) Molinari, V.; Giordano, C.; Antonietti, M.; Esposito, D., Titanium nitride-nickel nanocomposite as heterogeneous catalyst for the hydrogenolysis of aryl ethers. *Journal of the American Chemical Society* **2014**, *136* (5), 1758-1761.
- (13) Zaheer, M.; Hermannsdörfer, J.; Kretschmer, W. P.; Motz, G.; Kempe, R., Robust heterogeneous nickel catalysts with tailored porosity for the selective hydrogenolysis of aryl ethers. *ChemCatChem* **2014**, *6* (1), 91-95.
- (14) Gao, F.; Webb, J. D.; Hartwig, J. F., Chemo- and Regioselective Hydrogenolysis of Diaryl Ether C–O Bonds by a Robust Heterogeneous Ni/C Catalyst: Applications to the Cleavage of Complex Lignin-Related Fragments. *Angewandte Chemie International Edition* **2016**, *55* (4), 1474-1478.
- (15) Luo, H.; Klein, I. M.; Jiang, Y.; Zhu, H.; Liu, B.; Kenttämä, H. I.; Abu-Omar, M. M., Total utilization of miscanthus biomass, lignin and carbohydrates, using earth abundant nickel catalyst. *ACS Sustainable Chemistry & Engineering* **2016**, *4* (4), 2316-2322.
- (16) Dan-Hardi, M.; Serre, C.; Frot, T.; Rozes, L.; Maurin, G.; Sanchez, C.; Férey, G., A new photoactive crystalline highly porous titanium (IV) dicarboxylate. *Journal of the American Chemical Society* **2009**, *131* (31), 10857-10859.

- (17) Lee, J.; Farha, O. K.; Roberts, J.; Scheidt, K. A.; Nguyen, S. T.; Hupp, J. T., Metal–organic framework materials as catalysts. *Chemical Society Reviews* **2009**, *38* (5), 1450-1459.
- (18) Yoon, M.; Srirambalaji, R.; Kim, K., Homochiral metal–organic frameworks for asymmetric heterogeneous catalysis. *Chemical reviews* **2011**, *112* (2), 1196-1231.
- (19) Huang, Y.-B.; Liang, J.; Wang, X.-S.; Cao, R., Multifunctional metal–organic framework catalysts: synergistic catalysis and tandem reactions. *Chemical Society Reviews* **2017**, *46* (1), 126-157.
- (20) Wu, C. D.; Zhao, M., Incorporation of molecular catalysts in metal–organic frameworks for highly efficient heterogeneous catalysis. *Advanced Materials* **2017**, *29* (14), 1605446.
- (21) Becke, A. D., Density-functional exchange-energy approximation with correct asymptotic behavior. *Physical Review A* **1988**, *38* (6), 3098-3100.
- (22) Lee, C. T.; Yang, W. T.; Parr, R. G., DEVELOPMENT OF THE COLLE-SALVETTI CORRELATION-ENERGY FORMULA INTO A FUNCTIONAL OF THE ELECTRON-DENSITY. *Physical Review B* **1988**, *37* (2), 785-789.
- (23) Gupta, M.; da Silva, E. F.; Svendsen, H. F., Postcombustion CO₂ Capture Solvent Characterization Employing the Explicit Solvation Shell Model and Continuum Solvation Models. *J. Phys. Chem., B* **2016**, *120* (34), 9034-9050.
- (24) Mason, J. A.; Darago, L. E.; Lukens, W. W.; Long, J. R., Synthesis and O₂ Reactivity of a Titanium(III) Metal–Organic Framework. *Inorganic Chemistry* **2015**, *54* (20), 10096-10104.
- (25) Entley, W. R.; Treadway, C. R.; Wilson, S. R.; Girolami, G. S., The Hexacyanotitanate Ion: Synthesis and Crystal Structure of [NEt₄]₃[Ti^{III}(CN)₆] \cdot 4MeCN. *Journal of the American Chemical Society* **1997**, *119* (27), 6251-6258.
- (26) Buvaylo, E. A.; Melnyk, A. K.; Trachevsky, V. V.; Vassilyeva, O. Y.; Skelton, B. W., Divalent manganese, cobalt and nickel chloride complexes with neutral N²- and N³-based ligands derived from 2-pyridinecarbaldehyde: Synthesis, structural features and spectroscopic studies. *Polyhedron* **2016**, *105*, 238-245.
- (27) Chen, S.; Rousseau, R.; Raugei, S.; Dupuis, M.; DuBois, D. L.; Bullock, R. M., Comprehensive Thermodynamics of Nickel Hydride Bis(Diphosphine) Complexes: A Predictive Model through Computations. *Organometallics* **2011**, *30* (22), 6108-6118.
- (28) Ciancanelli, R.; Noll, B. C.; DuBois, D. L.; DuBois, M. R., Comprehensive Thermodynamic Characterization of the Metal–Hydrogen Bond in a Series of Cobalt-Hydride Complexes. *Journal of the American Chemical Society* **2002**, *124* (12), 2984-2992.
- (29) Wang, X.; Rinaldi, R., Corrigendum: Solvent Effects on the Hydrogenolysis of Diphenyl Ether with Raney Nickel and their Implications for the Conversion of Lignin. *ChemSusChem* **2012**, *5* (8), 1335-1335.

- (30) Ravel, B.; Newville, M., ATHENA, ARTEMIS, HEPHAESTUS: data analysis for X-ray absorption spectroscopy using IFEFFIT. *Journal of Synchrotron Radiation* **2005**, *12* (4), 537-541.
- (31) Rehr, J. J.; Albers, R. C., Theoretical approaches to x-ray absorption fine structure. *Reviews of Modern Physics* **2000**, *72* (3), 621-654.

Chapter 3. Multistep Engineering of Synergistic Catalysts in a Metal-Organic Framework for Tandem C-O Bond Cleavage

3.1 Introduction

The conversion of biomass into chemically or biologically valuable feedstocks is of great significance due to the abundance and renewable nature of biomass.¹⁻² However, the high oxygen content (typically ~40%) in biomass largely prevents its direct usage, and biomass must be first processed to reduce the oxygen content before utilization as fuel and commodity chemicals.³⁻⁴ Due to the high binding energy between C and O, efficient hydrodeoxygenation of lignocellulosic biomass by selective cleavage of C-O bonds (alcohols, ethers, and esters) in biomass still represents a great challenge.⁵ New efficient and economical strategies are needed to achieve these types of transformations to enable the bio-renewable industry and provide “greener” organic feedstocks.⁶

In Chapter 2, we discussed a MOF-supported single-site Ni-hydride catalyst for the cleavage of lignocellulosic C-O bonds. Among many strategies for the catalytic hydrodeoxygenation of lignocellulosic biomass,⁷ one-pot tandem catalysis has been shown as a powerful methodology to overcome the strong C-O binding energy and transform biomass into valuable hydrocarbon fuels.⁸⁻⁹ In particular, Marks and coworkers recently reported the pioneering work in using coupled tandem catalytic cycles to achieve ether, alcohol, and ester C-O bond hydrogenolysis.¹⁰ Thermodynamic analysis rationalized the reaction pathway: Pd nanoparticle (NP)-catalyzed exothermic hydrogenation cycle facilitates the preceding acid-catalyzed endothermic C-O dehydroalkoxylation cycle, making the overall tandem reaction decidedly exothermic.¹¹⁻¹² However, significant deactivation¹¹ of metallic Pd NPs at elevated reaction temperatures presented a barrier for developing a highly efficient catalytic process. The

homogenous character of $M(\text{OTf})_n$ ($M = \text{Hf}, \text{Al}, \text{Zr}, \text{etc}$) Lewis acid catalysts for C-O cleavage also makes it difficult to recycle and reuse these expensive catalysts. The tendency between Lewis acid sites $M(\text{OTf})_n$ and Pd NPs to interfere with each other adds an additional challenge for achieving orthogonal tandem catalysis and ensuring long-term catalyst activities. These problems also exist in other homogeneous multicentered catalytic reactions.¹³⁻¹⁴

The past two decades have witnessed the emergence of metal-organic frameworks (MOFs) as a highly versatile and tunable platform for the design of structurally uniformed solid catalysts.¹⁵⁻¹⁶ Compared to other porous materials, the compositions and structures of MOFs have nearly infinite possibilities. The large number of metal/metal-oxo nodes and functional organic linkers make MOFs a perfect matrix for designing multifunctional materials.¹⁷ The rigid, periodic and porous characteristics of MOF structures further prevent different catalytically active centers from interfering with each other, which allows the study and realization of truly orthogonal multicentered processes. MOF functionalities have historically been introduced via organic linker functionalization¹⁸⁻¹⁹ or through entrapment of catalytically active species in pores/cages/channels.²⁰⁻²¹ The diverse inorganic metal/metal-oxo nodes in MOFs have recently been exploited to construct single-site solid catalysts which do not have homogeneous counterparts.²²⁻²³ Post-synthetic transformation methodologies have also been developed to further tune the compositions and functions of pre-synthesized MOFs to produce hierarchical MOFs with micro- and meso-porosity.²⁴ However, stepwise engineering of MOF compositions/structures to introduce multifunctionalities is still underexplored, due to the lack of reliable methods for highly selective and precise elaborations of MOFs.

In this chapter, we surmised that MOFs could provide a versatile platform to introduce multiple catalytic active sites through precise and stepwise manipulations and modifications. The

catalytically active sites in the rigid MOF structures should facilitate orthogonal multicentered catalytic process with detrimental interference between different catalysts. Toward these ends, we targeted m-MOF-253 based on Al-OH chain secondary building units (SBUs) and a mixture of 2,2'-bipyridine-5,5'-dicarboxylate(dcbpy) and 1,4-benzenediacrylate (pdac) ligands to construct a MOF catalyst with multiple active sites via step-by-steps post-synthetic modifications. The pdac ligands were first selectively cleaved and removed via post-synthetic ozonolysis to open up the potentially active metal sites. Triflation of the Al-OH/OH₂ open sites with trimethyl triflate (Me₃SiOTf) significantly enhanced the Lewis acidity for dehydroalkoxylation. Coordination of the dcbpy ligands with PdCl₂(MeCN)₂ afforded the orthogonal Pd sites which were reduced in situ to generate metallic Pd NPs as the hydrogenation catalyst (**Figure 3-1**). In-depth characterization of each step of MOF manipulations indicated highly selective and precise transformations, providing great insight into MOF engineering. Benefiting from the well-defined active centers that were installed via sequential post-synthetic engineering of m-MOF-253, the MOF catalyst **1-OTf-Pd^{NP}** demonstrated outstanding catalytic performance in apparent hydrogenolysis of various etheric, alcoholic, and esteric C-O bonds to generate deoxygenated saturated alkanes under relatively mild conditions via a tandem dehydroalkoxylation-hydrogenation process. The reactivity of C-O bonds displayed an obvious trend of 3° > 2° > 1°. Control experiments further confirmed the heterogeneous nature and recyclability of **1-OTf-Pd^{NP}** catalyst and its superiority over homogeneous analogues.

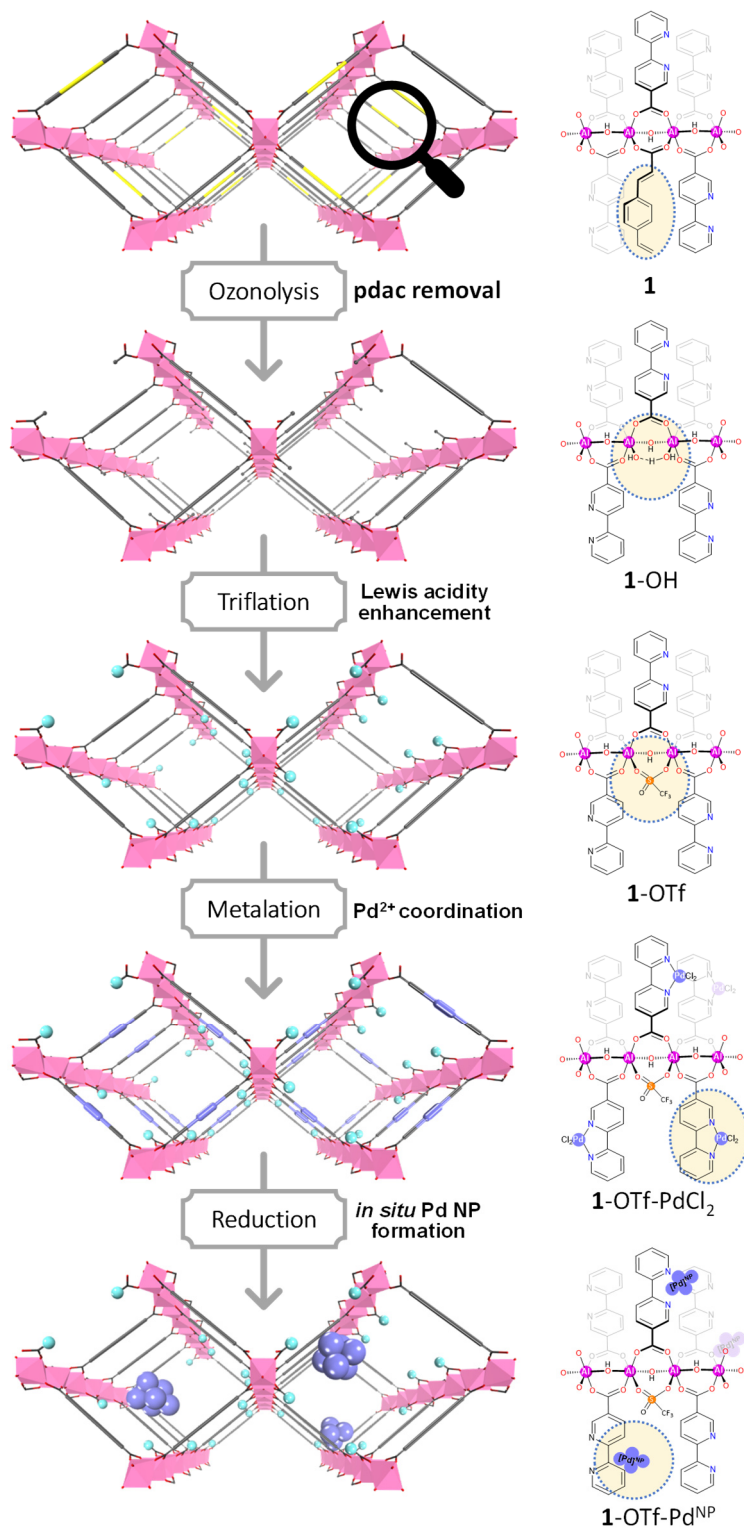


Figure 3-1. Schematic representation of sequential post-synthetic engineering of MOF 1. Reprinted with permission from *Journal of the American Chemical Society*, **2020**, 142, 4872-4882. Copyright 2020 American Chemical Society.

3.2 Results and Discussion

3.2.1 Synthesis of Mixed-Ligand MOF **1** and Removal of pdac Ligands via Ozonolysis

MOF **1** was synthesized solvothermally by heating a mixture of $\text{Al}(\text{NO}_3)_3 \cdot 9\text{H}_2\text{O}$, dcbpy, pdac and dimethylformamide (DMF) based on a modified literature procedure.²⁵⁻²⁶ The formula of the as-synthesized MOF **1** was determined to be $\text{Al}(\text{OH})(\text{dcbpy})_{0.81}(\text{pdac})_{0.19}$ based on ^1H NMR of digested m-MOF-253 (**Figure 3-2**), where the ratio between dcbpy and pdac was determined to be about 4:1.

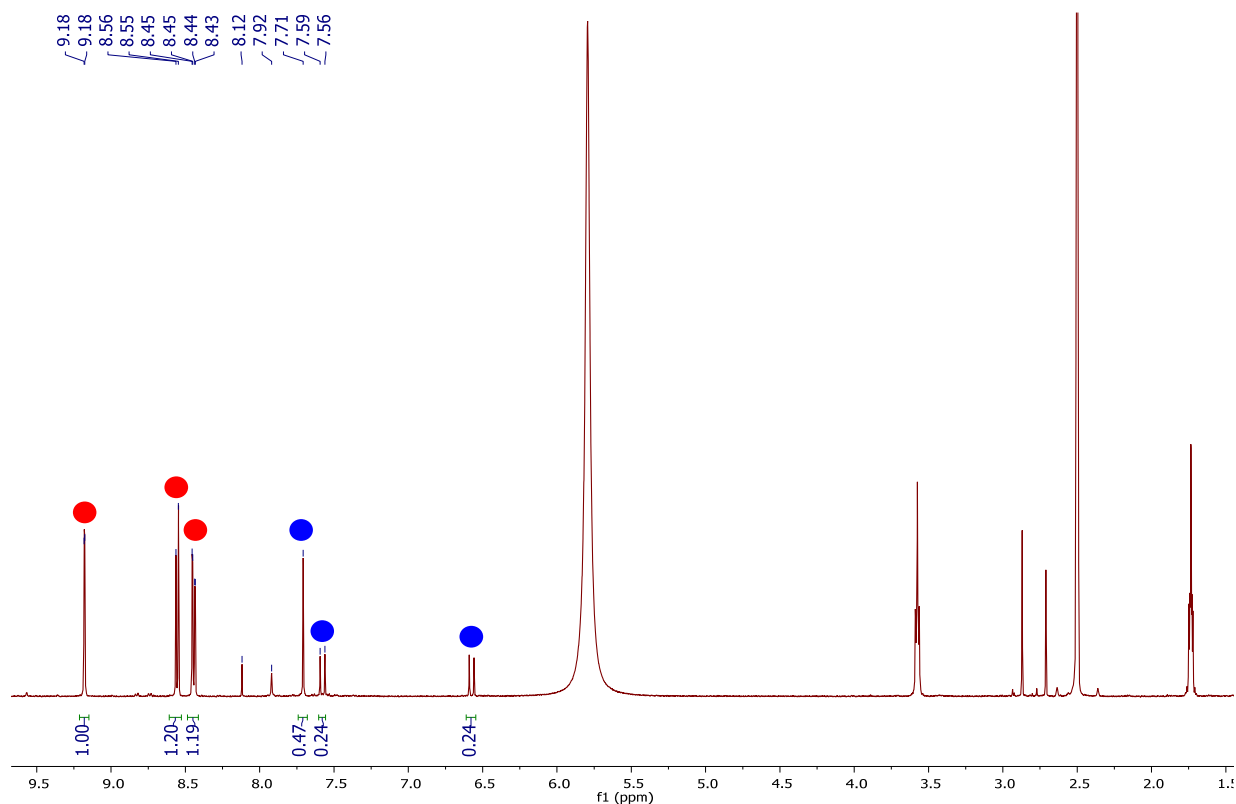


Figure 3-2. ^1H NMR spectrum of digested **1** in $\text{DMSO-}d_6$. Red and blue circles correspond to dcbpy and pdac ligands, respectively. Reprinted with permission from *Journal of the American Chemical Society*, **2020**, 142, 4872-4882. Copyright 2020 American Chemical Society.

Thermogravimetric analysis (TGA) of MOF **1** (**Figure 3-3**) showed the first weight loss of 7.9% in the 25 to 230 °C temperature range, corresponding to the removal of adsorbed solvents in the MOF. The second weight loss (82.0%) in the 230 - 800 °C temperature range corresponds to

decomposition of the MOF to metal oxides, consistent with a calculated weight loss of 81.8% based on the conversion of $\text{Al(OH)(dcbpy)}_{0.81}(\text{pdac})_{0.19}$ to $0.5 \text{ Al}_2\text{O}_3$.

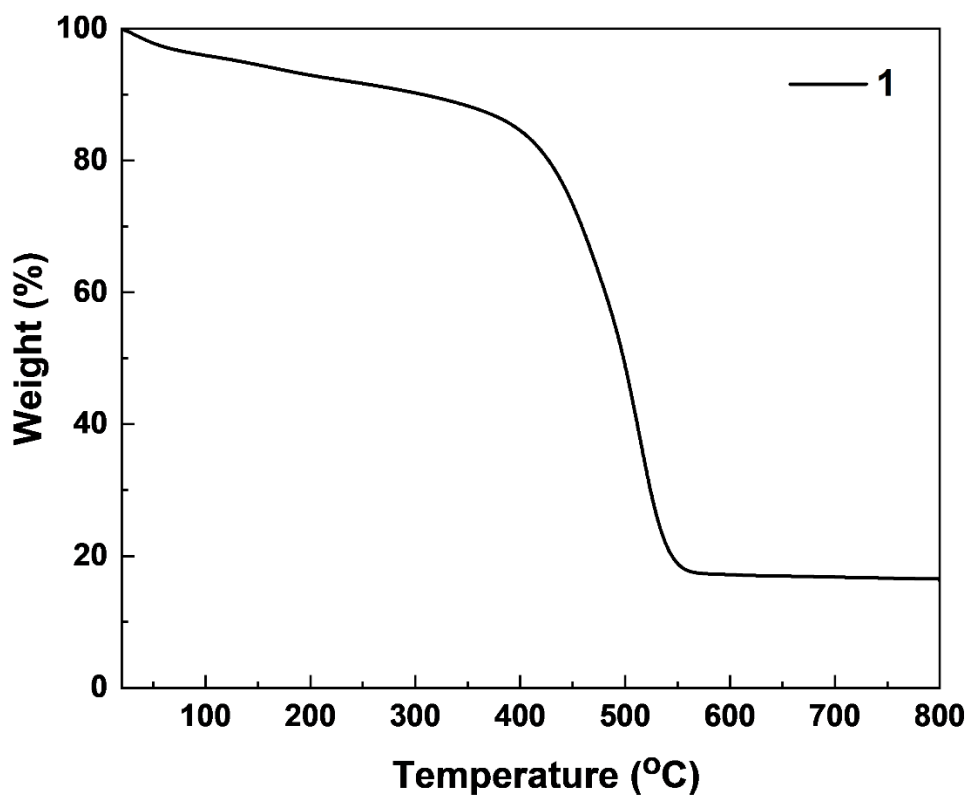


Figure 3-3. TGA curve of freshly prepared **1** in the 25-800 °C range. Reprinted with permission from *Journal of the American Chemical Society*, **2020**, 142, 4872-4882. Copyright 2020 American Chemical Society.

Scanning electron microscopy (SEM) and transmission electron microscopy (TEM) images showed MOF **1** adopted plate-like morphology (**Figure 3-4**), which is similar to that of Al(OH)(bpdC) (DUT-5).²⁵

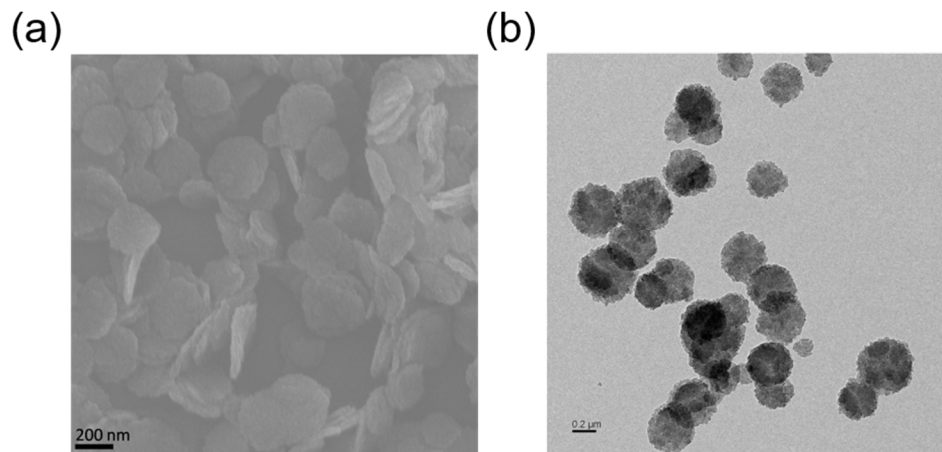


Figure 3-4. (a) SEM and (b) TEM images of as synthesized MOF **1**. Reprinted with permission from *Journal of the American Chemical Society*, **2020**, 142, 4872-4882. Copyright 2020 American Chemical Society.

Powder X-ray diffraction (PXRD) studies revealed that MOF **1** was isostructural to DUT-5 with excellent crystallinity (**Figure 3-5**).

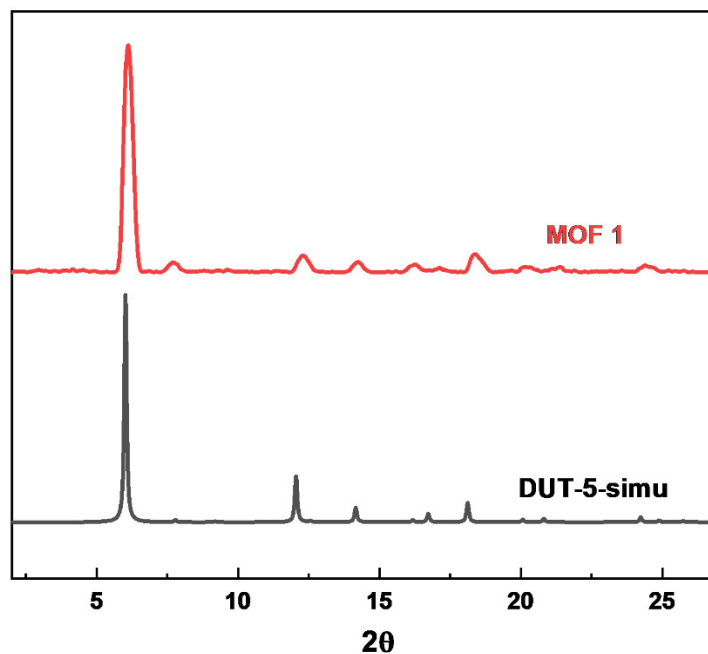


Figure 3-5. PXRD pattern of the freshly prepared MOF **1** (red) compared to that of DUT-5 (black).

The porosity of **1** was evaluated by nitrogen sorption isotherms and showed a type I isotherms with a Brunauer-Emmett-Teller (BET) surface area of 1499 m²/g, which is in agreement to that of DUT-5 (1613 m²/g, **Figure 3-6**).

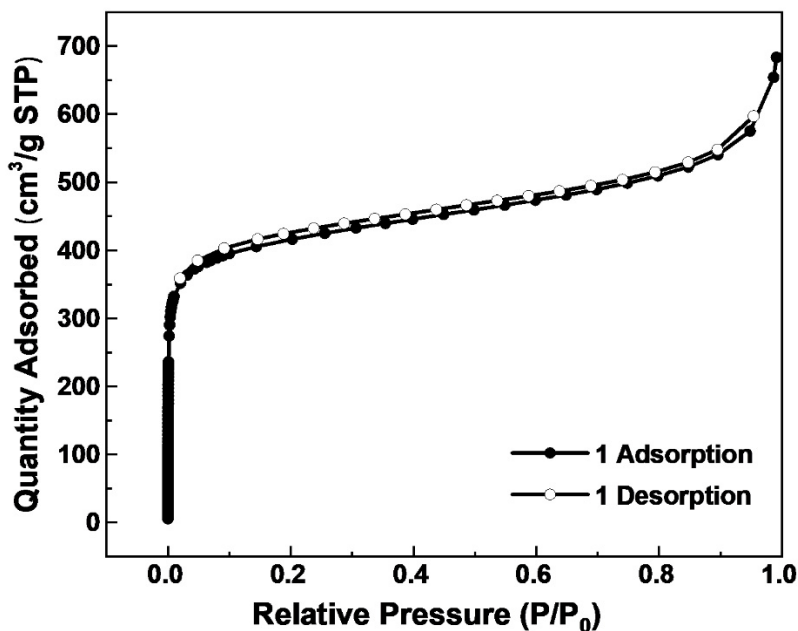
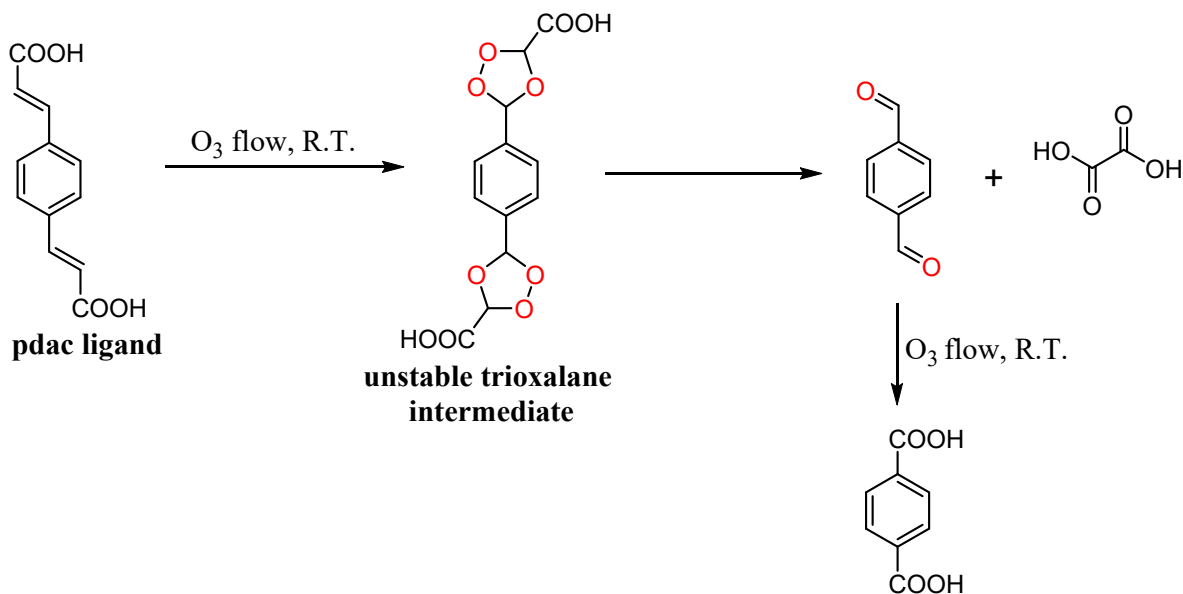


Figure 3-6. N₂ sorption isotherm of MOF **1**.

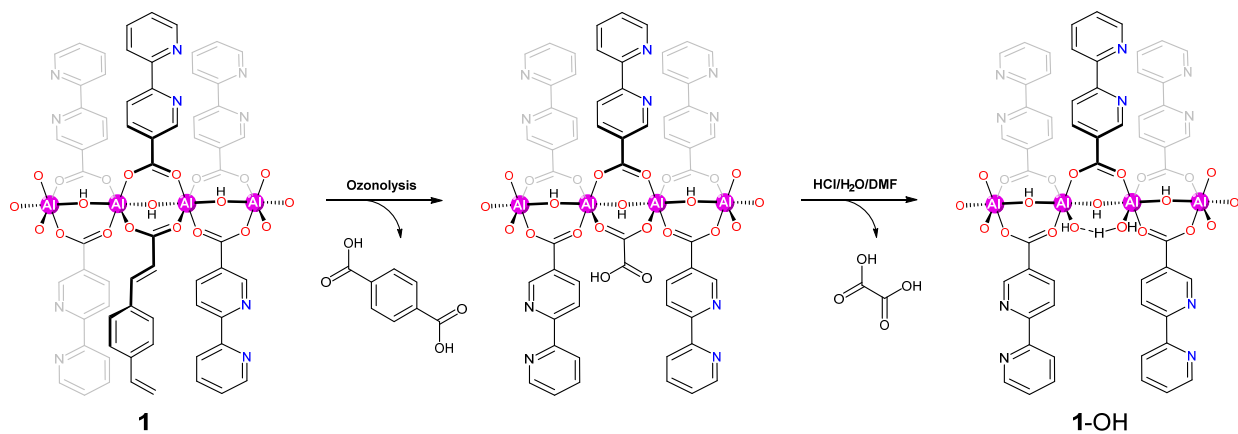
Post-synthetic transformations have recently been used to fine-tune micro- and meso-porosity of MOFs.^{24, 27} In particular, Maspocho and coworkers used ozonolysis to remove olefin-containing ligands from a mixed-ligand UiO-type MOF to afford both micro- and meso-porosity.²⁸ MOF **1** was treated with gaseous O₃ (0.42 mol/h @ 6 L/min O₂ flowing rate) to selectively remove the pdac ligands by cleaving the olefinic groups (**Scheme 3-1**).

Scheme 3-1. Schematic representation of ozonolysis treatment for the removal of pdac ligands.



Further washing with DMF/HCl (1M) (10:1 v:v) removed the residual organic fragments trapped in the pores to afford **1-OH** with $Al_2(OH)(OH_2)$ defect sites as a white solid (**Scheme 3-2**). 1H NMR of digested **1-OH** revealed complete removal of pdac ligands after ozonolysis (**Figure 3-7**).

Scheme 3-2. Chemical equation showing ozonolysis of **1** to afford **1-OH** with $Al_2(OH)(OH_2)$ defect sites. Reprinted with permission from *Journal of the American Chemical Society*, **2020**, 142, 4872-4882. Copyright 2020 American Chemical Society.



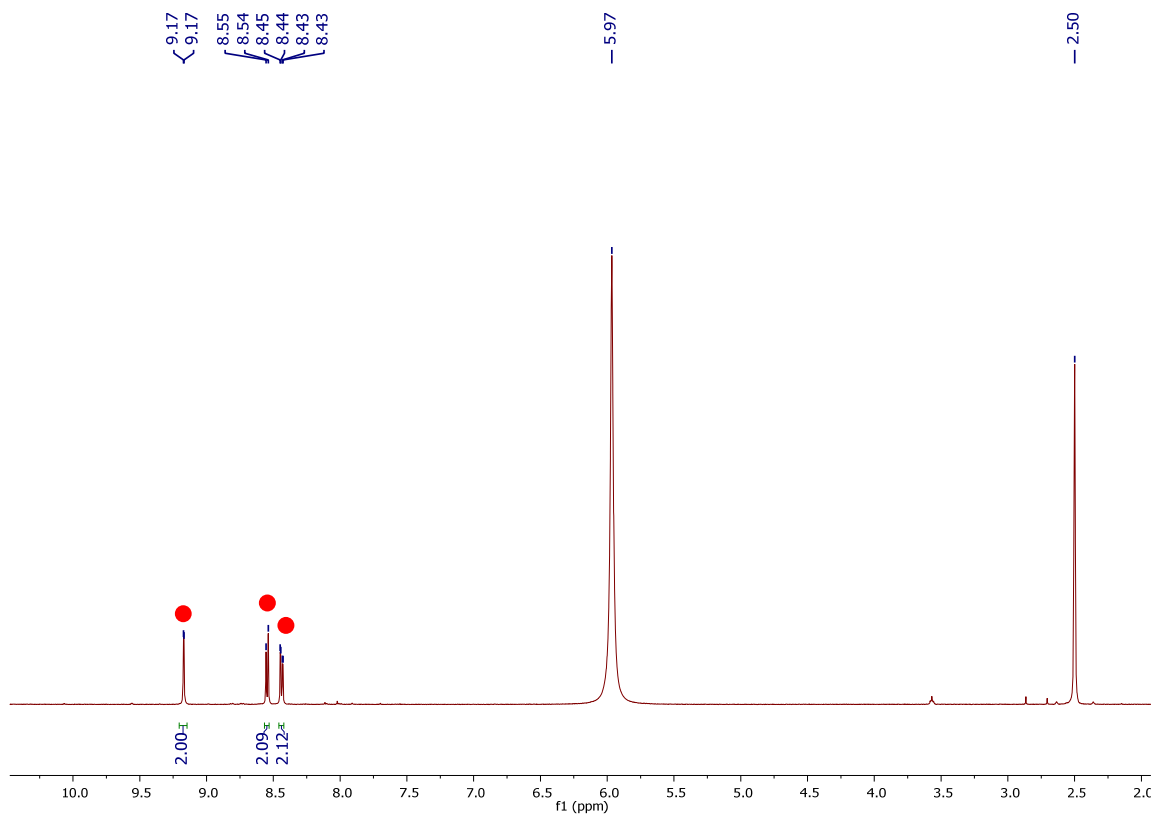


Figure 3-7. ^1H NMR spectrum of digested **1-OH** in $\text{DMSO-}d_6$. Red circles correspond to dcbpy ligands. No signals corresponding to pdac ligand are seen in the ^1H NMR spectrum, indicating complete removal of pdac ligands during ozonolysis. Reprinted with permission from *Journal of the American Chemical Society*, **2020**, 142, 4872-4882. Copyright 2020 American Chemical Society.

Figure 3-8 showed the TGA analysis of **1-OH**. The first weight loss (23.3%) in the 25 to 220 $^{\circ}\text{C}$ temperature range corresponds to the removal of adsorbed solvents in **1-OH**. The second weight loss (78.7%) in the 220 - 800 $^{\circ}\text{C}$ temperature range corresponds to the decomposition of **1-OH** to metal oxides, consistent with a calculated weight loss of 79.5% based on the conversion of $\text{Al}(\text{OH})(\text{dcbpy})_{0.81}(\text{OH})_{0.38}(\text{H}_2\text{O})_{0.38}$ to $0.5 \text{ Al}_2\text{O}_3$. Therefore, NMR and TGA analyses afforded a formula of $\text{Al}(\text{OH})(\text{dcbpy})_{0.81}(\text{OH})_{0.38}(\text{H}_2\text{O})_{0.38}$ for **1-OH**.

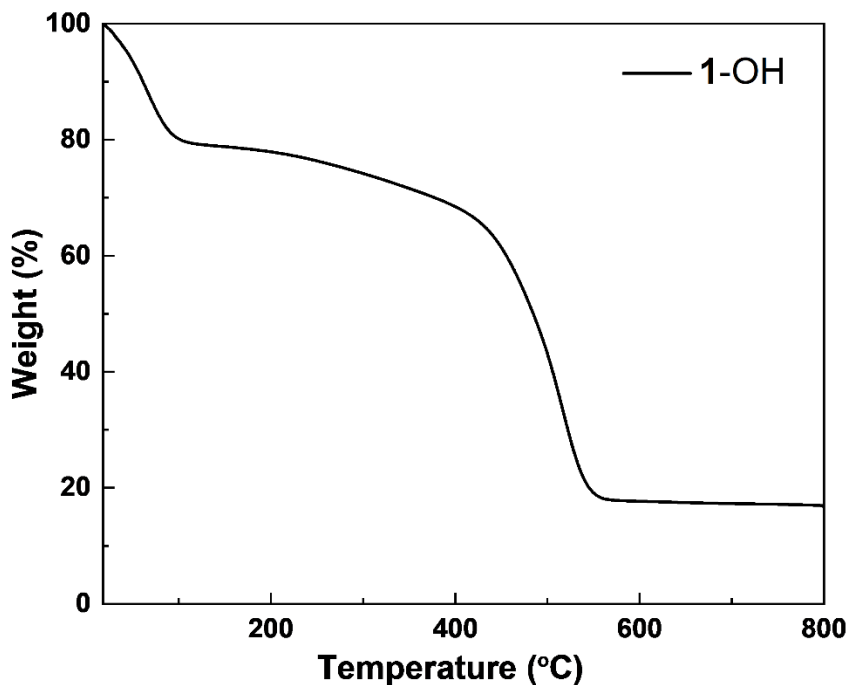


Figure 3-8. TGA curve of **1-OH** in the 25-800 °C temperature range. Reprinted with permission from *Journal of the American Chemical Society*, **2020**, 142, 4872-4882. Copyright 2020 American Chemical Society.

The crystallinity of **1** was maintained after ozonolysis as demonstrated by the similarity of PXRD patterns between **1** and **1-OH** (**Figure 3-9**). TEM imaging showed that **1-OH** maintained the plate-like morphology of **1**, with evenly distributed spongy cleavages (**Figure 3-10**).

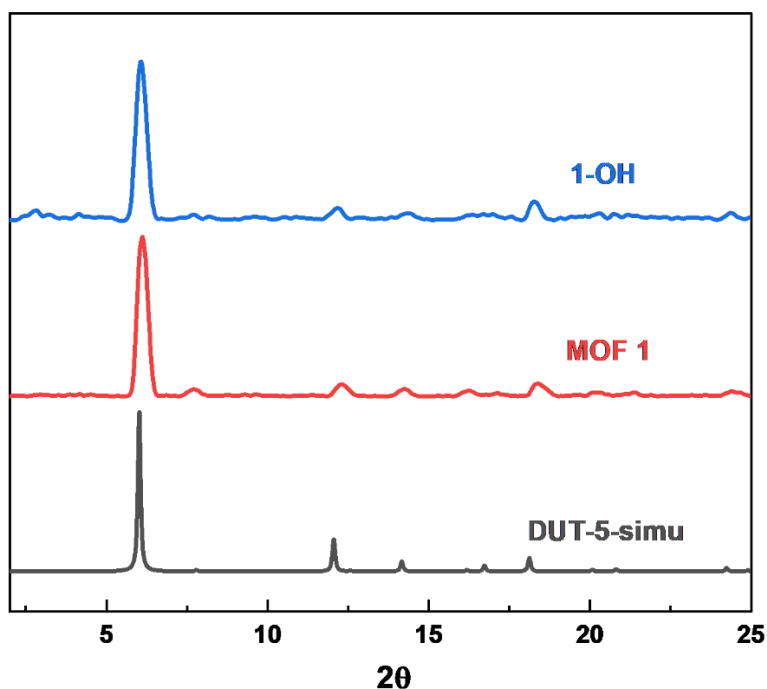


Figure 3-9. The similarity of PXRD patterns of **1** (red) and **1-OH** (blue) to the simulated pattern of DUT-5.

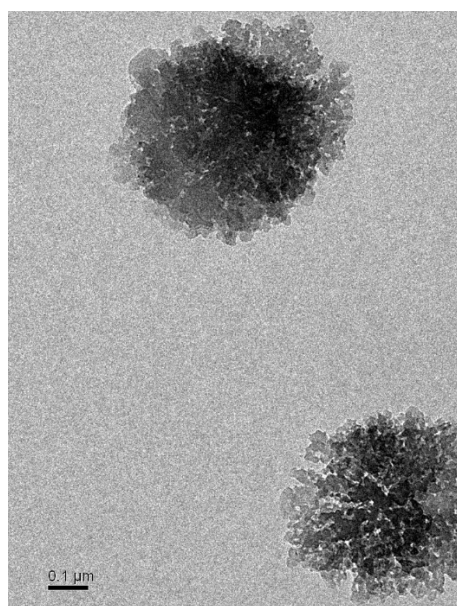


Figure 3-10. TEM image of **1-OH**. Reprinted with permission from *Journal of the American Chemical Society*, **2020**, 142, 4872-4882. Copyright 2020 American Chemical Society.

1-OH showed a BET surface area of 1190 m²/g with the hysteresis characteristic of mesoporosity (**Figure 3-11**). The removal of pdac ligands slightly reduced the BET surface area but

increased pore sizes in the 13 - 32 Å range (**Figure 3-12**). Ozonolysis of **1** thus generated mesopores which should facilitate substrate and product transport in catalytic reactions.

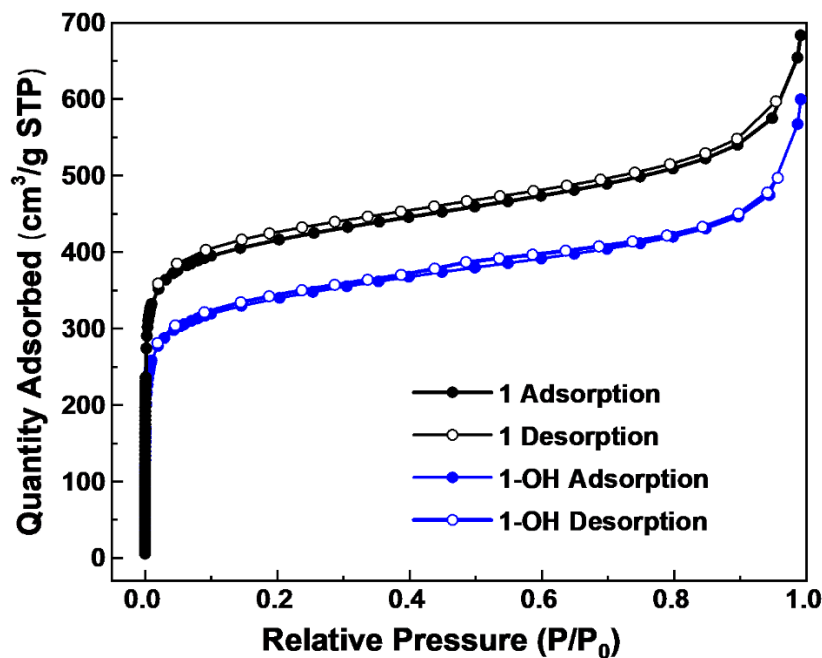


Figure 3-11. Comparison of N₂ sorption isotherms of **1** (black) and **1-OH** (blue).

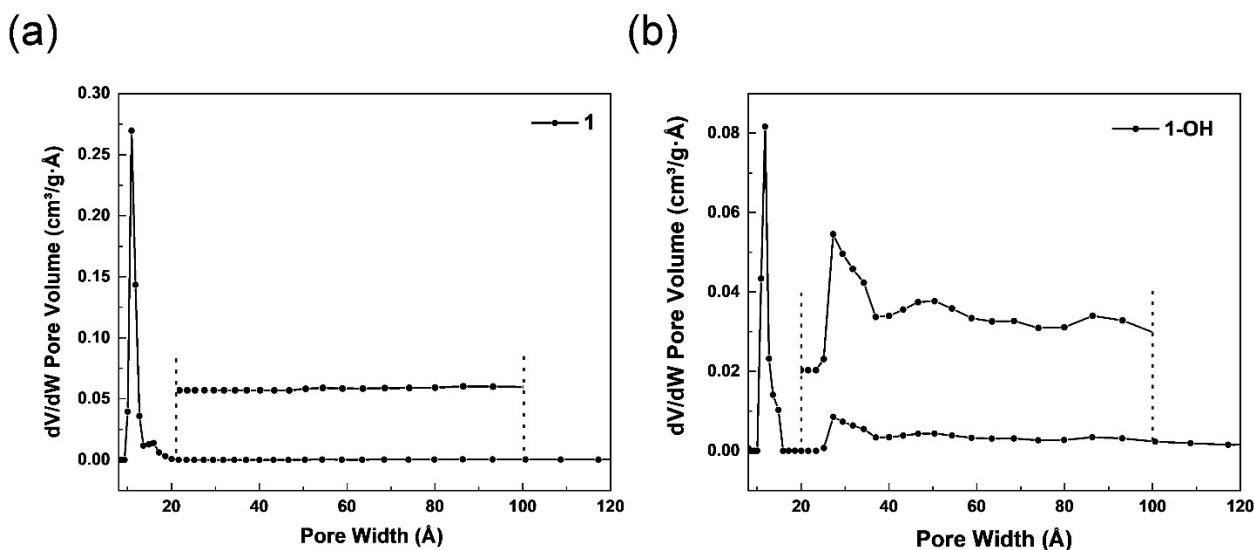
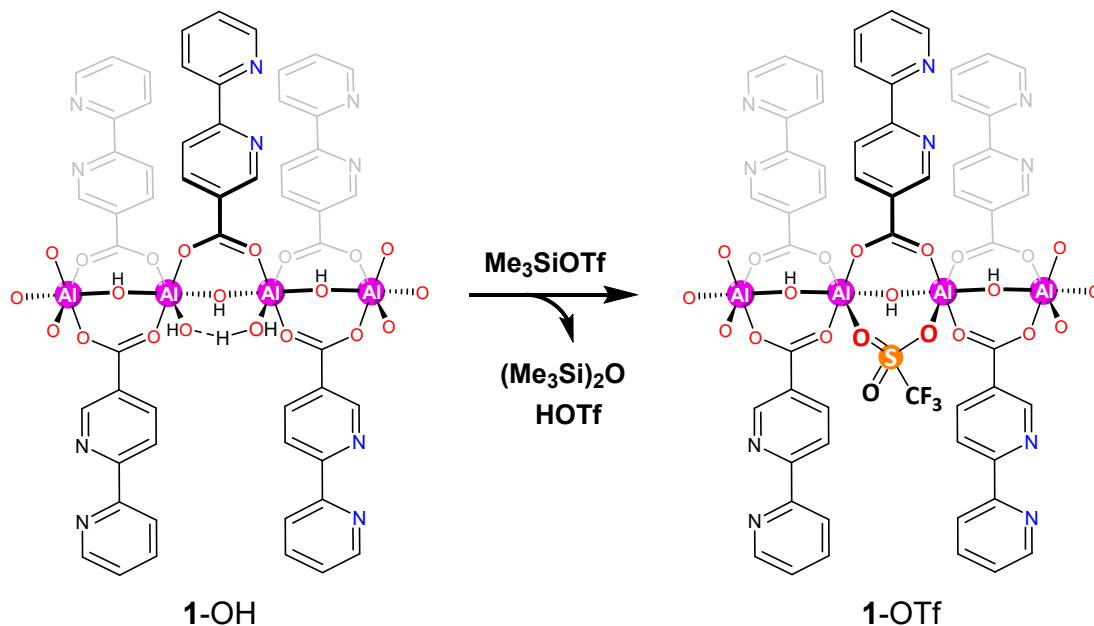


Figure 3-12. Pore size distributions of (a) **1** and (b) **1-OH**. Reprinted with permission from *Journal of the American Chemical Society*, **2020**, 142, 4872-4882. Copyright 2020 American Chemical Society.

3.2.2 Triflation of 1-OH and Lewis Acidity Determination for 1-OTf

Although MOF nodes have been widely used as Lewis acidic sites to catalyze a large broad of organic transformations, including dehydrations,²⁹ cyclizations,³⁰ and hydrolysis,³¹ the Lewis acidity of this MOF node-based metal sites is generally lower than the homogeneous benchmark $\text{Sc}(\text{OTf})_3$.³² In order to improve the Lewis acidity in MOFs, we recently reported a strategy of triflating MOF nodes to develop strong Lewis acidic sites.³³ The resultant materials have comparable Lewis acidity to that of $\text{Sc}(\text{OTf})_3$, and exhibited high catalytic reactivity. **1-OH** was sequentially activated with Me_3SiOTf in benzene at room temperature for 12h, giving **1-OTf** as a light-yellow solid (**Scheme 3-3**).

Scheme 3-3. Chemical equation showing triflation of **1-OH** to afford **1-OTf**. Reprinted with permission from *Journal of the American Chemical Society*, **2020**, 142, 4872-4882. Copyright 2020 American Chemical Society.



Me_3SiOTf readily removed all metal-bound OH/OH_2 moieties due to the formation of stronger bond between oxophilic Me_3Si groups and oxygen, which was confirmed by the

quantification of $(\text{Me}_3\text{Si})_2\text{O}$ base on ^1H NMR (**Figure 3-13**). The amount of $(\text{Me}_3\text{Si})_3\text{O}$ was measured to be 1.93 equiv. w.r.t. OH/OH₂ sites, agreeing well with the proposed activation process.

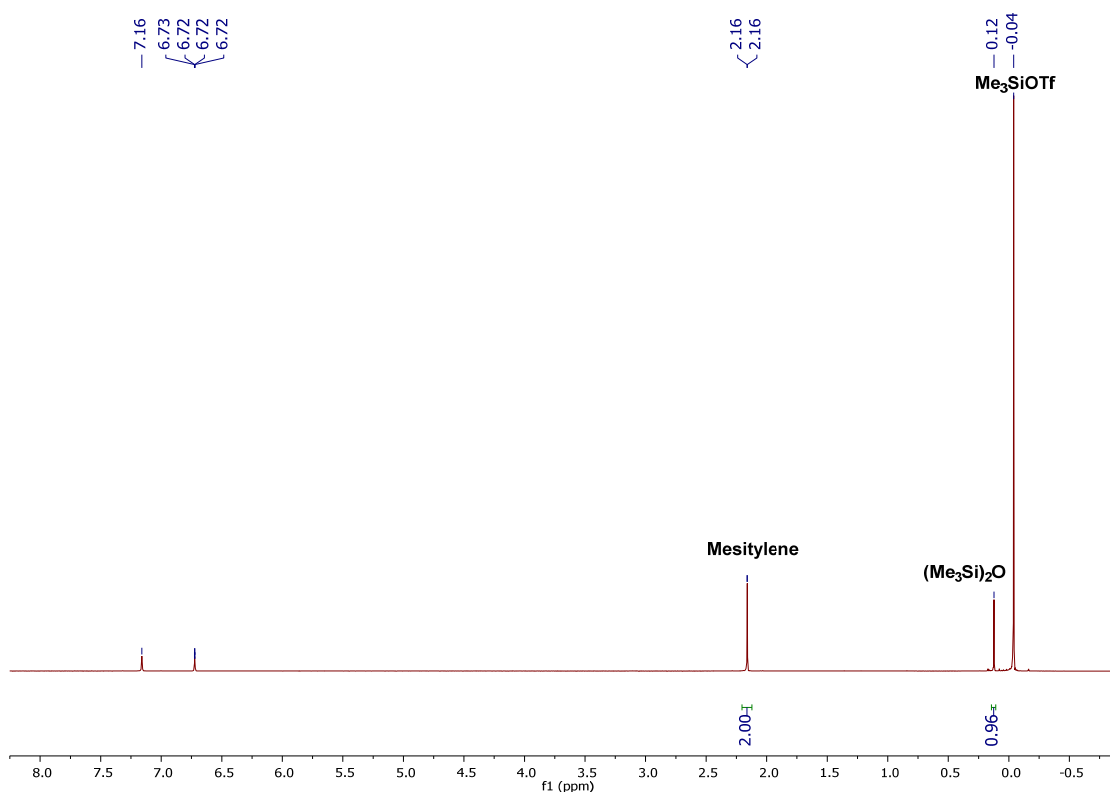


Figure 3-13. ^1H NMR spectrum of the supernatant from **1**-OH activation with Me_3SiOTf . The amount of $(\text{Me}_3\text{Si})_2\text{O}$ was determined to be 1.93 equiv. w.r.t. to the $\text{Al}_2(\text{OH})(\text{OH}_2)$ sites. Reprinted with permission from *Journal of the American Chemical Society*, **2020**, 142, 4872-4882. Copyright 2020 American Chemical Society.

Diffuse reflectance infrared Fourier transform spectroscopy (DRIFTS) was further used to support the removal of $\text{Al}_2(\text{OH})(\text{OH}_2)$ moieties. The increased absorption at $1231 - 1266 \text{ cm}^{-1}$ in **1**-OTf corresponded to the $\nu(\text{S}=\text{O}^{\text{OTf}})$ band (**Figure 3-14a**). The sharp stretching band at 3708 cm^{-1} was observed for bridging $\mu_2\text{-OH}$ groups in both **1** and **1**-OH,³⁴ but this band shifted significantly to 3687 cm^{-1} for **1**-OTf (**Figure 3-14b**). Electron-withdrawing OTf groups weaken the O-H bonds of $\mu_2\text{-OH}$ groups in **1**-OTf, leading to a shift to lower energy. The broad peak centered at 3689 cm^{-1}

¹ in **1**-OH was attributed to hydrogen bonding interactions between neighboring Al-OH and Al-OH₂ moieties.³⁵

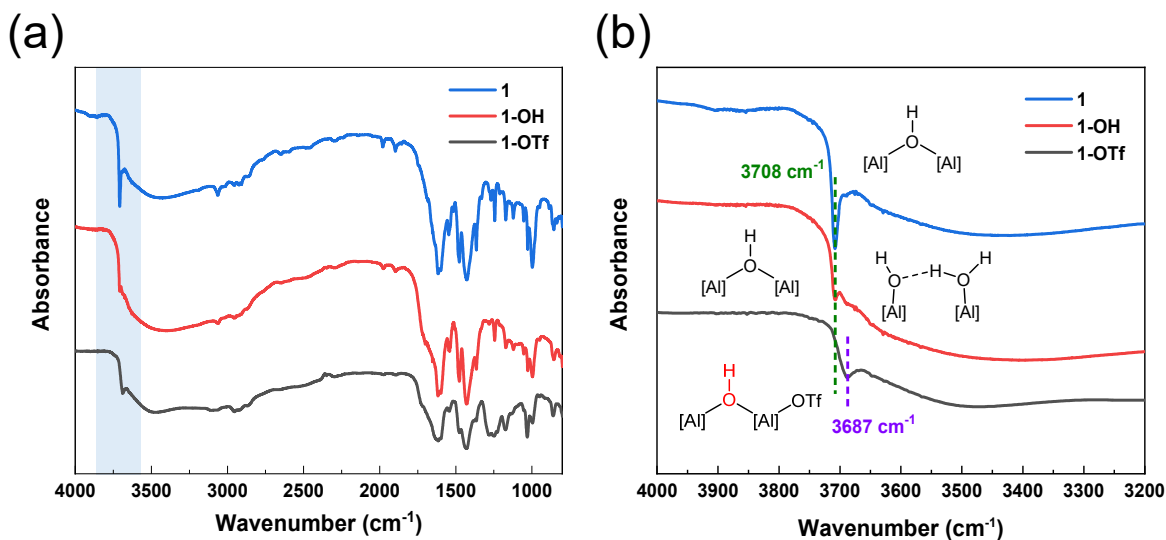


Figure 3-14. (a) DRIFT spectra of **1** (blue), **1**-OH (red), and **1**-OTf (black). (b) Zoomed-in view of the DRIFT spectra show a significant red shift of $\nu(\mu_2\text{-OH})$ from 3708 cm⁻¹ in **1** (blue) and **1**-OH (red) to 3687 cm⁻¹ in **1**-OTf (black). Reprinted with permission from *Journal of the American Chemical Society*, **2020**, 142, 4872-4882. Copyright 2020 American Chemical Society.

We quantified Lewis acidity enhancement in **1**-OTf by fluorescence spectroscopy of MOF-bound N-methylacridone (NMA).³³ Free NMA has an emission maximum (λ_{max}) at 433 nm when excited at 413 nm. Upon coordination to **1**-OTf, the Lewis acid adduct of NMA displayed a λ_{max} at 470 nm (**Figure 3-15**). The energy shift of NMA emission was previously established to be linearly related to the Lewis acidity of metal centers.³⁶⁻³⁷ Using the reported empirical equation, we calculated the ΔE value of **1**-OTf to be 0.93 eV, which is almost identical to the value measured by superoxide EPR spectroscopy. In comparison, **1**-OH only shifted the λ_{max} of NMA emission to 463 nm, with a calculated ΔE of 0.84 eV. Triflation of Al₂(OH)(OH₂) moieties thus significantly enhanced Lewis acidity of **1**-OTf for catalytic applications.

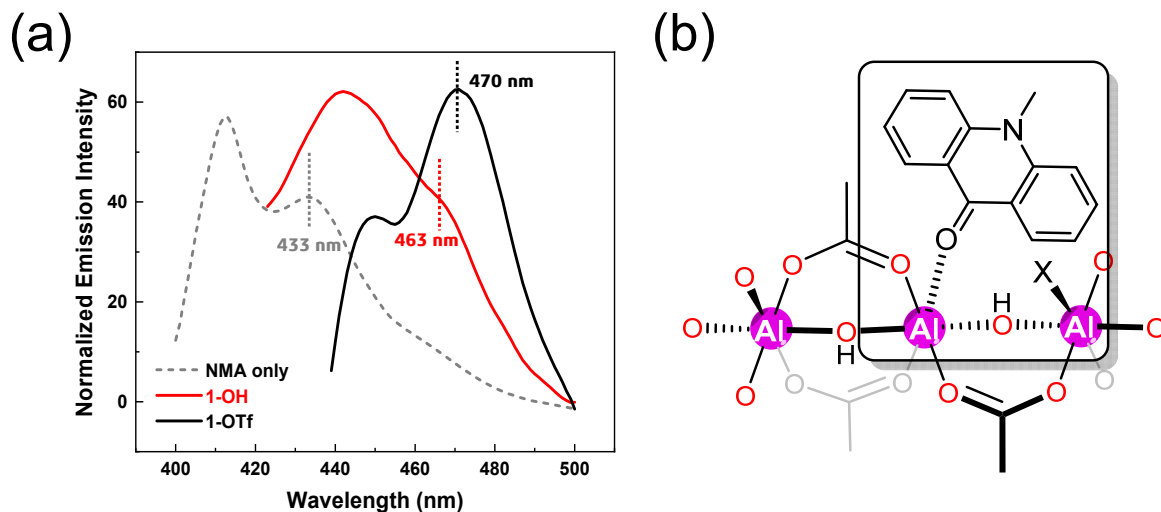


Figure 3-15. Fluorescence spectra of **1-OTf** (black), **1-OH** (red), and free NMA (dashed). Reprinted with permission from *Journal of the American Chemical Society*, **2020**, 142, 4872-4882. Copyright 2020 American Chemical Society.

3.2.3 Synthesis and Characterization of **1-OTf-PdCl₂** and **1-OTf-Pd^{NP}**

1-OTf was further metalated with PdCl₂(MeCN)₂ in THF to prepare the pre-catalyst **1-OTf-PdCl₂** (**Scheme 3-4**). Inductively coupled plasma-mass spectroscopy (ICP-MS) indicated a ratio of Al/Pd to be 2.10, which refers to the formula of **1-OTf-PdCl₂** to be Al(OH)(dcbpy)_{0.81}[PdCl₂(MeCN)₂]_{0.48}(OTf)_{0.38}. This formula was supported by TGA analysis, which gave a residual weight of 27.8% (expected 28.6%) after ramping the temperature to 800 °C (**Figure 3-16**).

Scheme 3-4. Chemical equation showing metalation of **1-OTf** with $\text{Pd}(\text{MeCN})_2\text{Cl}_2$ to afford **1-OTf-PdCl₂** and *in situ* reduction of **1-OTf-PdCl₂** to generate **1-OTf-Pd^{NP}**.

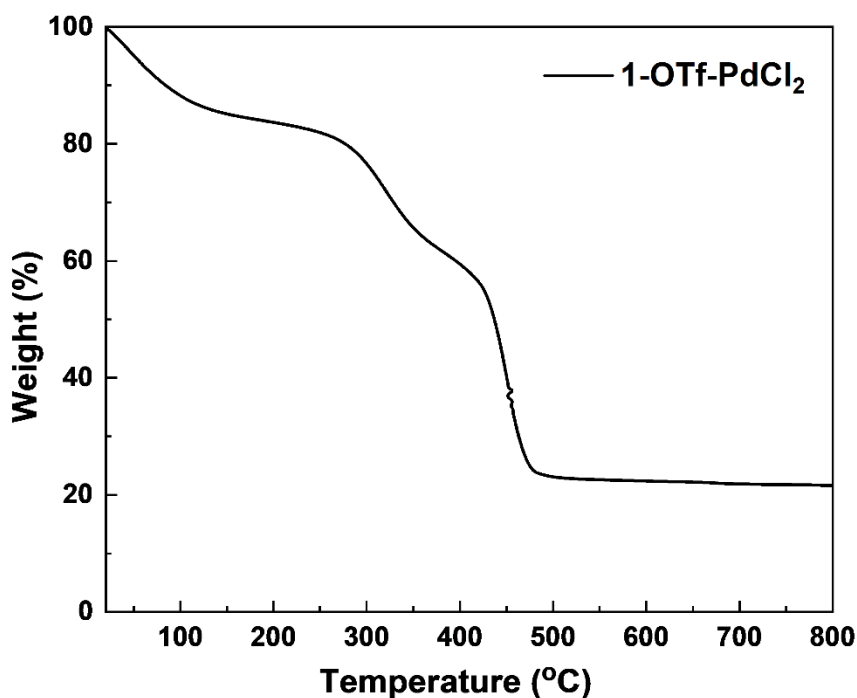
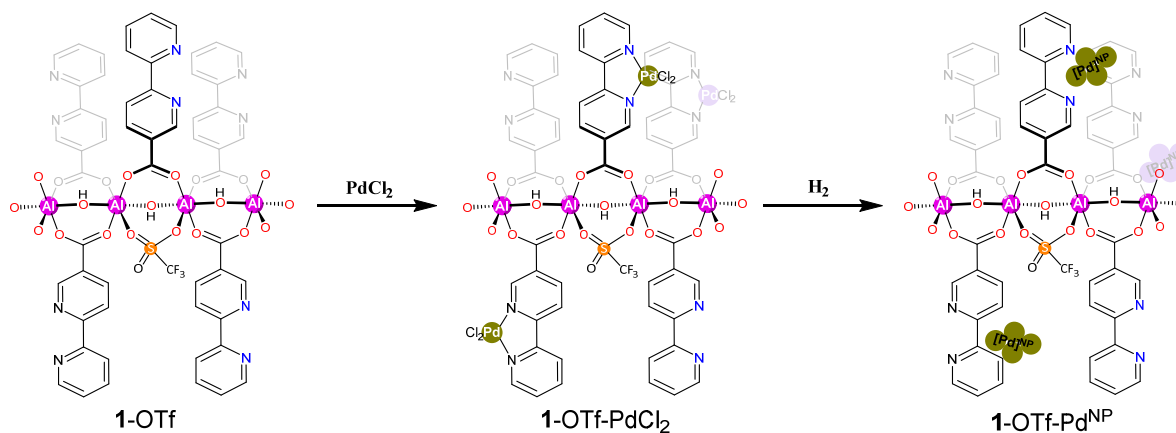


Figure 3-16. TGA curve of **1-OTf-PdCl₂** in the 25-800 °C range. Reprinted with permission from *Journal of the American Chemical Society*, **2020**, 142, 4872-4882. Copyright 2020 American Chemical Society.

TEM imaging showed that **1-OTf-PdCl₂** still maintained the plate-like morphology (**Figure 3-17**), whereas PXRD studies indicated that **1-OTf-PdCl₂** maintained crystalline structure of **1** (**Figure 3-18**).

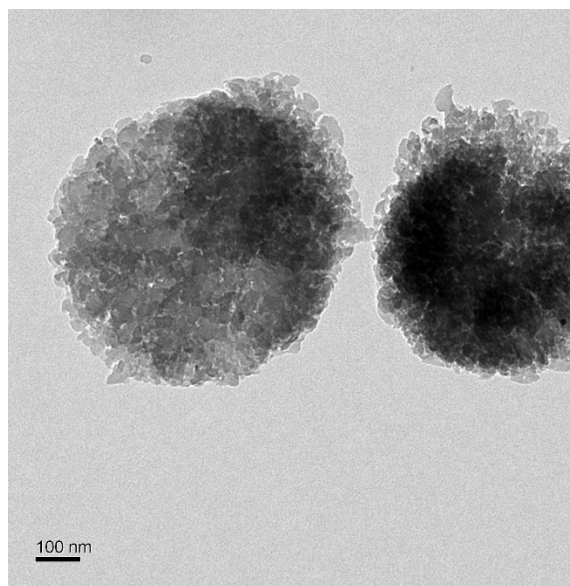


Figure 3-17. TEM image of **1-OTf-PdCl₂**. Reprinted with permission from *Journal of the American Chemical Society*, **2020**, 142, 4872-4882. Copyright 2020 American Chemical Society.

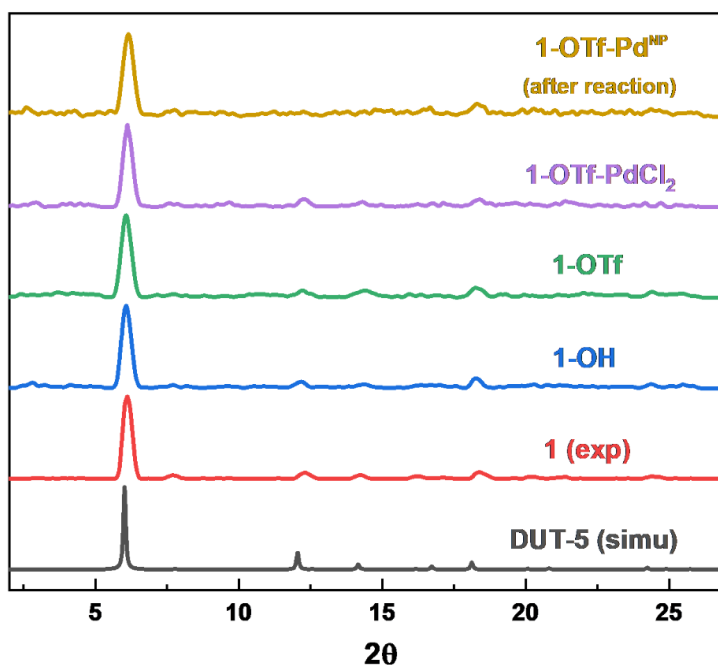


Figure 3-18. The similarity of PXRD patterns of **1** (red), **1-OH** (blue), **1-OTf** (green), **1-OTf-PdCl₂** (purple), and **1-OTf-Pd^{NP}** (khaki) to the simulated pattern of DUT-5 (black) indicates the crystallinity of the MOF was maintained after multi-step post-synthetic manipulations. Reprinted with permission from *Journal of the American Chemical Society*, **2020**, 142, 4872-4882. Copyright 2020 American Chemical Society.

Pd coordination environment of **1-OTf-PdCl₂** was studied by extended X-ray absorption fine structure (EXAFS) spectroscopy. The EXAFS data was collected at Pd K-edge and fitted with reported crystal structure of (bpy)PdCl₂.³⁸ The EXAFS feature of Pd centers in **1-OTf-PdCl₂** was well fit with the structure to afford nearly identical coordination geometry and bond lengths (**Figure 3-19**). Specifically, the Pd centers in **1-OTf-PdCl₂** coordinate to two chlorides and one bpy ligand in a near square planar geometry with an average Pd-N bond length of 2.04 ± 0.01 Å and an average Pd-Cl bond length of 2.30 ± 0.02 Å.

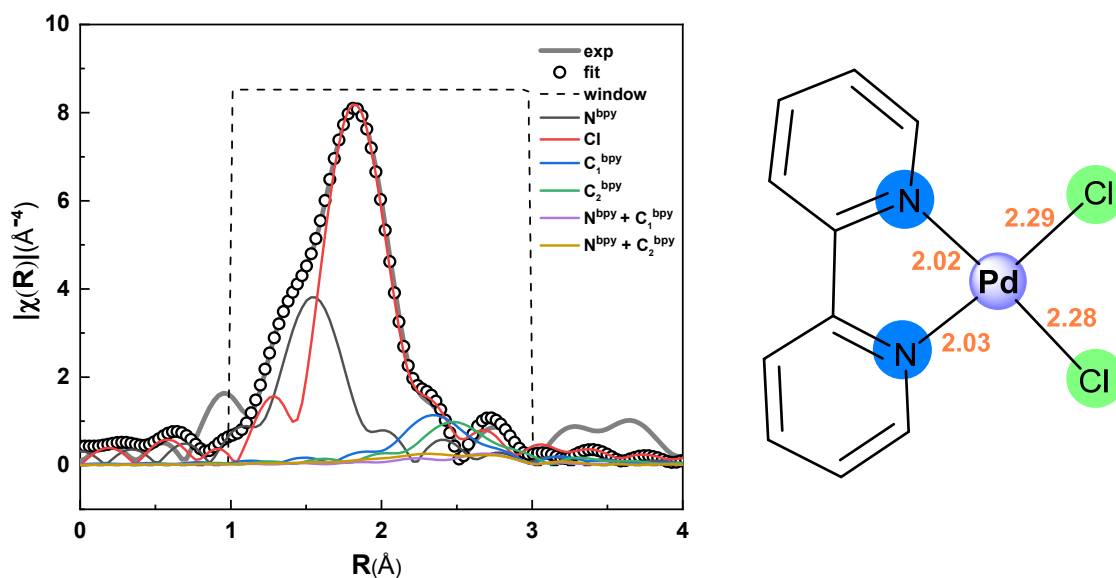


Figure 3-19. EXAFS spectrum (gray solid line) and fit (black circles) in R-space at the Pd K-edge adsorption of **1-OTf-PdCl₂**, with the fragment structure of (bpy)PdCl₂ for EXAFS fitting of the Pd coordination environment in **1-OTf-PdCl₂**. H atoms were omitted for clarity. Adapted with permission from *Journal of the American Chemical Society*, **2020**, 142, 4872-4882. Copyright 2020 American Chemical Society.

Upon treatment with H₂ in the catalytic reaction, the Pd^{II} centers in **1-OTf-PdCl₂** were readily reduced to form metallic Pd NPs in **1-OTf-Pd^{NP}**. To investigate the true catalytic active species during the reaction process, we characterized the MOF materials recovered from catalytic C-O cleavage reactions by PXRD, TEM, and XANES.

PXRD studies showed that the MOF after catalysis remained crystalline (**Figure 3-18**), whereas TEM imaging indicated the formation of Pd NPs which were dispersed evenly in the MOF matrix (**Figure 3-20**).

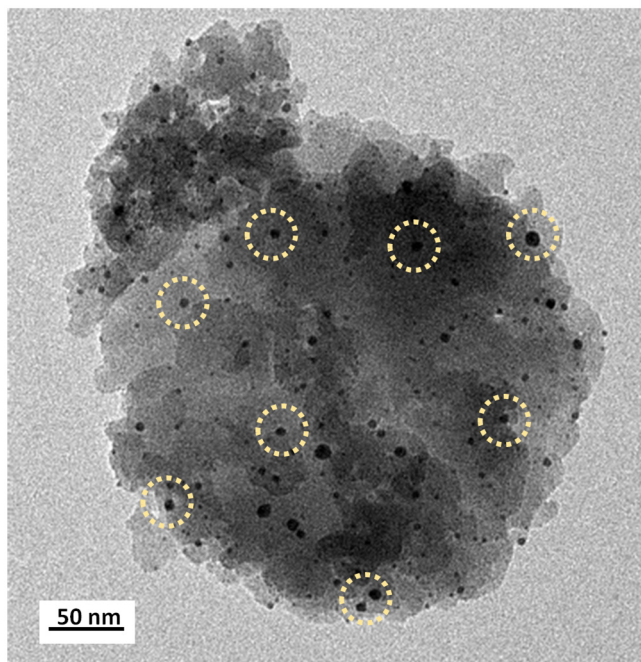


Figure 3-20. TEM image of **1-OTf-Pd^{NP}** shows evenly distributed Pd NPs in the MOF matrix after *in situ* reduction in catalytic reactions. Reprinted with permission from *Journal of the American Chemical Society*, **2020**, 142, 4872-4882. Copyright 2020 American Chemical Society.

Furthermore, XANES spectra at Pd K-edge of **1-OTf-PdCl₂**, **1-OTf-Pd^{NP}**, PdCl₂, and Pd foil are shown in **Figure 3-21**. The first oscillations of Pd metal appear immediately after the edge, positioned at 24367 and 24391 eV, correspond to 1s → 5p and 1s → 4f electronic transitions, respectively. PdCl₂ features the absorption peak at 24380 eV.³⁹ As compared to the peak positions of Pd(0) in Pd foil and Pd(II) in PdCl₂, XANES spectrum of **1-OTf-Pd^{NP}** contained features of both Pd(0) and Pd(II).

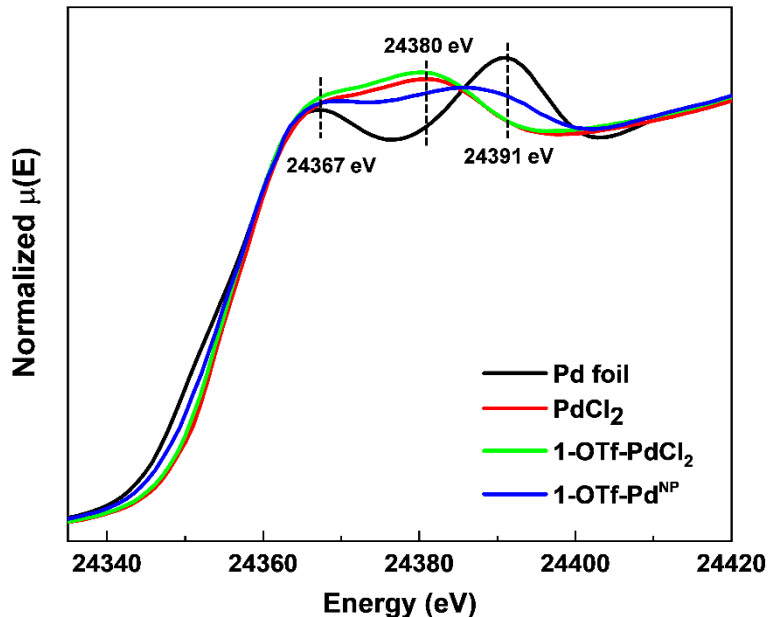


Figure 3-21. XANES Spectra of **1-OTf-PdCl₂**, **1-OTf-Pd^{NP}**, Pd foil, and PdCl₂. Reprinted with permission from *Journal of the American Chemical Society*, **2020**, 142, 4872-4882. Copyright 2020 American Chemical Society.

We conducted the linear combination fitting of the XANES spectrum of **1-OTf-Pd^{NP}** (the Pd-K edge: -20 eV to 60 eV) using the spectra of Pd foil and PdCl₂ as basis functions. The fitting gave ~48% Pd⁰ species in the recovered MOF (**Figure 3-22**); it is likely that surface Pd centers of **1-OTf-Pd^{NP}** were oxidized by air to afford Pd^{II} species when the samples were processed for XANES studies.

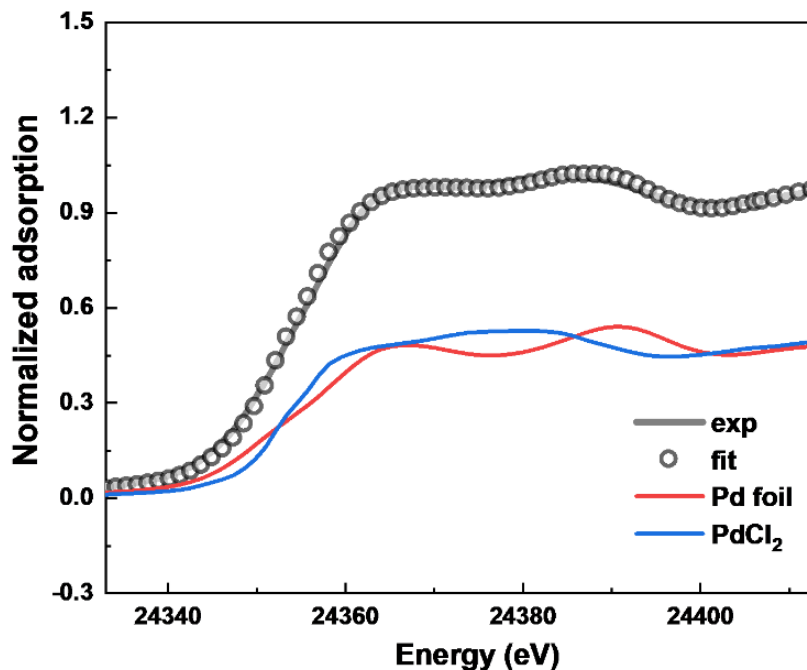


Figure 3-22. Linear combination fitting of 1-OTf-Pd^{NP} XANES feature using those of Pd foil and PdCl₂ as the basis functions. Reprinted with permission from *Journal of the American Chemical Society*, **2020**, 142, 4872-4882. Copyright 2020 American Chemical Society.

3.2.4 1-OTf-PdCl₂ Catalyzed Tandem Ether/alcohol C-O Bond Cleavage

Etheric and alcoholic C-O linkages widely exist in biomass-based feedstocks, which presents a major challenge in transforming biomass into chemicals and hydrocarbon fuels with low oxygen content.⁴⁰⁻⁴¹ The effective cleavage of such C-O bonds is of great importance and has drawn significant research interest during the past decade.^{10, 42} Acid catalysts have been proved to actively participate in the C-O bond formation from hydroalkoxylation between alcohols and alkenes,^{33, 43} as well as its reversible form, dehydroalkoxylation to cleavage an alkyl ether to an olefin and alcohol.¹¹⁻¹² Through coupling the exothermic alkene hydrogenation reaction with the dehydroalkoxylation process, which is endothermic with $\Delta H \approx + 10\sim 20$ kcal/mol, the overall C-O bond cleavage reaction becomes exothermic to provide a saturated alkane and alcohol as the product.^{11, 44} However, the key to realizing such a tandem process lies in the design of a catalytic system with both acid catalyst and hydrogenation catalyst without interference.

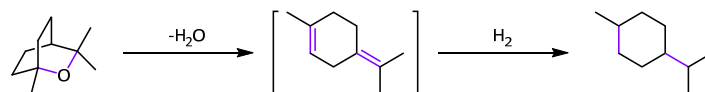
Multifunctional catalyst systems containing hydrogenation catalysts and acid catalysts, including homogeneous mineral acids, Lewis acids, or heterogeneous acidic materials, have been studied in such tandem processes.⁴⁵⁻⁴⁶ In particular, Marks and coworkers demonstrated that metal triflate salts and supported Pd metallic catalysts effectively catalyzed ether and alcohol (3°, 2°, and 1°) C-O bond hydrogenolysis to generate saturated hydrocarbons in a tandem manner.¹⁰⁻¹¹ However, these solution-based catalysts typically suffered from rapid catalyst deactivation, and required relatively harsh conditions with elevated reaction temperatures and high H₂ pressures, especially for difficult substrates like 2° and 1° alcohols/ethers. Furthermore, some dimerization or aromatization side products were usually detected after these reactions.

With isolated catalytic sites confined by the MOF framework, *in situ* generated **1**-OTf-Pd^{NP} catalyst is expected to significantly stabilize strongly Lewis acidic Al₂(μ₂-OTf) sites and evenly distributed Pd NPs to realize highly effective tandem catalysis. At the same time, the pore restriction in the 1D channels of **1**-OTf-Pd^{NP} can prevent undesired dimerization and aromatization to improve product selectivity.

1,8-cineole was used as a model compound to optimize the reaction conditions for tandem C-O bond cleavage (**Table 3-1**). Initial screening of solvents revealed that 1,8-cineole could be quantitatively converted to menthane in 1,2-dichloroethane at 0.2 mol% loading of **1**-OTf-PdCl₂ [w.r.t. Lewis acidic Al₂(μ₂-OTf) sites] and 100 °C under 20 bar of H₂ for 24 h (**Table 3-1**, entry 4). Nonpolar solvents such as octane and coordinating solvents such as THF gave lower catalytic performance, likely due to poor substrate solubility and poisoning of Lewis acidic metal sites, respectively. The highest TON of 800 was obtained when the catalyst loading was lowered to 0.1 mol%; this level of catalytic activity significantly outperformed previously reported catalytic systems. **1**-OTf-PdCl₂ is also advantageous to the well-studied homogeneous metal triflate plus

supported Pd NP system by avoiding the use of substoichiometric amounts of expensive metal triflates such as Hf(OTf)₄, Sc(OTf)₃, and Yb(OTf)₃.

Table 3-1. Screening of reaction conditions for **1**-OTf-PdCl₂ Catalyzed Tandem Etheric/Alcohol C-O Bond Cleavage.^a



Entry	Catalyst (mol % Loading)	Solvent	Temp./ °C	Yield of menthane / %	TON
1	1 -OTf-PdCl ₂ (0.5%)	Octane	130	74	148
2	1 -OTf-PdCl ₂ (0.5%)	THF	130	31	62
3	1 -OTf-PdCl ₂ (0.1%)	neat	130	40	400
4	1 -OTf-PdCl ₂ (0.2%)	1,2-dichloroethane	100	>99	>500
5	1 -OTf-PdCl ₂ (0.1%)	1,2-dichloroethane	100	80	800
6	-	1,2-dichloroethane	100	N.D.	-
7 ^b	1 -OTf (0.2 %)	1,2-dichloroethane	100	<1	-
8 ^c	1 -OH-PdCl ₂ (0.2 %)	1,2-dichloroethane	100	22	110
9 ^d	Al(OTf) ₃ + Pd (0.2 %)	1,2-dichloroethane	100	9	45
10 ^e	HOTf + Pd (0.2 %)	1,2-dichloroethane	100	3	15

^aReaction conditions: **1**-OTf-PdCl₂ (loading w.r.t. Al₂(μ₂-OTf), 0.6 mmol 1,8-cineole, 20 bar H₂, 1 mL solvent or neat condition, 24 h; Yield of menthane was determined by GC-MS analysis.

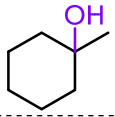
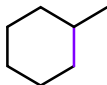
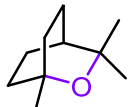
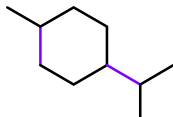
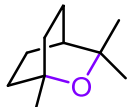
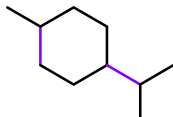
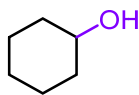
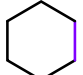
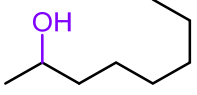
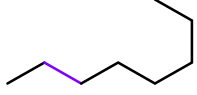
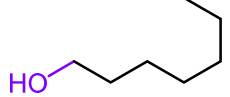
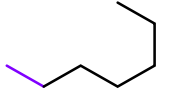
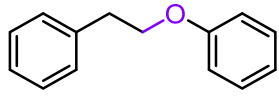
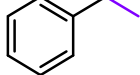
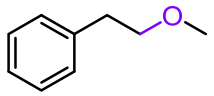
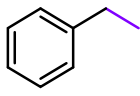
^bCatalysts: 0.2 mol% of **1**-OTf. ^cCatalysts: 0.2 mol% of **1**-OH-PdCl₂ (w.r.t. Al₂(OH)(OH₂)).

^dCatalysts: 0.2 mol% of Al(OTf)₃ + 0.25 mol% Pd(MeCN)₂Cl₂. ^eCatalysts: 0.2 mol% of HOTf + 0.25 mol% Pd(MeCN)₂Cl₂.

We next examined the substrate scope of **1**-OTf-PdCl₂ catalyzed tandem etheric/alcoholic C-O bond cleavage. A broad scope of substrates including tertiary (3°), secondary (2°), and primary (1°) alcohols/ethers were readily converted to alkanes by **1**-OTf-PdCl₂ under similar conditions (**Table 3-2**). Quantitative conversion of 3° alcohol (1-methylcyclohexanol) and 3° ether

(1,8-cineole) to saturated alkanes was achieved at 0.1-0.2 mol% loading of **1-OTf-PdCl₂** and at 100 °C (**Table 3-2**, entries 1 and 2). Reaction temperatures as high as 150 °C were needed to quantitatively convert 2° alcohols and ethers (cyclohexanol, 2-octanol, dicyclohexyl ether, and cyclohexyl phenyl ether) to corresponding saturated alkanes (**Table 3-2**, entries 4-7). 1° alcohol (1-heptanol) required even higher reaction temperatures of up to 200 °C and 0.5 mol% loading of **1-OTf-PdCl₂** to afford heptane in 92% yield (**Table 3-2**, entry 8). High product selectivity was observed for different kinds of substrates with **1-OTf-PdCl₂** as the precatalyst without detection of any undesired dimerization or aromatization product. The outstanding product selectivity of **1-OTf-PdCl₂** is attributed to the pore size exclusion by the uniform MOF channels and well-defined, site-isolated Lewis acids and Pd NPs in the MOF. Notably, 1° ethers with active β-hydrogen atoms, i.e., phenethoxybenzene and (2-methoxyethyl)benzene, underwent C-O bond cleavage at 150 °C and 130 °C, respectively, to produce ethylbenzene as the main product with a high selectivity over the over-hydrogenated product methylcyclohexane.

Table 3-2. Substrate Scope for 1-OTf-PdCl₂ Catalyzed Tandem Etheric/Alcoholic C-O Bond Cleavage.^a

Entry	Substrate	Catalyst Loading	Reaction Temperature	Product	Conversion (Yield)
1		0.1 mol%	100 °C		100% (>99%)
2		0.2 mol%	100 °C		100% (>99%)
3		0.1 mol%	100 °C		80% (80%)
4		0.1 mol%	150 °C		100% (>99%)
5		0.2 mol%	150 °C		100% (>99%)
6		0.5 mol%	200 °C		100% (92%)
7		0.2 mol%	150 °C		100% (89%) ^b
8		0.2 mol%	130 °C		70% (61%) ^b

^aUnless noted, all reactions performed with indicated amount of catalyst, 0.6 mmol of substrate, and 20 bar H₂ in 1.0 mL of 1,2-dichloroethane for 24 h. Conversions and yields determined by GC-MS integrals with mesitylene as the internal standard. Isolated yields for selected products were determined by ¹H NMR. ^bReaction performed in 1 bar H₂.

3.2.5 1-OTf-PdCl₂ Catalyzed Tandem Ester C-O Bond Cleavage

Ester functionalities also widely exist in bio-derived molecules such as triglycerides, fats, and oil components and are a promising source of renewable biodiesel fuel.⁴⁷⁻⁴⁸ Traditional decarboxylation methods usually required high reaction temperatures up to 500 °C to thermally

crack the C-O bond followed by the CO₂ release.⁴⁹⁻⁵⁰ Metal triflates + Pd/C systems have also been used in the tandem ester C-O bond cleavages, with moderate to good selectivities and yields.⁵¹⁻⁵²

1-OTf-PdCl₂ was also proved highly active for tandem ester C-O bond cleavage with a reactivity trend of 3° carbon > 2° carbon > 1° carbon (Table 3). The 3° ester terpinyl acetate was effectively cleaved to produce menthane at 0.2 mol% loading of **1**-OTf-PdCl₂ at 100 °C, affording a TON of 440 (Table 3-3, entry 1). The 2° ester L-menthyl acetate was decarboxylated in the presence of 0.5 mol% **1**-OTf-PdCl₂ at 150 °C to afford menthane in quantitative yield (Table 3-3, entry 2). Other 2° acetate or propionate esters, i.e., cyclohexyl acetate, and cyclohexyl propionate, readily underwent C-O cleavage at 0.5 mol% **1**-OTf-PdCl₂ at 150 °C to afford decarboxylated products in 62 to 84% yields (Table 3-3, entries 4-5). For the 1° ester octyl acetate, a higher temperature of 200 °C was needed to afford octane in 79% yield (Table 3-3, entry 6). Interestingly, 1° ester with active β-hydrogen atoms, i.e., phenethyl acetate, readily underwent C-O cleavage at 0.2 mol% loading of **1**-OTf-PdCl₂ and 130 °C to afford ethylbenzene in 94% yield (Table 3-3, entry 7). Moreover, the lactone 5-hexanolide also underwent tandem C-O cleavage to generate the saturated carboxylic acid (hexanoic acid) in 61% yield (Table 3-3, entry 8). Such a MOF-based tandem catalyst system thus provided a potential solution for cleavage of esteric C-O bonds.

Table 3-3. Substrate Scope for **1-OTf-PdCl₂** Catalyzed Ester C-O Bond Cleavage.^a

Entry	Substrate	Catalyst Loading	Reaction Temperature	Product	Conversion (Yield)
1		0.2 mol%	100 °C		100% (88%) ^b
2		0.5 mol%	150 °C		100% (>99%)
3		0.1 mol%	150 °C		45% (45%)
4		0.5 mol%	150 °C		84% (78%)
5		0.5 mol%	150 °C		91% (84%) ^b
6		0.5 mol%	150 °C		87% (62%) ^b
7		0.5 mol%	200 °C		100% (79%)
8		0.2 mol%	130 °C		100% (94%) ^c
9		0.2 mol%	130 °C		100% (61%)

^aUnless noted, all reactions performed with indicated amount of catalyst, 0.6 mmol of substrate, and 20 bar H₂ in 1.0 mL of 1,2-dichloroethane for 24 h. Conversions and yields were determined by GC-MS integrals with mesitylene as the internal standard. Isolated yields for selected products were determined by ¹H NMR ^bReaction performed for 36 h. ^cReaction performed in 1 bar H₂ for 6 h.

3.2.6 Heterogeneity of **1-OTf-Pd^{NP}**

Several lines of evidence support the heterogeneity of **1-OTf-PdCl₂** in tandem C-O bond cleavage reactions. The catalysts recovered from C-O bond cleavage reactions exhibited identical

PXRD patterns to pristine **1**, indicating structural stability of **1**-OTf-PdCl₂ in catalytic reactions (**Figure 3-18**).

Lewis acidity quantification on the MOF recovered from the catalytic reaction confirmed the maintenance of Lewis acidity in the catalytic process (**Figure 3-23**). ICP-MS analysis showed minimal leaching of Al (0.6%) and Pd (0.02%) into the supernatant after the first reaction run.

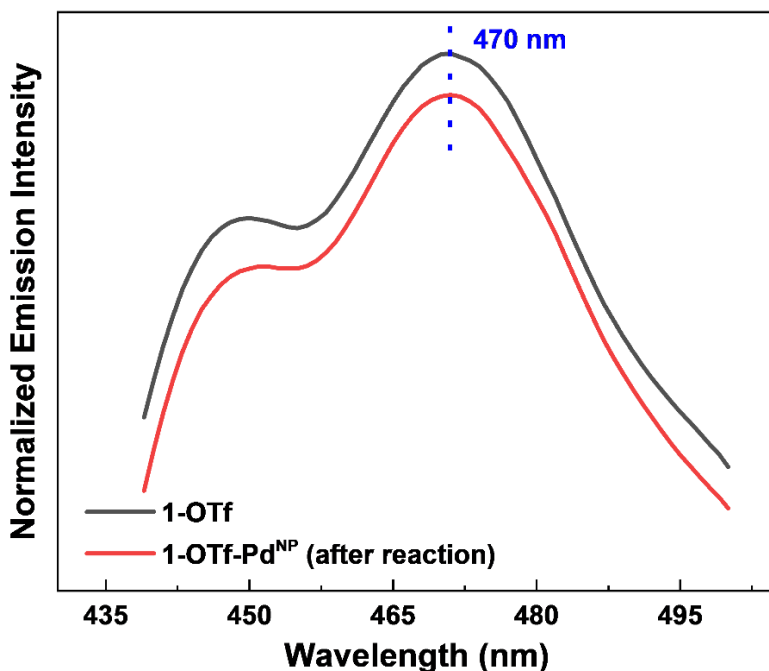


Figure 3-23. NMA fluorescence spectra upon binding to **1**-OTf (black) and **1**-OTf-Pd^{NP} recovered from C-O bond cleavage of 1-methylcyclohexanol (red). Reprinted with permission from *Journal of the American Chemical Society*, **2020**, 142, 4872-4882. Copyright 2020 American Chemical Society.

In order to determine the amount of leached OTf groups, we separated the MOF from the supernatant after **1**-OTf-PdCl₂ catalyzed C-O cleavage of 1-methylcyclohexanol. We performed ¹⁹F NMR analysis of both the supernatant and the digested MOF (digested with D₃PO₄). From the ¹⁹F NMR spectra (**Figure 3-24**), the sample taken from the supernatant showed no ¹⁹F peak (maroon) while the digested MOF gave an OTf ¹⁹F signal at -78 ppm (green). This result indicates negligible leaching of OTf groups during the catalytic reaction.

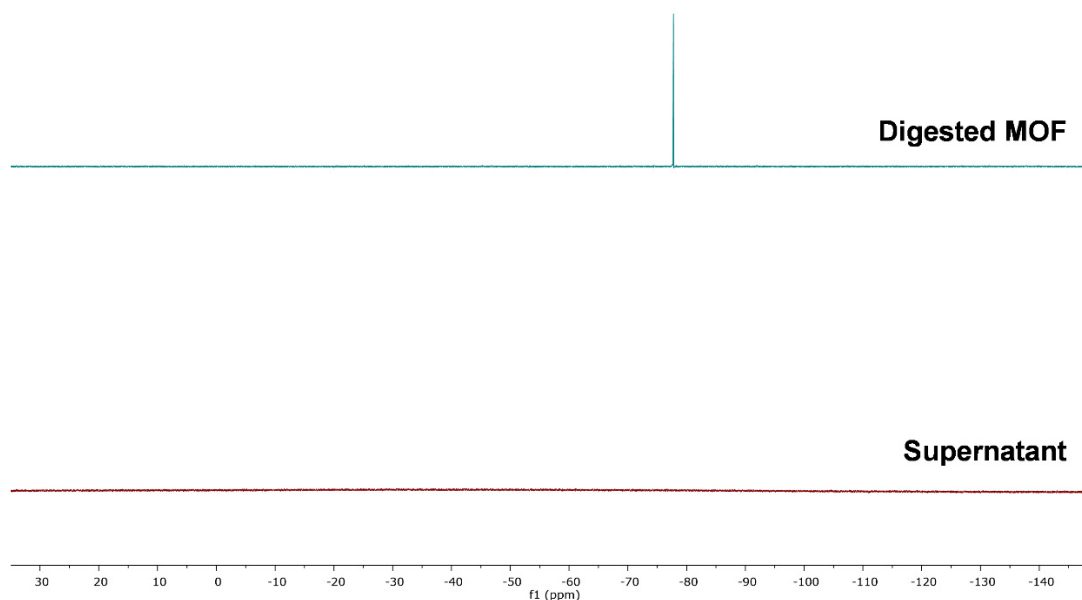


Figure 3-24. ^{19}F NMR spectra of the supernatant (maroon) and the digested MOF (green). Reprinted with permission from *Journal of the American Chemical Society*, **2020**, 142, 4872-4882. Copyright 2020 American Chemical Society.

“Hot filtration” test was performed to rule out the possibility of leached Lewis acidic metal species, soluble Brønsted acidic species, and homogeneous metal species contributing to the tandem C-O bond cleavage activity (**Figure 3-25**). Specifically, 0.2 mol% of **1-OTf-PdCl₂** was first used to catalyze tandem C-O cleavage of 1,8-cineole to give menthane (a mixture of cis/trans isomers) in 97% yield in 10 hours. Then, under inert atmosphere, the MOF and supernatant were separated via centrifugation and used as catalysts, respectively, for the tandem C-O bond cleavage reaction of cyclohexanol without further treatment. The recovered **1-OTf-PdCl₂** catalyst afforded cyclohexane in 99% yield in 10 hours, while less than 0.5% of the C-O cleavage product was detected in the reaction catalyzed by the supernatant. This result excludes the possibility of leached metal species or soluble acids contributing to the catalytic reactivity.

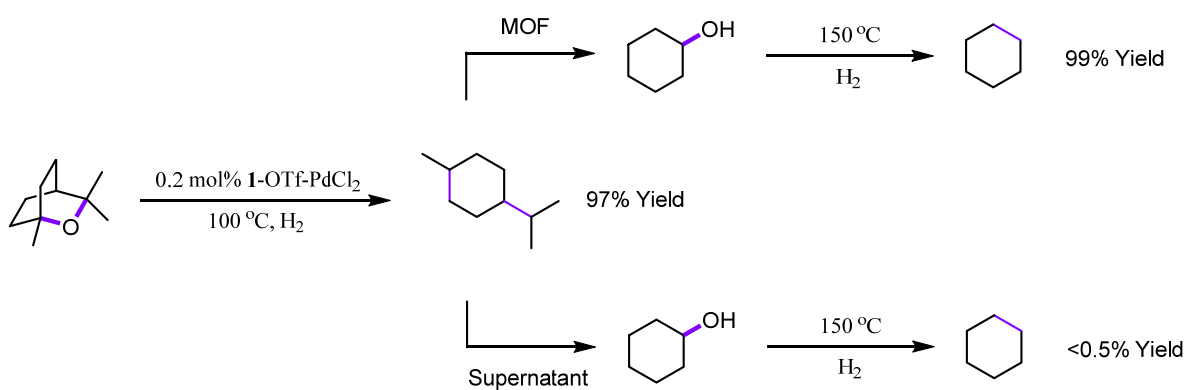


Figure 3-25. The “hot filtration” test of **1-OTf-PdCl₂** catalyzed tandem C-O bond cleavage reaction.

Impressively, **1-OTf-PdCl₂** was readily recovered by simple centrifugation and reused for at least 5 times without significant drop in catalytic activity (**Figure 3-26**). Moreover, **1-OTf-PdCl₂** catalyzed tandem C-O cleavage of 1,8-cinole at ~2 g scale (20 times larger scale) afforded menthane in 75% yield in 24 h under standard reaction conditions. The excellent thermal stability and recyclability make **1-OTf-PdCl₂** a potential catalyst for practical tandem etheric/alcoholic C-O bond cleavage.

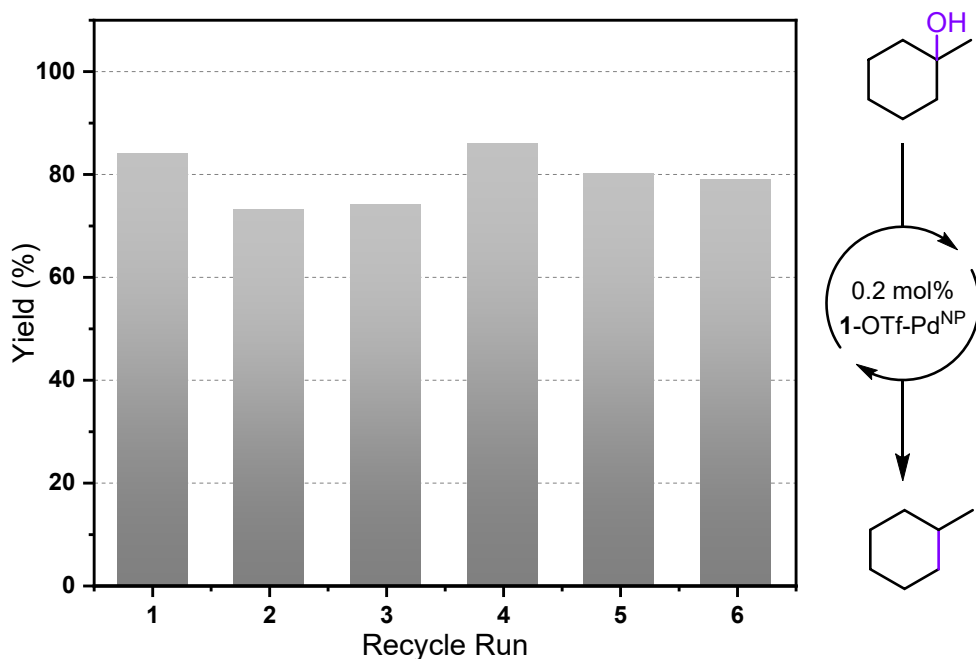


Figure 3-26. Recycle experiments for **1**-OTf-PdCl₂ catalyzed C-O bond cleavage of 1-methylcyclohexanol. Plots of methylcyclohexane yields (%) in six consecutive runs with 3 h of reaction time. Reprinted with permission from *Journal of the American Chemical Society*, 2020, 142, 4872-4882. Copyright 2020 American Chemical Society.

3.2.7 Proposed Tandem Pathway

Several control experiments were conducted to gain insights into the tandem catalytic pathway of **1**-OTf-PdCl₂ mediated C-O bond cleavage. In the absence of the MOF catalyst, 1,8-cinole was totally unreactive under the reaction condition (**Table 3-1**, entry 6). At a loading of 0.2 mol% **1**-OTf, a negligible amount of menthane was detected (**Table 3-1**, entry 7). The lack of activity of **1**-OTf is likely due to the unfavorable thermodynamics of the dehydroalkoxylation reaction. 0.2 mol% loading of **1**-OH-PdCl₂ gave a much lower menthane yield of 22% (**Table 3-1**, entry 8), consistent with much lower Lewis acidity of Al₂(OH)(OH₂) sites than Al₂(μ₂-OTf) sites. Under identical conditions, homogenous controls with Al(OTf)₃ plus Pd(MeCN)₂Cl₂ and HOTf plus Pd(MeCN)₂Cl₂ gave very low menthane yields of 9% and 3%, respectively (**Table 3-1**, entries 9 and 10). These results suggest that C-O bond cleavage by **1**-OTf-PdCl₂ occurs in a tandem

manner, where strong Lewis acidic $\text{Al}_2(\mu_2\text{-OTf})$ sites on the SBUs catalyze the dehydroalkoxylation of etheric/alcoholic C-O bonds to afford C=C bonds which are hydrogenated by nearby Pd NPs confined in the MOF channels. The hydrogenation reaction pushes the equilibrium to the right to form saturated hydrocarbons (**Figure 3-27**).

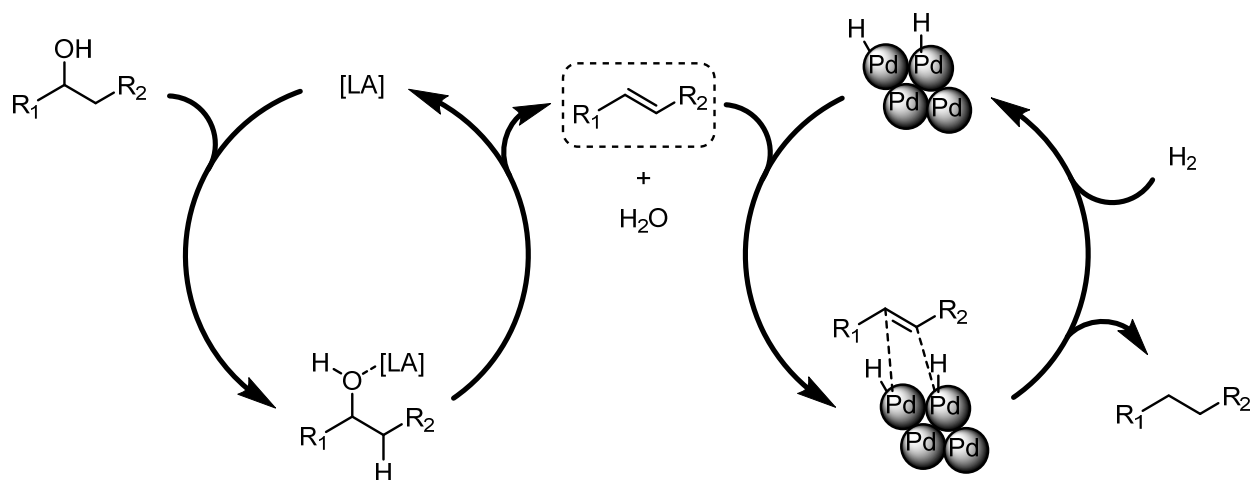


Figure 3-27. Proposed tandem pathway for **1-OTf-PdCl₂**-mediated C-O bond cleavage. Reprinted with permission from *Journal of the American Chemical Society*, **2020**, 142, 4872-4882. Copyright 2020 American Chemical Society.

3.3 Conclusion

In this chapter, we demonstrated a strategy to construct an orthogonal tandem catalyst based on m-MOF-253 with infinite Al-OH chain SBUs and a mixture of dcbpy and pdac bridging ligands. Step-by-step post-synthetic engineering generated a highly active and selective tandem catalyst for apparent hydrogenolysis of various etheric, alcoholic, and esteric C-O bonds to generate deoxygenated saturated alkanes. First, post-synthetic ozonolysis selectively cleaved and removed the pdac ligands. Triflation of the Al-OH/OH₂ open sites significantly enhanced the Lewis acidity for dehydroalkoxylation whereas coordination of the dcbpy ligands with $\text{PdCl}_2(\text{MeCN})_2$ afforded the orthogonal Pd sites which were reduced in situ to generate metallic Pd NPs as the hydrogenation catalyst. The resultant MOF catalyst **1-OTf-Pd^{NP}** showed outstanding

catalytic performance in apparent hydrogenolysis of various etheric, alcoholic, and esteric C-O bonds to generate deoxygenated saturated alkanes under relatively mild conditions via a tandem dehydroalkoxylation-hydrogenation process. The reactivity of C-O bonds displayed an obvious trend of $3^\circ > 2^\circ > 1^\circ$. Control experiments further confirmed the heterogeneous nature and recyclability of **1**-OTf-Pd^{NP} catalyst and its superiority over homogeneous analogues.

3.4 Experimental

3.4.1 Material and Methods

All the reactions and manipulations were carried out under N₂ with the use of a glovebox or Schlenk technique, unless otherwise indicated. Tetrahydrofuran and toluene were purified by passing through a neutral alumina column under N₂. Benzene, *d*₆-benzene, and *n*-octane were distilled over CaH₂. Substrates including alcohols, ethers and esters were purchased from Fisher or Aldrich, and dried over freshly activated 4Å molecular sieves and degassed by freeze-pump-thaw methods before storage in a glovebox for further use.

Powder X-ray diffraction (PXRD) data was collected on a Bruker D8 Venture diffractometer using Cu K α radiation source ($\lambda = 1.54178 \text{ \AA}$). N₂ sorption experiments were performed on a Micrometrics TriStar II 3020 instrument. Thermogravimetric analysis (TGA) was performed in air using a Shimadzu TGA-50 equipped with a platinum pan and heated at a rate of 1.5 °C per min. Fourier-transform infrared (FT-IR) spectra were collected using a Nexus 870 spectrometer (Thermo Nicolet) installed with Diffuse Reflectance Infrared Fourier Transform Spectroscopy (DRIFTS) system. Transmission electron microscopy (TEM) images were taken on a TECNAI F30 HRTEM. Scanning electron microscopy (SEM) images were taken on the Carl Zeiss Merlin, with the detectors of In-Lens, EsB, AsB, & SE2. Ozonolysis was performed on an Azcozon RMU-DG3 ozone generator, which produces up to ~0.42 mol/h ozone at a 6 L/min O₂ gas flow

rate. Inductively coupled plasma-mass spectrometry (ICP-MS) data was obtained with an Agilent 7700x ICP-MS and analyzed using ICP-MS MassHunter version B01.03. Samples were diluted in a 2% HNO₃ matrix and analyzed with a ¹⁵⁹Tb internal standard against a 12-point standard curve over the range from 0.1 ppb to 500 ppb. The correlation was >0.9997 for all analyses of interest. Data collection was performed in Spectrum Mode with five replicates per sample and 100 sweeps per replicate. EPR spectra were recorded on a Bruker Elexsys 500 X-band EPR spectrometer under irradiation of a white-light lamp (Fiber-Lite MI-150) by focusing the lamp on the sample cell in the ESR cavity at 15 K. Fluorescence measurement was performed using a Shimadzu RF-5301PC spectrofluorophotometer.

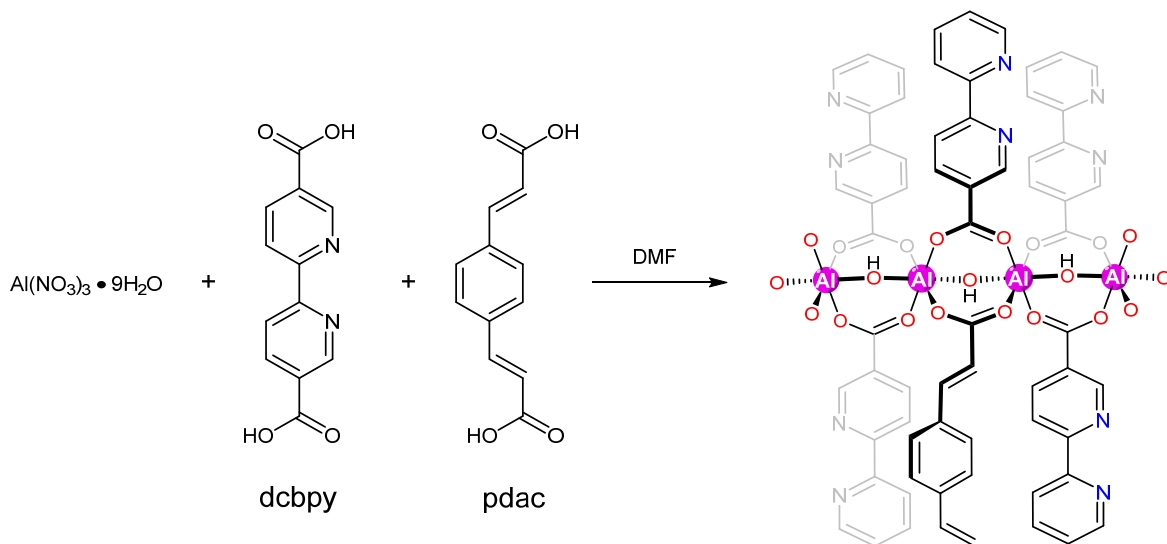
¹H NMR spectra were recorded on a Bruker NMR 500 DRX spectrometer at 500 MHz and referenced to the proton resonance resulting from incomplete deuteration of CDCl₃ (δ 7.26), DMSO-*d*₆ (δ 2.50), or C₆D₆ (δ 7.16). The following abbreviations are used herein: s: singlet, d: doublet, t: triplet, q: quartet, m: multiplet, br: broad, app: apparent. The conversions of reactions were determined by gas chromatography-mass spectrometry (GC-MS) using a Shimadzu GCMS-QP2010 Ultra equipped with SH-Rxi-5Sil MS 30 m \times 0.5 mm \times 0.25 μ m column.

3.4.2 Synthesis and Characterization of MOF 1

The synthetic procedure was based on literature reports for DUT-5 and MOF-253.²⁵⁻²⁶ In a typical synthesis, 2,2'-bipyridine-5,5'-dicarboxylic acid (dcbpy, 19.5 mg, 0.08 mmol) and 1,4-benzenediacrylic acid (pdac, 4.4 mg, 0.02 mmol) were dissolved in 3 mL DMF. Al(NO₃)₃·9H₂O (52 mg, 0.14 mmol) was added. The mixture was transferred to an 8-mL vial and heated at 120 °C for 12 h under stirring. After cooling to room temperature, the white solid was recovered by centrifugation and then sequentially washed with DMF three times, THF three times, and benzene

three times. This solid was then freeze-dried in benzene. After that, the white powder was further heated at 100 °C under vacuum to remove the trapped solvents in the pores (**Scheme 3-5**).

Scheme 3-5. Synthetic procedure for MOF 1. Reprinted with permission from *Journal of the American Chemical Society*, **2020**, 142, 4872-4882. Copyright 2020 American Chemical Society.



3.4.3 Synthesis and Characterization of 1-OH

We used ozonolysis to selectively cleave and remove the pdac ligand.²⁸ To ensure a continuous flow of ozone through the sample, we first mixed **1** (200 mg) with 2 g Ottawa sand (20-30 mesh) to improve O_3 permeability. We then pack the solid mixture into a thin glass column, which was later connected to the ozonator with a gas flow. The excess O_3 was quenched by KI aqueous solution. The reaction was run at room temperature for 15 min to ensure complete cleavage of pdac ligands. The resulted sample was washed with DMF/HCl (1M) (10:1, v:v) three times to remove the organic and inorganic fragments trapped in the pores of ozonized **1**, and washed with THF three times and benzene three times, followed by freeze-drying in benzene, and stored in a glovebox for further use.

3.4.4 Synthesis and Characterization of 1-OTf

In a N₂-filled glovebox, **1-OH** (0.10 mmol of -OH/OH₂) was weighed out in a 20 mL glass vial and dispersed in 10 mL of benzene. Trimethylsilyl trifluoromethanesulfonate (Me₃SiOTf, 0.18 mL, 1.0 mmol) was then added slowly to the suspension. The vessel was sealed with a Teflon cap and stir at room temperature for 12 h. The suspension was then washed with dry toluene 5 times. The resultant MOF was further extracted with hexane in a Soxhlet extractor to remove the trapped HOTf inside the MOF channels. 10 equiv. of LiCH₂SiMe₃ was added to the receiving flask to quench extracted HOTf during the Soxhlet extraction.³³ After solvent exchange with dry benzene, **1-OTf** was freeze-dried under vacuum overnight and stored inside a glovebox for further use.

3.4.5 Synthesis and Characterization of 1-OTf-PdCl₂

In a N₂-filled glovebox, **1-OTf** (0.2 mmol of bpy) was weighed out in a 20 mL glass vial. 10 mL of Pd(MeCN)₂Cl₂ solution in THF (20 mM) was then added. The mixture was stirred at room temperature for 12 h. The brown solid was then centrifuged and washed with THF three times and benzene three times. **1-OTf-PdCl₂** was then freeze-dried in benzene and stored in a glovebox for further use. ICP-MS analysis showed a Al/Pd molar ratio of 2.10, indicating ~60% of dcbpy ligands were metalated.

3.4.6 X-ray Absorption Study

X-ray absorption data of **1-OTf-PdCl₂** were collected at Beamline 10-BM at the Advanced Photon Source (APS) at Argonne National Laboratory. Spectra were collected at the palladium K-edge (24350 eV) in the transmission mode. The X-ray beam was monochromatized by a Si(111) monochromator and detuned by 15% to reduce the contribution of higher-order harmonics below the level of noise. A metallic palladium foil standard was used as a reference for energy calibration and was measured simultaneously with experimental samples. The incident beam intensity (I_0),

transmitted beam intensity (I_t), and reference (I_r) were measured by 20 cm ionization chambers with gas compositions of 38% N₂ and 62% Ar, 5% N₂ and 95% Ar, and 100% N₂, respectively. Data were collected over three regions: -200 to -50 eV (5 eV step size, dwell time of 1 s), -50 to 100 eV (1 eV step size, dwell time of 2 s), 100 to 850 eV (0.05 eV step size, dwell time of 6 s). Multiple X-ray absorption spectra were collected at room temperature for each sample. Samples were grounded and mixed with polyethylene glycol (PEG) and packed in a 6-shooter sample holder to achieve adequate absorption length.

Data was processed using the Athena and Artemis programs of the IFEFFIT package based on FEFF 6.⁵³⁻⁵⁴ Prior to merging, spectra were calibrated against the reference spectra and aligned to the first peak in the smoothed first derivative of the absorption spectrum, the background noise was removed, and the spectra were processed to obtain a normalized unit edge step.

Fitting of the EXAFS region was performed using the Artemis program of the IFEFFIT package. Fitting was performed in R space, with a k -weight of 3 for palladium samples. Refinement was performed by optimizing an amplitude factor S_0^2 and energy shift ΔE_0 which are common to all paths, in addition to parameters for bond length (ΔR) and Debye-Waller factor (σ^2). The fitting model for **1**-OTf-PdCl₂ was based on the single crystal structure JIPGAR obtained from CCDC.³⁸

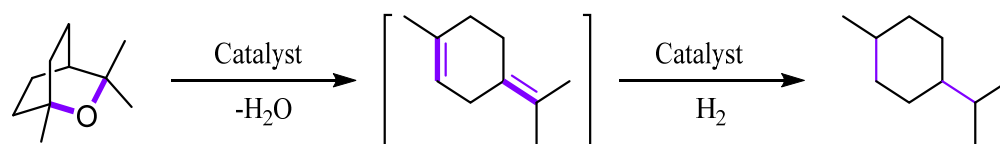
3.4.7 Quantification of Lewis Acidity by N-methylacridone Fluorescence

The fluorescent indicator *N*-methylacridone (NMA) was purchased from Sigma-Aldrich. The fluorescence measurement was performed using a Shimadzu RF-5301PC spectrofluorophotometer with an excitation wavelength of 413 nm. NMA was dissolved in MeCN to form an NMA solution with a concentration of 10 μ M to give a reference emission wavelength that was measured to be 433 nm (Figure S14, dashed line). For the measurement of MOF Lewis acidity, 0.1 mmol of **1**-OH or **1**-OTf [by the amount of Al₂(OH)(OH₂) or Al₂(OTf)] was added to

a 2-dram vial in an N₂-filled glovebox. 4 mL of NMA solution (10 μM in MeCN) was then added to the vial. The resulting mixture was sonicated for 2 min until the MOF was well suspended, and then the suspension was transferred to a fluorescence cuvette for measurement using an excitation wavelength of 413 nm. The emission maxima for NMA-bound **1-OH** and **1-OTf** were measured to be 463 nm and 470 nm, respectively, which correspond to ΔE values of 0.84 eV and 0.93 eV, respectively (Figure S14).³⁶⁻³⁷

3.4.8 A typical procedure for **1-OTf-PdCl₂** catalyzed tandem ether/alcohol C-O bond cleavage

Scheme 3-6. **1-OTf-PdCl₂** catalyzed 1,8 cineole C-O bond cleavage.



In a nitrogen-filled glovebox, **1-OTf-PdCl₂** (2.0 mg, 1.2 μmol Al₂(μ₂-OTf) sites), 1,8-cineole (100 μL, 0.6 mmol), and 1.0 mL of 1,2-dichloroethane were transferred to a Parr reactor to make an even suspension. The Parr reactor was then sealed under nitrogen, purged with hydrogen several times and charged with hydrogen to 20 bar. After stirring at 100 °C for 24 hours, the pressure was released, and the MOF catalyst was removed from the reaction mixture via centrifugation. The supernatant was analyzed by GC-MS to give menthane (a mixture of cis/trans isomers) in >99% yield with 100% conversion of 1,8-cineole. After one reaction run, ICP-MS analysis showed the leaching of 0.6% Al and 0.02% Pd into the solution.

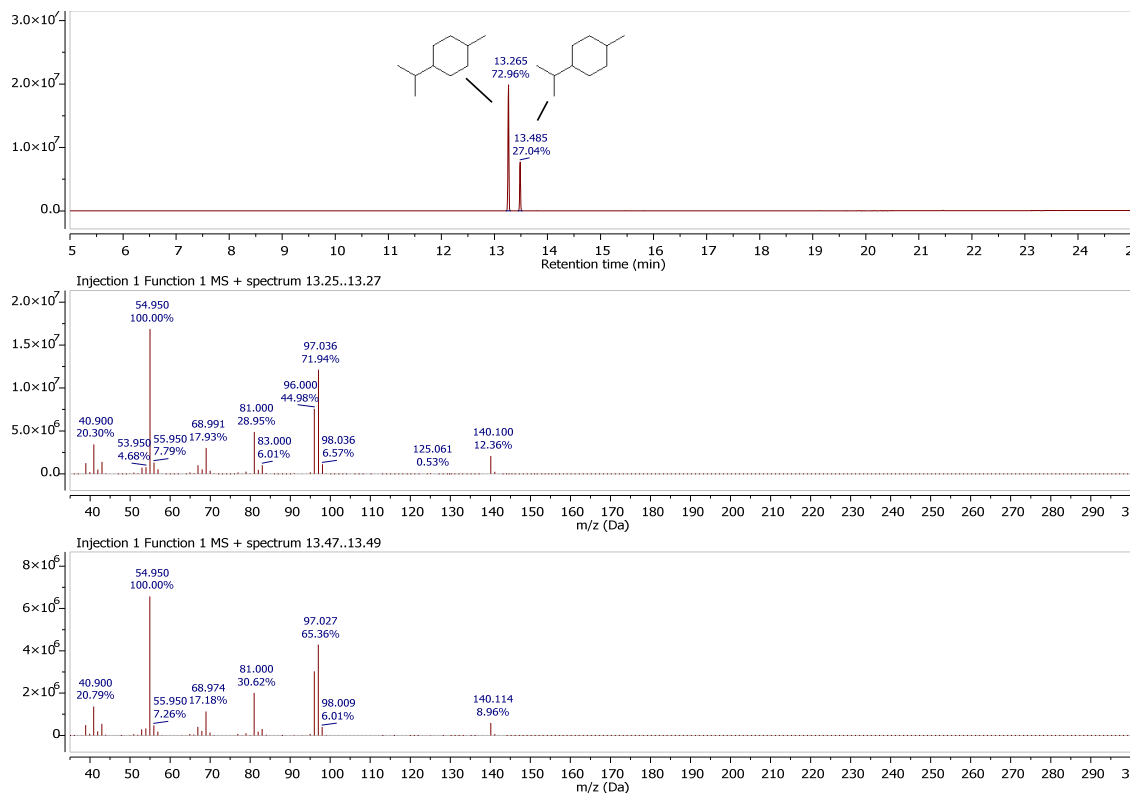
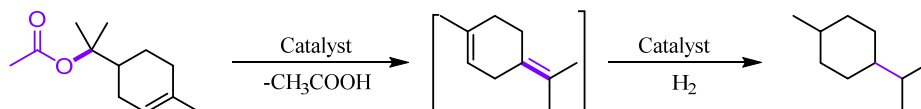


Figure 3-28. GC-MS spectrum of **1**-OTf-PdCl₂ catalyzed tandem ether/alcohol C-O bond cleavage of 1,8-cineole (The two MS spectra correspond to the cis/trans isomer of menthane). Reprinted with permission from *Journal of the American Chemical Society*, **2020**, 142, 4872-4882. Copyright 2020 American Chemical Society.

3.4.9 Condition optimization for **1**-OTf-PdCl₂ catalyzed tandem ester C-O bond cleavage

Scheme 3-7. **1**-OTf-PdCl₂ catalyzed terpinyl acetate C-O bond cleavage.



In a N₂-filled glovebox, **1**-OTf-PdCl₂ (5.0 mg, 3.0 μmol Al₂(μ₂-OTf) sites), terpinyl acetate (123 μL, 0.6 mmol), and 1.0 mL of 1,2-dichloroethane was transferred to a Parr reactor to make an even suspension. The Parr reactor was then sealed under nitrogen, purged with hydrogen several times and charged with hydrogen to 20 bar. After stirring at 100 °C for 24 hours, the pressure was released, and the MOF catalyst was removed from the reaction mixture via centrifugation. The supernatant was analyzed by GC-MS to give menthane (a mixture of cis/trans isomers) in 88%

yield with 100% substrate conversion. After one reaction run, 0.6% of Al and 0.15% of Pd are detected in the solution by ICP-MS analysis.

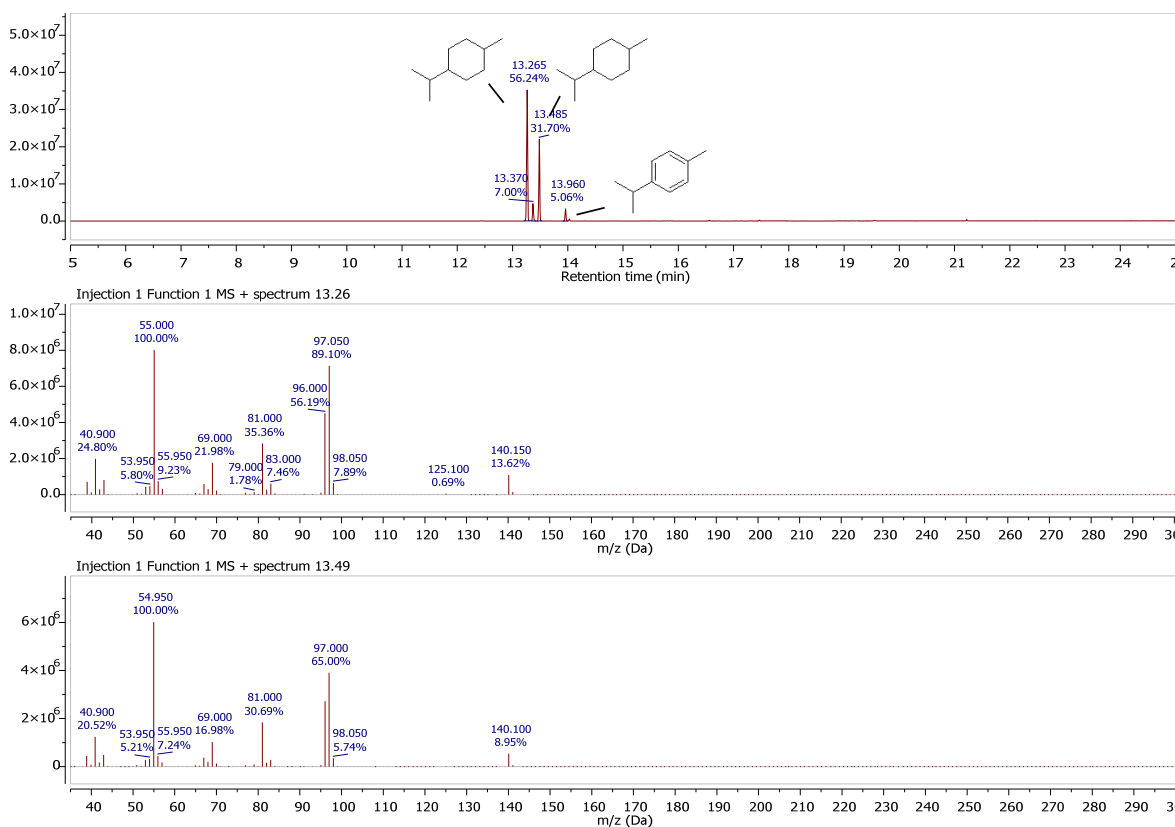


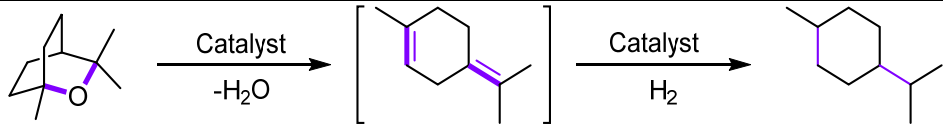
Figure 3-29. GC-MS spectra of 1-OTf-PdCl₂ catalyzed tandem ester C-O bond cleavage of terpinyl acetate (The two MS spectra correspond to the cis/trans isomers of menthane). Reprinted with permission from *Journal of the American Chemical Society*, 2020, 142, 4872-4882. Copyright 2020 American Chemical Society.

3.4.10 Condition optimization for 1-OTf-PdCl₂

Early trials of 1-OTf-PdCl₂ catalyzed tandem ether/alcohol C-O bond cleavage were conducted using 1,8-cineole as the substrate at 0.5 mol% of catalyst loading (w.r.t. Al₂(μ₂-OTf) sites), 20 bar of H₂ pressure, and 130 °C for 24 h. Several different kinds of solvents, including n-octane, n-hexane, 1,2-dichloroethane, 1,4-dichlorobutane, THF and neat conditions, were tested. 1,2-dichloroethane and 1,4-dichlorobutane outperformed other solvents, with quantitative substrate conversions and >99% yield of menthane by GC-MS. Further lowering the catalyst

loading to 0.2 mol% and reaction temperature to 100 °C in 1,2-dichloroethane still gave quantitative conversion (**Table 3-4**, Entry 4). The maximum TON at 100 °C was achieved at 0.1 mol% catalyst loading, with a TON of 800 (**Table 3-4**, Entry 5).

Table 3-4. Condition optimization for 1-OTf-PdCl₂ catalyzed tandem ether/alcohol C-O bond cleavage of 1,8-cineole

					
Entry	Cat. Loading / %	Solvent	p(H ₂) / bar	Temp./ °C	Yield / %
1	0.5	Octane	20	130	74
2	0.5	Hexane	20	130	61
3	0.5	1,2-dichloroethane	20	130	>99
4	0.5	1,4-dichlorobutane	20	130	>99
5	0.2	1,2-dichloroethane	20	100	>99
6	0.1	1,2-dichloroethane	20	100	80
7	0.5	THF	20	130	31
8	0.1	neat	20	130	40

Reaction conditions: 1-OTf-PdCl₂ (catalyst loading w.r.t. Al₂(μ₂-OTf)), 0.6 mmol 1,8-cineole, 20 bar H₂, 1 mL solvent or neat condition, 24 h; Yield was determined by GC-MS analysis.

3.4.11 Background reactions and control experiments

As shown in the substrate study, we have demonstrated this tandem strategy in catalyzing various C-O bonds, which includes etheric, alcoholic, and esteric C-O bonds. We attributed the excellent reactivity to the generation of truly orthogonal Lewis acidic and Pd nanoparticle sites in

one artificial engineered mesopores in facilitating this transformation. In order to better understand the reaction pathway, several additional experiments were carried out to compare the catalytic performance of homogeneous analogues and determine tandem reaction pathways of **1-OTf-PdCl₂** catalyzed C-O bond cleavage.

Both HOTf acid and Al(OTf)₃ were tested together with Pd source [Pd(MeCN)₂Cl₂] in tandem C-O bond cleavage of 1,8-cineole, with the same active site loadings as **1-OTf-PdCl₂**. Strong Brønsted acid (HOTf) produced 3% menthane along with significant amounts of unsaturated alkenes isomers (**Table 3-5**, Entry 2), while homogeneous metal triflates gave a slightly better menthane yield of 9% (**Table 3-5**, Entry 3). Additionally, a combination of Pd/C (10 %) and Al(OTf)₃ gave only slightly higher yield than [Pd(MeCN)₂Cl₂] plus Al(OTf)₃ (**Table 3-5**, Entry 4). These results indicated undesired deactivation of homogeneous species and possible interference between the homogeneous acids and Pd sources [Pd(MeCN)₂Cl₂].

While 0.2 mol% of **1-OTf-PdCl₂** catalyzed nearly quantitative conversion of 1,8-cineole to menthane, no target product was detected without adding the MOF catalyst (**Table 3-5**, entry 1) or using the same loading of **1-OTf** (MOF catalyst with only strong Lewis acidic Al₂(μ₂-OTf) sites but no Pd sites, **Table 3-5**, entry 4). However, unsaturated alkenes isomers were detected with the **1-OTf** catalyst, demonstrating the ability of Lewis acidic sites to catalyze the reverse reaction of the alkene hydroalkoxylation process. When combined with the hydrogenation catalyst (Pd NPs in the MOF), such C-O cleavage proceeded smoothly (**Table 3-5**, entry 7). Furthermore, when **1-OH-PdCl₂** catalyst (MOF catalyst with weak Lewis acidic Al₂(OH)(OH₂) sites and Pd sites, see below for detailed synthesis and characterization) was used (**Table 3-5**, entry 6), menthane was detected in a much lower yield (22%), indicating the significant contribution of Lewis acidity to C-O bond cleavage.

Table 3-5. Background and control experiments for **1-OTf-PdCl₂** catalyzed tandem ether/alcohol C-O bond cleavage of 1,8-cineole.^a

Entry	Cat. & Loading / %	Temp./ °C	Yield of menthane	Other Products
1 ^b	-	100	N.D.	
2 ^c	0.2 mol% of HOTf + 0.25 mol% PdCl ₂ (MeCN) ₂	100	3%	
3 ^d	0.2 mol% of Al(OTf) ₃ + 0.25 mol% PdCl ₂ (MeCN) ₂	100	9%	
4 ^e	0.2 mol% of Al(OTf) ₃ + 0.25 mol% Pd/C	100	20%	
5 ^f	0.2 mol% of 1-OTf	100	<1%	
6 ^g	0.2 mol% of 1-OH- PdCl ₂	100	22	
7	0.2 mol% of 1- OTf-Pd	100	>99%	N.D.

^aReaction conditions: 0.6 mmol 1,8-cineole, 20 bar H₂, 1 mL 1,2-dichloroethane, 100 °C, 24 h; Yields of different product and related isomers(iso) were determined by GC-MS analysis. ^bReaction was conduct w/o. catalyst. ^c0.2 mol% of Al(OTf)₃ + 0.25 mol% PdCl₂(MeCN)₂ was used as catalysts. ^dCatalysts: 0.2 mol% of HOTf + 0.25 mol% PdCl₂(MeCN)₂ was used as catalysts. ^e0.2 mol% of Al(OTf)₃ + 0.25 mol% Pd/C (10%) was used as catalysts. ^f**1-OTf** was used as catalyst, 0.2 mol% loading (w.r.t. Al₂(μ₂-OTf) sites). ^g**1-OH-PdCl₂** (synthesized by Pd metalation of **1-OH**, similar Pd loading with **1-OTf-PdCl₂**) was used as catalyst, 0.2 mol% loading (w.r.t. Al₂(OH)(OH₂) sites).

3.4.12 Synthesis and Characterization of 1-OTf-Pd^{NP}

In order to test the effects of Lewis acidity on C-O bond cleavage, **1-OH** (0.1 mmol of bpy) was weighed out in a 20 mL glass vial in a N₂-filled glovebox. 5 mL Pd(MeCN)₂Cl₂ solution in THF (20 mM) was then added. The mixture was stirred under room temperature for 12 h. The brown solid was then centrifuged and washed with THF three times and benzene three times. **1-OH-PdCl₂** was then freeze-dried in benzene and stored in a glovebox for further use. In situ hydrogenation further afforded **1-OH-Pd^{NP}**.

3.4.13 Recycle and reuse experiments in 1-OTf-PdCl₂ catalyzed tandem C-O bond cleavage

In a N₂-filled glovebox, **1-OTf-PdCl₂** (2.0 mg, 1.2 μmol Al₂(μ₂-OTf) sites), 1-methylcyclohexanol (75 μL, 0.6 mmol), and 1.0 mL of 1,2-dichloroethane was transferred into a Parr reactor to make an even suspension. The Parr reactor was then sealed under nitrogen, purged with hydrogen several times and charged with hydrogen to 20 bar. The reaction was stopped after stirring at 100 °C for 3 h to ensure an incomplete substrate conversion with a kinetic yield. The pressure was released, and the reaction slurry was then centrifuged to recover the MOF catalyst. The supernatant was analyzed by GC-MS to give menthane (a mixture of cis/trans isomers) in 84% yield.

The recovered MOF was washed with 1,2-dichloroethane 3 times before being used for another catalytic round. A new solution of 1-methylcyclohexanol (75 μL, 0.6 mmol) in 1,2-dichloroethane (1.0 mL) was then added. The reaction mixture was stirred at 100 °C for another 3 h, and then worked up and recycled using the same procedure. The catalyst was recycled and reused for at least 5 times without a significant drop of catalytic activity.

3.5 References

- (1) Zakzeski, J.; Bruijninx, P. C. A.; Jongerius, A. L.; Weckhuysen, B. M., The Catalytic Valorization of Lignin for the Production of Renewable Chemicals. *Chemical Reviews* **2010**, *110* (6), 3552-3599.
- (2) Ragauskas, A. J.; Beckham, G. T.; Biddy, M. J.; Chandra, R.; Chen, F.; Davis, M. F.; Davison, B. H.; Dixon, R. A.; Gilna, P.; Keller, M.; Langan, P.; Naskar, A. K.; Saddler, J. N.; Tschaplinski, T. J.; Tuskan, G. A.; Wyman, C. E., Lignin Valorization: Improving Lignin Processing in the Biorefinery. *Science* **2014**, *344* (6185), 1246843.
- (3) Tuck, C. O.; Pérez, E.; Horváth, I. T.; Sheldon, R. A.; Poliakoff, M., Valorization of Biomass: Deriving More Value from Waste. *Science* **2012**, *337* (6095), 695.
- (4) Sheldon, R. A., Utilisation of biomass for sustainable fuels and chemicals: Molecules, methods and metrics. *Catalysis Today* **2011**, *167* (1), 3-13.
- (5) Ragauskas, A. J.; Williams, C. K.; Davison, B. H.; Britovsek, G.; Cairney, J.; Eckert, C. A.; Frederick, W. J.; Hallett, J. P.; Leak, D. J.; Liotta, C. L.; Mielenz, J. R.; Murphy, R.; Templer, R.; Tschaplinski, T., The Path Forward for Biofuels and Biomaterials. *Science* **2006**, *311* (5760), 484.
- (6) Xie, H.; Gathergood, N., *The role of green chemistry in biomass processing and conversion*. Wiley Online Library: 2013.
- (7) Song, Y.; Li, Z.; Ji, P.; Kaufmann, M.; Feng, X.; Chen, J. S.; Wang, C.; Lin, W., Metal–Organic Framework Nodes Support Single-Site Nickel(II) Hydride Catalysts for the Hydrogenolysis of Aryl Ethers. *ACS Catalysis* **2019**, *9* (2), 1578-1583.
- (8) Yang, M.; Qi, H.; Liu, F.; Ren, Y.; Pan, X.; Zhang, L.; Liu, X.; Wang, H.; Pang, J.; Zheng, M.; Wang, A.; Zhang, T., One-Pot Production of Cellulosic Ethanol via Tandem Catalysis over a Multifunctional Mo/Pt/WO_x Catalyst. *Joule* **2019**, *3* (8), 1937-1948.
- (9) Huang, H.; Denard, C. A.; Alamillo, R.; Crisci, A. J.; Miao, Y.; Dumesic, J. A.; Scott, S. L.; Zhao, H., Tandem Catalytic Conversion of Glucose to 5-Hydroxymethylfurfural with an Immobilized Enzyme and a Solid Acid. *ACS Catalysis* **2014**, *4* (7), 2165-2168.
- (10) Lohr, T. L.; Li, Z.; Marks, T. J., Thermodynamic Strategies for C–O Bond Formation and Cleavage via Tandem Catalysis. *Accounts of Chemical Research* **2016**, *49* (5), 824-834.
- (11) Atesin, A. C.; Ray, N. A.; Stair, P. C.; Marks, T. J., Etheric C–O Bond Hydrogenolysis Using a Tandem Lanthanide Triflate/Supported Palladium Nanoparticle Catalyst System. *Journal of the American Chemical Society* **2012**, *134* (36), 14682-14685.
- (12) Assary, R. S.; Atesin, A. C.; Li, Z.; Curtiss, L. A.; Marks, T. J., Reaction Pathways and Energetics of Etheric C–O Bond Cleavage Catalyzed by Lanthanide Triflates. *ACS Catalysis* **2013**, *3* (9), 1908-1914.

- (13) Cui, M.; Qian, Q.; He, Z.; Zhang, Z.; Ma, J.; Wu, T.; Yang, G.; Han, B., Bromide promoted hydrogenation of CO₂ to higher alcohols using Ru–Co homogeneous catalyst. *Chemical Science* **2016**, 7 (8), 5200-5205.
- (14) Li, R.; Zhou, Y.; Xu, X.; Dong, G., Direct Vicinal Difunctionalization of Thiophenes Enabled by the Palladium/Norbornene Cooperative Catalysis. *Journal of the American Chemical Society* **2019**, 141 (48), 18958-18963.
- (15) Dan-Hardi, M.; Serre, C.; Frot, T.; Rozes, L.; Maurin, G.; Sanchez, C.; Férey, G., A new photoactive crystalline highly porous titanium (IV) dicarboxylate. *Journal of the American Chemical Society* **2009**, 131 (31), 10857-10859.
- (16) Yoon, M.; Srirambalaji, R.; Kim, K., Homochiral Metal–Organic Frameworks for Asymmetric Heterogeneous Catalysis. *Chemical Reviews* **2012**, 112 (2), 1196-1231.
- (17) Huang, Y.-B.; Liang, J.; Wang, X.-S.; Cao, R., Multifunctional metal–organic framework catalysts: synergistic catalysis and tandem reactions. *Chemical Society Reviews* **2017**, 46 (1), 126-157.
- (18) Feng, L.; Wang, Y.; Yuan, S.; Wang, K.-Y.; Li, J.-L.; Day, G. S.; Qiu, D.; Cheng, L.; Chen, W.-M.; Madrahimov, S. T.; Zhou, H.-C., Porphyrinic Metal–Organic Frameworks Installed with Brønsted Acid Sites for Efficient Tandem Semisynthesis of Artemisinin. *ACS Catalysis* **2019**, 9 (6), 5111-5118.
- (19) Zhao, M.; Ou, S.; Wu, C.-D., Porous Metal–Organic Frameworks for Heterogeneous Biomimetic Catalysis. *Accounts of Chemical Research* **2014**, 47 (4), 1199-1207.
- (20) Shen, L.; Luo, M.; Huang, L.; Feng, P.; Wu, L., A Clean and General Strategy To Decorate a Titanium Metal–Organic Framework with Noble-Metal Nanoparticles for Versatile Photocatalytic Applications. *Inorganic Chemistry* **2015**, 54 (4), 1191-1193.
- (21) Huang, Y.; Zhang, Y.; Chen, X.; Wu, D.; Yi, Z.; Cao, R., Bimetallic alloy nanocrystals encapsulated in ZIF-8 for synergistic catalysis of ethylene oxidative degradation. *Chemical Communications* **2014**, 50 (70), 10115-10117.
- (22) Comito, R. J.; Fritzsche, K. J.; Sundell, B. J.; Schmidt-Rohr, K.; Dincă, M., Single-Site Heterogeneous Catalysts for Olefin Polymerization Enabled by Cation Exchange in a Metal–Organic Framework. *Journal of the American Chemical Society* **2016**, 138 (32), 10232-10237.
- (23) Ikuno, T.; Zheng, J.; Vjunov, A.; Sanchez-Sanchez, M.; Ortuño, M. A.; Pahls, D. R.; Fulton, J. L.; Camaioni, D. M.; Li, Z.; Ray, D.; Mehdi, B. L.; Browning, N. D.; Farha, O. K.; Hupp, J. T.; Cramer, C. J.; Gagliardi, L.; Lercher, J. A., Methane Oxidation to Methanol Catalyzed by Cu-Oxo Clusters Stabilized in NU-1000 Metal–Organic Framework. *Journal of the American Chemical Society* **2017**, 139 (30), 10294-10301.
- (24) Feng, L.; Yuan, S.; Zhang, L.-L.; Tan, K.; Li, J.-L.; Kirchon, A.; Liu, L.-M.; Zhang, P.; Han, Y.; Chabal, Y. J.; Zhou, H.-C., Creating Hierarchical Pores by Controlled Linker Thermolysis in

Multivariate Metal–Organic Frameworks. *Journal of the American Chemical Society* **2018**, *140* (6), 2363-2372.

(25) Senkovska, I.; Hoffmann, F.; Fröba, M.; Getzschmann, J.; Böhlmann, W.; Kaskel, S., New highly porous aluminium based metal-organic frameworks: Al(OH)(ndc) (ndc=2,6-naphthalene dicarboxylate) and Al(OH)(bpdc) (bpdc=4,4' -biphenyl dicarboxylate). *Microporous and Mesoporous Materials* **2009**, *122* (1), 93-98.

(26) Bloch, E. D.; Britt, D.; Lee, C.; Doonan, C. J.; Uribe-Romo, F. J.; Furukawa, H.; Long, J. R.; Yaghi, O. M., Metal Insertion in a Microporous Metal–Organic Framework Lined with 2,2'-Bipyridine. *Journal of the American Chemical Society* **2010**, *132* (41), 14382-14384.

(27) Tu, B.; Pang, Q.; Wu, D.; Song, Y.; Weng, L.; Li, Q., Ordered Vacancies and Their Chemistry in Metal–Organic Frameworks. *Journal of the American Chemical Society* **2014**, *136* (41), 14465-14471.

(28) Guillerm, V.; Xu, H.; Albalad, J.; Imaz, I.; MasPOCH, D., Postsynthetic Selective Ligand Cleavage by Solid–Gas Phase Ozonolysis Fuses Micropores into Mesopores in Metal–Organic Frameworks. *Journal of the American Chemical Society* **2018**, *140* (44), 15022-15030.

(29) Yang, D.; Ortuño, M. A.; Bernales, V.; Cramer, C. J.; Gagliardi, L.; Gates, B. C., Structure and Dynamics of Zr6O8 Metal–Organic Framework Node Surfaces Probed with Ethanol Dehydration as a Catalytic Test Reaction. *Journal of the American Chemical Society* **2018**, *140* (10), 3751-3759.

(30) Vermoortele, F.; Vandichel, M.; Van de Voorde, B.; Ameloot, R.; Waroquier, M.; Van Speybroeck, V.; De Vos, D. E., Electronic Effects of Linker Substitution on Lewis Acid Catalysis with Metal–Organic Frameworks. *Angewandte Chemie International Edition* **2012**, *51* (20), 4887-4890.

(31) Mondloch, J. E.; Katz, M. J.; Isley III, W. C.; Ghosh, P.; Liao, P.; Bury, W.; Wagner, G. W.; Hall, M. G.; DeCoste, J. B.; Peterson, G. W.; Snurr, R. Q.; Cramer, C. J.; Hupp, J. T.; Farha, O. K., Destruction of chemical warfare agents using metal–organic frameworks. *Nature Materials* **2015**, *14* (5), 512-516.

(32) Horike, S.; Dincă, M.; Tamaki, K.; Long, J. R., Size-Selective Lewis Acid Catalysis in a Microporous Metal-Organic Framework with Exposed Mn²⁺ Coordination Sites. *Journal of the American Chemical Society* **2008**, *130* (18), 5854-5855.

(33) Ji, P.; Feng, X.; Oliveres, P.; Li, Z.; Murakami, A.; Wang, C.; Lin, W., Strongly Lewis Acidic Metal–Organic Frameworks for Continuous Flow Catalysis. *Journal of the American Chemical Society* **2019**, *141* (37), 14878-14888.

(34) Copéret, C., Surface and Interfacial Chemistry. *CHIMIA International Journal for Chemistry* **2012**, *66* (3), 125-129.

- (35) Feng, X.; Ji, P.; Li, Z.; Drake, T.; Oliveres, P.; Chen, E. Y.; Song, Y.; Wang, C.; Lin, W., Aluminum Hydroxide Secondary Building Units in a Metal–Organic Framework Support Earth-Abundant Metal Catalysts for Broad-Scope Organic Transformations. *ACS Catalysis* **2019**, *9* (4), 3327-3337.
- (36) Ohkubo, K.; Menon, S. C.; Orita, A.; Otera, J.; Fukuzumi, S., Quantitative Evaluation of Lewis Acidity of Metal Ions with Different Ligands and Counterions in Relation to the Promoting Effects of Lewis Acids on Electron Transfer Reduction of Oxygen. *The Journal of Organic Chemistry* **2003**, *68* (12), 4720-4726.
- (37) Ji, P.; Drake, T.; Murakami, A.; Oliveres, P.; Skone, J. H.; Lin, W., Tuning Lewis Acidity of Metal–Organic Frameworks via Perfluorination of Bridging Ligands: Spectroscopic, Theoretical, and Catalytic Studies. *Journal of the American Chemical Society* **2018**, *140* (33), 10553-10561.
- (38) Jack, L.; Yellowlees, L. J.; Parsons, S., CCDC 660772: Experimental Crystal Structure Determination. Cambridge Crystallographic Data Centre: 2008.
- (39) Dai, G.-L.; Lai, S.-Z.; Luo, Z.; Tang, Z.-Y., Selective Syntheses of Z-Alkenes via Photocatalyzed Decarboxylative Coupling of N-Hydroxyphthalimide Esters with Terminal Arylalkynes. *Organic Letters* **2019**, *21* (7), 2269-2272.
- (40) Gallezot, P., Conversion of biomass to selected chemical products. *Chemical Society Reviews* **2012**, *41* (4), 1538-1558.
- (41) Serrano-Ruiz, J. C.; Dumesic, J. A., Catalytic routes for the conversion of biomass into liquid hydrocarbon transportation fuels. *Energy & Environmental Science* **2011**, *4* (1), 83-99.
- (42) García, V.; Pääkilä, J.; Ojamo, H.; Muurinen, E.; Keiski, R. L., Challenges in biobutanol production: How to improve the efficiency? *Renewable and Sustainable Energy Reviews* **2011**, *15* (2), 964-980.
- (43) Yu, X.; Seo, S.; Marks, T. J., Effective, Selective Hydroalkoxylation/Cyclization of Alkynyl and Allenyl Alcohols Mediated by Lanthanide Catalysts. *Journal of the American Chemical Society* **2007**, *129* (23), 7244-7245.
- (44) Lohr, T. L.; Marks, T. J., Orthogonal tandem catalysis. *Nature Chemistry* **2015**, *7* (6), 477-482.
- (45) Zhao, C.; Kou, Y.; Lemonidou, A. A.; Li, X.; Lercher, J. A., Highly Selective Catalytic Conversion of Phenolic Bio-Oil to Alkanes. *Angewandte Chemie International Edition* **2009**, *48* (22), 3987-3990.
- (46) Yan, N.; Yuan, Y.; Dykeman, R.; Kou, Y.; Dyson, P. J., Hydrodeoxygenation of Lignin-Derived Phenols into Alkanes by Using Nanoparticle Catalysts Combined with Brønsted Acidic Ionic Liquids. *Angewandte Chemie International Edition* **2010**, *49* (32), 5549-5553.
- (47) Olson, E. S.; Aulich, T. R.; Sharma, R. K.; Timpe, R. C., Ester fuels and chemicals from biomass. *Applied Biochemistry and Biotechnology* **2003**, *108* (1), 843-851.

- (48) Borugadda, V. B.; Goud, V. V., Biodiesel production from renewable feedstocks: Status and opportunities. *Renewable and Sustainable Energy Reviews* **2012**, *16* (7), 4763-4784.
- (49) Zhao, C.; Brück, T.; Lercher, J. A., Catalytic deoxygenation of microalgae oil to green hydrocarbons. *Green Chemistry* **2013**, *15* (7), 1720-1739.
- (50) Lestari, S.; Mäki-Arvela, P.; Beltramini, J.; Lu, G. Q. M.; Murzin, D. Y., Transforming Triglycerides and Fatty Acids into Biofuels. *ChemSusChem* **2009**, *2* (12), 1109-1119.
- (51) Lohr, T. L.; Li, Z.; Assary, R. S.; Curtiss, L. A.; Marks, T. J., Mono- and tri-ester hydrogenolysis using tandem catalysis. Scope and mechanism. *Energy & Environmental Science* **2016**, *9* (2), 550-564.
- (52) Lohr, T. L.; Li, Z.; Marks, T. J., Selective Ether/Ester C–O Cleavage of an Acetylated Lignin Model via Tandem Catalysis. *ACS Catalysis* **2015**, *5* (11), 7004-7007.
- (53) Rehr, J. J.; Albers, R. C., Theoretical approaches to x-ray absorption fine structure. *Rev. Mod. Phys* **2000**, *72* (3), 621.
- (54) Ravel, B.; Newville, M., ATHENA, ARTEMIS, HEPHAESTUS: data analysis for X-ray absorption spectroscopy using IFEFFIT. *J. Synchrotron Radiat* **2005**, *12* (4), 537-541.

Chapter 4. Metal-Organic Framework with Dual Active Sites in Engineered Mesopores for Bioinspired Synergistic Catalysis

4.1 Introduction

Functionalization of azaarene derivatives is of great significance due to their prevalence in bioactive and drug molecules ranging from antihistamine drugs to anticancer drugs,¹⁻⁴ Transition metal catalysts are typically ineffective for the modification of azaarene derivatives owing to strong coordination of azaarenes to metal centers.⁵⁻⁶ Photoredox catalysis presents an alternative solution to functionalizing azaarene derivatives by generating active open-shell species via single electron transfer.⁷ For example, the addition of photoredox-generated radicals to vinylpyridines has provided access to new functionalized pyridines.⁸⁻⁹ Despite the potential of azaarene derivatives as “privileged” scaffolds in drug discovery,² photocatalytic transformations of azaarenes have not been widely studied.

As a versatile family of porous molecular materials, metal-organic frameworks (MOFs) have been explored for many applications,¹⁰⁻¹¹ including gas storage and separation,¹² drug delivery,¹³⁻¹⁴ sensing,¹⁵ solar energy conversion,¹⁶ and heterogeneous catalysis.¹⁷ Although MOFs have been extensively explored as single-site solid catalysts,¹⁸⁻¹⁹ few multi-functional MOFs with two or more catalytic centers have been rationally designed.²⁰⁻²¹ The ability to hierarchically install multiple active sites in a MOF structure provides a unique opportunity to engineer enzyme-inspired cooperative catalysts that cannot be obtained in homogeneous solutions or on traditional heterogeneous supports.²²⁻²³

Enzymes use active sites in three-dimensional grooves or pockets to catalyze chemical transformations.²⁴⁻²⁶ The active sites typically comprise multiple functional units that are broadly categorized as binding centers and catalytic centers.²⁷⁻²⁸ Binding centers anchor substrates or

intermediates to facilitate their conversion to products by catalytic centers. Synergistic cooperation between these functional units is responsible for the extremely high activity and selectivity of enzymes.

In Chapter 3, we discussed the design and synthesis of **1-OTf-PdCl₂** through hierarchical installation of orthogonal strong Lewis acid and bpy-PdCl₂ catalysts for highly efficient cleavage of etheric, alcoholic, and esteric C-O bonds in a tandem pathway. Chapter 3 demonstrated the potential of sequential engineering of multiple catalytic sites in MOF **1** to address outstanding challenges in sustainable catalysis. In this chapter, we further take advantage of the framework of MOF **1** to hierarchically assemble synergistic strong Lewis acidic sites as binding centers and Ir-based photosensitizers as catalytic centers in mesopores for bioinspired synergistic catalysis (**Figure 4-1**). Ozonolysis of Al-MOF (**1**) with mixed 2,2'-bipyridyl-5,5-dicarboxylate (dcbpy) and 1,4-benzenediacrylate (pdac) ligands followed by triflation generated Lewis acidic Al-OTf sites in the mesopores. Subsequent installation of [Ir(ppy)₂(dcbpy)]Cl (**L₁**, ppy = 2-phenylpyridine) sites afforded **1-OTf-Ir** with both Lewis acidic sites and photoredox sites. **1-OTf-Ir** effectively catalyzed reductive cross-coupling of N-hydroxyphthalimide esters or aryl bromomethyl ketones with vinyl- or alkynyl-azaarenes to afford new azaarene derivatives. **1-OTf-Ir** also provided alternative routes to anticholinergic drugs Pheniramine and Chlorpheniramine.

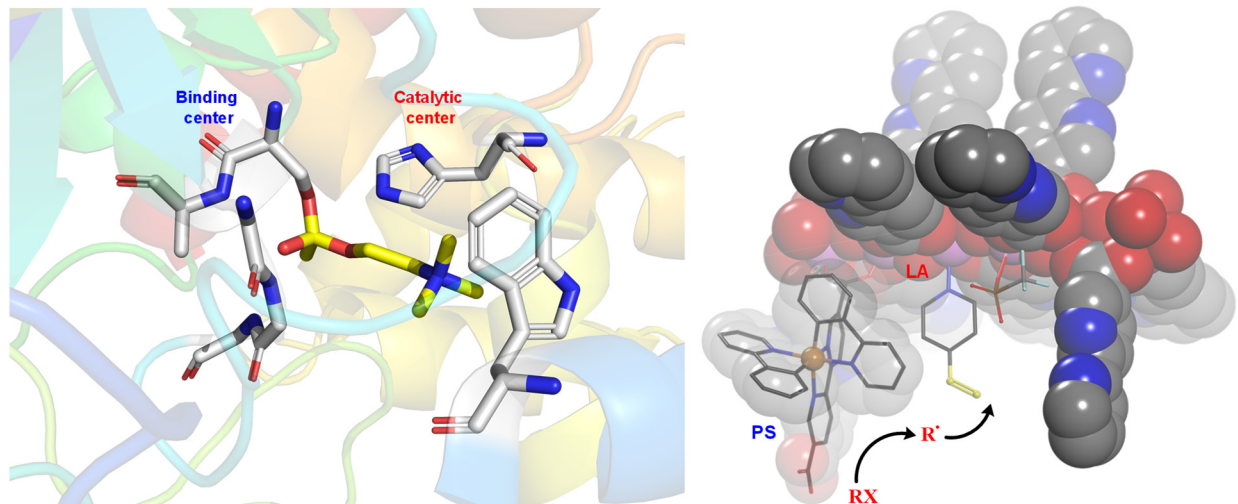


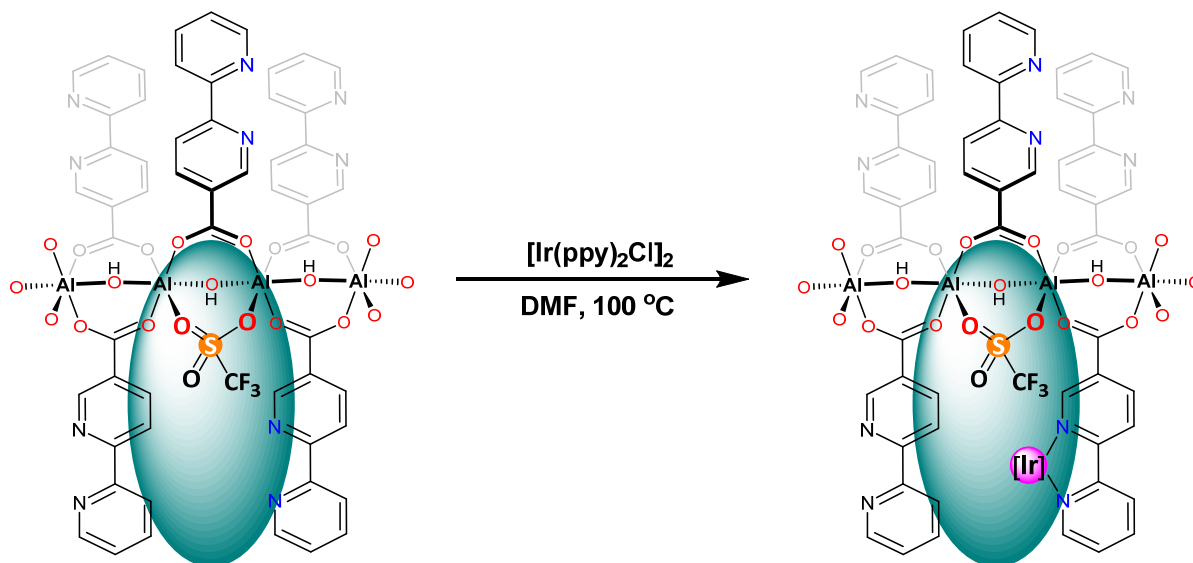
Figure 4-1. Comparison between an enzyme active site with binding center and catalytic center (left) and an engineered mesopore in **1-OTf-Ir** with Lewis acid as binding center and Ir-photosensitizer as catalytic center (right). Reprinted with permission from *Journal of the American Chemical Society*, **2020**, 142, 8602-8607. Copyright 2020 American Chemical Society.

4.2 Results and Discussion

4.2.1 Synthesis and Characterization of **1-OTf-Ir**

1-OTf was synthesized and characterized according to Chapter 3.²⁹⁻³¹ In a N₂-filled glovebox, **1-OTf** (0.1 mmol of bpy) was weighed out in a 75 mL high pressure glass vessel. 20 mL of [Ir(ppy)₂Cl]₂³⁵ solution in DMF (10 mM) was then added. The mixture was stirred at 100 °C for 3 days (**Scheme 4-1**). The bright-orange solid was then centrifuged and washed with DMF three times, THF three times, and benzene three times. The resultant solid was freeze-dried and stored in a glovebox for further use. ICP-MS analysis showed an Al/Ir molar ratio of ~10:1, indicating ~13% of dcbpy ligands were metalated.

Scheme 4-1. Synthetic route to **1-OTf-Ir**. Reprinted with permission from *Journal of the American Chemical Society*, **2020**, 142, 8602-8607. Copyright 2020 American Chemical Society.



Treatment of **1-OTf** with $[\text{Ir}(\text{ppy})_2\text{Cl}]_2$ afforded **1-OTf-Ir** with Ir-photosensitizer (Ir-PS) loadings of 10.4 mol% as determined by ^1H NMR spectra of digested **1-OTf-Ir** (**Figure 4-2**). The highest Ir-PS loading of 17.3 mol% is slightly lower than the density (20.0 mol%) of mesopores (**Figure 4-3**), supporting the installation of Ir-PSs inside the mesopores.

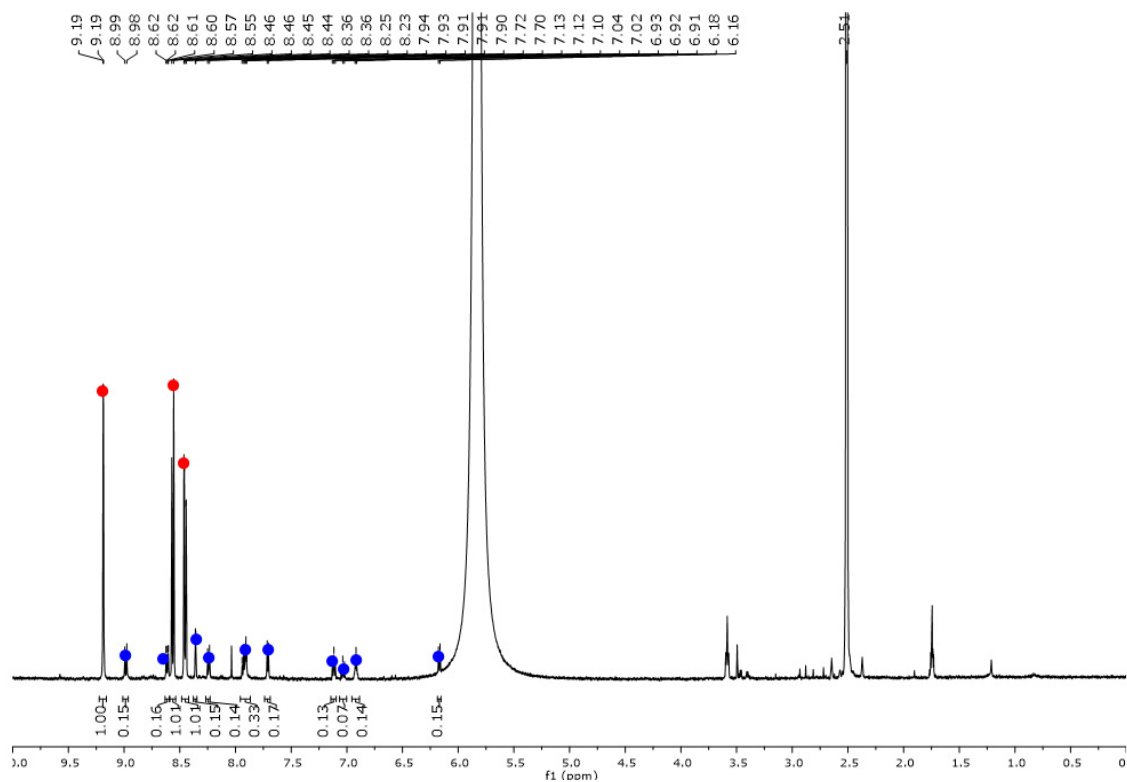


Figure 4-2. ^1H NMR spectrum of digested **1-OTf-Ir** in $\text{DMSO-}d_6$. Red circles correspond to dbcyl ligands, while blue circles correspond to L_1 ligands. Reprinted with permission from *Journal of the American Chemical Society*, **2020**, 142, 8602-8607. Copyright 2020 American Chemical Society.

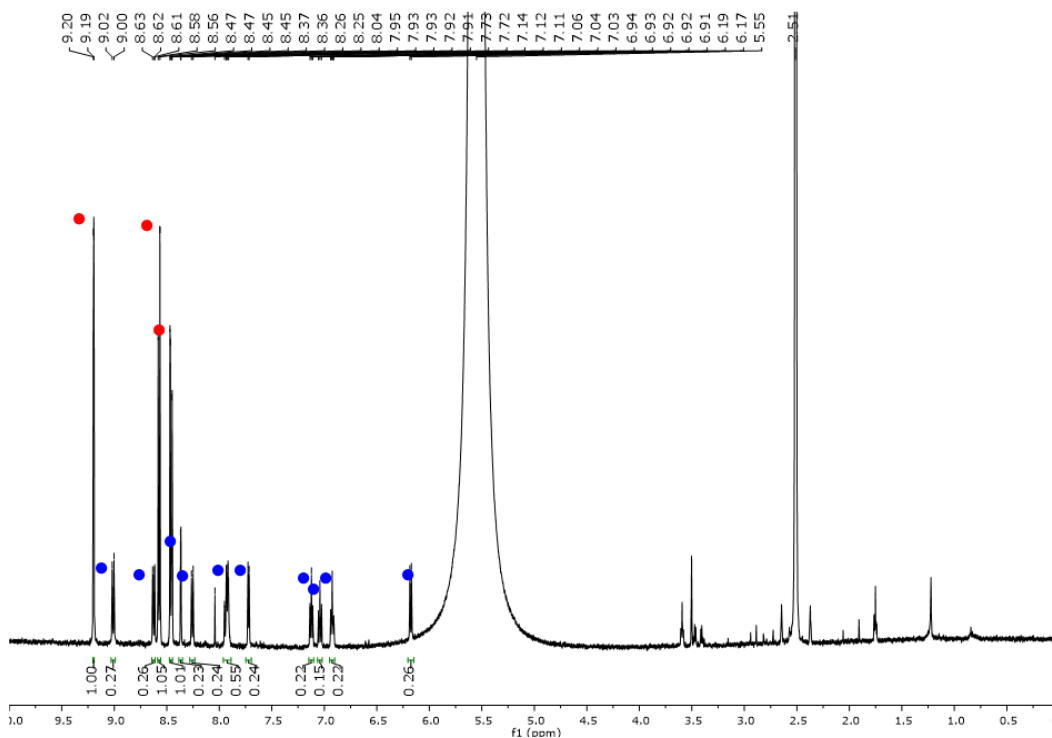


Figure 4-3. ^1H NMR spectrum of digested **1-OTf-Ir-high** in $\text{DMSO-}d_6$. Red circles correspond to dcbpy ligands, while blue circles correspond to L_1 ligands. Reprinted with permission from *Journal of the American Chemical Society*, **2020**, 142, 8602-8607. Copyright 2020 American Chemical Society.

We further examined the crystallinity of the as-synthesized **1-OTf-Ir**. PXRD studies showed that **1-OTf-Ir** retained the crystallinity of **1** by their similarity of PXRD patterns (**Figure 4-4**). UV-Vis and luminescence spectra (**Figure 4-5**) of **1-OTf-Ir** exhibited characteristic absorption, excitation, and emission properties of $\text{Ir}(\text{Me}_2\text{dcbpy})(\text{ppy})_2\text{Cl}$ (Me_2L_1), which supports the successful introduction of Ir-based photosensitizers into **1-OTf**.

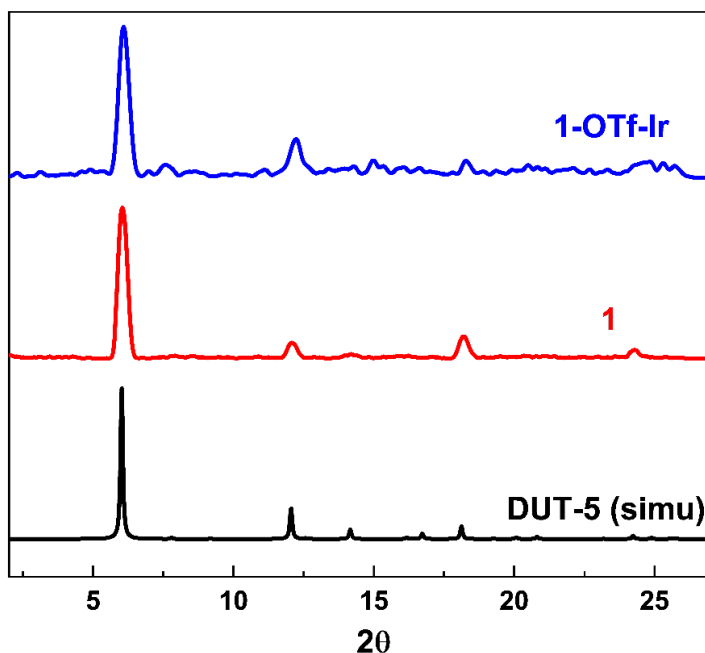


Figure 4-4. PXRD patterns of **1** (red), and **1-OTf-Ir** (blue) in comparison to the simulated pattern for DUT-5. Reprinted with permission from *Journal of the American Chemical Society*, **2020**, 142, 8602-8607. Copyright 2020 American Chemical Society.

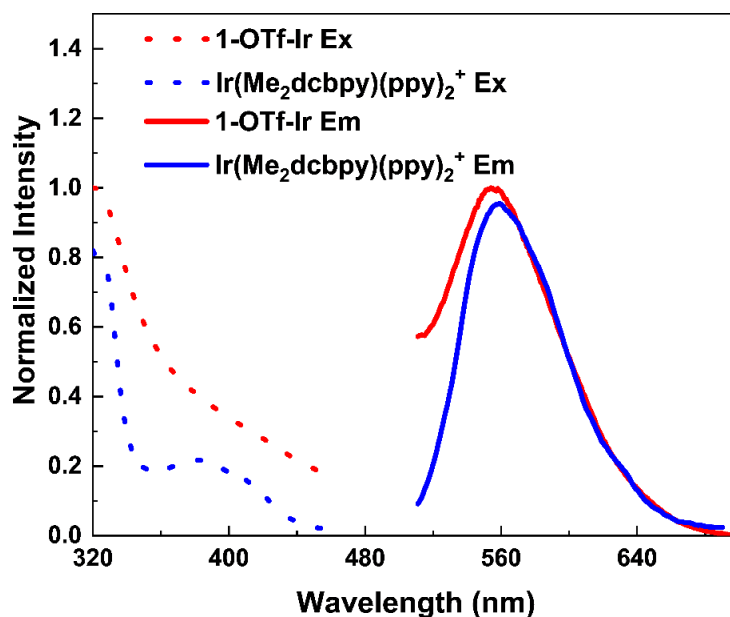


Figure 4-5. Normalized UV-vis spectra and emission spectra (with 368 nm excitation) of **1-OTf-Ir** in comparison to Me_2L_1 ligands in DMF with a concentration of 20 μM based on Ir. Reprinted with permission from *Journal of the American Chemical Society*, **2020**, 142, 8602-8607. Copyright 2020 American Chemical Society.

The extended X-ray absorption fine structure (EXAFS) feature of Ir centers in **1-OTf-Ir** was well fit to the $\text{Ir}(\text{bpy})(\text{ppy})_2^+$ structure to afford nearly identical coordination geometry (**Figure 4-6**).

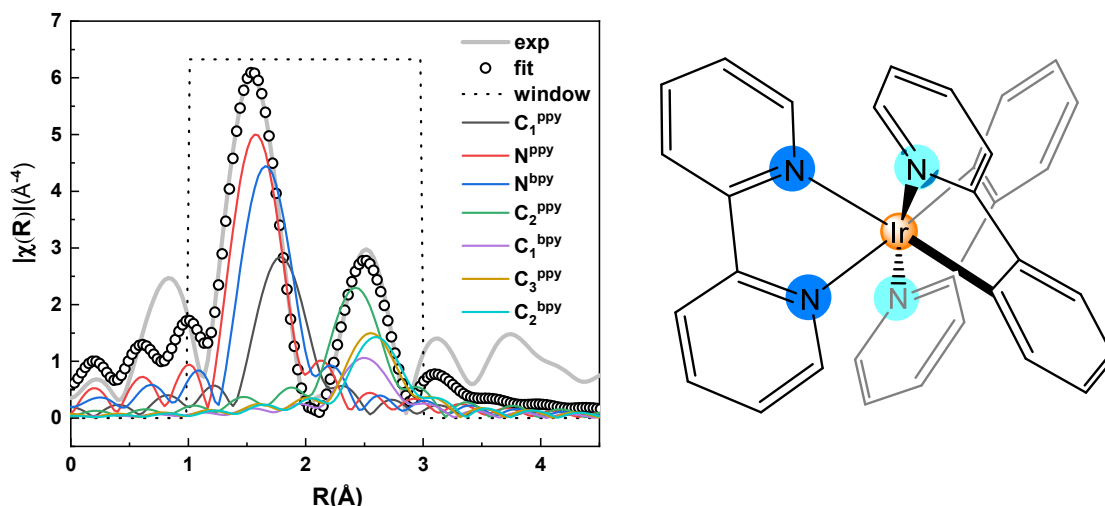


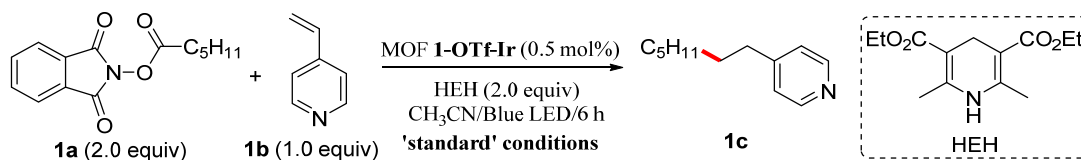
Figure 4-6. EXAFS spectrum (gray solid line) and fit (black circles) in R-space at the Ir L_3 -edge adsorption of **1-OTf-Ir**, with the fragment structure of $\text{Ir}(\text{bpy})_3$ for EXAFS fitting of the Ir coordination environment in **1-OTf-Ir**. H atoms were omitted for clarity. Reprinted with permission from *Journal of the American Chemical Society*, **2020**, 142, 8602-8607. Copyright 2020 American Chemical Society.

4.2.2 **1-OTf-Ir** Catalyzed Reductive Cross-Coupling Reactions

We proposed the confinement of the in-situ generated active species in nano pockets³⁶ could accelerate the cross-coupling reactions while suppress side reactions. We tested this bioinspired photocatalytic strategy on reductive cross-coupling of *N*-hydroxyphthalimide (NHP) esters with vinyl- or alkynyl-azaarenes. At 0.5 mol% **1-OTf-Ir** loading (based on Lewis acid sites), pentanyl *N*-hydroxyphthalimide ester (**1a**) and 4-vinylpyridine (**2a**) coupled in the presence of Hantzsch ester (HEH) reductant in CH_3CN under blue LED irradiation (400-500 nm) at room temperature to afford **1c** in 90% yield in 6 h (standard condition, **Table 4-1**, entry 1). At the same Lewis acid loading, **1-OTf-Ir** with low (4.5 mol%) and high (17.3 mol%) Ir-PS loadings produced **1c** in lower yields (**Table 4-1**, entries 2 and 3). Reactions in 1,2-dichloroethane (DCE), toluene,

and dimethoxyethane (DME) afforded **1c** in lower yields (**Table 4-1**, entries 4-6). Reducing the amount of **1a** to 1.5 equiv gave **1c** in 77% yield (**Table 4-1**, entry 7). Without light or **1-OTf-Ir**, no product was observed (**Table 4-1**, entries 8 and 9). The use of Me_2L_1 and $\text{Al}(\text{OTf})_3$ as the homogeneous control generated **1c** in 16% yield (**Scheme 4-8**, experimental part).

Table 4-1. Optimization of reaction conditions.^a



Entry	Variations from the 'standard' conditions	1c (%) ^b
1	No variation	90
2	MOF 1-OTf-Ir -low instead of MOF 1-OTf-Ir	38
3	MOF 1-OTf-Ir -high instead of MOF 1-OTf-Ir	61
4	DCE instead of CH_3CN	50
5	Toluene instead of CH_3CN	45
6	DME instead of CH_3CN	58
7	1a (1.5 equiv)	77
8	Without light	none
9	Without MOF 1-OTf-Ir	trace
10	MOF 1-OH-Ir instead of MOF 1-OTf-Ir	10
11	MOF 1-OTf instead of MOF 1-OTf-Ir	8

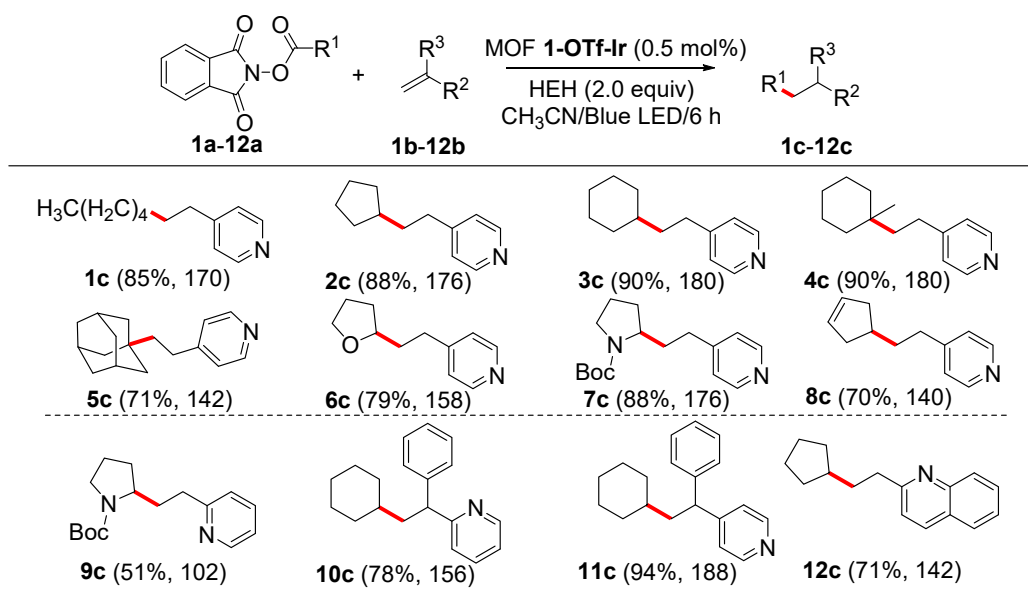
^a Reactions were conducted at 0.1 mmol scale. ^b GC yields.

A variety of redox-active NHP esters were examined for reductive cross-coupling reactions under standard conditions. As shown in **Table 4-2**, primary, secondary, and tertiary alkyl NHP

esters underwent cross-couplings with 4-vinylpyridine to afford **1c-4c** in 85%-90% isolated yields. Sterically demanding adamantyl group was tolerated to afford **5c** in 71% yield. NHP esters bearing heterocycles (tetrahydrofuran and pyrrolidine) worked well to afford **6c** and **7c** in 79% and 88% isolated yields, respectively. Cyclopentenyl group was also tolerated to afford **8c** in 70% yield.

Different vinyl-azaarenes were also tested. Cross-coupling between 2-vinylpyridine and proline-derived NHP ester gave **9c** in 51% yield. 2-(1-Phenylvinyl)pyridine and 4-(1-phenylvinyl)pyridine served as competent coupling partners to produce **10c** and **11c** in 78% and 94% isolated yields, respectively. The use of 2-vinylquinoline afforded **12c** in 71% yield.

Table 4-2. 1-OTf-Ir catalyzed reductive cross-coupling of vinylazarenes with NHP esters.^a Reprinted with permission from *Journal of the American Chemical Society*, 2020, 142, 8602-8607. Copyright 2020 American Chemical Society.

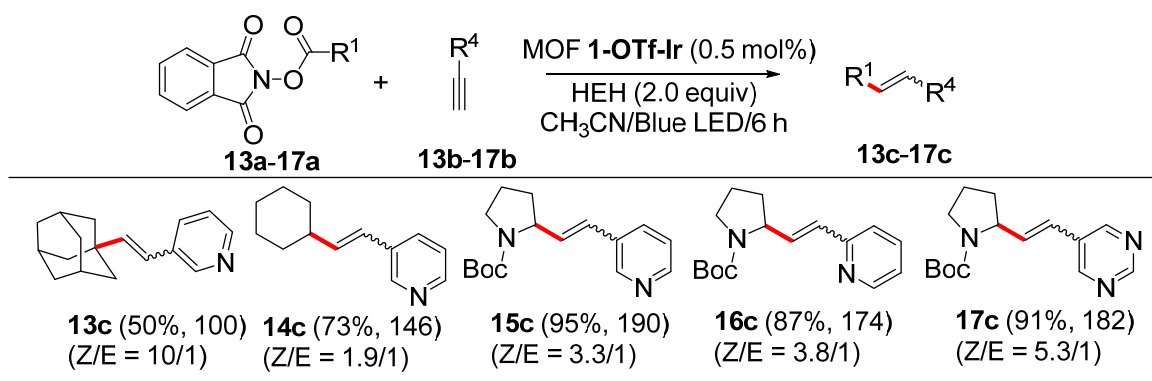


^a Reactions were conducted at 0.1 mmol scale, yield of isolated products.

We also investigated reductive cross-coupling of NHP esters with alkynyl-azaarenes under standard conditions (**Table 4-3**). 3-Ethynylpyridine reacted with adamantyl and cyclohexyl NHP esters to afford **13c** and **14c** in 50% and 73% isolated yields, respectively. Cross-couplings of proline-derived NHP ester with 3-ethynylpyridine, 2-ethynylpyridine, and 5-ethynylpyrimidine

afforded **15c**, **16c**, and **17c** in 95%, 87%, and 91% isolated yields, respectively. The highest turnover number of 190 was achieved for **15c**. Both Z and E isomers formed in these reactions, likely due to rapid isomerization of the vinyl radical intermediate. The Z/E ratio of cross-coupling products depended on both coupling partners and varied from 1.9/1 to 10/1. It is worth noting that several coupling products such as **5c**, **7c**, **10c** and **17c** are important scaffolds in drug molecules.

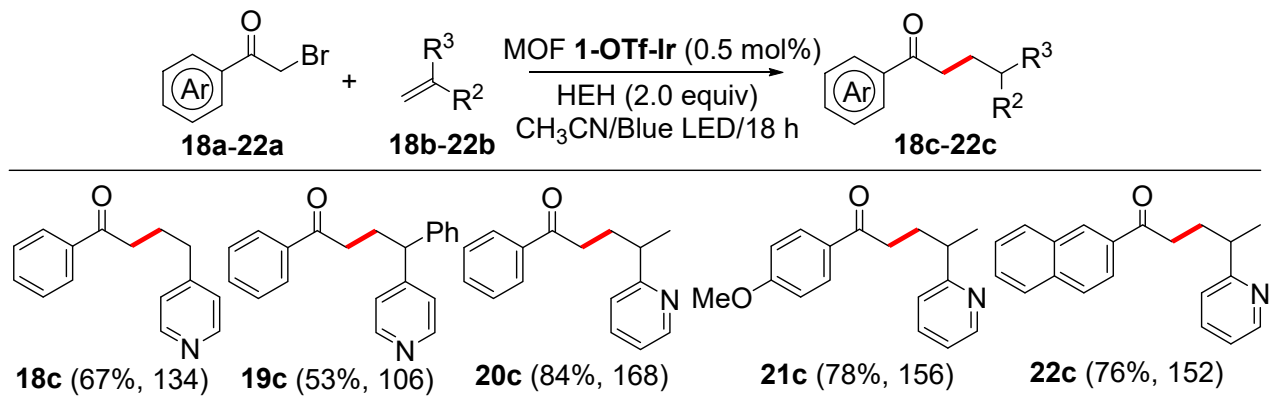
Table 4-3. 1-OTf-Ir catalyzed reductive cross-coupling of alkynylazaarenes with NHP esters.^a Reprinted with permission from *Journal of the American Chemical Society*, **2020**, 142, 8602-8607. Copyright 2020 American Chemical Society.



^a Reactions were conducted at 0.1 mmol scale, yield of isolated products.

Aryl bromomethyl ketones were also used as radical precursors for reductive cross-coupling reactions (**Table 4-4**). Bromoacetophenone reacted with 4-vinylpyridine, 1-phenyl-1-(4-pyridyl)ethene, and 2-isopropenylpyridine to give **18c-20c** in 53%-84% isolated yields. *p*-Methoxyphenacyl bromide and 2-naphthacyl bromide served as competent coupling partners to afford **21c** and **22c** in 78% and 76% isolated yields, respectively.

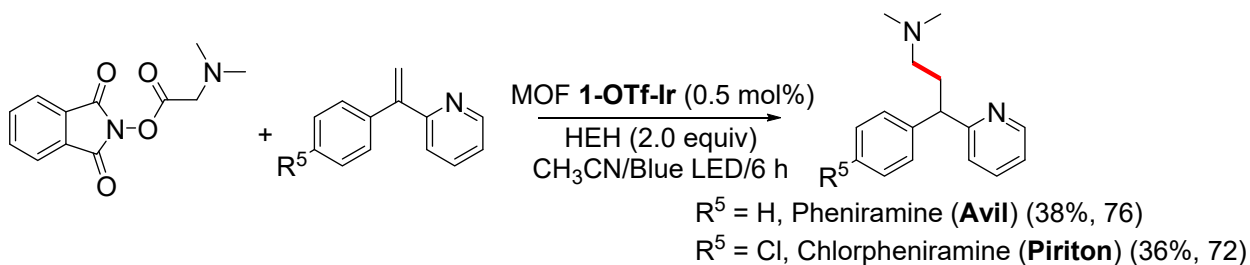
Table 4-4. 1-OTf-Ir catalyzed reductive cross-coupling of aryl bromomethyl ketones.^a Reprinted with permission from *Journal of the American Chemical Society*, **2020**, 142, 8602-8607. Copyright 2020 American Chemical Society.



^a Reactions were conducted at 0.1 mmol scale, yield of isolated products.

We further tested the use of the photocatalytic reductive coupling in drug molecule synthesis. As shown in **Table 4-5**, dimethylglycine-derived NHP ester coupled with 2-(1-phenylvinyl)pyridine under standard conditions to afford Pheniramine in 38% yield. Chlorpheniramine was similarly synthesized in 36% yield.

Table 4-5. 1-OTf-Ir catalyzed the synthesis of marketed drug molecules. Reprinted with permission from *Journal of the American Chemical Society*, **2020**, 142, 8602-8607. Copyright 2020 American Chemical Society.



4.2.3 Mechanistic Studies

1-OTf-Ir was stable under catalytic conditions as indicated by the retention of the PXRD pattern for the recovered MOF (**Figure 4-7**) and the leaching of <0.1% Al and <0.1% Ir into the supernatant.

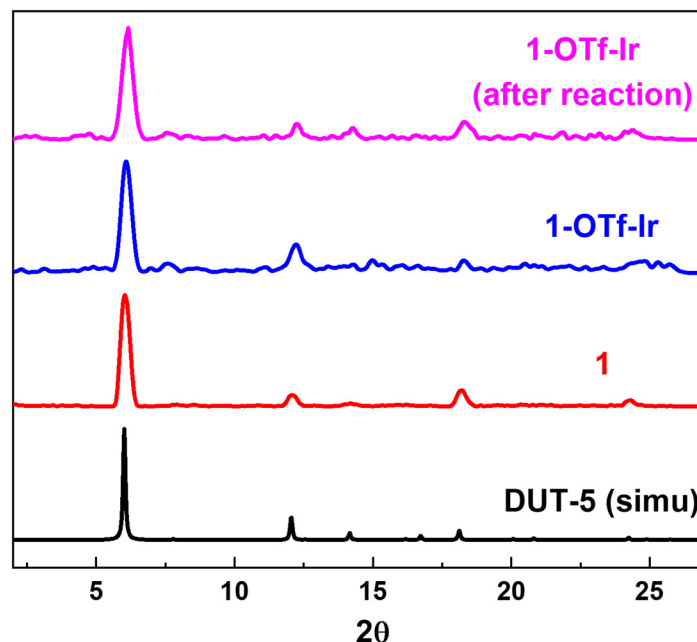


Figure 4-7. PXRD patterns of **1** (red), **1-OTf-Ir** (blue), and **1-OTf-Ir (after reaction)** (pink) in comparison to the simulated pattern for DUT-5.

1-OTf-Ir was recovered and used in five runs of reductive cross-coupling between 4-vinylpyridine and pentanyl NHP ester with no decrease in catalytic activity (**Figure 4-8**), where Pentanyl N-hydroxyphthalimide ester (52.3 mg, 0.20 mmol, 2.0 equiv), 4-vinylpyridine (10.5 mg, 0.10 mmol, 1.0 equiv), Hantzsch ester (50.7 mg, 0.20 mmol, 2.0 equiv), and **1-OTf-Ir** (0.50 μmol , 0.5 mol%, based on Lewis acid site) were mixed in dry CH_3CN (0.5 mL) in a closable flask. The resulting mixture was stirred under blue LED irradiation at room temperature in an N_2 atmosphere for 6 hours. After reaction, the MOF catalyst was recovered via centrifugation, washed with dry CH_3CN (1.0 mL \times 3), and then used for subsequent cycles of reactions. The aforementioned procedure was repeated four times.

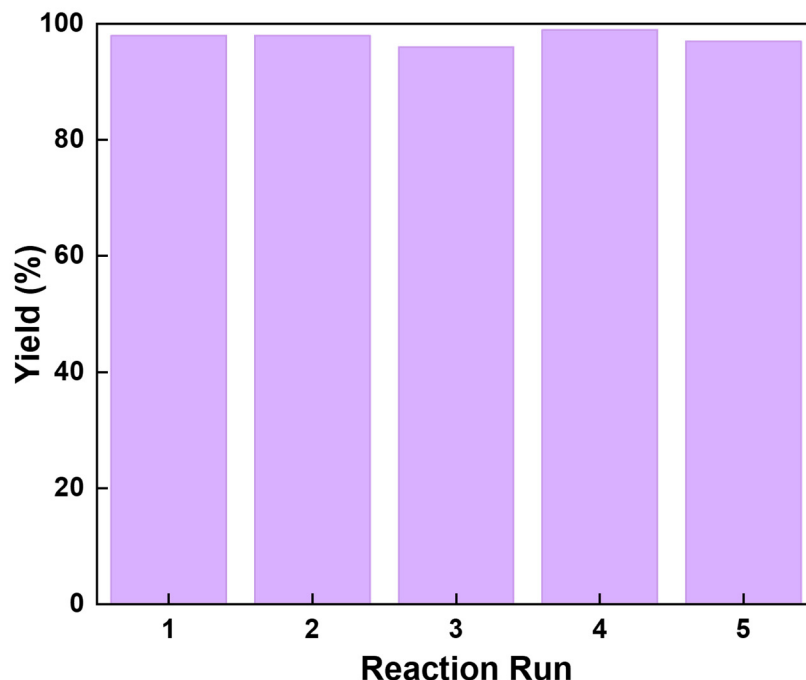


Figure 4-8. Yields of **1c** with recovered MOF **1-OTf-Ir** in five consecutive runs. Reprinted with permission from *Journal of the American Chemical Society*, **2020**, 142, 8602-8607. Copyright 2020 American Chemical Society.

The optimal Lewis acid to Ir-PS ratio of 3.8 in **1-OTf-Ir** is similar to those of binding centers to catalytic centers in enzymes,²⁷ but much lower than those of homogeneous catalytic systems ($> 10/1$).⁸ The excellent catalytic activity of **1-OTf-Ir** may be attributed to the pore confinement effect, which facilitates the reaction of reactive radicals and activated azaarenes in an enzyme-inspired fashion.²⁴

Several control experiments were conducted to shed light on the reaction mechanism. **1-OH-Ir** containing only Ir-PS gave the coupling product **1c** in 10% yield (**Figure 4-9**). **1-OTf** with only Lewis acidic sites catalyzed the reductive cross-coupling to afford **1c** in 8% yield (**Figure 4-9**). These results indicate the crucial role of both PSs and strong Lewis acids.

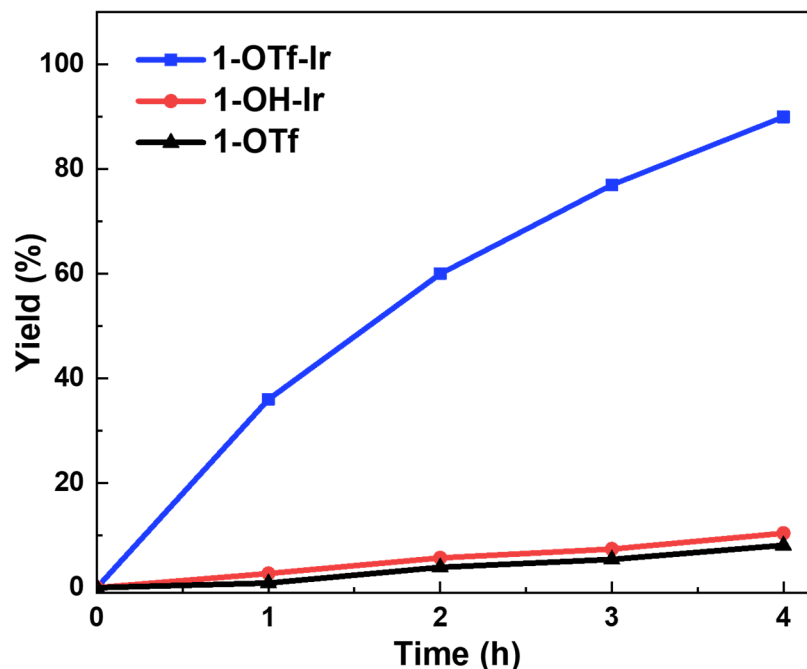
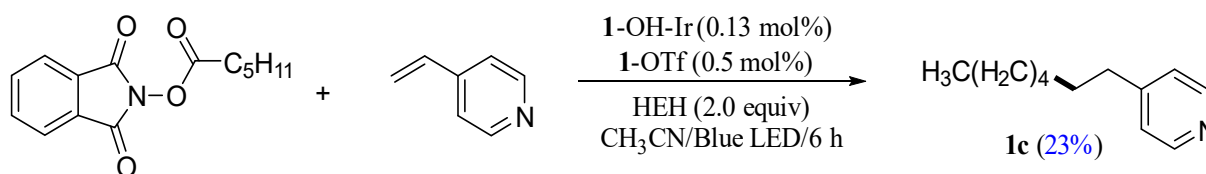


Figure 4-9. Time-dependent yields of **1c** with different catalysts. Reprinted with permission from *Journal of the American Chemical Society*, **2020**, 142, 8602-8607. Copyright 2020 American Chemical Society.

Pentanyl *N*-hydroxyphthalimide ester (52.3 mg, 0.20 mmol, 2.0 equiv), 4-vinylpyridine (10.5 mg, 0.10 mmol, 1.0 equiv), Hantzsch ester (50.7 mg, 0.20 mmol, 2.0 equiv), **1-OH-Ir** (0.13 μ mol, 0.13 mol% based on Ir site) and **1-OTf** (0.50 μ mol, 0.5 mol% based on Lewis acid site) were mixed in dry CH₃CN (0.5 mL) in a closable flask (**Scheme 4-2**). The resulting mixture was stirred under blue LED irradiation at room temperature in an N₂ atmosphere for 6 hours. After reaction, the suspension was filtered, and the filtrate was then subjected to GC-MS analysis, affording 23% yield for product **1c**. The catalytic result using combination of **1-OH-Ir** and **1-OTf** as the catalyst supports the advantage of integrating both active centers in the mesopores.

Scheme 4-2. Control reaction catalyzed by **1-OTf** and **1-OH-Ir**.



Upon excitation at 365 nm, luminescence of **1**-OTf-Ir was quenched by both HEH and **1a**, but not **1b** (Figure 4-10). Luminescence quenching by HEH and **1a** were well fitted to the Stern-Völmer equation to give a $K_{sv}(\text{HEH})$ of 0.232 ± 0.011 and a $K_{sv}(\mathbf{1a})$ of 0.164 ± 0.018 , suggesting preferential quenching of $[\text{Ir}^{\text{III}}]^*$ species by HEH over **1a**.

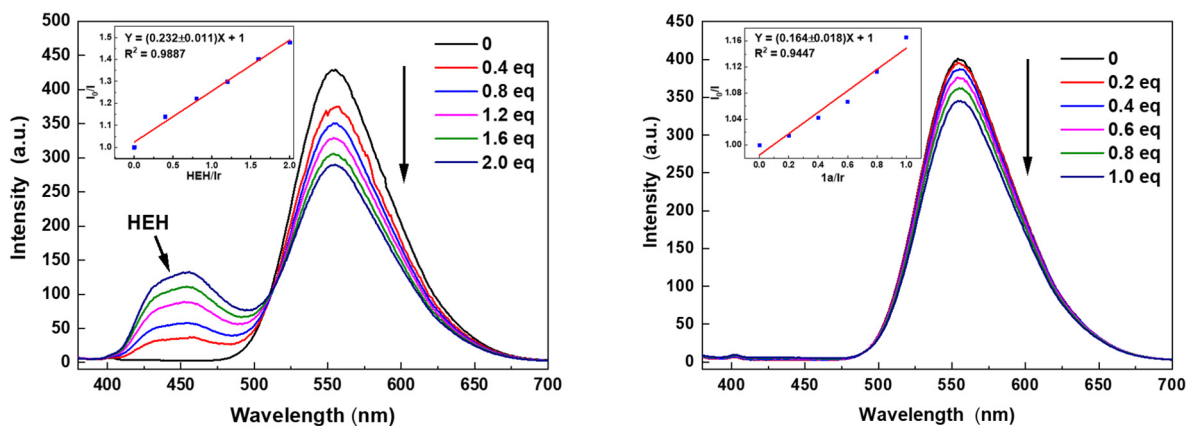


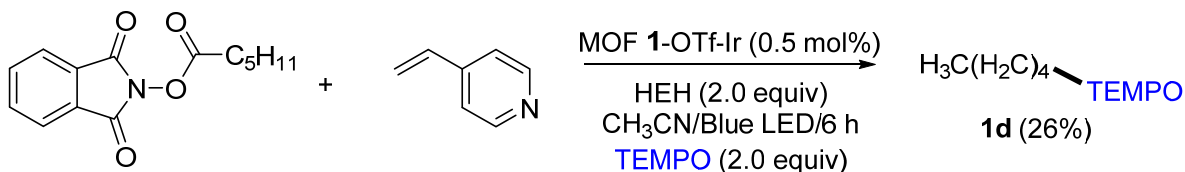
Figure 4-10. Emission spectra of **1**-OTf-Ir (10 μM based on Ir component, CH_3CN) after the addition of different amounts of HEH (left) or **1a** (right) with 365 nm excitation. Insets show the plots of I_0/I of **1**-OTf-Ir as a function of equivalents of HEH (left) or **1a** (right). Reprinted with permission from *Journal of the American Chemical Society*, **2020**, 142, 8602-8607. Copyright 2020 American Chemical Society.

In addition, radical capture by (2,2,6,6-tetramethylpiperidin-1-yl)oxyl (TEMPO) or 1,1-diphenylethene completely shut down the formation of **1c** but generated 1-pentyloxy-2,2,6,6-tetramethylpiperidine (**1d**) or 1,1-diphenylheptane (**1e**) in 26% and 91% yields, respectively (Schemes 4-3 and 4-4). This result suggests the presence of pentanyl radical in the reaction.

Radical capture experiment with TEMPO. Pentanyl *N*-hydroxyphthalimide ester (52.3 mg, 0.20 mmol, 2.0 equiv), 4-vinylpyridine (10.5 mg, 0.10 mmol, 1.0 equiv), Hantzsch ester (50.7 mg, 0.20 mmol, 2.0 equiv), (2,2,6,6-tetramethylpiperidin-1-yl)oxyl (TEMPO) (31.3 mg, 0.20 mmol, 2.0 equiv), and **1**-OTf-Ir (0.50 μmol , 0.5 mol%, based on Lewis acid site) were mixed in dry CH_3CN (0.5 mL) in a closable flask. The resulting mixture was stirred under blue LED irradiation at room temperature in an N_2 atmosphere for 6 hours. After reaction, the suspension

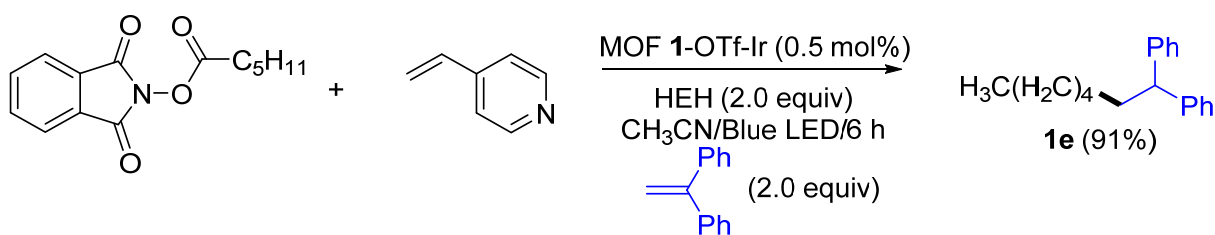
was filtered, and the filtrate was then subjected to GC-MS analysis. 1-Pentyloxy-2,2,6,6-tetramethylpiperidine (**1d**) was detected in 26% yield without the observation of product **1c**.

Scheme 4-3. Radical capture experiment with TEMPO.



Radical capture experiment with 1,1-diphenylethene. Pentan-1-yl *N*-hydroxyphthalimide ester (52.3 mg, 0.20 mmol, 2.0 equiv), 4-vinylpyridine (10.5 mg, 0.10 mmol, 1.0 equiv), Hantzsch ester (50.7 mg, 0.20 mmol, 2.0 equiv), 1,1-diphenylethene (36.1 mg, 0.20 mmol, 2.0 equiv), and 1-OTf-Ir (0.50 μmol , 0.5 mol%, based on Lewis acid site) were mixed in dry CH_3CN (0.5 mL) in a closable flask. The resulting mixture was stirred under blue LED irradiation at room temperature in an N_2 atmosphere for 6 hours. After reaction, the suspension was filtered, and the filtrate was then subjected to GC-MS analysis. 1,1-Diphenylheptane (**1e**) was detected in 91% yield without the observation of product **1c**.

Scheme 4-4. Radical capture experiment with 1,1-diphenylethene.



On the basis of these experimental results and literature precedents,^{8-9, 37} we propose a reaction mechanism as shown in **Figure 4-11**. Reduction of photoexcited $[\text{Ir}^{\text{III}}]^*$ in by HEH furnishes $\text{HEH}^{\cdot+}$ radical cation and strongly reducing $[\text{Ir}^{\text{II}}]$ center, which competently reduces substrates **a** to give alkyl radical and regenerate the $[\text{Ir}^{\text{III}}]$ species. In the meantime, substrates **b** coordinates to the Lewis acidic site in the same mesopore to afford electron-deficient pyridine

derivative **A** which is susceptible to attack by alkyl radical. Subsequent radical addition generates radical intermediate **B**, which undergoes hydrogen atom transfer with $\text{HEH}^{\bullet+}$ to afford Lewis acid-bound product **C** and EH^+ cation. An incoming substrate releases product **P** and restarts the catalytic cycle on the right. As the active centers are engineered into the same mesopore, the reactive intermediates are confined in the mesopore, resulting in high local concentrations to facilitate the coupling reaction.

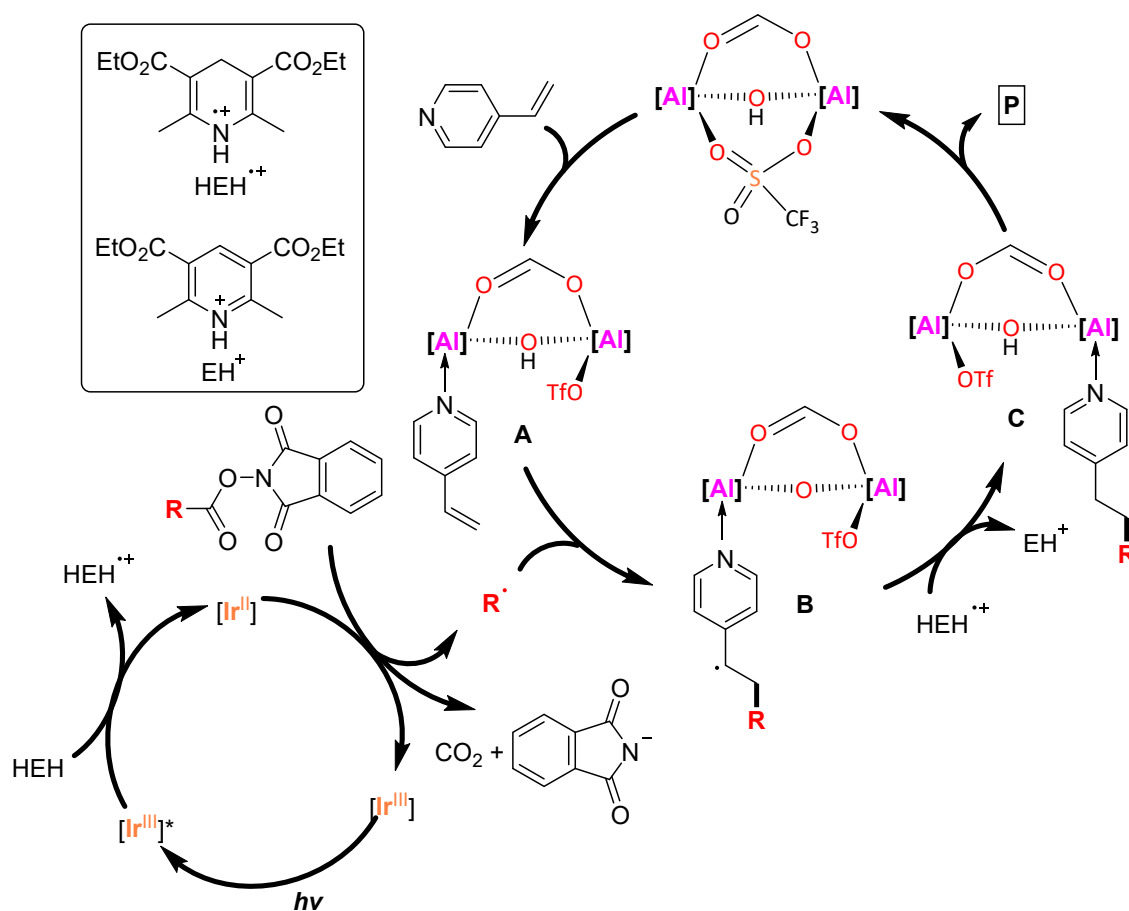


Figure 4-11. Proposed reaction mechanism for 1-OTf-Ir catalyzed reductive cross-coupling of azaarenes with esters. Reprinted with permission from *Journal of the American Chemical Society*, 2020, 142, 8602-8607. Copyright 2020 American Chemical Society.

4.3 Conclusion

In this chapter, we have engineered mesopores in an Al-MOF for the installation of strongly Lewis acid sites and Ir-PSs to perform bioinspired synergistic catalysis. **1-OTf-Ir** effectively catalyzed reductive cross-coupling of *N*-hydroxyphthalimide esters or aryl bromomethyl ketones with vinyl- or alkynyl-azaarenes to afford functionalized azaarene derivatives with turnover numbers of up to 190. **1-OTf-Ir** was also used to synthesize anticholinergic drugs Pheniramine and Chlorpheniramine. **1-OTf-Ir** significantly outperformed homogeneous and other controls as a result of the close proximity of both binding centers and catalytic centers in the mesopore which facilitates the coupling between activated vinyl- or alkynyl-azaarenes and alkyl radicals. This work highlights the potential of enzyme-inspired multifunctional MOFs in synergistic catalysis.

4.4 Experimental

4.4.1 Material and Methods

All the reactions and manipulations were carried out under N₂ with the use of a glovebox or Schlenk technique, unless otherwise indicated. All the solvents were dried by standard procedures. *N*-Hydroxyphthalimide esters, 2-(1-phenylvinyl)pyridine, 2-vinylquinoline, 4-(1-phenylvinyl)pyridine, 2-isopropenylpyridine and 2-(1-*p*-chlorophenylvinyl)pyridine were prepared according to literature methods.³⁸⁻³⁹ All other chemicals were purchased from Fisher or Aldrich and used directly unless otherwise indicated.

Powder X-ray diffraction (PXRD) data was collected on a Bruker D8 Venture diffractometer using Cu K α radiation source ($\lambda = 1.54178 \text{ \AA}$). N₂ sorption experiments were performed on a Micrometrics TriStar II 3020 instrument. Thermogravimetric analysis (TGA) was performed in air using a Shimadzu TGA-50 equipped with a platinum pan and heated at a rate of 1.5 °C per min. Transmission electron microscopy (TEM) images were taken on a TECNAI F30

HRTEM. Scanning electron microscopy (SEM) images were taken on the Carl Zeiss Merlin, with the detectors of In-Lens, EsB, AsB, & SE2. Ozonolysis was performed on an Azcozon RMU-DG3 ozone generator, which produces up to ~0.42 mol/h ozone at a 6 L/min O₂ gas flow rate. Inductively coupled plasma-mass spectrometry (ICP-MS) data was obtained with an Agilent 7700x ICP-MS and analyzed using ICP-MS Mass Hunter version B01.03. Samples were diluted in a 2% HNO₃ matrix and analyzed with a ¹⁵⁹Tb internal standard against a 12-point standard curve over the range from 0.1 ppb to 500 ppb. The correlation was >0.9997 for all analyses of interest. Data collection was performed in Spectrum Mode with five replicates per sample and 100 sweeps per replicate. EPR spectra were recorded on a Bruker Elexsys 500 X-band EPR spectrometer under irradiation of a white-light lamp (Fiber-Lite MI-150) by focusing the lamp on the sample cell in the ESR cavity at 15 K. Fluorescence measurement was performed using a Shimadzu RF-5301PC spectrofluorophotometer.

¹H NMR and ¹³C NMR spectra were recorded on a Bruker NMR 500 DRX spectrometer at 500 MHz and 126 MHz, respectively. The following abbreviations are used herein: s: singlet, d: doublet, t: triplet, q: quartet, m: multiplet, br: broad, app: apparent.

4.4.2 Synthesis of 1-OTf-Ir

In a N₂-filled glovebox, 1-OTf (0.1 mmol of bpy) was weighed out in a 75 mL high pressure glass vessel. 20 mL of [Ir(ppy)₂Cl]₂³⁵ solution in DMF (10 mM) was then added. The mixture was stirred at 100 °C for 3 days. The bright-orange solid was then centrifuged and washed with DMF three times, THF three times, and benzene three times. The resultant solid was freeze-dried and stored in a glovebox for further use. ICP-MS analysis showed an Al/Ir molar ratio of ~10:1, indicating ~13% of dcbpy ligands were metalated.

4.4.3 X-ray Absorption Study

Data collection. X-ray absorption data of **1-OTf-Ir** was collected at Beamline 10-BM at the Advanced Photon Source (APS) at Argonne National Laboratory. Spectra were collected at the iridium L₃-edge (11215 eV) in transmission mode. The X-ray beam was monochromatized by a Si(111) monochromator and detuned by 50% to reduce the contribution of higher-order harmonics below the level of noise. A metallic platinum foil standard was used as a reference for energy calibration and was measured simultaneously with experimental samples. The incident beam intensity (I_0), transmitted beam intensity (I_t), and reference (I_r) were measured by 20 cm ionization chambers with gas compositions of 44% N₂ and 56% Ar, 5% N₂ and 95% Ar, and 100% N₂, respectively. Data were collected over six regions: -250 to -30 eV (10 eV step size, dwell time of 0.25 s), -30 to -12 eV (5 eV step size, dwell time of 0.5 s), -12 to 30 eV (1.1 eV step size, dwell time of 1 s), 30 eV to 6 Å⁻¹, (0.05 Å⁻¹ step size, dwell time of 2 s), 6 Å⁻¹ to 12 Å⁻¹, (0.05 Å⁻¹ step size, dwell time of 4 s), 12 Å⁻¹ to 15 Å⁻¹, (0.05 Å⁻¹ step size, dwell time of 8 s). Multiple X-ray absorption spectra were collected at room temperature for each sample. Samples were ground and mixed with polyethyleneglycol (PEG) and packed in a 6-shooter sample holder to achieve adequate absorption length.

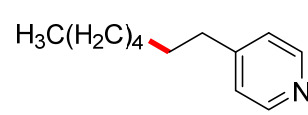
Data processing. Data was processed using the Athena and Artemis programs of the IFEFFIT package based on FEFF 6. Prior to merging, spectra were calibrated against the reference spectra and aligned to the first peak in the smoothed first derivative of the absorption spectrum, the background noise was removed, and the spectra were processed to obtain a normalized unit edge step.

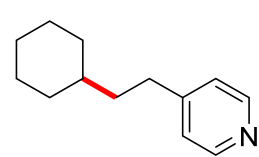
EXAFS fitting of 1-OTf-Ir. Fitting of the EXAFS region was performed using the Artemis program of the IFEFFIT package. Fitting was performed in R space, with a k -weight of 3 for

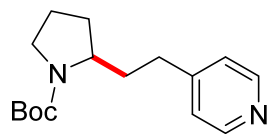
iridium samples. Refinement was performed by optimizing an amplitude factor S_0^2 and energy shift ΔE_0 which are common to all paths, in addition to parameters for bond length (ΔR) and Debye-Waller factor (σ^2). The fitting model for **1-OTf-Ir** was based on the single crystal structure QUSQIG obtained from CCDC.

4.4.4 Synergistic Catalytic Reactions

General procedure for reductive cross-coupling of *N*-hydroxyphthalimide esters with vinylpyridines. *N*-Hydroxyphthalimide ester (0.20 mmol, 2.0 equiv), vinyl-pyridine (0.10 mmol, 1.0 equiv), Hantzsch ester (0.20 mmol, 2.0 equiv), and **1-OTf-Ir** (0.50 μ mol, 0.5 mol%, based on Lewis acid site) were mixed in dry CH_3CN (0.5 mL) in a closable flask. The resulting mixture was stirred under blue LED irradiation at room temperature in an N_2 atmosphere for 6 hours. After the reaction, the solvent was removed under vacuum. The residue was then subjected to column chromatography on silica gel using *n*-hexane, ethyl acetate and triethylamine as eluent to give products **1c-12c**.

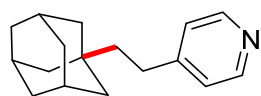
 **1c:** Yield 85%. White oil. ^1H NMR (500 MHz, Chloroform-*d*) δ 8.49 (s, 2H), 7.12 (d, $J = 5.7$ Hz, 2H), 2.63 – 2.57 (m, 2H), 1.62 (p, $J = 7.4$ Hz, 2H), 1.35 – 1.22 (m, 8H), 0.88 (t, $J = 7.0$ Hz, 3H). ^{13}C NMR (126 MHz, CDCl_3) δ 152.2, 149.5, 124.2, 35.4, 31.9, 30.4, 29.3, 29.2, 22.8, 14.2. Characterization data matched that reported in the literature.⁴⁰

 **2c:** Yield 90%. White oil. ^1H NMR (500 MHz, Chloroform-*d*) δ 8.48 (d, $J = 6.0$ Hz, 2H), 7.13 (d, $J = 6.0$ Hz, 2H), 2.66 – 2.59 (m, 2H), 1.79 – 1.61 (m, 5H), 1.55 – 1.47 (m, 2H), 1.29 – 1.11 (m, 4H), 0.98 – 0.88 (m, 2H). ^{13}C NMR (126 MHz, CDCl_3) δ 153.0, 149.2, 124.2, 38.2, 37.4, 33.3, 32.8, 26.7, 26.4. Characterization data matched that reported in the literature.⁴¹



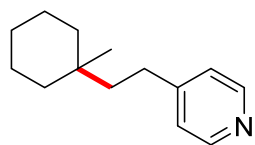
3c: Yield 88%. White oil. ^1H NMR (500 MHz, Chloroform-*d*) δ 8.46 (s, 2H), 7.12 (d, $J = 19.3$ Hz, 2H), 3.91 – 3.66 (m, 1H), 3.47 – 3.22 (m, 2H), 2.67 – 2.46 (m, 2H), 2.18 – 1.90 (m, 2H), 1.89 – 1.54 (m, 4H), 1.43 (s, 9H).

^{13}C NMR (126 MHz, CDCl_3) δ 154.8, 151.7, 151.2, 149.7, 124.0, 79.4, 79.2, 57.1, 56.8, 46.7, 46.3, 34.8, 32.2, 30.7, 30.2, 28.7, 23.9. Characterization data matched that reported in the literature.⁴²



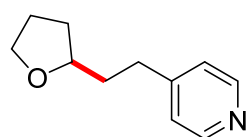
4c: Yield 71%. White oil. ^1H NMR (500 MHz, Chloroform-*d*) δ 8.49 – 8.43 (m, 2H), 7.11 (d, $J = 6.1$ Hz, 2H), 2.57 – 2.51 (m, 2H), 1.98 (s, 3H), 1.76 –

1.61 (m, 6H), 1.53 (d, $J = 2.9$ Hz, 6H), 1.39 – 1.32 (m, 2H). ^{13}C NMR (126 MHz, CDCl_3) δ 153.2, 149.6, 124.1, 45.7, 42.5, 37.3, 32.6, 28.8, 28.8. HRMS (ESI) calcd for $\text{C}_{17}\text{H}_{23}\text{N}$ [$\text{M}+\text{H}$] 242.1864, found 242.1935.



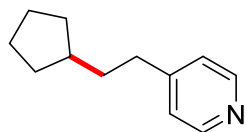
5c: Yield 90%. White oil. ^1H NMR (500 MHz, Chloroform-*d*) δ 8.47 (d, $J = 5.0$ Hz, 2H), 7.12 (d, $J = 5.6$ Hz, 2H), 2.57 – 2.49 (m, 2H), 1.54 – 1.41 (m, 7H), 1.37 – 1.27 (m, 5H), 0.94 (s, 3H).. ^{13}C NMR (126 MHz, CDCl_3) δ 157.5,

130.6, 129.5, 129.4, 128.9, 127.9, 126.3, 124.7, 123.2, 114.5, 77.1, 69.2, 34.2, 26.2. HRMS (ESI) calcd for $\text{C}_{14}\text{H}_{21}\text{N}$ [$\text{M}+\text{H}$] 204.1701, found 204.1885.

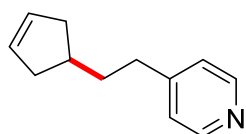


6c: Yield 79%. White oil. ^1H NMR (500 MHz, Chloroform-*d*) δ 8.49 (d, $J = 5.8$ Hz, 2H), 7.17 (d, $J = 6.1$ Hz, 2H), 3.92 – 3.70 (m, 3H), 2.83 – 2.62 (m, 2H), 2.04 – 1.73 (m, 5H), 1.53 – 1.44 (m, 1H). ^{13}C NMR (126 MHz, CDCl_3)

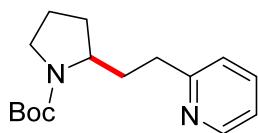
δ 152.1, 149.2, 124.2, 78.3, 67.9, 36.3, 32.3, 31.5, 25.9. Characterization data matched that reported in the literature.⁴¹



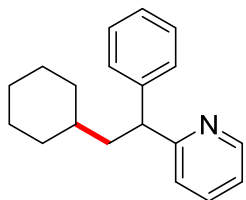
7c: Yield 88%. White oil. ^1H NMR (500 MHz, Chloroform-*d*) δ 8.56 – 8.39 (m, 2H), 7.11 (d, $J = 6.0$ Hz, 2H), 2.66 – 2.57 (m, 2H), 1.84 – 1.71 (m, 3H), 1.67 – 1.47 (m, 6H), 1.18 – 1.06 (m, 2H). ^{13}C NMR (126 MHz, CDCl_3) δ 152.3, 149.5, 124.1, 39.7, 37.0, 34.6, 32.7, 25.3. HRMS (ESI) calcd for $\text{C}_{12}\text{H}_{17}\text{N}$ [$\text{M}+\text{H}$] 176.1395, found 176.1683.



8c: Yield 70%. White oil. ^1H NMR (500 MHz, Chloroform-*d*) δ 8.49 (d, $J = 5.2$ Hz, 2H), 7.15 (d, $J = 6.0$ Hz, 2H), 5.67 (s, 2H), 2.68 – 2.60 (m, 2H), 2.51 (dd, $J = 14.1, 8.7$ Hz, 2H), 2.29 – 2.18 (m, 1H), 2.02 (dd, $J = 13.6, 6.5$ Hz, 2H), 1.77 – 1.69 (m, 2H). ^{13}C NMR (126 MHz, CDCl_3) δ 152.5, 149.3, 129.9, 124.2, 39.0, 37.2, 37.2, 34.2.⁴¹

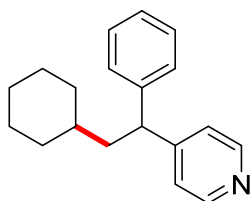


9c: Yield 51%. White oil. ^1H NMR (500 MHz, Chloroform-*d*) δ 8.51 (d, $J = 4.9$ Hz, 1H), 7.73 – 7.58 (m, 1H), 7.37 – 7.10 (m, 2H), 3.98 – 3.75 (m, 1H), 3.48 – 3.26 (m, 2H), 2.94 – 2.71 (m, 2H), 2.27 – 1.70 (m, 6H), 1.44 (s, 9H). ^{13}C NMR (126 MHz, CDCl_3) δ 161.7, 161.3, 154.9, 148.9, 147.6, 138.1, 137.1, 123.7, 123.0, 121.6, 121.4, 79.2, 79.1, 57.2, 57.0, 46.7, 46.3, 35.2, 35.0, 34.6, 34.2, 30.8, 30.1, 28.7, 23.9, 23.2. Characterization data matched that reported in the literature.⁴³

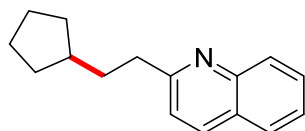


10c: Yield 78%. White oil. ^1H NMR (500 MHz, Chloroform-*d*) δ 8.56 (d, $J = 3.9$ Hz, 1H), 7.55 (t, $J = 7.7$ Hz, 1H), 7.37 – 7.32 (m, 2H), 7.28 (t, $J = 7.7$ Hz, 2H), 7.20 – 7.14 (m, 2H), 7.07 (dd, $J = 7.5, 4.9$ Hz, 1H), 4.23 (t, $J = 7.9$

Hz, 1H), 2.14 – 2.04 (m, 1H), 2.02 – 1.93 (m, 1H), 1.77 (t, $J = 14.3$ Hz, 2H), 1.68 – 1.55 (m, 3H), 1.16 – 1.06 (m, 4H), 1.02 – 0.88 (m, 2H). ^{13}C NMR (126 MHz, CDCl_3) δ 164.5, 149.3, 144.2, 136.5, 128.6, 128.2, 126.4, 122.8, 121.3, 50.7, 42.9, 35.1, 33.7, 33.3, 26.7, 26.3, 26.3. Characterization data matched that reported in the literature.⁴⁴



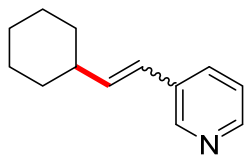
11c: Yield 94%. White oil. ^1H NMR (500 MHz, Chloroform- d) δ 8.48 (d, $J = 5.1$ Hz, 2H), 7.32 – 7.27 (m, 2H), 7.24 – 7.18 (m, 3H), 7.17 – 7.14 (m, 2H), 4.04 (t, $J = 8.0$ Hz, 1H), 1.97 – 1.87 (m, 2H), 1.75 (t, $J = 13.8$ Hz, 2H), 1.69 – 1.57 (m, 3H), 1.19 – 1.06 (m, 4H), 1.01 – 0.88 (m, 2H). ^{13}C NMR (126 MHz, CDCl_3) δ 154.6, 149.9, 143.5, 128.8, 128.0, 126.7, 123.4, 47.6, 42.9, 34.9, 33.5, 33.4, 26.6, 26.2, 26.2. Characterization data matched that reported in the literature.⁴¹



12c: Yield 71%. White oil. ^1H NMR (500 MHz, Chloroform- d) δ 8.32 – 8.09 (m, 2H), 7.82 (d, $J = 8.1$ Hz, 1H), 7.74 (t, $J = 7.8$ Hz, 1H), 7.54 (t, $J = 7.4$ Hz, 1H), 7.37 (d, $J = 8.6$ Hz, 1H), 3.08 (s, 2H), 1.96 – 1.74 (m, 5H), 1.70 – 1.58 (m, 2H), 1.58 – 1.45 (m, 2H), 1.24 – 1.14 (m, 2H). ^{13}C NMR (126 MHz, CDCl_3) δ 162.7, 127.8, 126.9, 126.4, 124.1, 121.7, 118.0, 40.2, 36.6, 32.8, 25.4. HRMS (ESI) calcd for $\text{C}_{16}\text{H}_{19}\text{N}$ [$\text{M}+\text{H}$] 226.1551, found 226.1710.

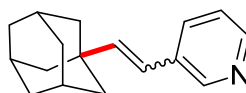
General procedure for reductive cross-coupling of N-hydroxyphthalimide esters with alkynylpyridines. *N*-Hydroxyphthalimide ester (0.20 mmol, 2.0 equiv), alkynylpyridine (0.10 mmol, 1.0 equiv), Hantzsch ester (0.20 mmol, 2.0 equiv), and **1**-OTf-Ir (0.50 μmol , 0.5 mol%, based on Lewis acid site) were mixed in dry CH_3CN (0.5 mL) in a closable flask. The resulting mixture was stirred under blue LED irradiation at room temperature in an N_2 atmosphere for 6

hours. After the reaction, the solvent was removed under vacuum. The residue was then subjected to column chromatography on silica gel using *n*-hexane, ethyl acetate and triethylamine as eluent to give products **13c-17c**.



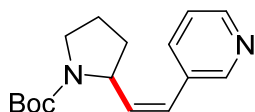
13c: Yield 73%. White oil. A mixture of Z and E isomers with a molar ratio of Z/E = 1.9/1 as determined by ^1H NMR. The E isomer was isolated in the pure form via repeated column chromatographic separation on silica gel. ^1H

NMR (500 MHz, Chloroform-*d*) δ 8.56 (s, 1H), 8.42 (d, $J = 4.0$ Hz, 1H), 7.70 (dt, $J = 7.9, 2.0$ Hz, 1H), 7.24 (dd, $J = 7.9, 4.8$ Hz, 1H), 6.36 – 6.21 (m, 2H), 2.21 – 2.08 (m, 2H), 1.85 – 1.74 (m, 4H), 1.72 – 1.65 (m, 1H), 1.37 – 1.27 (m, 2H), 1.23 – 1.14 (m, 2H). ^{13}C NMR (126 MHz, CDCl_3) δ 147.5, 147.3, 141.3, 139.8, 133.1, 123.7, 123.6, 41.4, 32.8, 26.2, 26.1. Characterization data matched that reported in the literature.



14c: Yield 50%. White oil. A mixture of Z and E isomers with a molar ratio of Z/E = 10.0/1 as determined by ^1H NMR. The Z isomer was isolated in the

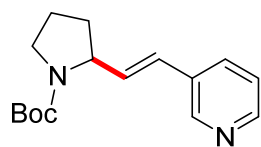
pure form via repeated column chromatographic separation on silica gel. ^1H NMR (500 MHz, Chloroform-*d*) δ 8.50 (s, 2H), 7.64 (d, $J = 7.8$ Hz, 1H), 7.34 (s, 1H), 6.28 (d, $J = 12.8$ Hz, 1H), 5.55 (d, $J = 12.8$ Hz, 1H), 1.94 (d, $J = 2.9$ Hz, 1H), 1.90 – 1.85 (m, 3H), 1.65 – 1.59 (m, 3H), 1.58 – 1.52 (m, 8H). ^{13}C NMR (126 MHz, CDCl_3) δ 159.3, 146.4, 138.3, 131.2, 123.6, 122.0, 120.7, 43.4, 36.6, 28.5. HRMS (ESI) calcd for $\text{C}_{17}\text{H}_{21}\text{N}$ [$\text{M}+\text{H}$] 240.1708, found 240.1925.



15c-Z: Yield 73%. White oil. ^1H NMR (500 MHz, Chloroform-*d*) δ 8.64 – 8.39 (m, 2H), 7.88 – 7.48 (m, 1H), 7.27 (dd, $J = 7.8, 4.7$ Hz, 1H), 6.35 (d, J

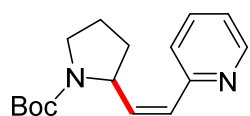
= 11.6 Hz, 1H), 5.74 (t, $J = 10.6$ Hz, 1H), 4.75 – 4.56 (m, 1H), 3.56 – 3.36 (m, 2H), 2.34 – 2.07 (m, 2H), 1.98 – 1.78 (m, 2H), 1.60 – 1.12 (m, 9H). ^{13}C NMR (126 MHz, CDCl_3) δ 154.7, 149.7,

147.9, 137.4, 135.9, 132.8, 124.2, 123.3, 79.5, 54.9, 46.7, 34.0, 28.5, 24.0. Characterization data matched that reported in the literature.



16c-E: Yield 22%. White oil. ^1H NMR (500 MHz, Chloroform-*d*) δ 8.57 (s, 1H), 8.50 – 8.40 (m, 1H), 7.75 – 7.53 (m, 1H), 7.28 – 7.23 (m, 1H), 6.52 – 5.64 (m, 2H), 4.71 – 4.28 (m, 1H), 3.56 – 3.33 (m, 2H), 2.30 – 2.04 (m, 2H),

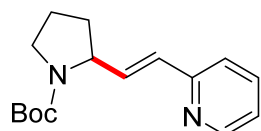
1.97 – 1.75 (m, 2H), 1.61 – 1.33 (m, 9H). ^{13}C NMR (126 MHz, CDCl_3) δ 154.7, 148.2, 147.9, 137.6, 133.7, 133.1, 125.9, 123.7, 79.5, 59.1, 46.5, 32.6, 28.6, 23.2. Characterization data matched that reported in the literature.



16c-Z: Yield 69%. White oil. ^1H NMR (500 MHz, Chloroform-*d*) δ 8.57 (d, $J = 4.9$ Hz, 1H), 7.86 – 7.56 (m, 2H), 7.22 – 7.05 (m, 1H), 6.48 – 6.32 (m,

1H), 6.03 – 5.74 (m, 1H), 5.50 – 5.25 (m, 1H), 3.58 – 3.39 (m, 2H), 2.40 – 2.31 (m, 1H), 1.96 – 1.77 (m, 2H), 1.55 – 1.15 (m, 9H). ^{13}C NMR (126 MHz, CDCl_3) δ 154.9, 149.1, 139.9, 136.2, 134.3, 126.6, 124.1, 123.3, 121.4, 79.2, 64.1, 63.8, 56.0, 55.3, 47.4, 46.7, 28.4, 24.6, 24.1.

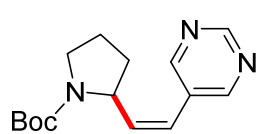
Characterization data matched that reported in the literature.



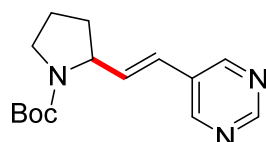
16c-E: Yield 18%. White oil. ^1H NMR (500 MHz, Chloroform-*d*) δ 8.71 – 8.60 (m, 1H), 8.16 (d, $J = 8.5$ Hz, 1H), 7.72 – 7.54 (m, 2H), 7.47 – 7.30 (m,

1H), 6.85 – 6.64 (m, 1H), 4.62 – 4.50 (m, 1H), 3.57 – 3.33 (m, 2H), 2.23 – 2.09 (m, 1H), 2.01 – 1.86 (m, 3H), 1.50 – 1.35 (m, 9H). ^{13}C NMR (126 MHz, CDCl_3) δ 154.7, 154.0, 150.0, 137.1, 124.5, 124.0, 123.2, 123.1, 79.8, 59.0, 58.7, 46.9, 46.5, 32.3, 31.4, 28.6, 24.0, 23.2.

Characterization data matched that reported in the literature.

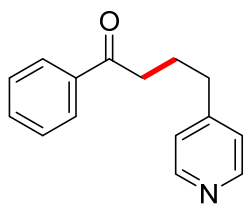


17c-Z: Yield 76%. White oil. ^1H NMR (500 MHz, Chloroform-*d*) δ 9.07 (s, 1H), 8.90 – 8.56 (m, 2H), 6.29 (d, J = 11.7 Hz, 1H), 5.86 (t, J = 10.5 Hz, 1H), 4.66 – 4.48 (m, 1H), 3.60 – 3.35 (m, 2H), 2.30 – 2.04 (m, 1H), 2.01 – 1.74 (m, 3H), 1.57 – 1.14 (m, 9H). ^{13}C NMR (126 MHz, CDCl_3) δ 156.8, 156.5, 156.3, 154.5, 139.7, 130.8, 121.0, 120.5, 79.7, 55.0, 54.7, 47.1, 46.7, 33.9, 33.3, 28.5, 24.5, 24.0. Characterization data matched that reported in the literature.

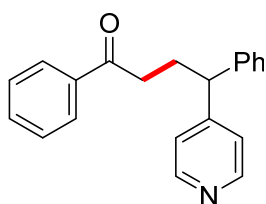


17c-E: Yield 15%. White oil. ^1H NMR (500 MHz, Chloroform-*d*) δ 9.09 (s, 1H), 8.76 (s, 2H), 6.47 – 6.26 (m 2H), 4.60 – 4.38 (m, 1H), 3.54 – 3.35 (m, 2H), 2.21 – 2.04 (m, 1H), 1.99 – 1.74 (m, 3H), 1.44 (s, 9H). ^{13}C NMR (126 MHz, CDCl_3) δ 157.0, 156.6, 154.7, 154.3, 136.1, 130.9, 122.3, 79.7, 58.9, 58.8, 46.9, 46.5, 32.5, 31.8, 28.6, 24.0, 23.2. Characterization data matched that reported in the literature.

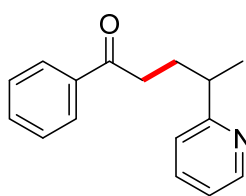
General procedure for reductive cross-coupling of aryl bromomethyl ketones with vinylpyridines. Aryl bromomethyl ketones (0.20 mmol, 2.0 equiv), vinyl-pyridine (0.10 mmol, 1.0 equiv), Hantzsch ester (0.20 mmol, 2.0 equiv), and **1**-OTf-Ir (0.50 μmol , 0.5 mol%, based on Lewis acid site) were mixed in dry CH_3CN (0.5 mL) in a closable flask. The resulting mixture was stirred under blue LED irradiation at room temperature in an N_2 atmosphere for 6 hours. After the reaction, the solvent was removed under vacuum. The residue was then subjected to column chromatography on silica gel using *n*-hexane, ethyl acetate and triethylamine as eluent to give products **18c-22c**.



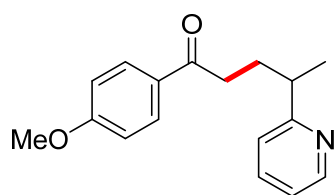
18c: Yield 67%. White solid. ^1H NMR (500 MHz, Chloroform-*d*) δ 8.51 (d, $J = 4.7$ Hz, 2H), 7.96 – 7.89 (m, 2H), 7.57 (t, $J = 7.4$ Hz, 1H), 7.46 (t, $J = 7.7$ Hz, 2H), 7.17 (d, $J = 5.6$ Hz, 2H), 3.00 (t, $J = 7.1$ Hz, 2H), 2.77 – 2.70 (m, 2H), 2.11 (dt, $J = 14.7, 7.2$ Hz, 2H). ^{13}C NMR (126 MHz, CDCl_3) δ 199.6, 151.4, 149.5, 136.9, 133.3, 128.8, 128.1, 124.2, 37.5, 34.6, 24.5. HRMS (ESI) calcd for $\text{C}_{15}\text{H}_{15}\text{NO}$ [$\text{M}+\text{H}$] 226.1187, found 226.1325.



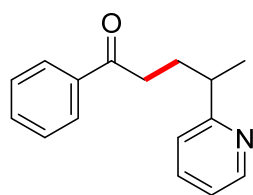
19c: Yield 53%. White solid. ^1H NMR (500 MHz, Chloroform-*d*) δ 8.51 (d, $J = 5.5$ Hz, 2H), 7.88 – 7.82 (m, 2H), 7.54 (t, $J = 7.4$ Hz, 1H), 7.42 (t, $J = 7.7$ Hz, 2H), 7.35 – 7.29 (m, 2H), 7.26 – 7.21 (m, 5H), 4.04 (t, $J = 7.9$ Hz, 1H), 2.94 (t, $J = 7.3$ Hz, 2H), 2.58 – 2.46 (m, 2H). ^{13}C NMR (126 MHz, CDCl_3) δ 199.5, 154.2, 149.6, 142.3, 136.9, 133.3, 129.1, 128.8, 128.1, 128.1, 127.2, 123.5, 50.0, 36.5, 29.1. Characterization data matched that reported in the literature.



20c: Yield 84%. White oil. ^1H NMR (500 MHz, Chloroform-*d*) δ 8.56 (d, $J = 4.8$ Hz, 1H), 7.87 (d, $J = 7.7$ Hz, 2H), 7.62 (t, $J = 8.0$ Hz, 1H), 7.52 (t, $J = 7.5$ Hz, 1H), 7.41 (t, $J = 7.7$ Hz, 2H), 7.17 (d, $J = 7.9$ Hz, 1H), 7.15 – 7.09 (m, 1H), 3.06 – 2.98 (m, 1H), 2.96 – 2.81 (m, 2H), 2.26 – 2.02 (m, 2H), 1.35 (d, $J = 6.8$ Hz, 3H). ^{13}C NMR (126 MHz, CDCl_3) δ 200.3, 165.5, 148.9, 137.1, 137.0, 133.0, 128.6, 128.2, 122.1, 121.6, 41.3, 36.7, 31.4, 21.2. Characterization data matched that reported in the literature.



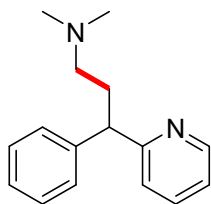
21c: Yield 78%. White oil. ^1H NMR (500 MHz, Chloroform-*d*) δ 8.55 (d, $J = 4.0$ Hz, 1H), 7.85 (d, $J = 8.9$ Hz, 2H), 7.60 (td, $J = 7.7, 1.9$ Hz, 1H), 7.16 (d, $J = 7.9$ Hz, 1H), 7.11 (ddd, $J = 7.5, 4.9, 1.2$ Hz, 1H), 6.88 (d, $J = 8.9$ Hz, 2H), 3.83 (s, 3H), 3.03 – 2.94 (m, 1H), 2.90 – 2.73 (m, 2H), 2.22 – 2.00 (m, 2H), 1.34 (d, $J = 6.9$ Hz, 3H). ^{13}C NMR (126 MHz, CDCl_3) δ 199.0, 165.7, 163.4, 149.3, 136.7, 130.4, 130.1, 122.0, 121.5, 113.7, 55.5, 41.6, 36.4, 31.7, 21.2. HRMS (ESI) calcd for $\text{C}_{17}\text{H}_{19}\text{NO}_2$ [$\text{M}+\text{H}$] 270.1445, found 270.1669.



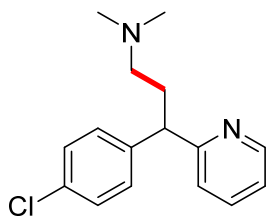
22c: Yield 76%. White solid. ^1H NMR (500 MHz, Chloroform-*d*) δ 8.58 (d, $J = 4.9$ Hz, 1H), 8.37 (s, 1H), 7.97 (d, $J = 8.7$ Hz, 1H), 7.91 (d, $J = 8.2$ Hz, 1H), 7.85 (d, $J = 8.6$ Hz, 2H), 7.63 (t, $J = 7.5$ Hz, 1H), 7.57 (t, $J = 7.5$ Hz, 1H), 7.53 (t, $J = 7.6$ Hz, 1H), 7.21 (d, $J = 7.9$ Hz, 1H), 7.15 (dd, $J = 7.6, 4.9$ Hz, 1H), 3.08 – 2.96 (m, 3H), 2.31 – 2.10 (m, 2H), 1.38 (d, $J = 6.9$ Hz, 3H). ^{13}C NMR (126 MHz, CDCl_3) δ 200.3, 165.6, 149.2, 136.9, 135.6, 134.3, 132.6, 129.8, 129.7, 128.5, 127.9, 126.8, 124.0, 122.1, 121.6, 41.5, 36.8, 31.7, 21.3. HRMS (ESI) calcd for $\text{C}_{20}\text{H}_{19}\text{NO}$ [$\text{M}+\text{H}$] 290.1500, found 290.1650.

Synthesis of Pheniramine and Chlorpheniramine. Fresh prepared *N*-hydroxyphthalimide ester (0.50 mmol, 5.0 equiv), vinylpyridine (0.10 mmol, 1.0 equiv), Hantzsch ester (0.50 mmol, 5.0 equiv), and **1**-OTf-Ir (0.50 μmol , 0.5 mol%, based on Lewis acid site) were mixed in dry CH_3CN (0.5 mL) in a closable flask. The resulting mixture was stirred under blue LED irradiation at room temperature in an N_2 atmosphere for 6 hours. After the reaction, the solvent was removed under vacuum. The residue was then subjected to column chromatography

on silica gel using *n*-hexane, ethyl acetate and triethylamine as eluent to give the products Pheniramine and Chlorpheniramine.



Pheniramine: Yield 38%. White oil. ^1H NMR (500 MHz, Chloroform-*d*) δ 8.56 (dd, $J = 4.9, 0.9$ Hz, 1H), 7.55 (t, $J = 7.7$ Hz, 1H), 7.34 (d, $J = 7.8$ Hz, 2H), 7.28 (t, $J = 7.6$ Hz, 2H), 7.18 (dd, $J = 17.1, 8.0$ Hz, 2H), 7.11 – 7.06 (m, 1H), 4.15 (t, $J = 6.3$ Hz, 1H), 2.55 – 2.45 (m, 1H), 2.41 – 2.19 (m, 9H). ^{13}C NMR (126 MHz, CDCl_3) δ 149.4, 136.6, 128.7, 128.1, 126.7, 123.0, 121.5, 57.8, 51.4, 45.3, 32.6.



Chlorpheniramine: Yield 36%. White oil. ^1H NMR (500 MHz, Chloroform-*d*) δ 8.55 (d, $J = 4.1$ Hz, 1H), 7.55 (td, $J = 7.7, 1.7$ Hz, 1H), 7.33 – 7.21 (m, 4H), 7.14 (d, $J = 7.8$ Hz, 1H), 7.09 (dd, $J = 7.1, 5.1$ Hz, 1H), 4.12 (t, $J = 7.2$ Hz, 1H), 2.47 – 2.37 (m, 1H), 2.19 (m, 9H). ^{13}C NMR (126 MHz, CDCl_3) δ 163.2, 149.5, 142.3, 136.6, 132.3, 129.5, 128.7, 122.9, 121.6, 57.8, 50.7, 45.6, 33.0.

4.4.5 Time-dependent Experiment

Time-dependent experiment 1 (T1). Pentanyl *N*-hydroxyphthalimide ester (52.3 mg, 0.20 mmol, 2.0 equiv), 4-vinylpyridine (10.5 mg, 0.10 mmol, 1.0 equiv), Hantzsch ester (50.7 mg, 0.20 mmol, 2.0 equiv), and **1**-OTf-Ir (0.50 μmol , 0.5 mol%, based on Lewis acid site) were mixed in dry CH_3CN (0.5 mL) in a closable flask. The resulting mixture was stirred under blue LED irradiation at room temperature in an N_2 atmosphere for 6 hours. The reaction progress was tracked by GC-MS every two hours.

Time-dependent experiment 2 (T2). The reaction procedure is similar to that of **T1**. The only difference is that **1**-OTf-Ir catalyst was replaced by **1**-OTf catalyst.

Time-dependent experiment 3 (T3). The reaction procedure is similar to that of **T1**. The only difference is that **1-OTf-Ir** catalyst was replaced by **1-OH-Ir** catalyst.

4.4.6 Synthesis of **1-OTf-Ir-high** and **1-OTf-Ir-low**

Preparation of 1-OTf-Ir-high. In a N₂-filled glovebox, **1-OTf** (0.05 mmol of bpy) was weighed out in a 75 mL high pressure glass vessel. 20 mL of [Ir(ppy)₂Cl]₂ solution in DMF (10 mM) was then added. The mixture was stirred at 110 °C for 3 days. The resultant solid was freeze-dried. ICP-MS analysis showed an Al/Ir molar ratio of ~5.5:1. Meanwhile, ¹H NMR spectrum of digested **1-OTf-Ir-high** indicated the ratio between vacant dc bpy and metalated dc bpy is ~3.6:1 (**Figure 4-12**). Based on both ICP-MS and ¹H NMR analysis, we concluded the chemical formula of **1-OTf-Ir-high** to be Al(OH)(dc bpy)_{0.63}[L₁]_{0.17}(OTf)₄.

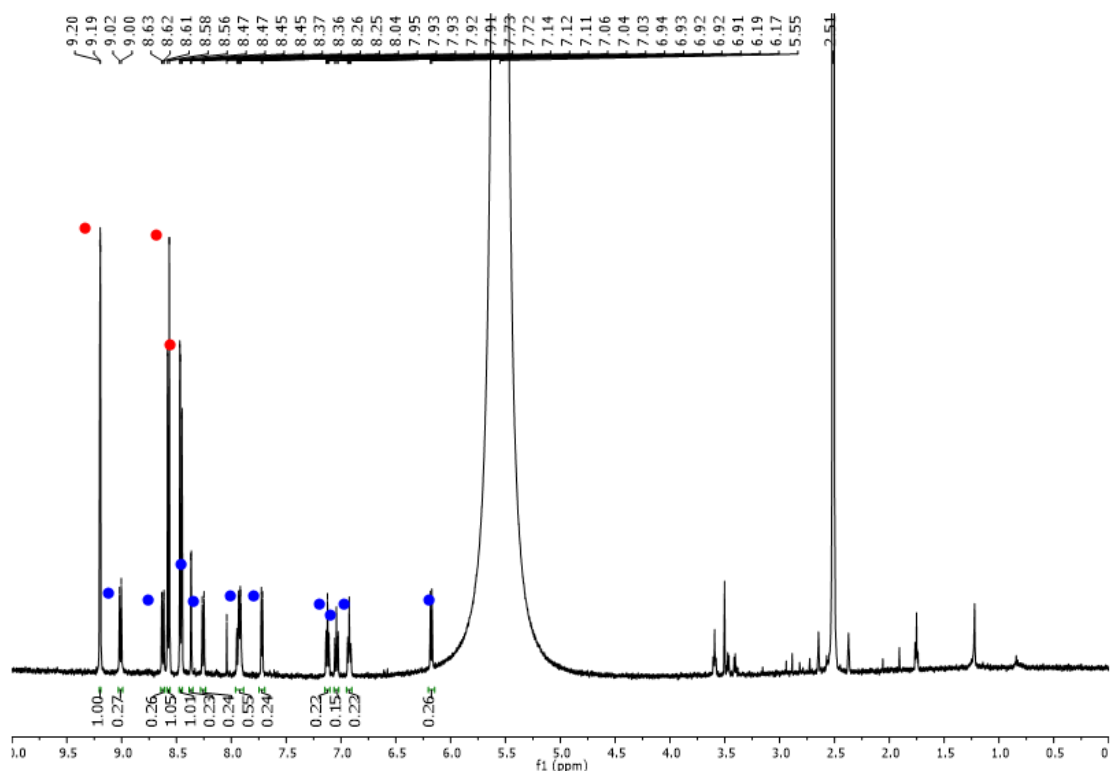


Figure 4-12. ¹H NMR spectrum of digested **1-OTf-Ir-high** in DMSO-*d*₆. Red circles correspond to dc bpy ligands, while blue circles correspond to L₁ ligands. Reprinted with permission from *Journal of the American Chemical Society*, **2020**, 142, 8602-8607. Copyright 2020 American Chemical Society.

Preparation of 1-OTf-Ir-low. In a N₂-filled glovebox, 1-OTf (0.1 mmol of bpy) was weighed out in a 75 mL high pressure glass vessel. 5 mL of [Ir(ppy)₂Cl]₂ solution in DMF (10 mM) was then added. The mixture was stirred at 80 °C for 3 days. The bright-orange solid was then centrifuged and washed with DMF three times, THF three time, and benzene three times. The resultant solid was freeze-dried and stored in a glovebox for further use. ICP-MS analysis showed an Al/Ir molar ratio of ~21.2:1, indicating an Ir loading of 4.5%. In addition, ¹H NMR spectrum of digested 1-OTf-Ir-low indicated the ratio between vacant dcbpy and metalated dcbpy is ~16.6:1 (Figure 4-13). Based on both ICP-MS and ¹H NMR analysis, we concluded the chemical formula of 1-OTf-Ir-low to be Al(OH)(dcbpy)_{0.75}[L₁]_{0.05}(OTf)₄.

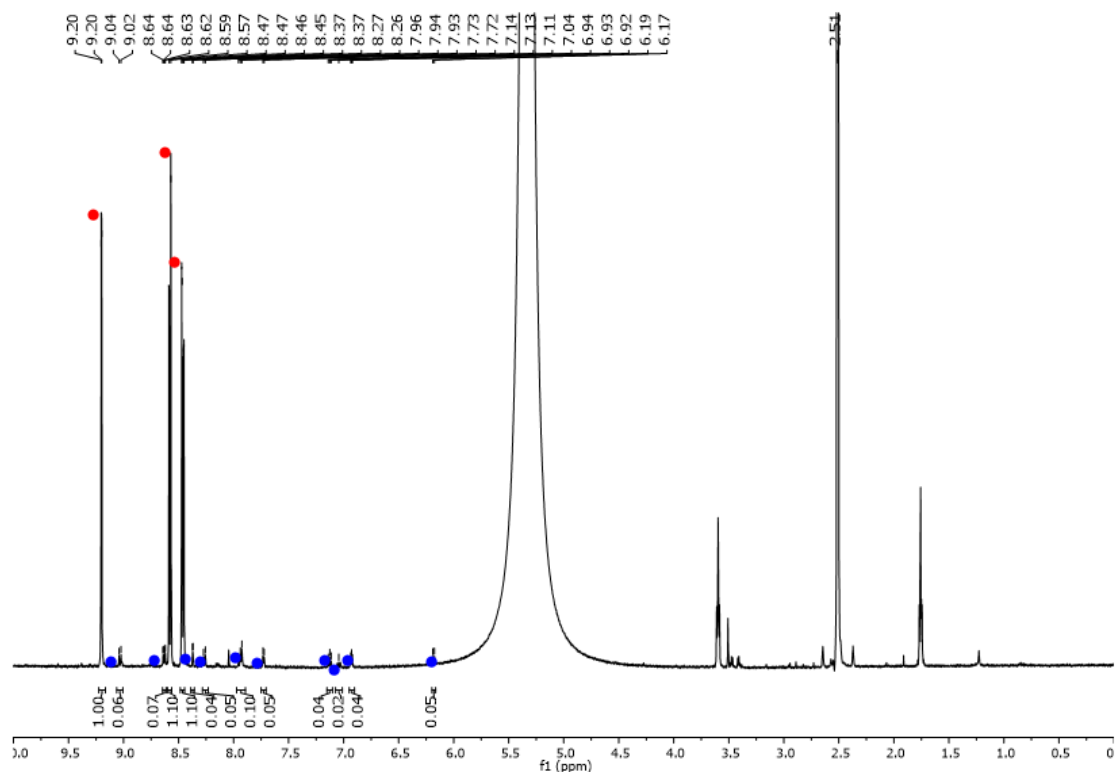


Figure 4-13. ¹H NMR spectrum of digested 1-OTf-Ir-low in DMSO-*d*₆. Red circles correspond to dcbpy ligands, while blue circles correspond to L₁ ligands. Reprinted with permission from *Journal of the American Chemical Society*, 2020, 142, 8602-8607. Copyright 2020 American Chemical Society.

4.4.7 Synthesis of 1-Ir and 1-OH-Ir

In a N₂-filled glovebox, **1** or **1-OH** (0.1 mmol of bpy) was weighed out in a 75 mL high pressure glass vessel. 20 mL of [Ir(ppy)₂Cl]₂ solution in DMF (10 mM) was then added. The mixture was stirred at 100 °C for 3 days. The resultant solid was then centrifuged and washed with DMF three times, THF three times, and benzene three times. The resultant solid (**1-Ir** or **1-OH-Ir**) was freeze-dried and then stored in a glovebox for further use. The crystallinity of both **1-Ir** and **1-OH-Ir** were confirmed by PXRD analysis (**Figure 4-14**).

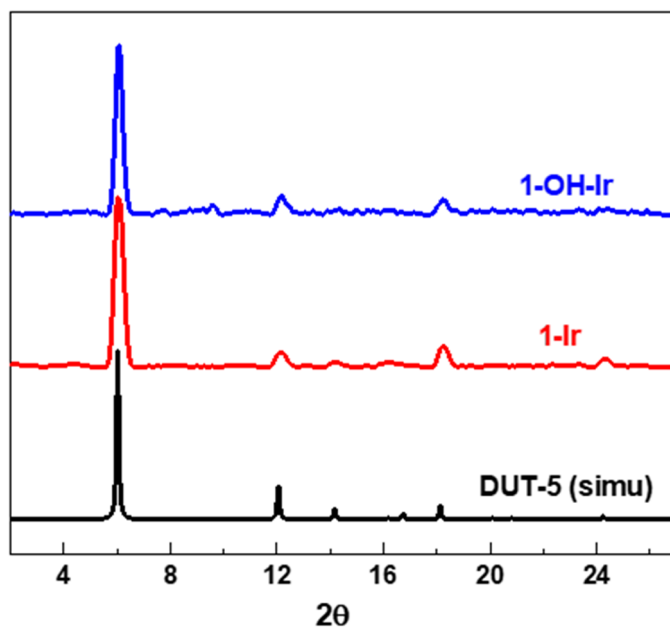


Figure 4-14. PXRD patterns of **1-Ir** and **1-OH-Ir** in comparison to the simulated pattern for DUT-5. Reprinted with permission from *Journal of the American Chemical Society*, **2020**, 142, 8602-8607. Copyright 2020 American Chemical Society.

¹H NMR spectrum of digested **1-OH-Ir** indicated the ratio between free dcbpy and metalated dcbpy is ~7.1:1 (**Figure 4-15**), corresponding to an Ir loading of 9.8 mol% w.r.t. Al site. On the other hand, ¹H NMR spectrum of digested **1-Ir** showed two sets of peaks assignable to dcbpy and pdac ligands, respectively, with only negligible peaks of L₁ ligands (**Figure 4-16**).

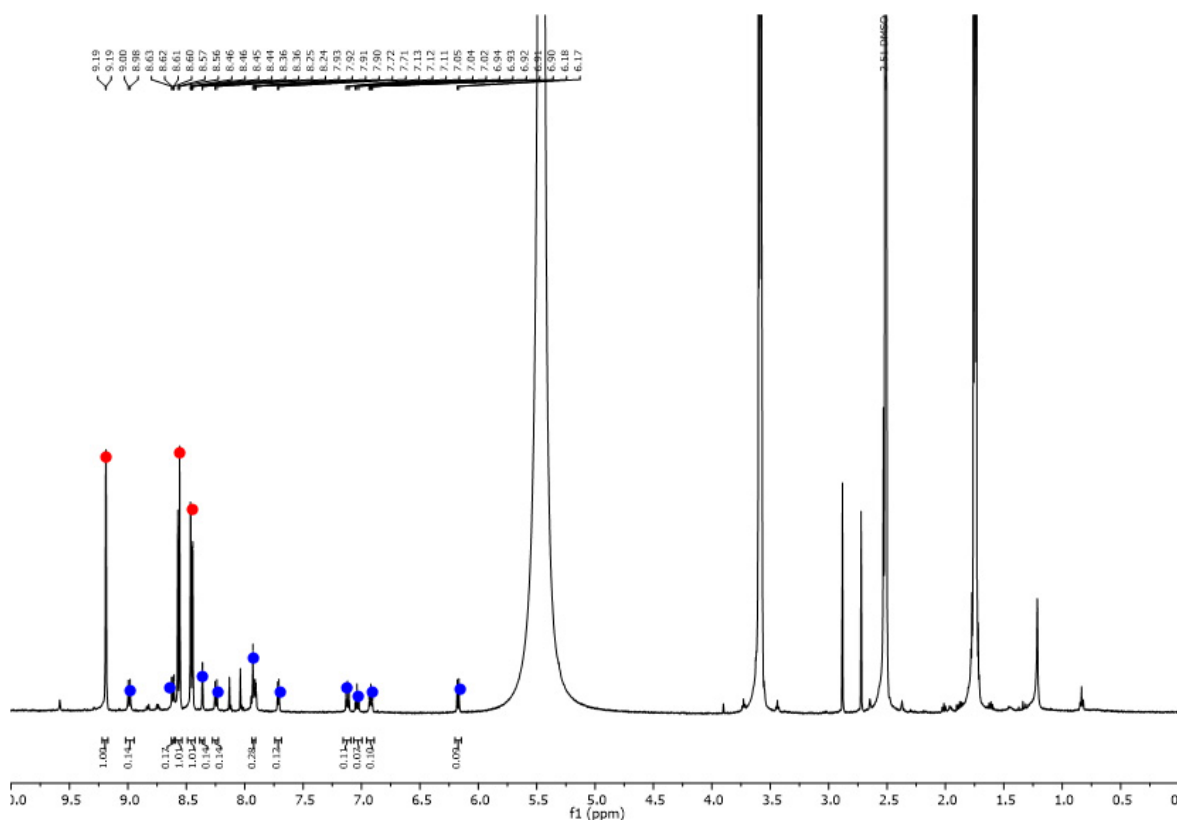


Figure 4-15. ^1H NMR spectrum of digested **1-OH-Ir** in $\text{DMSO-}d_6$. Red circles correspond to dcbpy ligands, while blue circles correspond to L_1 ligands. Reprinted with permission from *Journal of the American Chemical Society*, **2020**, 142, 8602-8607. Copyright 2020 American Chemical Society.

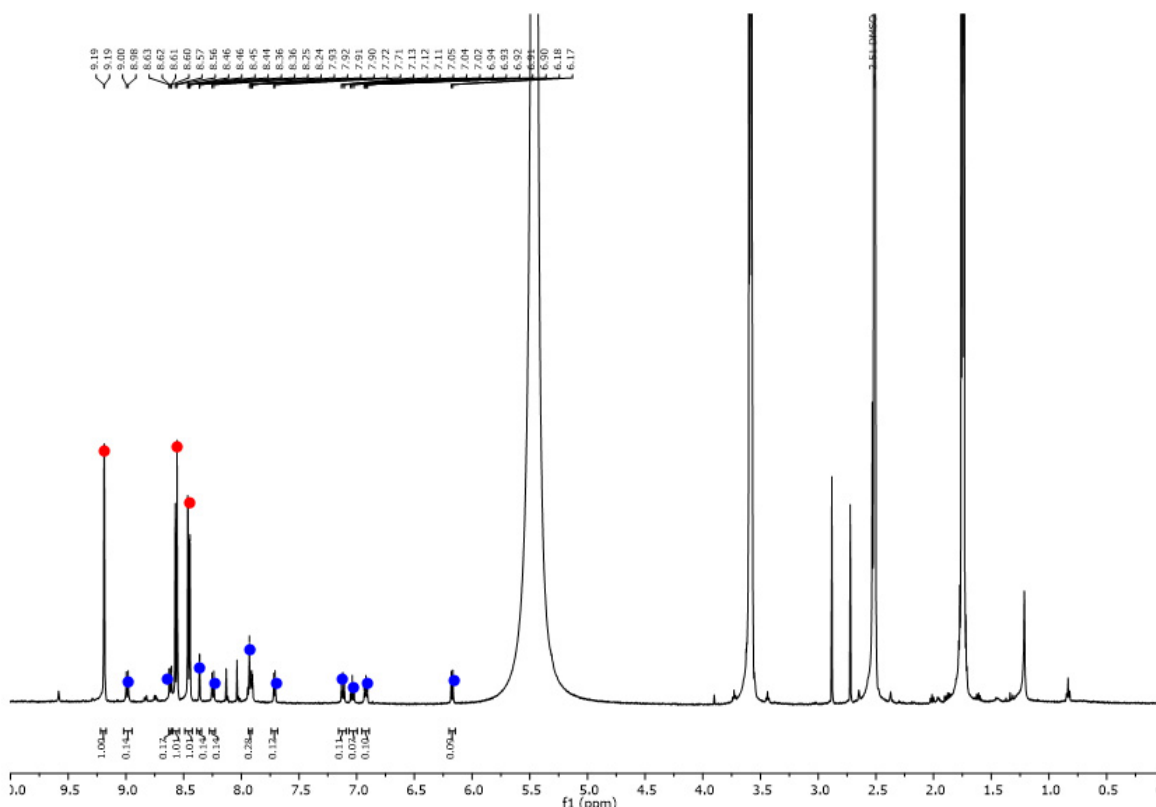
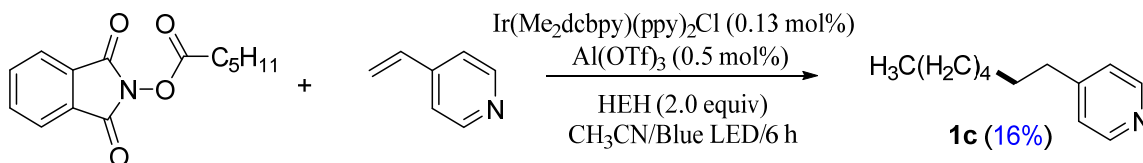


Figure 4-16. ^1H NMR spectrum of digested **1-Ir** in $\text{DMSO-}d_6$. Red circles correspond to dcbpy ligands and blue circles correspond to pdac ligands. Only negligible peaks of L_1 ligands are observed. Reprinted with permission from *Journal of the American Chemical Society*, **2020**, 142, 8602-8607. Copyright 2020 American Chemical Society.

4.4.8 Control Experiment

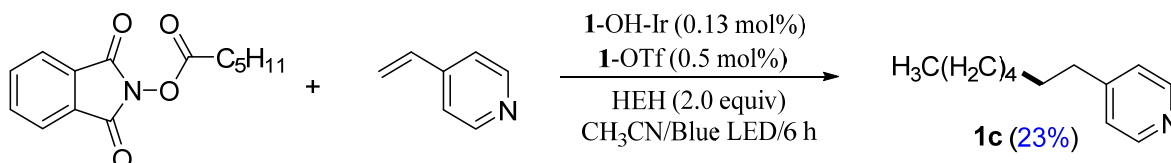
Homogeneous control. Pentan-1-yl *N*-hydroxyphthalimide ester (52.3 mg, 0.20 mmol, 2.0 equiv), 4-vinylpyridine (10.5 mg, 0.10 mmol, 1.0 equiv), Hantzsch ester (50.7 mg, 0.20 mmol, 2.0 equiv), H_2L_1 (0.13 μmol , 0.13 mol%) and $\text{Al}(\text{OTf})_3$ (0.50 μmol , 0.5 mol%) were mixed in dry CH_3CN (0.5 mL) in a closable flask. The resulting mixture was stirred under blue LED irradiation at room temperature in an N_2 atmosphere for 6 hours. After reaction, the suspension was filtered, and the filtrate was then subjected to GC-MS analysis. Product **1c** was detected in 16% yield (Scheme 4-5).

Scheme 4-5. Homogeneous control with Ir(Me₂dc bpy)(ppy)₂Cl and Al(OTf)₃.



Control reaction catalyzed by a mixture of 1-OTf and 1-OH-Ir. Pentanoyl *N*-hydroxyphthalimide ester (52.3 mg, 0.20 mmol, 2.0 equiv), 4-vinylpyridine (10.5 mg, 0.10 mmol, 1.0 equiv), Hantzsch ester (50.7 mg, 0.20 mmol, 2.0 equiv), 1-OH-Ir (0.13 μmol, 0.13 mol% based on Ir site) and 1-OTf (0.50 μmol, 0.5 mol% based on Lewis acid site) were mixed in dry CH₃CN (0.5 mL) in a closable flask. The resulting mixture was stirred under blue LED irradiation at room temperature in an N₂ atmosphere for 6 hours. After reaction, the suspension was filtered, and the filtrate was then subjected to GC-MS analysis. Product **1c** was detected in 23% yield (**Scheme 4-6**).

Scheme 4-6. Control reaction catalyzed by 1-OTf and 1-OH-Ir.



4.4.9 NMR Spectra

The NMR spectra for compounds **1c-22c**, Pheniramine, and Chlorpheniramine can be found in the Supporting Information of **Metal-Organic Framework with Dual Active Sites in Engineered Mesopores for Bioinspired Synergistic Catalysis**.

Link: https://pubs.acs.org/doi/suppl/10.1021/jacs.0c02966/suppl_file/ja0c02966_si_001.pdf.

4.5 References

- (1) Kiuru, P.; Yli-Kauhaluoma, J., Pyridine and Its Derivatives. *Heterocycles in Natural Product Synthesis* 2011, 267-297.
- (2) Thiel, O., *Heterocyclic Chemistry in Drug Discovery*. Edited by Jie Jack Li. *Angewandte Chemie International Edition* 2013, 52 (51), 13515-13515.
- (3) Goetz, A. E.; Garg, N. K., Regioselective reactions of 3,4-pyridynes enabled by the aryne distortion model. *Nature Chemistry* **2013**, 5 (1), 54-60.
- (4) Vitaku, E.; Smith, D. T.; Njardarson, J. T., Analysis of the Structural Diversity, Substitution Patterns, and Frequency of Nitrogen Heterocycles among U.S. FDA Approved Pharmaceuticals. *Journal of Medicinal Chemistry* **2014**, 57 (24), 10257-10274.
- (5) Seregin, I. V.; Gevorgyan, V., Direct transition metal-catalyzed functionalization of heteroaromatic compounds. *Chemical Society Reviews* **2007**, 36 (7), 1173-1193.
- (6) Feuerstein, M.; Doucet, H.; Santelli, M., Efficient coupling of heteroaryl halides with arylboronic acids in the presence of a palladium–tetraphosphine catalyst. *Journal of Organometallic Chemistry* **2003**, 687 (2), 327-336.
- (7) Prier, C. K.; Rankic, D. A.; MacMillan, D. W. C., Visible Light Photoredox Catalysis with Transition Metal Complexes: Applications in Organic Synthesis. *Chemical Reviews* **2013**, 113 (7), 5322-5363.
- (8) Lee, K. N.; Lei, Z.; Ngai, M.-Y., β -Selective Reductive Coupling of Alkenylpyridines with Aldehydes and Imines via Synergistic Lewis Acid/Photoredox Catalysis. *Journal of the American Chemical Society* **2017**, 139 (14), 5003-5006.
- (9) Cao, K.; Tan, S. M.; Lee, R.; Yang, S.; Jia, H.; Zhao, X.; Qiao, B.; Jiang, Z., Catalytic Enantioselective Addition of Prochiral Radicals to Vinylpyridines. *Journal of the American Chemical Society* **2019**, 141 (13), 5437-5443.
- (10) Furukawa, H.; Cordova, K. E.; O’Keeffe, M.; Yaghi, O. M., The Chemistry and Applications of Metal-Organic Frameworks. *Science* **2013**, 341 (6149), 1230444.
- (11) Wen, R.; Guo, J.; Yu, A.; Zhai, J.; Wang, Z. L., Humidity-Resistive Triboelectric Nanogenerator Fabricated Using Metal Organic Framework Composite. *Advanced Functional Materials* **2019**, 29 (20), 1807655.
- (12) Lin, R.-B.; Xiang, S.; Xing, H.; Zhou, W.; Chen, B., Exploration of porous metal–organic frameworks for gas separation and purification. *Coordination Chemistry Reviews* **2019**, 378, 87-103.
- (13) Horcajada, P.; Gref, R.; Baati, T.; Allan, P. K.; Maurin, G.; Couvreur, P.; Férey, G.; Morris, R. E.; Serre, C., Metal–Organic Frameworks in Biomedicine. *Chemical Reviews* **2012**, 112 (2), 1232-1268.

- (14) Duan, X.; Chan, C.; Lin, W., Nanoparticle-Mediated Immunogenic Cell Death Enables and Potentiates Cancer Immunotherapy. *Angewandte Chemie International Edition* **2019**, *58* (3), 670-680.
- (15) Hu, Z.; Deibert, B. J.; Li, J., Luminescent metal–organic frameworks for chemical sensing and explosive detection. *Chemical Society Reviews* **2014**, *43* (16), 5815-5840.
- (16) Chueh, C.-C.; Chen, C.-I.; Su, Y.-A.; Konnerth, H.; Gu, Y.-J.; Kung, C.-W.; Wu, K. C. W., Harnessing MOF materials in photovoltaic devices: recent advances, challenges, and perspectives. *Journal of Materials Chemistry A* **2019**, *7* (29), 17079-17095.
- (17) Dan-Hardi, M.; Serre, C.; Frot, T.; Rozes, L.; Maurin, G.; Sanchez, C.; Férey, G., A new photoactive crystalline highly porous titanium (IV) dicarboxylate. *Journal of the American Chemical Society* **2009**, *131* (31), 10857-10859.
- (18) Jiao, L.; Wang, Y.; Jiang, H.-L.; Xu, Q., Metal–Organic Frameworks as Platforms for Catalytic Applications. *Advanced Materials* **2018**, *30* (37), 1703663.
- (19) Drake, T.; Ji, P.; Lin, W., Site Isolation in Metal–Organic Frameworks Enables Novel Transition Metal Catalysis. *Accounts of Chemical Research* **2018**, *51* (9), 2129-2138.
- (20) Huang, Y.-B.; Liang, J.; Wang, X.-S.; Cao, R., Multifunctional metal–organic framework catalysts: synergistic catalysis and tandem reactions. *Chemical Society Reviews* **2017**, *46* (1), 126-157.
- (21) Wu, C.-D.; Zhao, M., Incorporation of Molecular Catalysts in Metal–Organic Frameworks for Highly Efficient Heterogeneous Catalysis. *Advanced Materials* **2017**, *29* (14), 1605446.
- (22) Zhao, M.; Ou, S.; Wu, C.-D., Porous Metal–Organic Frameworks for Heterogeneous Biomimetic Catalysis. *Accounts of Chemical Research* **2014**, *47* (4), 1199-1207.
- (23) Nath, I.; Chakraborty, J.; Verpoort, F., Metal organic frameworks mimicking natural enzymes: a structural and functional analogy. *Chemical Society Reviews* **2016**, *45* (15), 4127-4170.
- (24) Ringe, D.; Petsko, G. A., How Enzymes Work. *Science* **2008**, *320* (5882), 1428.
- (25) Enzymes Are Wonderful Catalysts. *Introduction to Enzyme and Coenzyme Chemistry* **2012**, 26-49.
- (26) Pravda, L.; Berka, K.; Svobodová Vařeková, R.; Sehnal, D.; Banáš, P.; Laskowski, R. A.; Koča, J.; Otyepka, M., Anatomy of enzyme channels. *BMC Bioinformatics* **2014**, *15* (1), 379.
- (27) Structural Components of Enzymes. *Enzymes* **2000**, 42-75.
- (28) Koshland Jr, D. E., The Key–Lock Theory and the Induced Fit Theory. *Angewandte Chemie International Edition in English* **1995**, *33* (23-24), 2375-2378.

- (29) Senkovska, I.; Hoffmann, F.; Fröba, M.; Getzschmann, J.; Böhlmann, W.; Kaskel, S., New highly porous aluminium based metal-organic frameworks: Al(OH)(ndc) (ndc=2,6-naphthalene dicarboxylate) and Al(OH)(bpdc) (bpdc=4,4' -biphenyl dicarboxylate). *Microporous and Mesoporous Materials* **2009**, *122* (1), 93-98.
- (30) Bloch, E. D.; Britt, D.; Lee, C.; Doonan, C. J.; Uribe-Romo, F. J.; Furukawa, H.; Long, J. R.; Yaghi, O. M., Metal Insertion in a Microporous Metal–Organic Framework Lined with 2,2'-Bipyridine. *Journal of the American Chemical Society* **2010**, *132* (41), 14382-14384.
- (31) Song, Y.; Feng, X.; Chen, J. S.; Brzezinski, C.; Xu, Z.; Lin, W., Multistep Engineering of Synergistic Catalysts in a Metal–Organic Framework for Tandem C–O Bond Cleavage. *Journal of the American Chemical Society* **2020**.
- (32) Albalad, J.; Xu, H.; Gándara, F.; Haouas, M.; Martineau-Corcós, C.; Mas-Ballesté, R.; Barnett, S. A.; Juanhuix, J.; Imaz, I.; MasPOCH, D., Single-Crystal-to-Single-Crystal Postsynthetic Modification of a Metal–Organic Framework via Ozonolysis. *Journal of the American Chemical Society* **2018**, *140* (6), 2028-2031.
- (33) Guillerm, V.; Xu, H.; Albalad, J.; Imaz, I.; MasPOCH, D., Postsynthetic Selective Ligand Cleavage by Solid–Gas Phase Ozonolysis Fuses Micropores into Mesopores in Metal–Organic Frameworks. *Journal of the American Chemical Society* **2018**, *140* (44), 15022-15030.
- (34) Ji, P.; Feng, X.; Oliveres, P.; Li, Z.; Murakami, A.; Wang, C.; Lin, W., Strongly Lewis Acidic Metal–Organic Frameworks for Continuous Flow Catalysis. *Journal of the American Chemical Society* **2019**, *141* (37), 14878-14888.
- (35) Sprouse, S.; King, K. A.; Spellane, P. J.; Watts, R. J., Photophysical effects of metal-carbon σ bonds in ortho-metalated complexes of iridium(III) and rhodium(III). *Journal of the American Chemical Society* **1984**, *106* (22), 6647-6653.
- (36) Ohkubo, K.; Menon, S. C.; Orita, A.; Otera, J.; Fukuzumi, S., Quantitative Evaluation of Lewis Acidity of Metal Ions with Different Ligands and Counterions in Relation to the Promoting Effects of Lewis Acids on Electron Transfer Reduction of Oxygen. *The Journal of Organic Chemistry* **2003**, *68* (12), 4720-4726.
- (37) Trowbridge, A.; Reich, D.; Gaunt, M. J., Multicomponent synthesis of tertiary alkylamines by photocatalytic olefin-hydroaminoalkylation. *Nature* **2018**, *561* (7724), 522-527.
- (38) Cheng, W.-M.; Shang, R.; Fu, M.-C.; Fu, Y., Photoredox-Catalysed Decarboxylative Alkylation of N-Heteroarenes with N-(Acyloxy)phthalimides. *Chemistry – A European Journal* **2017**, *23* (11), 2537-2541.
- (39) Yang, H.; Wang, E.; Yang, P.; Lv, H.; Zhang, X., Pyridine-Directed Asymmetric Hydrogenation of 1,1-Diarylethenes. *Organic Letters* **2017**, *19* (19), 5062-5065.
- (40) Lobo Ferreira, A. I. M. C.; Rodrigues, A. S. M. C.; Villas, M.; Tojo, E.; Rebelo, L. P. N.; Santos, L. M. N. B. F., Crystallization and Glass-Forming Ability of Ionic Liquids: Novel Insights into Their Thermal Behavior. *ACS Sustainable Chemistry & Engineering* **2019**, *7* (3), 2989-2997.

- (41) Capaldo, L.; Fagnoni, M.; Ravelli, D., Vinylpyridines as Building Blocks for the Photocatalyzed Synthesis of Alkylpyridines. *Chemistry – A European Journal* **2017**, *23* (27), 6527-6530.
- (42) Schwarz, J.; König, B., Metal-free, visible-light-mediated, decarboxylative alkylation of biomass-derived compounds. *Green Chemistry* **2016**, *18* (17), 4743-4749.
- (43) Le, C.; Liang, Y.; Evans, R. W.; Li, X.; MacMillan, D. W. C., Selective sp³ C–H alkylation via polarity-match-based cross-coupling. *Nature* **2017**, *547* (7661), 79-83.
- (44) Gao, L.; Wang, G.; Cao, J.; Yuan, D.; Xu, C.; Guo, X.; Li, S., Organocatalytic decarboxylative alkylation of N-hydroxy-phthalimide esters enabled by pyridine-boryl radicals. *Chemical Communications* **2018**, *54* (82), 11534-11537.

Chapter 5. Titanium Hydroxide Secondary Building Units in Metal-Organic Frameworks Catalyze Hydrogen Evolution under Visible Light

5.1 Introduction

In Chapter 4, we discussed that metal-organic framework (MOF)-based multifunctional solid catalyst, **1**-OTf-Ir, efficiently photocatalyzed reductive cross-coupling reactions under blue LED light irradiation. This result suggests several advantages of MOF-based photocatalysts: close proximity between photosensitizers and catalytic sites facilitates multielectron transfer, well-defined structures provide a versatile platform for the incorporation of multiple active sites, and site-isolation avoids the quenching of reactive species. In addition to photocatalytic organic transformations, many photocatalytic small molecule transformations, including hydrogen evolution reaction (HER), water oxidation reaction (WOR), and CO₂ reduction reaction (CO₂RR) have received intense attention due to their importance to solar energy conversion, which has the potential to avert the depletion of fossil fuels and the rapid global climate change.¹⁻⁴

Visible light driven water splitting has long been considered as a promising pathway for clean and renewable hydrogen production and exhibits potential in replacing fossil fuels to address the global energy crisis.⁵ To date, titanium dioxide (TiO₂) has been most widely used as the photocatalytic materials for hydrogen production due to its outstanding stability, high activity, nontoxicity, and low cost characteristics.⁶⁻⁸ TiO₂-based materials with cocatalysts (Pt, Au, etc) or cocatalysts free systems were well established and demonstrated feasible hydrogen production. However, these photocatalysts are typically active only in the UV region (which just accounts for 3-5% of the total solar energy) owing to its wide HOMO-LUMO gap. The ubiquitous defects on the surface of TiO₂ make it difficult to study the catalytic mechanism at the molecular level.⁹⁻¹⁰ More recently, titanium-oxo clusters (TOCs) with well-defined structures have been studied for

photocatalytic hydrogen production.¹¹⁻¹³ However, the difficulty in incorporating efficient photosensitizers into these systems also leads to only UV-region absorption and limits the efficiency in hydrogen production process. Additionally, titanium complexes, such as titanium tetrachloride, have also been reported for photocatalytic HER.¹⁴⁻¹⁵ Their HER mechanism was well studied at the molecular level, but these homogeneous systems are limited by low stability, absorption in the UV spectrum, and the inability to recycle and reuse.

Over the past decade, titanium-based MOFs (Ti-MOFs) have been studied for artificial photosynthesis.¹⁶⁻¹⁸ For example, amino-functionalized Ti-MOFs have been used as light-harvesting antenna to drive photocatalytic HER by encapsulated Pt nanoparticles and molecular Co catalysts.¹⁹ However, as photosensitizers, Ti-MOFs are limited by low molar absorptivities, large HOMO-LUMO gaps, and relatively short excited state lifetimes. We surmised that synthetic tunability of MOFs could be leveraged to design new Ti-MOFs with much enhanced activities of and for discovering new fundamental insights into photocatalytic HER.

In this chapter, I will discuss the synthesis of two new MOFs, Ti₃-BPDC-Ir and Ti₃-BPDC-Ru, by doping [Ir(ppy)₂(dcbpy)]Cl (**L**₁, ppy = 2-phenylpyridine) or [Ru(bpy)₂(dcbpy)]Cl₂ (**L**₂, bpy = 2,2'-bipyridine,) photosensitizers into the Ti₃-BPDC (BPDC = biphenyl-4,4'-dicarboxylate) framework for efficient visible light-driven HER (**Figure 5-1**).²⁰⁻²¹ Experimental and computational studies reveal the catalytic HER pathway via electron injection into Ti^{IV}(OH)₂ SBUs to generate Ti^{III}-OH which is protonated and followed by proton-coupled electron transfer to afford the key Ti^{IV}-H intermediate. Protonation of the Ti^{IV}-H species produces hydrogen and regenerates catalytic Ti^{IV}₃(OH)₂ SBUs.

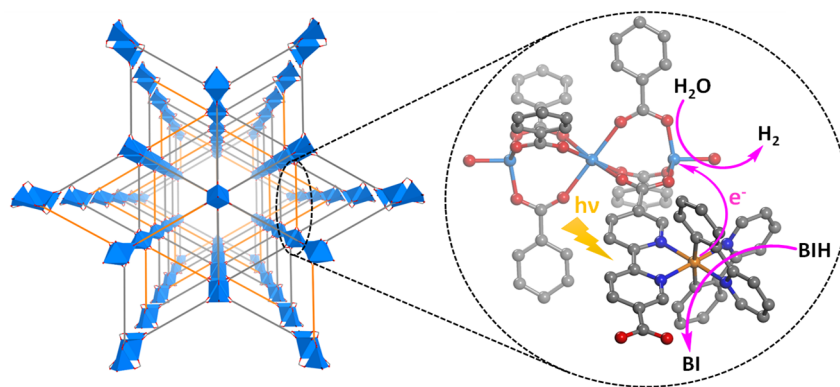


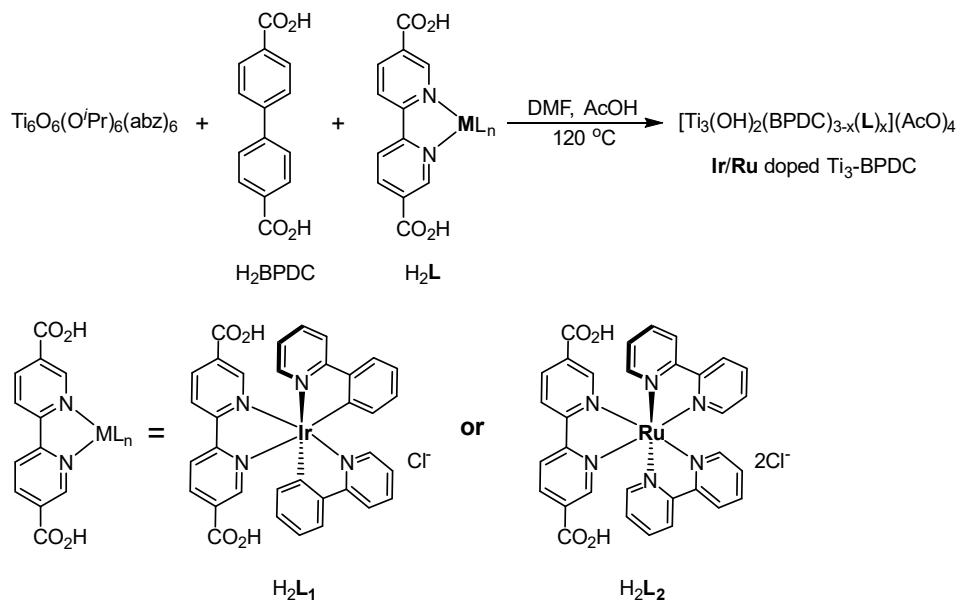
Figure 5-1. Schematic showing photocatalytic HER by $\text{Ti}_3\text{-BPDC-Ir}$ via electron injection from photo-reduced $[\text{Ir}^{\text{III}}(\text{ppy})_2(\text{dcbpy}^-)]^0$ ligands into $\text{Ti}_3(\text{OH})_2$ SBUs. Ti, Ir, O, and N atoms are shown in blue, gold, red, and mazarine, respectively. Reprinted with permission from *Journal of the American Chemical Society*, **2019**, 141, 12219-12223. Copyright 2019 American Chemical Society.

5.2 Results and Discussion

5.2.1 Synthesis of $\text{Ti}_3\text{-BPDC-Ir}$ and $\text{Ti}_3\text{-BPDC-Ru}$

$\text{Ti}_6\text{O}_6(\text{O}^i\text{Pr})_6(\text{abz})_6$ cluster (2.00 mg) (abz = 4-aminobenzoate),²² biphenyl-4,4'-dicarboxylic acid (3.30 mg), H_2L_1 (1.26 mg) or H_2L_2 (1.25 mg), glacial acetic acid (60 μL), and DMF (1.5 mL) were charged in a 4 mL Pyrex vial. The mixture was heated in a 120 $^\circ\text{C}$ oven for 3 days. After cooling to room temperature, gold-orange and deep-red crystalline solids of $\text{Ti}_3\text{-BPDC-Ir}$ and $\text{Ti}_3\text{-BPDC-Ru}$ were harvested, respectively. The resulting solid was recovered by centrifugation and then sequentially washed with DMF three times, with THF three times, and with benzene three times. The solid was then freeze-dried in benzene. The yields for $\text{Ti}_3\text{-BPDC-Ir}$ and $\text{Ti}_3\text{-BPDC-Ru}$ were $\sim 35\%$ and 46% , respectively. ICP-MS analysis of $\text{Ti}_3\text{-BPDC-Ir}$ showed a Ti/Ir ratio of 3.15, indicating about one Ir per Ti_3 node. ICP-MS analysis of $\text{Ti}_3\text{-BPDC-Ru}$ showed a Ti/Ru ratio of 4.82, indicating about 0.6 Ru per Ti_3 node.

Scheme 5-1. Schematic showing the synthesis of Ti₃-BPDC-Ir and Ti₃-BPDC-Ru. Reprinted with permission from *Journal of the American Chemical Society*, **2019**, 141, 12219-12223. Copyright 2019 American Chemical Society.



Optical imaging (**Figure 5-2**) and scanning electron microscopy (SEM) imaging (**Figure 5-3**) showed that both Ti₃-BPDC-Ir and Ti₃-BPDC-Ru adopted the same rhombic morphology as Ti₃-BPDC.

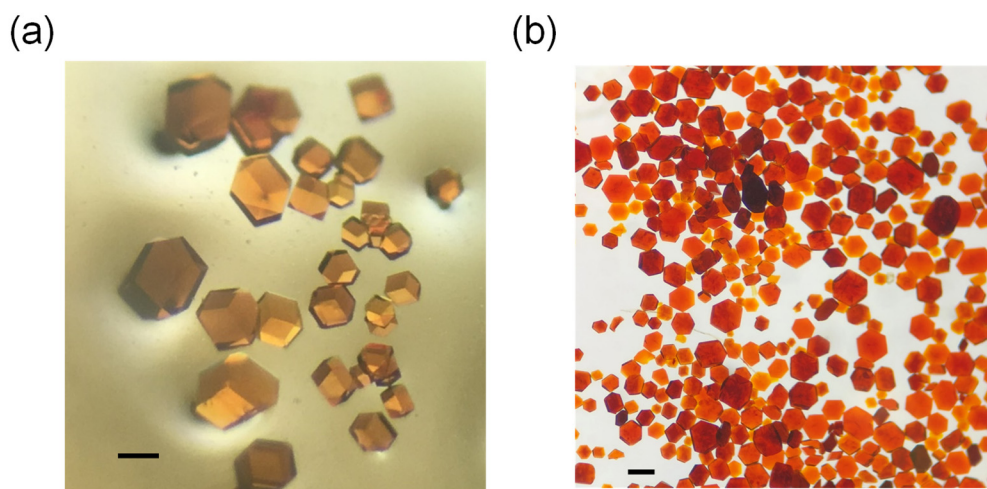


Figure 5-2. Optical photographs of (a) Ti₃-BPDC-Ir and (b) Ti₃-BPDC-Ru. Scale bar is 50 μm . Reprinted with permission from *Journal of the American Chemical Society*, **2019**, 141, 12219-12223. Copyright 2019 American Chemical Society.

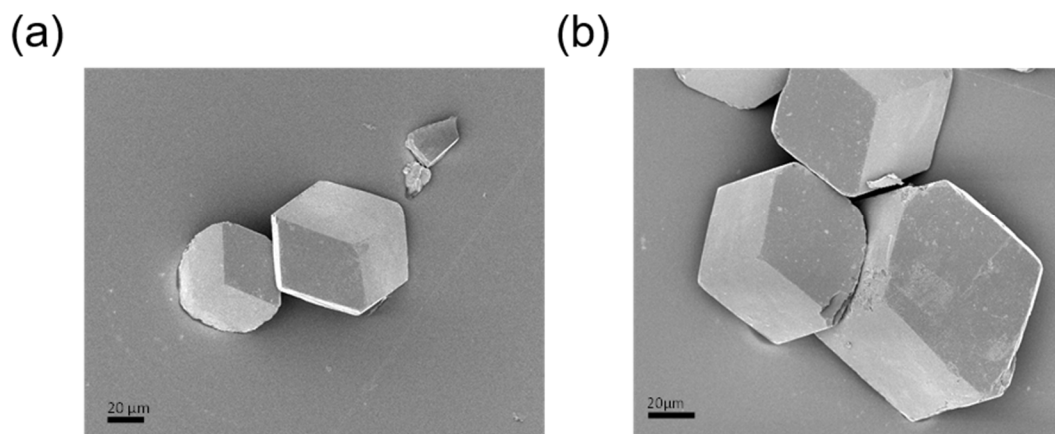


Figure 5-3. SEM image of (a) Ti₃-BPDC-Ir and (b) Ti₃-BPDC-Ru. Reprinted with permission from *Journal of the American Chemical Society*, **2019**, 141, 12219-12223. Copyright 2019 American Chemical Society.

Powder X-ray diffraction (PXRD) studies further revealed that Ti₃-BPDC-Ir and Ti₃-BPDC-Ru were highly crystalline and isostructural to Ti₃-BPDC (**Figure 5-4**).

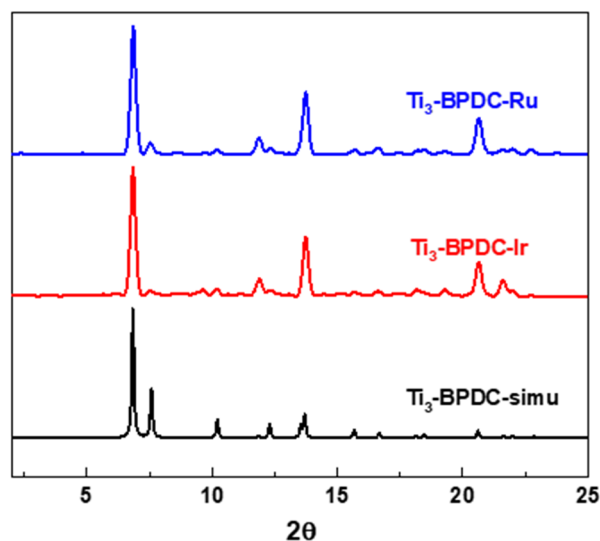


Figure 5-4. PXRD patterns of synthesized Ti₃-BPDC-Ir (red) and Ti₃-BPDC-Ru (blue) in comparison to the simulated Ti₃-BPDC pattern. Reprinted with permission from *Journal of the American Chemical Society*, **2019**, 141, 12219-12223. Copyright 2019 American Chemical Society.

5.2.2 ^1H NMR Analysis

^1H NMR Analysis of Digested $\text{Ti}_3\text{-BPDC-Ir}$ To determine the ratio of Ti and Ir in $\text{Ti}_3\text{-BPDC-Ir}$, 2.0 mg $\text{Ti}_3\text{-BPDC-Ir}$ was dried under vacuum and then digested in 50 μL D_3PO_4 , the mixture was then sonicated for 10 min, followed by addition of 500 μL DMSO-d_6 and 50 μL D_2O , and analyzed by ^1H NMR. The ratio of Ti and Ir was determined to be approximately 3:1 in molar ratio by comparing the peaks in each corresponding ligand in ^1H NMR analysis (**Figure 5-5**), which gave the chemical formula of $\text{Ti}_3(\text{OH})_2(\text{BPDC})_2(\text{L}_1)_1(\text{AcO})_4$, consistent to the ICP-MS analysis.

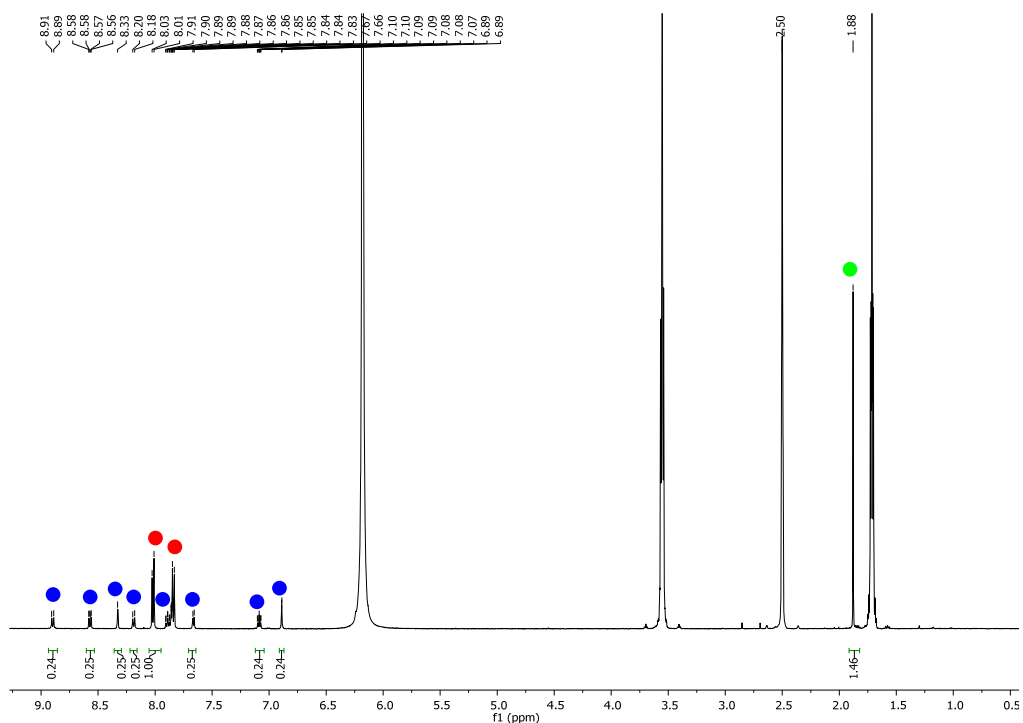


Figure 5-5. ^1H NMR spectra of digested $\text{Ti}_3\text{-BPDC-Ir}$ in DMSO-d_6 . Red, blue and green circles correspond to BPDC, L_1 and acetates, respectively. Reprinted with permission from *Journal of the American Chemical Society*, **2019**, 141, 12219-12223. Copyright 2019 American Chemical Society.

^1H NMR analysis of digested $\text{Ti}_3\text{-BPDC-Ru}$ To determine the ratio of Ti and Ru in $\text{Ti}_3\text{-BPDC-Ru}$, 3.0 mg $\text{Ti}_3\text{-BPDC-Ru}$ was dried under vacuum and then digested in 50 μL D_3PO_4 , the

mixture was then sonicated for 10 min, followed by adding 500 μL DMSO- d_6 and 50 μL D $_2$ O, and analyzed by ^1H NMR. The ratio of Ti and Ru was determined to be approximately 5:1 in molar ratio by comparing the peaks in each corresponding ligand in ^1H NMR analysis (**Figure 5-6**), which gave the chemical formula of $\text{Ti}_3(\text{OH})_2(\text{BPDC})_{2.4}(\text{L}2)_{0.6}(\text{AcO})_4$, consistent to the ICP-MS analysis.

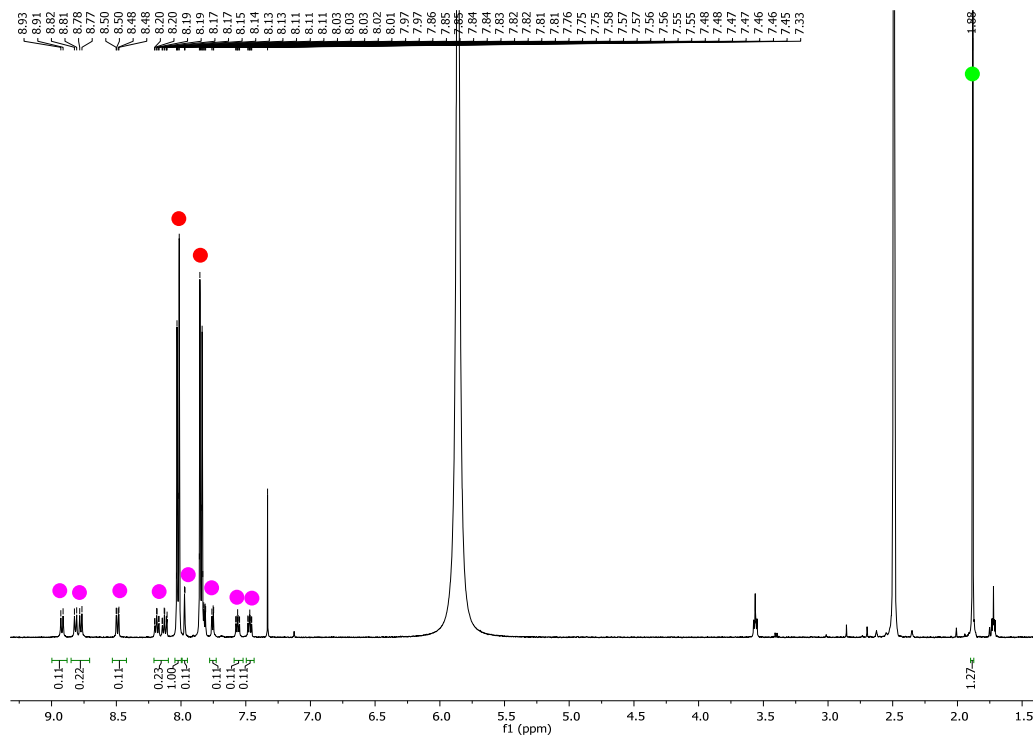


Figure 5-6. ^1H NMR spectra of digested Ti_3 -BPDC-Ru in DMSO- d_6 . Red, pink, and green circles correspond to BPDC, L $_2$ and acetates, respectively. Reprinted with permission from *Journal of the American Chemical Society*, **2019**, 141, 12219-12223. Copyright 2019 American Chemical Society.

5.2.3 Thermogravimetric Analysis

Thermogravimetric analysis of Ti_3 -BPDC-Ir The first weight loss (11.4%) in the 25 to 190 $^\circ\text{C}$ temperature range corresponds to the removal of adsorbed solvents in the pores of the MOF. The second weight loss (71.7%) in the 190-600 $^\circ\text{C}$ temperature range corresponds to

decomposition of the MOF to metal oxides, consistent with a calculated weight loss of 72.2% based on the conversion of $\text{Ti}_3(\text{OH})_2(\text{BPDC})_2(\text{L}_1)_1(\text{AcO})_4$ to $(\text{TiO}_2)_3(\text{IrO}_2)$ (**Figure 5-7**).

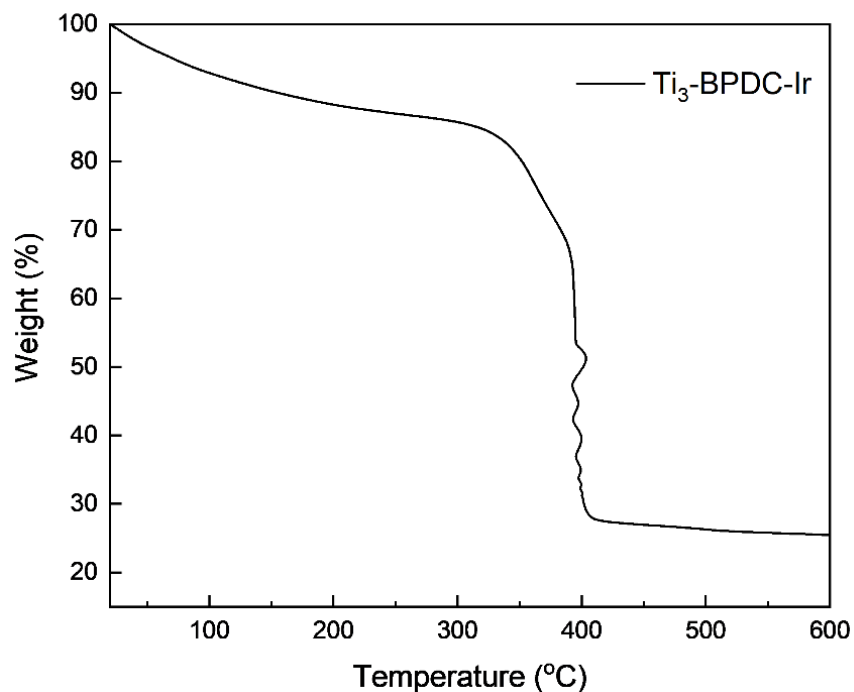


Figure 5-7. TGA curve of freshly prepared $\text{Ti}_3\text{-BPDC-Ir}$ in 25~600 °C range. Reprinted with permission from *Journal of the American Chemical Society*, **2019**, 141, 12219-12223. Copyright 2019 American Chemical Society.

Thermogravimetric analysis of $\text{Ti}_3\text{-BPDC-Ru}$ The first weight loss (14.8%) in the 25 to 250 °C temperature range corresponds to the removal of adsorbed solvents in the pores of the MOF. The second weight loss (77.5%) in the 250-600 °C temperature range corresponds to decomposition of the MOF to metal oxides, consistent with a calculated weight loss of 77.6% based on the conversion of $\text{Ti}_3(\text{OH})_2(\text{BPDC})_{2.4}(\text{L}_2)_{0.6}(\text{AcO})_4$ to $(\text{TiO}_2)_3(\text{RuO}_2)_{0.6}$ (**Figure 5-8**).

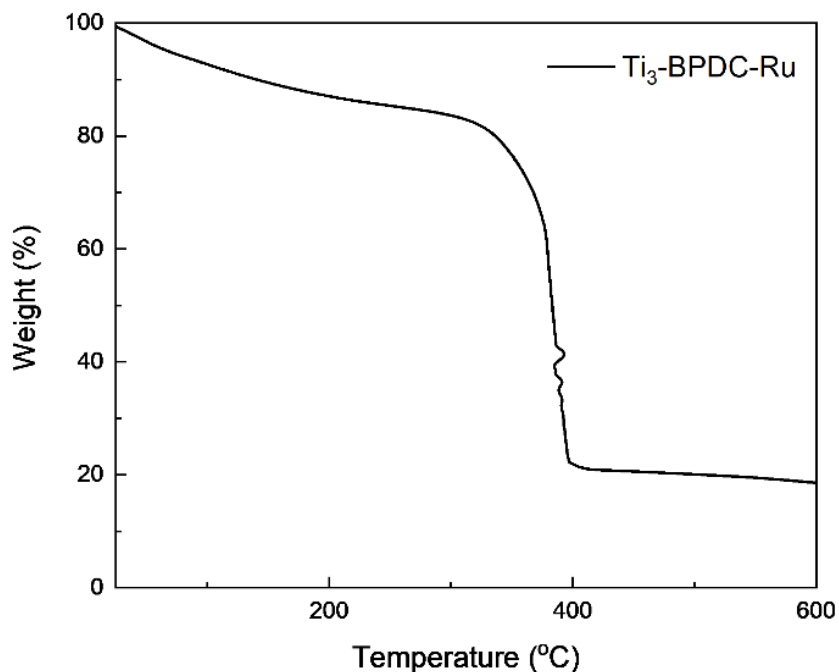


Figure 5-8. TGA curve of freshly prepared Ti₃-BPDC-Ru in 25~600 °C range. Reprinted with permission from *Journal of the American Chemical Society*, **2019**, 141, 12219-12223. Copyright 2019 American Chemical Society.

5.2.4 Visible Light-Driven Hydrogen Evolution Reaction (HER)

Visible light-driven ($\lambda > 400$ nm) HER activities of Ti₃-BPDC-Ir and Ti₃-BPDC-Ru were studied in an O₂-free acetonitrile (MeCN) solution with H₂O as the proton source and 1,3-dimethyl-2-phenyl-2,3-dihydro-1H-benzo[d]imidazole (BIH) as the sacrificial agent (MeCN:H₂O = 20:0.5 V/V). Photocatalytic HER was carried out in an external illumination type reaction vessel with a magnetic stirrer. Samples were prepared in 4.5 mL septum-sealed glass vials. Each sample was made up to a volume of 2.15 mL including 2.0 mL CH₃CN, 0.05 mL H₂O, 64 mg BIH (0.3 mmol) and 0.1 mL triethylamine (TEA). Samples contained 0.1 mg Ti₃-BPDC-Ir or Ti₃-BPDC-Ru. Sample vials were capped and deoxygenated by bubbling nitrogen through for 20 min to ensure complete air removal. The solution was irradiated by a 230 W solid state light source with a 400 nm filter. After HER, the amount of H₂ generated was quantified by gas chromatography (GC)

analysis of the headspace gas in the reactor. The turnover number (TON) [defined as $n(1/2H_2)$] reached 6632 for Ti_3 -BPDC-Ir and 786 for Ti_3 -BPDC-Ru after 72 h of visible light irradiation, with the apparent quantum yield of 0.080% and 0.018%, respectively (**Figure 5-9**).

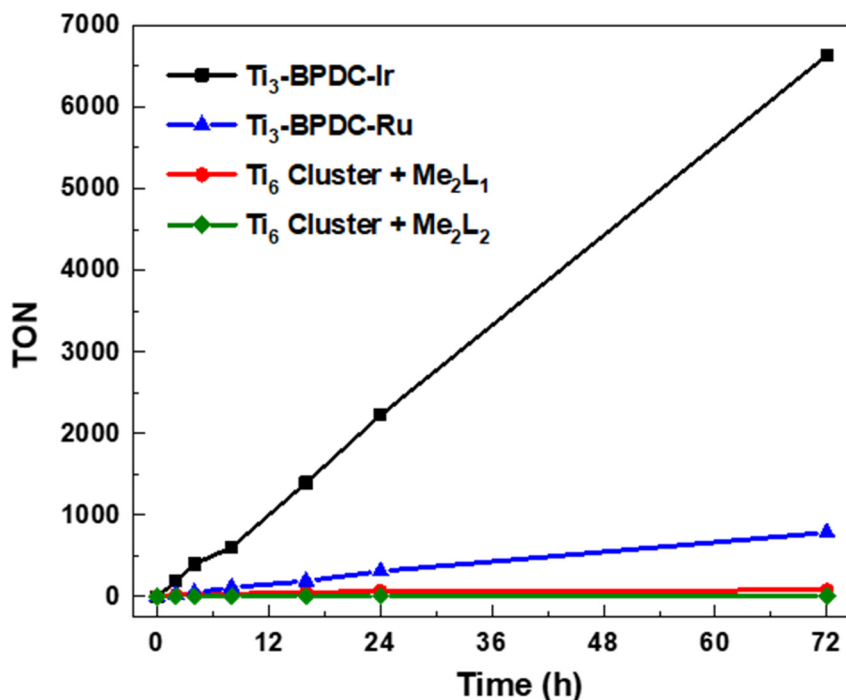


Figure 5-9. Time-dependent HER TONs of Ti_3 -BPDC-Ir and Ti_3 -BPDC-Ru along with homogenous controls. Reprinted with permission from *Journal of the American Chemical Society*, **2019**, 141, 12219-12223. Copyright 2019 American Chemical Society.

After photocatalytic HER, both Ti_3 -BPDC-Ir and Ti_3 -BPDC-Ru maintained their PXRD patterns (**Figure 5-10**) with <1% leaching of Ti into the solution, indicating their structural stability under reaction conditions. In comparison, the homogeneous mixtures of $Ti_6O_6(OiPr)_6(abz)_6$ and photosensitizing ligands L_1 or L_2 exhibited modest TONs of 80 and 13, respectively. The significant enhancement of photocatalytic HER activities of the MOFs over their homogeneous controls demonstrated the important role of hierarchical assembly of L_1 or L_2 photosensitizers and catalytic $Ti_3(OH)_2$ SBUs in facilitating multi-electron transfer to drive photocatalytic HER.

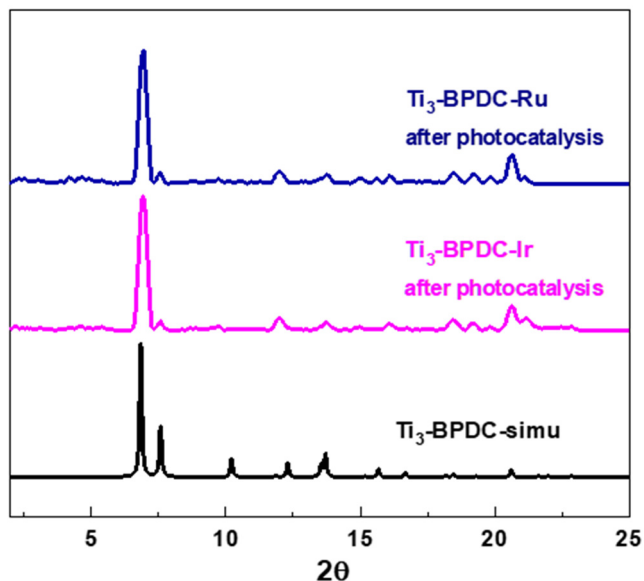


Figure 5-10. PXRD patterns of $\text{Ti}_3\text{-BPDC-Ir}$ and $\text{Ti}_3\text{-BPDC-Ru}$ after photocatalysis in comparison to the simulated pattern of $\text{Ti}_3\text{-BPDC}$. Reprinted with permission from *Journal of the American Chemical Society*, **2019**, 141, 12219-12223. Copyright 2019 American Chemical Society.

5.2.5 Photophysical Studies

UV-vis study of $\text{Ti}_3\text{-BPDC-Ir}$ and $\text{Ti}_3\text{-BPDC-Ru}$ indicated that both L_1 and L_2 were successfully introduced into the corresponding MOF (**Figure 5-11**).

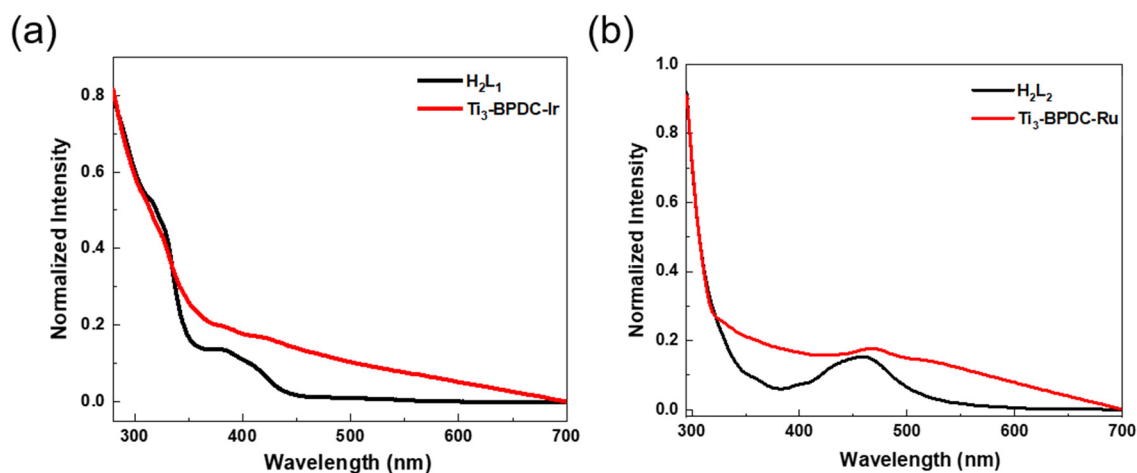


Figure 5-11. Normalized UV-vis spectra of (a) $\text{Ti}_3\text{-BPDC-Ir}$ and (b) $\text{Ti}_3\text{-BPDC-Ru}$ in comparison to their homogeneous photosensitizing ligands in DMF with a concentration of $20 \mu\text{M}$ based on Ir/Ru. Reprinted with permission from *Journal of the American Chemical Society*, **2019**, 141, 12219-12223. Copyright 2019 American Chemical Society.

We next examined whether the excited photosensitizer was reductively quenched by BIH or oxidatively quenched by $\text{Ti}_3(\text{OH})_2$ SBUs to initiate photocatalytic HER. Luminescence spectroscopy showed that the emissions of both $\text{Ti}_3\text{-BPDC-Ir}$ and $\text{Ti}_3\text{-BPDC-Ru}$ could be efficiently quenched by BIH in MeCN (**Figure 5-12**).

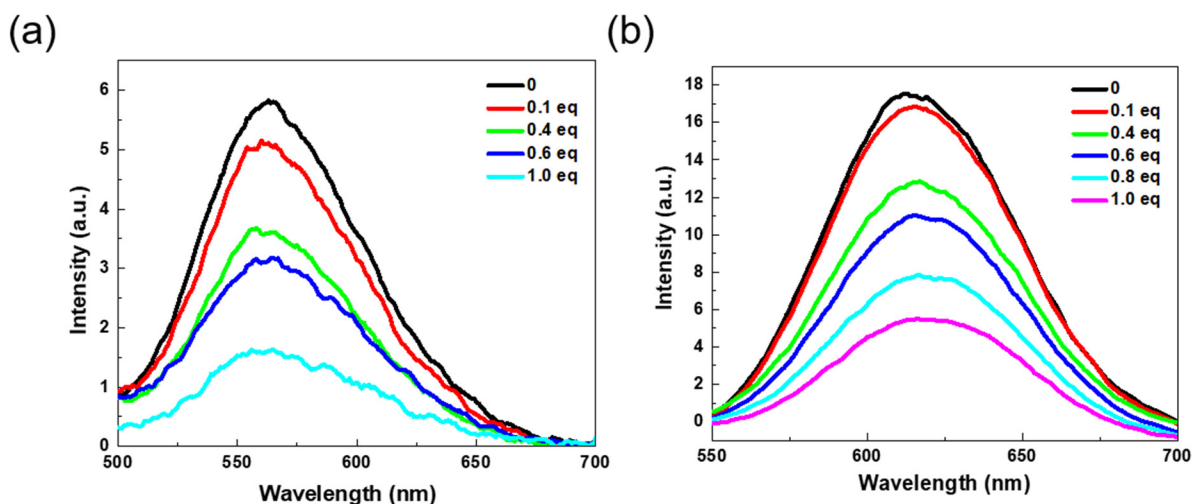


Figure 5-12. Emission spectra of (a) $\text{Ti}_3\text{-BPDC-Ir}$ and (b) $\text{Ti}_3\text{-BPDC-Ru}$ ($20 \mu\text{M}$ based on Ir/Ru) after the addition of different equivalents of BIH with 365 or 450 nm excitation, respectively. Reprinted with permission from *Journal of the American Chemical Society*, **2019**, 141, 12219-12223. Copyright 2019 American Chemical Society.

To quantitatively assess the quenching process, we determined luminescence intensities of homogeneous photosensitizers Me_2L_1 and Me_2L_2 in the presence of BIH and $\text{Ti}_6\text{O}_6(\text{OiPr})_6(\text{abz})_6$ in MeCN. As shown in **Figure 5-13**, and **Figure 5-14**, the luminescence of Me_2L_1 and Me_2L_2 was efficiently quenched by BIH but not $\text{Ti}_6\text{O}_6(\text{OiPr})_6(\text{abz})_6$ cluster.

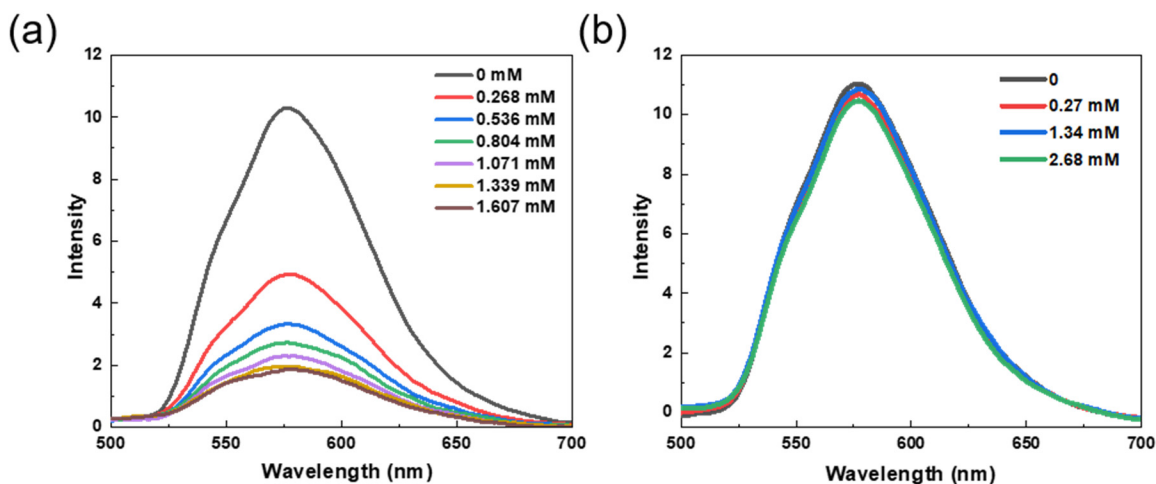


Figure 5-13. Emission spectra of Me₂L₁ (30 μmol) after the addition of different amounts of BIH (a) and Ti₆ cluster (b) in 2 mL of MeCN with 365 nm excitation. Reprinted with permission from *Journal of the American Chemical Society*, **2019**, 141, 12219-12223. Copyright 2019 American Chemical Society.

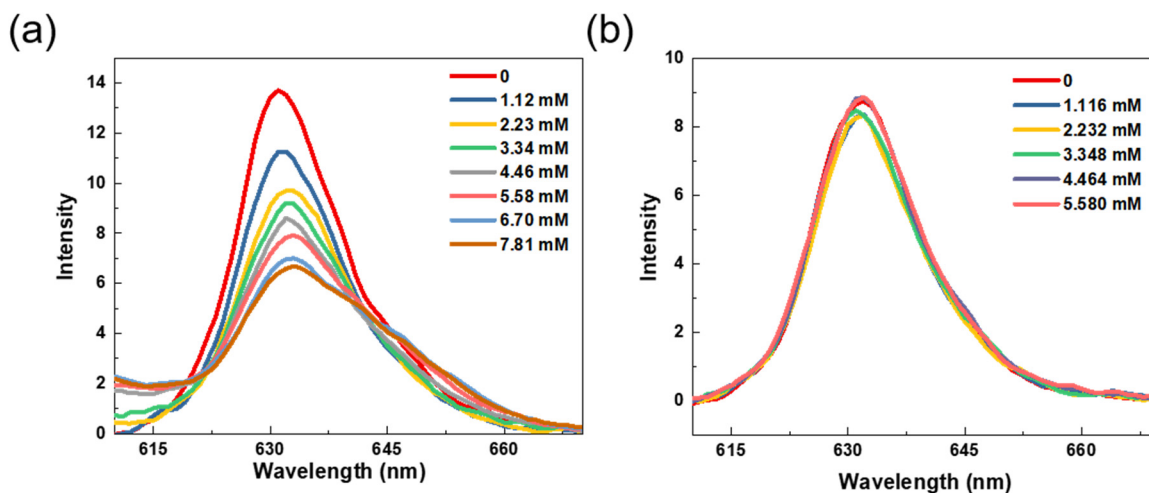


Figure 5-14. Emission Spectra of Me₂L₂ (30 μM) after addition of different amount of BIH (a) and different amount Ti₆ cluster (b) in 2 ml of CH₃CN under 450 nm excitation. Reprinted with permission from *Journal of the American Chemical Society*, **2019**, 141, 12219-12223. Copyright 2019 American Chemical Society.

The luminescence quenching of Me₂L₁ and Me₂L₂ by BIH was fitted to the Stern-Völmer equation to afford K_{SV} values of 3.36 mM⁻¹ and 0.15 mM⁻¹, respectively, indicating more efficient quenching for Ti₃-BPDC-Ir (**Figure 5-15**). These results suggest that photocatalytic HER in Ti₃-

BPDC-Ir initiates via electron transfer from BIH to the excited L_1 or L_2 , and the reduced L_1 or L_2 transfer electron to the $Ti_3(OH)_2$ SBU to drive HER.

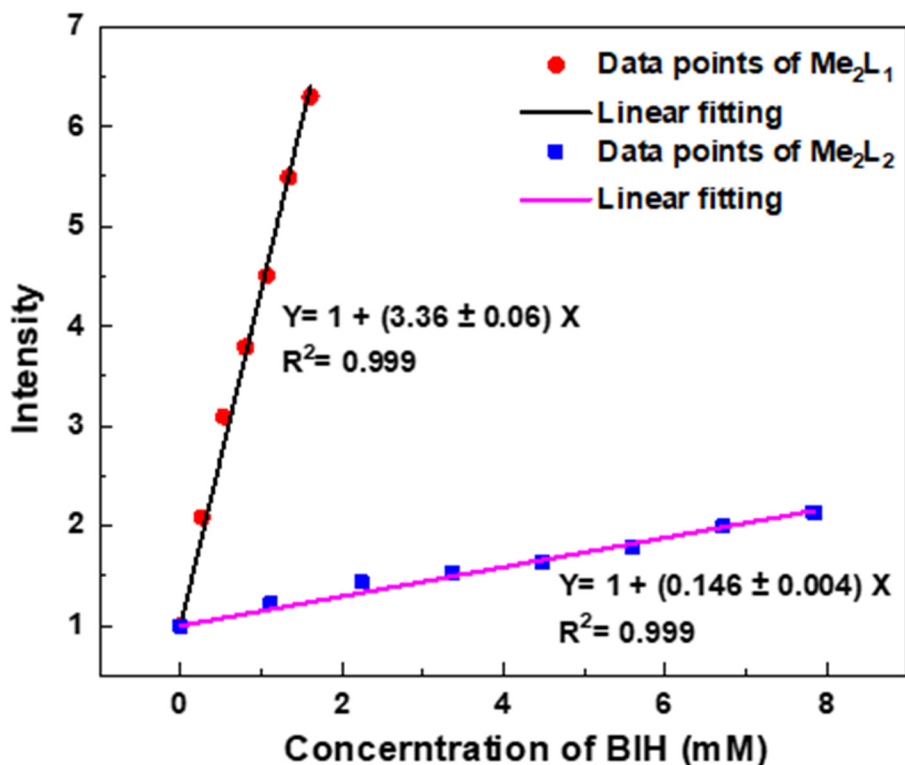


Figure 5-15. Plots of I_0/I of Me_2L_1 and Me_2L_2 as a function of the concentration of BIH (mM). Reprinted with permission from *Journal of the American Chemical Society*, **2019**, 141, 12219-12223. Copyright 2019 American Chemical Society.

5.2.6 Electrochemical Studies

Cyclic voltammograms (CVs) of $Ti_6O_6(OiPr)_6(abz)_6$ and Ti_3 -BPDC were then studied to provide additional insight into the HER process. With the addition of H_2O/H^+ , $Ti_6O_6(OiPr)_6(abz)_6$ showed an irreversible reduction peak with an onset potential of -0.17 V (**Figure 5-16**). A similar CV feature was also observed for Ti_3 -BPDC, suggesting that the H_2 production commences upon the injection of one electron.

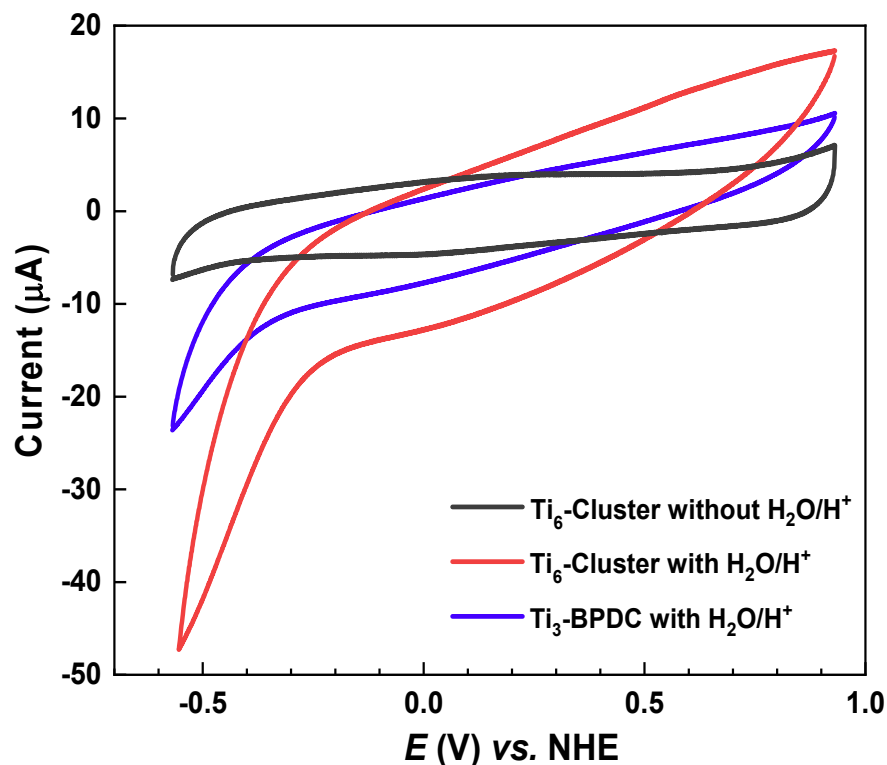


Figure 5-16. CVs of 0.5 mg Ti₃-BPDC coated on electrode surface and 5mM Ti₆ cluster in a 20 mL 0.1 M TBAH/CH₃CN solution with or without 250 µL H₂O and 250 µL TFA. TBAH = Tetrabutylammonium hexafluorophosphate. Reprinted with permission from *Journal of the American Chemical Society*, **2019**, 141, 12219-12223. Copyright 2019 American Chemical Society.

Electron paramagnetic spectroscopy (EPR) confirmed the existence of Ti^{III} centers upon visible light irradiation of Ti₃-BPDC-Ir and Ti₃-BPDC-Ru in the absence of a proton source. Upon irradiation, Ti₃-BPDC-Ir and Ti₃-BPDC-Ru exhibited an additional peak with the g-value of 1.983 and 1.985, respectively, over the homogeneous Me₂L₁ and Me₂L₂ ligands (**Figure 5-17** and **Figure 5-18**). These signals are attributed to the Ti^{III} species.²³⁻²⁴

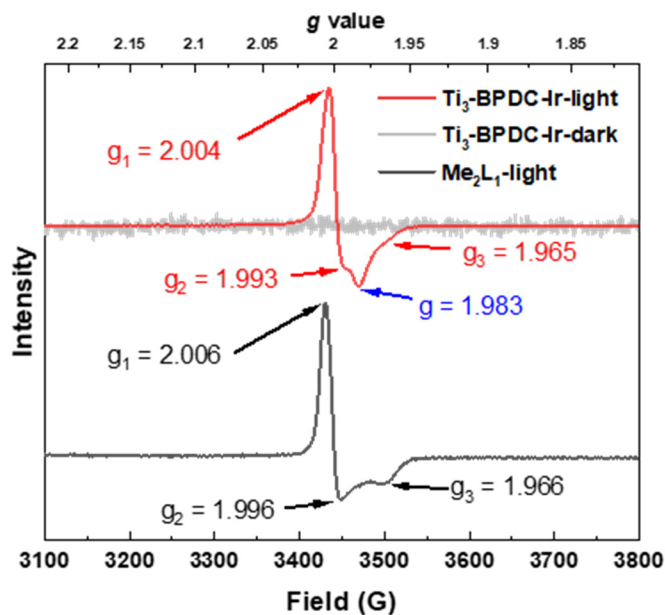


Figure 5-17. EPR spectra of $\text{Ti}_3\text{-BPDC-Ir}$ in the dark or under light irradiation. Reprinted with permission from *Journal of the American Chemical Society*, **2019**, 141, 12219-12223. Copyright 2019 American Chemical Society.

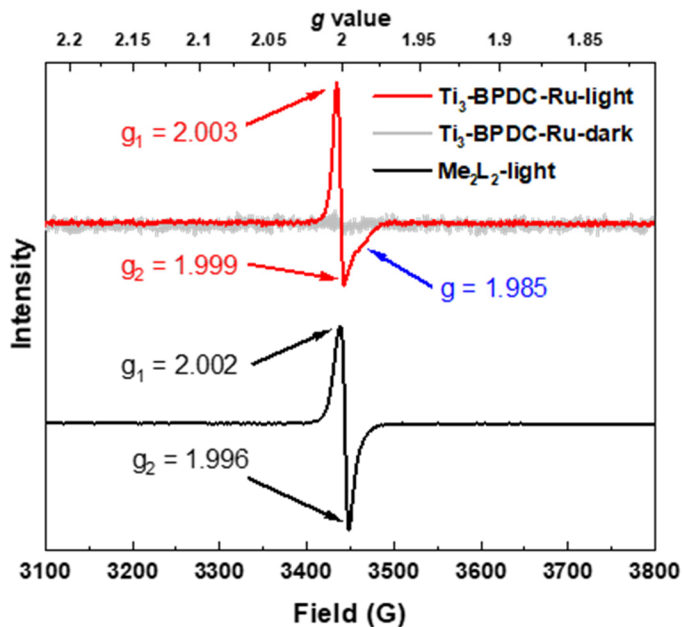


Figure 5-18. EPR spectra of $\text{Ti}_3\text{-BPDC-Ru}$ in the dark or under light irradiation. Reprinted with permission from *Journal of the American Chemical Society*, **2019**, 141, 12219-12223. Copyright 2019 American Chemical Society.

The Ti pre-edge peak of Ti₃-BPDC-Ru after photoirradiation shifted by 0.58 eV to the lower energy compared to those of Ti₃-BPDC-Ru before photoirradiation and Ti₃-BPDC after photoirradiation (**Figure 5-19**). The filling of one electron into the d orbitals lowers their energy and thus decreases the energy of the 1s→3d transition.

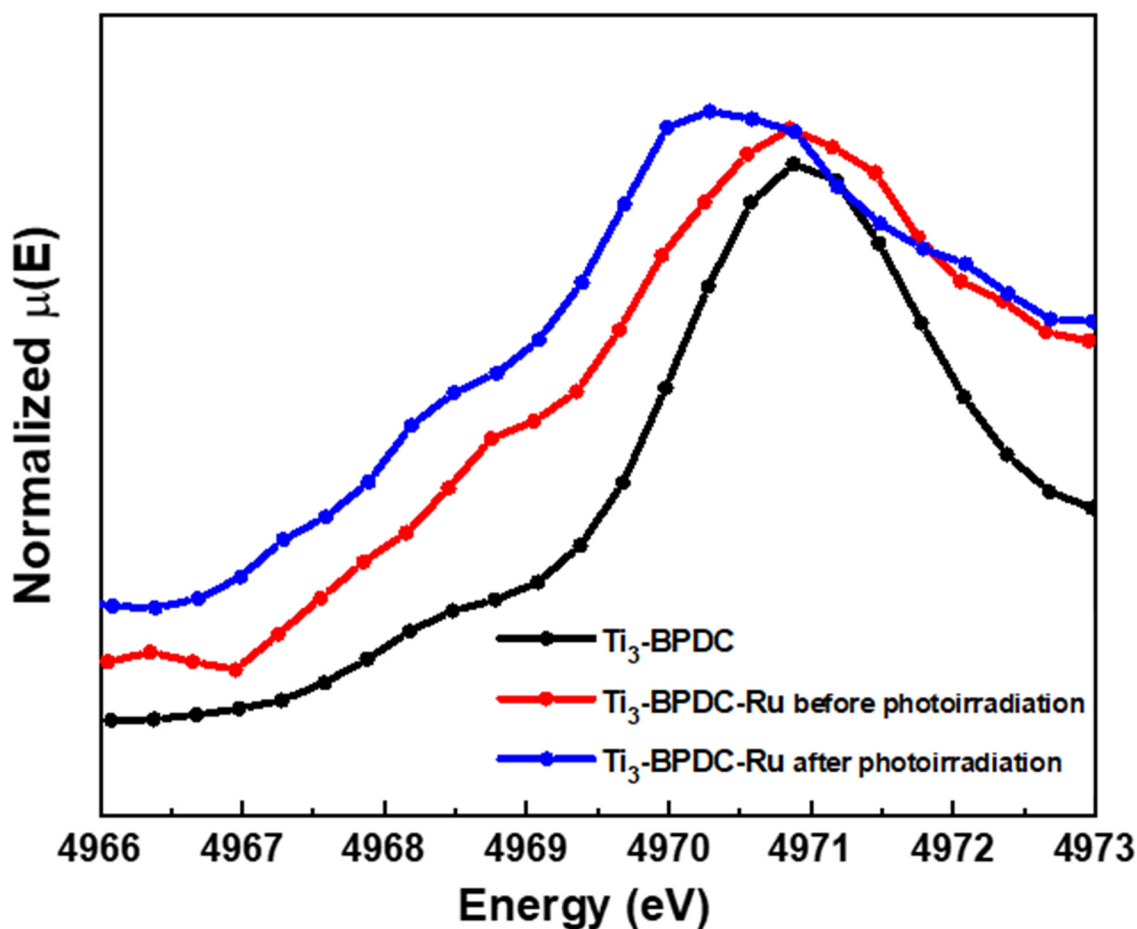


Figure 5-19. XANES analysis demonstrated the generation of Ti^{III} species after photoirradiation. Reprinted with permission from *Journal of the American Chemical Society*, **2019**, 141, 12219-12223. Copyright 2019 American Chemical Society.

CV scans showed the HER catalytic peak of Ti₃-BPDC with an onset potential of -0.18 V vs NHE in a MeCN solution with H₂O and trifluoroacetic acid (TFA) (MeCN:H₂O:TFA = 20:0.25:0.25, V/V/V) (**Figure 5-16**). The proton concentration of this solution is 10^{7.65} higher than that of photocatalytic HER condition (MeCN:H₂O = 20:0.5, V/V).

Based on the Nernst equation, the proton reduction potential (E) is calculated as follows:

$$E = E_0 + 0.059 \log_{10}[H^+]$$

In the condition of CV test (250 ul TFA and 250 ul H₂O per 20 ml CH₃CN):

$$E_1 = -0.18 \text{ V} = E_0 + 0.059 \log_{10}[H^+]_1$$

In the condition of photocatalytic HER (500 ul H₂O per 20 ml CH₃CN):

$$E_2 = E_0 + 0.059 \log_{10}[H^+]_2$$

As the ratio of [H⁺]₁ to [H⁺]₂ is approximately equal to the proton concentration of 250 ul TFA and 250 ul H₂O to the solution of 500 ul H₂O, which is approximately 10^{7.65}.

$$E_2 - E_1 = 0.059 \log_{10} \left(\frac{[H^+]_2}{[H^+]_1} \right) = -0.45 \text{ V}, E_2 = -0.63 \text{ V}$$

The energy needed to drive the HER by Ti₃(OH)₂ SBUs in Ti₃-BPDC-Ir or Ti₃-BPDC-Ru under the photocatalytic conditions is estimated to be 0.63 eV ($\Delta E'$) based on the Nernst equation.

5.2.7 Proposed Reaction Mechanism

On the basis of photophysical and electrochemical results, we propose the photocatalytic HER cycle for Ti₃-BPDC-Ir in **Scheme 5-2**. Under visible light irradiation, the L₁ ligand [Ir(ppy)₂(dcbpy)]⁺ is excited to the [Ir(ppy)₂(dcbpy)]^{+*} state, which is reduced by BIH to generate [Ir(ppy)₂(dcbpy)]. Photo-reduced [Ir(ppy)₂(dcbpy)] transfer electron to the Ti₃(OH)₂ SBU to afford Ti^{III} species. CV scans showed that Me₂L₁ and Me₂L₂ displayed the first reduction peaks at -0.72 V and -0.67 V, respectively (**Figure 5-20**, **Figure 5-21**), which is large enough to drive HER by Ti₃(OH)₂ SBUs ($\Delta E' = 0.63$ eV). The smaller energy gap of [Ru(bpy)₂(dcbpy)]⁺ / [Ru(bpy)₂(dcbpy)]²⁺ (0.67 eV) than [Ir(ppy)₂(dcbpy)] / [Ir(ppy)₂(dcbpy)]⁺ (0.72 eV) also explains much higher HER activity of Ti₃-BPDC-Ir (TON = 6632) over Ti₃-BPDC-Ru (TON = 786).

Scheme 5-2. Proposed catalytic cycle for the visible-light-driven HER catalyzed by Ti³⁺-BPDC-Ir. Reprinted with permission from *Journal of the American Chemical Society*, 2019, 141, 12219-12223. Copyright 2019 American Chemical Society.

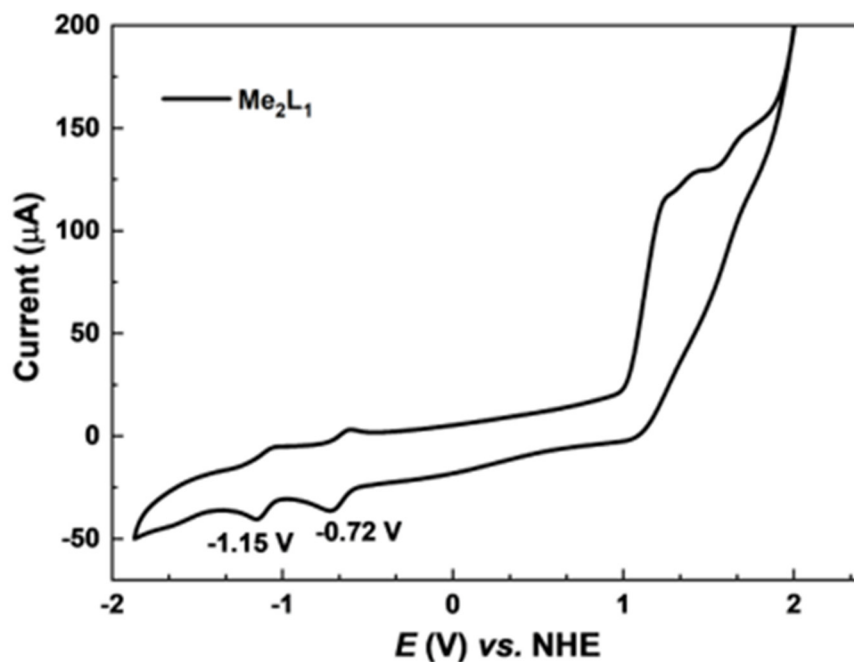
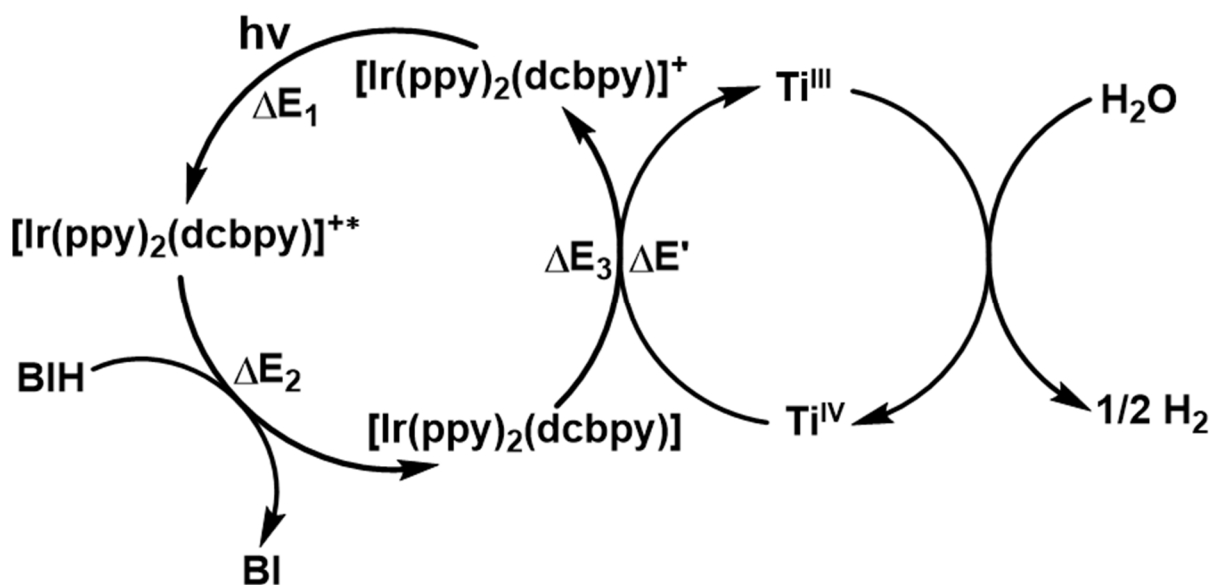


Figure 5-20. CV of Me₂L₁ in 0.1 M TBAH/CH₃CN (Tetrabutylammonium hexafluorophosphate). Potential sweep rate was 100 mV/s. Reprinted with permission from *Journal of the American Chemical Society*, 2019, 141, 12219-12223. Copyright 2019 American Chemical Society.

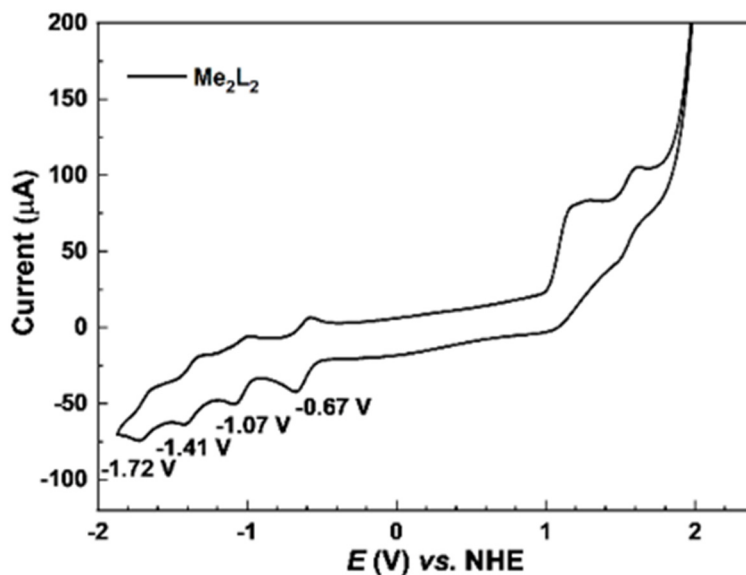
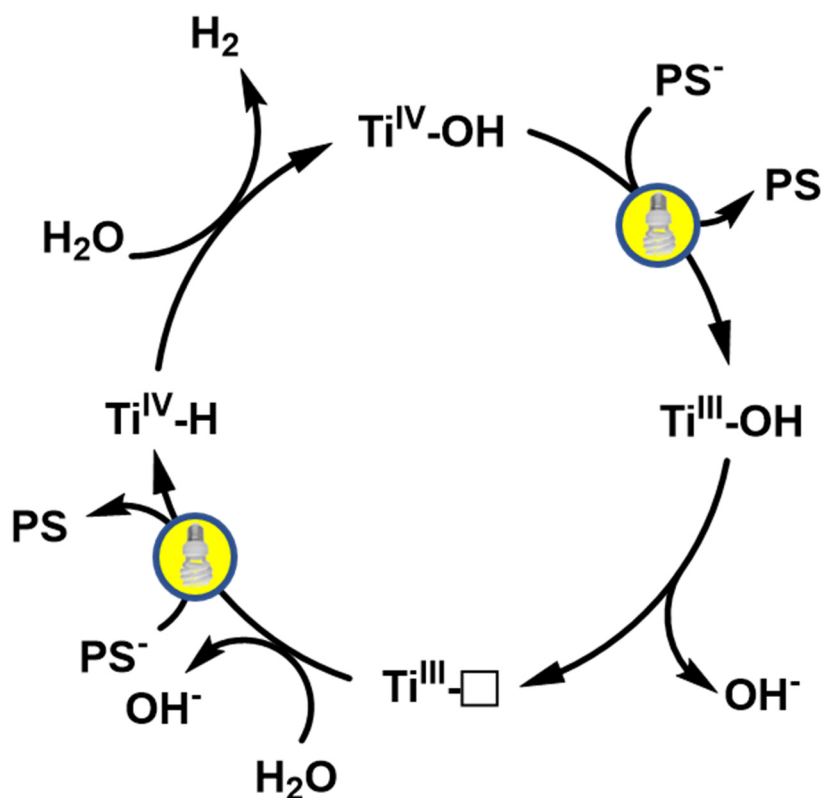


Figure 5-21. CV of Me_2L_1 in 0.1 M TBAH/ CH_3CN (Tetrabutylammonium hexafluorophosphate). Potential sweep rate was 100 mV/s. Reprinted with permission from *Journal of the American Chemical Society*, 2019, 141, 12219-12223. Copyright 2019 American Chemical Society.

Based on the well-defined structure of catalytic centers in MOFs, we further propose photocatalytic HER via a Ti^{IV} -hydride intermediate (**Scheme 5-3**). The Ti^{IV} -OH site first accepts one electron from the reduced photosensitizer [$\text{Ir}(\text{ppy})_2(\text{dcbpy})$] to form the Ti^{III} -OH species. The electron-rich Ti^{III} center makes the hydroxyl group basic which can be protonated by water to generate a vacant coordination site on the Ti^{III} center [$\text{pK}_b(\text{Ti}^{\text{III}}\text{-OH}) = 4.14$ vs. $\text{pK}_b(\text{Ti}^{\text{IV}}\text{-OH}) = 12.68$]. The low-coordinate Ti^{III} center undergoes proton coupled electron transfer (PCET) by accepting the proton from H_2O and the electron from another reduced photosensitizer [$\text{Ir}(\text{ppy})_2(\text{dcbpy})$] to form the Ti^{IV} -hydride intermediate. Protonation of Ti^{IV} -hydride produces hydrogen and regenerates the Ti^{IV} -OH catalyst.

Scheme 5-3. Detailed catalytic mechanism on the Ti site via the $\text{Ti}^{\text{IV+}}/\text{Ti}^{\text{III}}$ cycle. Reprinted with permission from *Journal of the American Chemical Society*, 2019, 141, 12219-12223. Copyright 2019 American Chemical Society.



5.3 Conclusion

In this chapter, we have synthesized two new Ti MOFs by doping $[\text{Ir}(\text{ppy})_2(\text{dcbpy})]\text{Cl}$ - or $[\text{Ru}(\text{bpy})_2(\text{dcbpy})]\text{Cl}_2$ -derived dicarboxylate ligands into the Ti-BPDC framework and demonstrated their applications in visible light-driven hydrogen evolution. The proximity of multiple photosensitizers to the catalytic $\text{Ti}_3(\text{OH})_2$ SBU facilitates multielectron transfer upon photoexcitation, leading to 80-fold enhancement in HER activity over the corresponding homogeneous controls. Photophysical, and electrochemical established the reductive quenching of the photoexcited photosensitizers by BIH as the initiating step of photocatalytic HER followed by electron transfer from the reduced photosensitizers to $\text{Ti}_3(\text{OH})_2$ SBUs. Protonation of $\text{Ti}^{\text{III}}\text{-OH}$ generates the Ti^{III} species with a vacant coordination site which undergoes proton-coupled electron

transfer to afford the key $\text{Ti}^{\text{IV}}\text{-H}$ intermediate. This work thus provides new insights into the design of multifunctional Ti MOFs with catalytic SBUs and photosensitizing ligands for photocatalytic applications.

5.4 Experimental

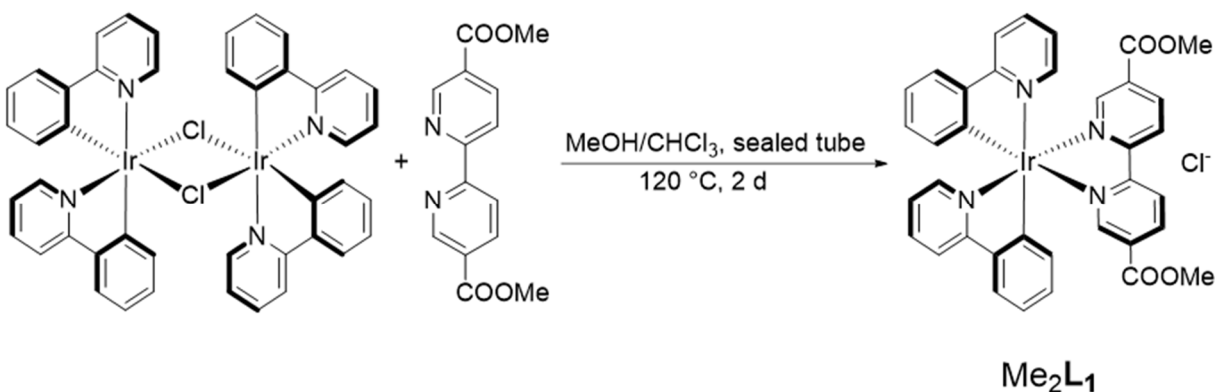
5.4.1 Material and Methods

All starting materials were purchased from Sigma-Aldrich and Fisher (USA) unless otherwise noted and used without further purification. Powder X-ray diffraction (PXRD) data was collected on a Bruker D8 Venture diffractometer using a $\text{Cu K}\alpha$ radiation source ($\lambda = 1.54178 \text{ \AA}$). N_2 sorption experiments were performed on a Micromeritics TriStar II 3020 instrument. Thermogravimetric analysis (TGA) was performed in air using a Shimadzu TGA-50 equipped with a platinum pan and heated at a rate of $1.5 \text{ }^\circ\text{C}$ per min. Electron paramagnetic resonance (EPR) spectra were collected with a Bruker Elexsys 500 X-band EPR spectrometer at 20 K. Inductively coupled plasma-mass spectrometry data was obtained with an Agilent 7700x ICP-MS and analyzed using ICP-MS MassHunter version B01.03. Samples were diluted in a 2% HNO_3 matrix and analyzed with a ^{159}Tb internal standard against a 12-point standard curve over the range from 0.1 ppb to 500 ppb. The correlation was >0.9997 for all analyses of interest. Data collection was performed in Spectrum Mode with five replicates per sample and 100 sweeps per replicate. Cyclic voltammograms (CVs) were recorded on a CHI420 electrochemistry workstation with regular 3 electrode systems. Measurements were recorded using a glassy carbon disk working electrode ($S = 0.07 \text{ cm}^2$) and a platinum wire as the counter electrode. The $\text{Ag}/\text{AgCl}/1 \text{ M KCl}$ electrode was used as the reference electrode in all experiments. ^1H and ^{13}C NMR spectra were recorded on a Bruker NMR 500 DRX spectrometer at 500 MHz referenced to the proton resonance resulting from incomplete deuteration of CDCl_3 (δ 7.26) or in $\text{DMSO-}d_6$ (δ 2.50). Amounts of H_2 generated

in the photocatalytic experiments were determined by gas chromatography (GC) using an SRI 8610C Gas Chromatograph with the nitrogen carrier gas and a TCD detector. Steady-state and time resolved emission spectra were recorded on an Edinburgh FLS 920 spectrometer.

5.4.2 Synthesis of Me₂L₁

Scheme 5-4. Schematic representation of the synthetic procedure for Me₂L₁. Reprinted with permission from *Journal of the American Chemical Society*, **2019**, 141, 12219-12223. Copyright 2019 American Chemical Society.



Ir₂(ppy)₄Cl₂ (216 mg, 0.2 mmol), dimethyl [2,2'-bipyridine]-5,5'-dicarboxylate (110 mg, 0.4 mmol), methanol (10 mL) and chloroform (10 mL) were added to a 100 mL thick-walled Pyrex tube. The tube was sealed and heated at 120 °C for 2 days. After cooling to ambient temperature, the solvent was removed under reduced pressure and the crude product was purified by column chromatography (SiO₂, CHCl₃/MeOH, 10:1 to 5:1) to yield the product as a light yellow solid (275 mg, 85%). ¹H NMR (500 MHz, CDCl₃): δ 10.17 (d, J = 8.5 Hz, 2H), 8.79 (dd, J₁ = 8.5 Hz, J₂ = 2.0 Hz, 2H), 8.45 (d, J = 2.0 Hz, 2H), 7.93 (d, J = 8.0 Hz, 2H), 7.77 (td, J₁ = 8.0 Hz, J₂ = 1.5 Hz, 2H), 7.70 (dd, J₁ = 7.0 Hz, J₂ = 1.0 Hz, 2H), 7.44 (d, J = 5.5 Hz, 2H), 7.08 (td, J₁ = 8.0 Hz, J₂ = 1.0 Hz, 2H), 7.02 – 6.93 (m, 4H), 6.30 (dd, J₁ = 7.5 Hz, J₂ = 1.0 Hz, 2H), 3.85 (s, 3H). ¹³C NMR (125 MHz, CDCl₃): δ 167.70, 163.20, 158.07, 151.04, 148.89, 148.37, 143.15, 140.80, 138.37, 131.57, 131.01, 130.10, 128.22, 124.96, 123.35, 123.03, 119.89, 53.05.

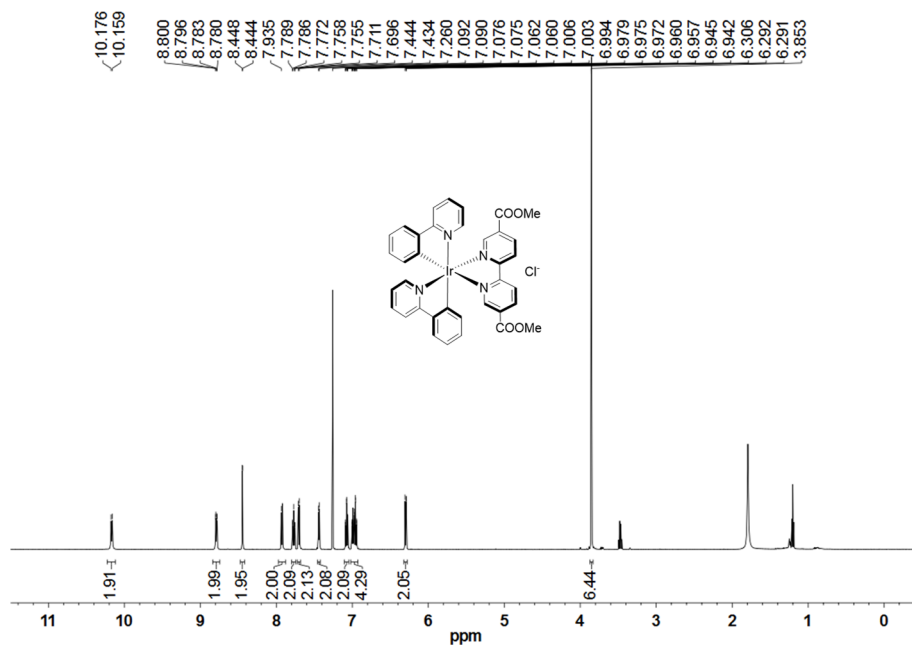


Figure 5-22. ^1H NMR spectrum of Me_2L_1 (500 MHz) in CDCl_3 . Reprinted with permission from *Journal of the American Chemical Society*, **2019**, 141, 12219-12223. Copyright 2019 American Chemical Society.

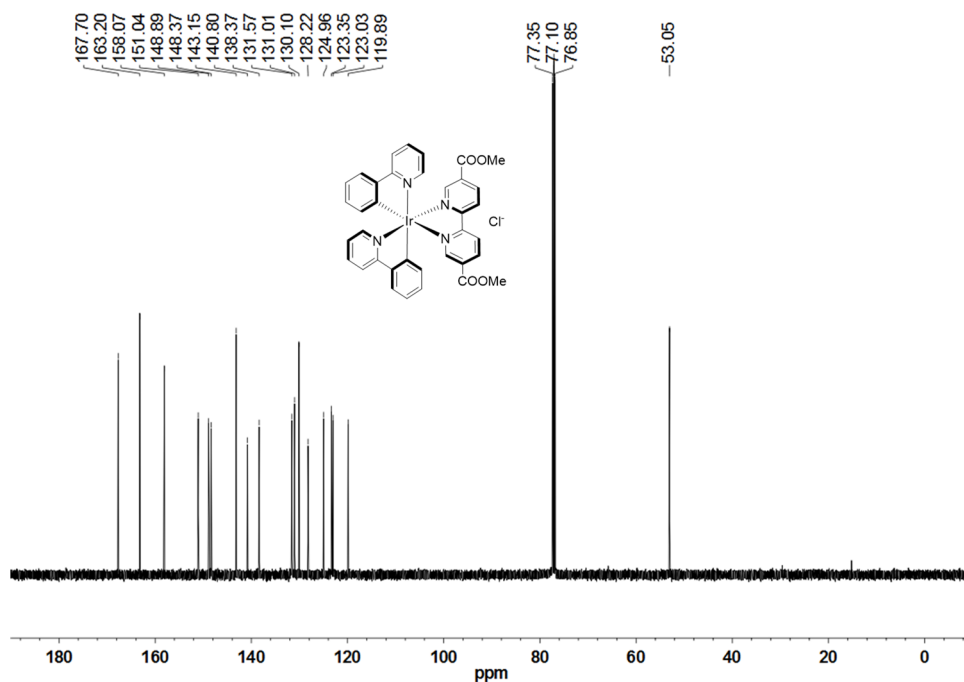
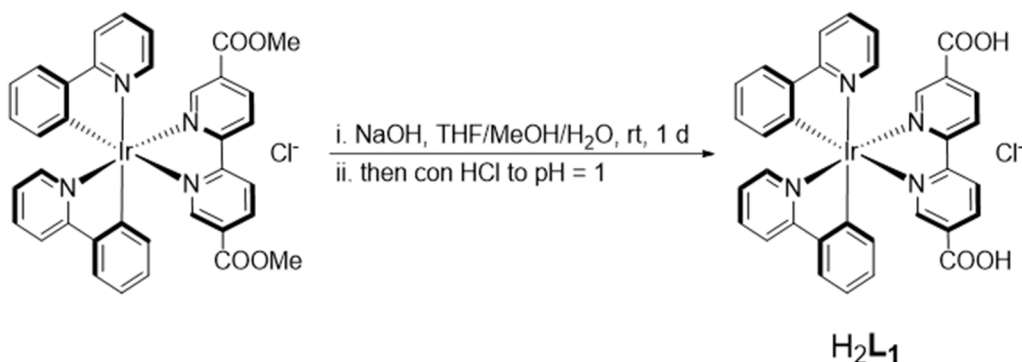


Figure 5-23. ^{13}C NMR spectrum of Me_2L_1 (500 MHz) in CDCl_3 . Reprinted with permission from *Journal of the American Chemical Society*, **2019**, 141, 12219-12223. Copyright 2019 American Chemical Society.

5.4.3 Synthesis of H₂L₁

Scheme 5-5. Schematic representation of the synthetic procedure for H₂L₁. Reprinted with permission from *Journal of the American Chemical Society*, **2019**, 141, 12219-12223. Copyright 2019 American Chemical Society.



Me₂L₁ (162 mg, 0.2 mmol), MeOH (6 mL) and THF (6 mL) were added to a 50 mL flask. After the solid was fully dissolved, an aqueous solution of NaOH (80 mg NaOH in 4 mL deionized water) was added dropwise to the solution while stirring. The solution was stirred at ambient temperature for 1 d. After THF and MeOH were removed under reduced pressure, the solution was acidified by adding concentrated HCl until pH = 1. The precipitated solid was filtered under reduced pressure, washed with deionized water, and ether, and finally dried under vacuum to afford H₂L₁ as a fine yellow powder (148 mg, 95%). ¹H NMR (500 MHz, DMSO-*d*₆): δ 8.76 (d, *J* = 8.4 Hz, 2H), 8.41 (dd, *J*₁ = 8.2 Hz, *J*₂ = 1.8 Hz, 2H), 8.35 (m, 2H), 8.25 (d, *J* = 7.9 Hz, 2H), 7.90 (m, 2H), 7.57 (dd, *J*₁ = 6.9 Hz, *J*₂ = 1.4 Hz, 2H), 7.15 (t, *J* = 6.9 Hz, 2H), 6.98 (t, *J* = 7.5 Hz, 2H), 6.87 (t, *J* = 7.5, 4H), 6.16 (d, *J* = 7.7 Hz, 2H). HR-MS (ESI, positive mode): *m/z*, expected for [C₃₄H₂₄O₄N₄Ir]⁺ [(M-Cl)]⁺ 745.1427, found 745.1437.

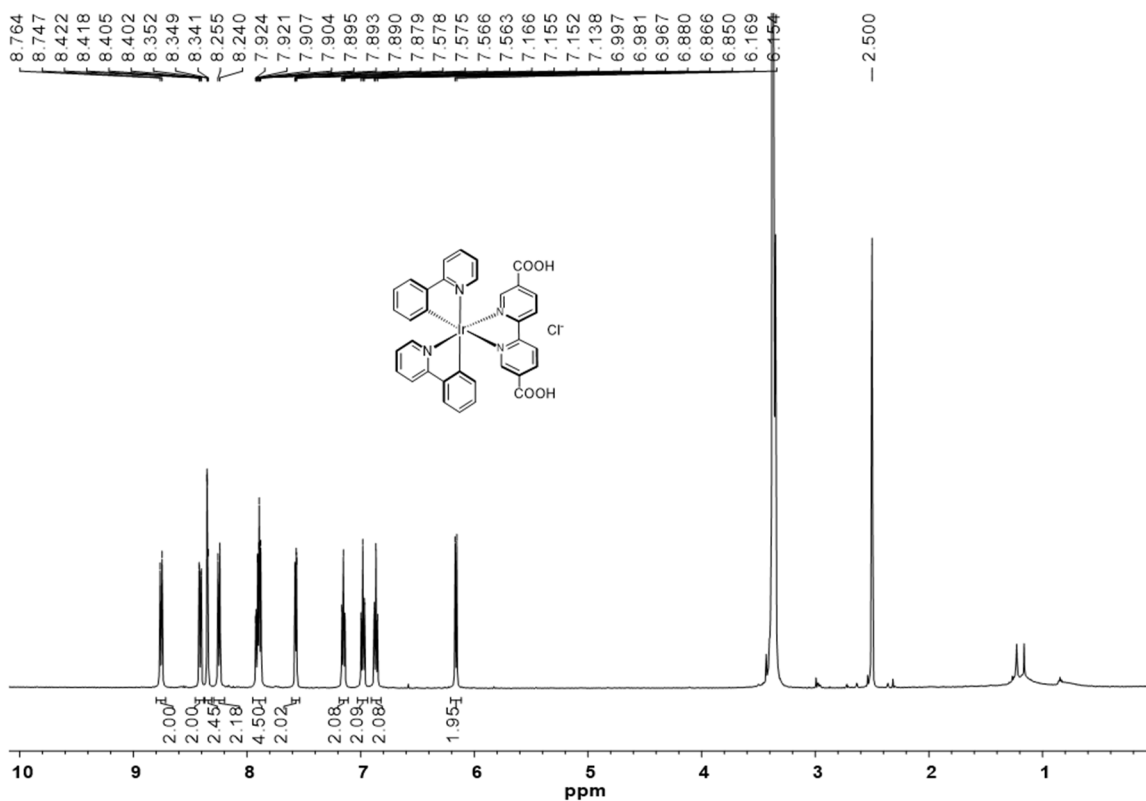
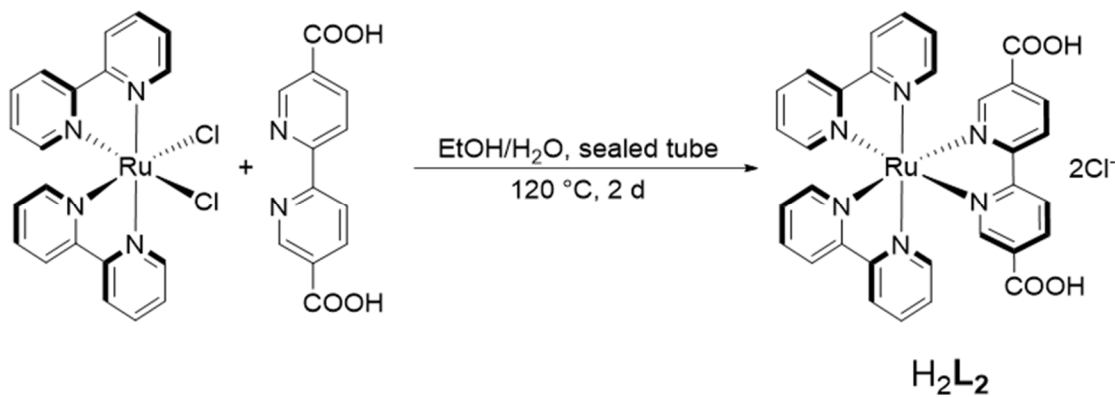


Figure 5-24. ^1H NMR spectrum of H_2L_1 (500 MHz) in $\text{DMSO-}d_6$. Reprinted with permission from *Journal of the American Chemical Society*, **2019**, 141, 12219-12223. Copyright 2019 American Chemical Society.

5.4.4 Synthesis of H_2L_2

Scheme 5-6. Schematic representation of the synthetic procedure for H_2L_2 . Reprinted with permission from *Journal of the American Chemical Society*, **2019**, 141, 12219-12223. Copyright 2019 American Chemical Society.



Ru(bpy)₂Cl₂ (242 mg, 0.5 mmol), 2,2'-bipyridine-5,5'-dicarboxylic acid (122 mg, 0.5 mmol), ethanol (10 mL) and deionized water (10 mL) were added to a 100 mL thick-walled Pyrex tube. The tube was sealed and heated at 120 °C for 2 days. After cooling to ambient temperature, reduced pressure and the crude product was recrystallized from a MeOH/diethyl ether to yield the product as a brown solid (321 mg, 88%). ¹H NMR (500 MHz, DMSO-*d*₆): δ 9.03 (d, J = 8.3 Hz, 2H), 8.89 (m, 4H), 8.53 (d, J = 8.4, 2H), 8.21 (m, 4H), 8.00 (s, 2H), 7.86 (d, J₁ = 5.6 Hz, 2H), 7.79 (d, J = 5.8 Hz, 2H), 7.60 (t, J = 6.6 Hz, 2H), 7.51 (t, J = 6.7, 2H). HR-MS (ESI, positive mode): m/z, expected for [C₃₂H₂₄N₆O₄ClRu]⁺ [(M-Cl)]⁺ 693.0591, found 693.0584.

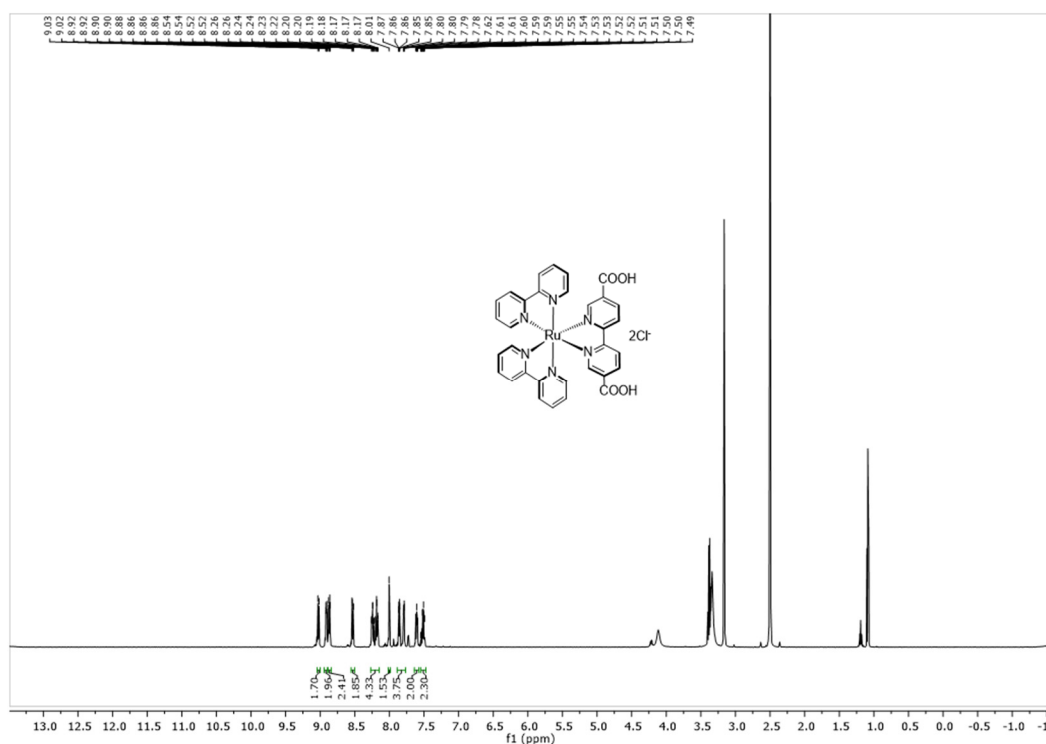


Figure 5-25. ¹H NMR spectrum of H₂L₂ (500 MHz) in DMSO-*d*₆. Reprinted with permission from *Journal of the American Chemical Society*, **2019**, 141, 12219-12223. Copyright 2019 American Chemical Society.

5.4.5 Synthesis of Ti₃-BPDC-Ir and Ti₃-BPDC-Ru

Ti₆O₆(OⁱPr)₆(abz)₆ cluster (2.00 mg), biphenyl-4,4'-dicarboxylic acid (3.30 mg), H₂L₁ (1.26 mg) or H₂L₂ (1.25 mg), glacial acetic acid (60 uL), and DMF (1.5 mL) were charged in a 4

mL Pyrex vial. The mixture was heated in a 120 °C oven for 3 days. After cooling to room temperature, gold-orange color (Ti₃-BPDC-Ir) or deep-red color (Ti₃-BPDC-Ru) crystalline solids were harvested. The resulting solid was recovered by centrifugation and then sequentially washed with DMF three times, with THF three times, and with benzene three times. The solid was then freeze-dried in benzene. Yield: Ti₃-BPDC-Ir, 0.96 mg (35%); Ti₃-BPDC-Ru, 1.88 mg (46%).

5.4.6 Fitting of Luminescence Quenching by BIH

Fitting of Luminescence Quenching of Me₂L₁ The reductive quenching mechanism was supported by fitting the data of luminescence quenching of Me₂L₁ by BIH to the Stern-Volmer equation,

$$\frac{I_0}{I} = 1 + K_{sv}C_{BIH}$$

where K_{SV} is the Stern-Völmer constant, and I₀/I is the ratio of luminescence intensity in the absence and presence of BIH. I₀/I showed a good linear relationship with respect to the concentration of BIH (C_{BIH}) with R² = 0.999 and K_{SV} = 3.36 M⁻¹, as shown in **Figure 5-15**.

Fitting of Luminescence Quenching of Me₂L₂. The reductive quenching mechanism was supported by fitting the data of luminescence quenching of Me₂L₂ by BIH to the Stern-Volmer equation,

$$\frac{I_0}{I} = 1 + K_{sv}C_{BIH}$$

where K_{SV} is the Stern-Völmer constant, and I₀/I is the ratio of luminescence intensity in the absence and presence of BIH. I₀/I showed a good linear relationship with respect to the concentration of BIH (C_{BIH}) with R² = 0.999 and K_{SV} = 0.15 M⁻¹, as shown in **Figure 5-15**.

5.4.7 Apparent Quantum Yield Determinations

Apparent quantum yield of HER: a Xenon lamp was used as the light source and the apparent quantum yield was measured using different band-pass optical filters by a standard

ferrioxalate actinometry.²⁵⁻²⁶ 1 mL of the ferrioxalate (0.15 M, prepared by dissolving 736.9 mg of potassium ferrioxalate hydrate in 10 mL of 0.05 M H₂SO₄) was added to a quartz cuvette (l = 1 cm). The actinometry solution was irradiated with Xenon lamp (with certain wavelength band-pass optical filter, 450 nm ± 2 nm for Ti₃-BPDC-Ru, and 380 nm ± 2 nm for Ti₃-BPDC-Ir) for 90 seconds. After irradiation, 175 µL of the phenanthroline solution (50 mg of 1,10-phenanthroline and 11.25 g of sodium acetate dissolving in 10 mL of 0.05 M H₂SO₄) was added to the cuvette. The solution was kept in dark for 30 min to ensure complete coordination. The absorbance of the actinometry solution was monitored at 510 nm. The absorbance of a non-irradiated (in dark) sample was also measured at 510 nm. Conversion was calculated using eq 1:

$$mol Fe^{2+} = \frac{V \cdot \Delta A}{l \cdot \epsilon} \quad (1)$$

Where V is the final volume (0.001175 L) after complexation with phenanthroline, ΔA is the difference in absorbance at 510 nm between the irradiated and non-irradiated solutions, l is the path length (1 cm) and ε is the molar absorptivity at 510 nm (11,100 L·mol⁻¹·cm⁻¹). Therefore, the photo flux can be calculated using eq 2:

$$photo\ flux = \frac{mol\ Fe^{2+}}{\Phi \cdot t \cdot f} \quad (2)$$

Where Φ is the quantum yield for the ferrioxalate actinometer,²⁷ t is the time (90 s), and f is the fraction of light absorbed at certain wavelength of band-pass optical filter (~1).

Lastly, after quantifying the amount of H₂ under the irradiation of certain wavelength using band-pass optical filter, the apparent quantum yield was calculated by eq 3:

$$\Phi = \frac{number\ of\ evolved\ H_2\ molecules \times 2}{photo\ flux \cdot t \cdot f} \quad (3)$$

Apparent quantum yields for Ti₃-BPDC-Ir and Ti₃-BPDC-Ru were calculated to be 0.080% and 0.018%, respectively.

5.5 References

- (1) Chen, X.; Liu, L.; Yu, P. Y.; Mao, S. S., Increasing Solar Absorption for Photocatalysis with Black Hydrogenated Titanium Dioxide Nanocrystals. *Science* **2011**, *331* (6018), 746.
- (2) Liu, N.; Schneider, C.; Freitag, D.; Venkatesan, U.; Marthala, V. R. R.; Hartmann, M.; Winter, B.; Spiecker, E.; Osvet, A.; Zolnhofer, E. M.; Meyer, K.; Nakajima, T.; Zhou, X.; Schmuki, P., Hydrogenated Anatase: Strong Photocatalytic Dihydrogen Evolution without the Use of a Co-Catalyst. *Angewandte Chemie International Edition* **2014**, *53* (51), 14201-14205.
- (3) Li, D.; Kassymova, M.; Cai, X.; Zang, S.-Q.; Jiang, H.-L., Photocatalytic CO₂ reduction over metal-organic framework-based materials. *Coordination Chemistry Reviews* **2020**, *412*, 213262.
- (4) Liu, S.; Zhang, C.; Sun, Y.; Chen, Q.; He, L.; Zhang, K.; Zhang, J.; Liu, B.; Chen, L.-F., Design of metal-organic framework-based photocatalysts for hydrogen generation. *Coordination Chemistry Reviews* **2020**, *413*, 213266.
- (5) Kudo, A.; Miseki, Y., Heterogeneous photocatalyst materials for water splitting. *Chemical Society Reviews* **2009**, *38* (1), 253-278.
- (6) Kubacka, A.; Fernández-García, M.; Colón, G., Advanced Nanoarchitectures for Solar Photocatalytic Applications. *Chemical Reviews* **2012**, *112* (3), 1555-1614.
- (7) Naldoni, A.; Altomare, M.; Zoppellaro, G.; Liu, N.; Kment, Š.; Zbořil, R.; Schmuki, P., Photocatalysis with Reduced TiO₂: From Black TiO₂ to Cocatalyst-Free Hydrogen Production. *ACS Catalysis* **2019**, *9* (1), 345-364.
- (8) Zuo, F.; Bozhilov, K.; Dillon, R. J.; Wang, L.; Smith, P.; Zhao, X.; Bardeen, C.; Feng, P., Active Facets on Titanium(III)-Doped TiO₂: An Effective Strategy to Improve the Visible-Light Photocatalytic Activity. *Angewandte Chemie International Edition* **2012**, *51* (25), 6223-6226.
- (9) Matthews, P. D.; King, T. C.; Wright, D. S., Structure, photochemistry and applications of metal-doped polyoxotitanium alkoxide cages. *Chemical Communications* **2014**, *50* (85), 12815-12823.
- (10) Ji, P.; Song, Y.; Drake, T.; Veroneau, S. S.; Lin, Z.; Pan, X.; Lin, W., Titanium(III)-Oxo Clusters in a Metal–Organic Framework Support Single-Site Co(II)-Hydride Catalysts for Arene Hydrogenation. *Journal of the American Chemical Society* **2018**, *140* (1), 433-440.
- (11) Fang, W.-H.; Zhang, L.; Zhang, J., A 3.6 nm Ti₅₂–Oxo Nanocluster with Precise Atomic Structure. *Journal of the American Chemical Society* **2016**, *138* (24), 7480-7483.
- (12) Gao, M.-Y.; Fang, W.-H.; Wen, T.; Zhang, L.; Zhang, J., Connecting Titanium-Oxo Clusters by Nitrogen Heterocyclic Ligands to Produce Multiple Cluster Series with Photocatalytic H₂ Evolution Activities. *Crystal Growth & Design* **2017**, *17* (7), 3592-3595.

- (13) Hong, Z.-F.; Xu, S.-H.; Yan, Z.-H.; Lu, D.-F.; Kong, X.-J.; Long, L.-S.; Zheng, L.-S., A Large Titanium Oxo Cluster Featuring a Well-Defined Structural Unit of Rutile. *Crystal Growth & Design* **2018**, *18* (9), 4864-4868.
- (14) Kryukov, A. I.; Korzhak, A. V.; Kuchmii, S. Y., Photocatalytic formation of hydrogen in alcoholic solutions of titanium tetrachloride. *Theoretical and Experimental Chemistry* **1984**, *20* (2), 161-168.
- (15) Kryukov, A. I.; Korzhak, A. V.; Kuchmii, S. Y., Photolysis of titanium tetrachloride in ethanol under the action of light with $\lambda=254$ nm. *Theoretical and Experimental Chemistry* **1984**, *20* (1), 34-40.
- (16) Nguyen, H. L.; Gándara, F.; Furukawa, H.; Doan, T. L. H.; Cordova, K. E.; Yaghi, O. M., A Titanium–Organic Framework as an Exemplar of Combining the Chemistry of Metal– and Covalent–Organic Frameworks. *Journal of the American Chemical Society* **2016**, *138* (13), 4330-4333.
- (17) Assi, H.; Mouchaham, G.; Steunou, N.; Devic, T.; Serre, C., Titanium coordination compounds: from discrete metal complexes to metal–organic frameworks. *Chemical Society Reviews* **2017**, *46* (11), 3431-3452.
- (18) Shen, L.; Luo, M.; Huang, L.; Feng, P.; Wu, L., A Clean and General Strategy To Decorate a Titanium Metal–Organic Framework with Noble-Metal Nanoparticles for Versatile Photocatalytic Applications. *Inorganic Chemistry* **2015**, *54* (4), 1191-1193.
- (19) Li, Z.; Xiao, J.-D.; Jiang, H.-L., Encapsulating a Co(II) Molecular Photocatalyst in Metal–Organic Framework for Visible-Light-Driven H₂ Production: Boosting Catalytic Efficiency via Spatial Charge Separation. *ACS Catalysis* **2016**, *6* (8), 5359-5365.
- (20) Navarro Amador, R.; Carboni, M.; Meyer, D., Sorption and photodegradation under visible light irradiation of an organic pollutant by a heterogeneous UiO-67–Ru–Ti MOF obtained by post-synthetic exchange. *RSC Advances* **2017**, *7* (1), 195-200.
- (21) Wang, C.; Xie, Z.; deKrafft, K. E.; Lin, W., Doping Metal–Organic Frameworks for Water Oxidation, Carbon Dioxide Reduction, and Organic Photocatalysis. *Journal of the American Chemical Society* **2011**, *133* (34), 13445-13454.
- (22) Hong, K.; Chun, H., Nonporous titanium–oxo molecular clusters that reversibly and selectively adsorb carbon dioxide. *Inorganic chemistry* **2013**, *52* (17), 9705-9707.
- (23) Horiuchi, Y.; Toyao, T.; Saito, M.; Mochizuki, K.; Iwata, M.; Higashimura, H.; Anpo, M.; Matsuoka, M., Visible-Light-Promoted Photocatalytic Hydrogen Production by Using an Amino-Functionalized Ti(IV) Metal–Organic Framework. *The Journal of Physical Chemistry C* **2012**, *116* (39), 20848-20853.
- (24) Chiesa, M.; Paganini, M. C.; Livraghi, S.; Giamello, E., Charge trapping in TiO₂ polymorphs as seen by Electron Paramagnetic Resonance spectroscopy. *Physical Chemistry Chemical Physics* **2013**, *15* (24), 9435-9447.

- (25) Kuhn, H. J.; Braslavsky, S. E.; Schmidt, R., Chemical actinometry (IUPAC Technical Report). *Pure and Applied Chemistry* **2004**, *76* (12), 2105-2146.
- (26) Cismesia, M. A.; Yoon, T. P., Characterizing chain processes in visible light photoredox catalysis. *Chemical Science* **2015**, *6* (10), 5426-5434.
- (27) Murov, S. L.; Carmichael, I.; Hug, G. L., *Handbook of photochemistry*. CRC Press: 1993.

Chapter 6. Cerium-Based Metal-Organic Layers Catalyze Hydrogen

Evolution Reaction through Dual Photoexcitation

6.1 Introduction

In Chapter 5, we discussed the synthesis of two new titanium metal-organic frameworks (MOFs), Ti₃-BPDC-Ir and Ti₃-BPDC-Ru, by doping [Ir(ppy)₂(dcbpy)]Cl or [Ru(bpy)₂(dcbpy)]Cl₂ into the Ti₃-BPDC framework. The proximity of multiple photosensitizers to the catalytic Ti₃(OH)₂ SBU facilitates multielectron transfer upon photoexcitation, leading to 80-fold enhancement in hydrogen evolution reaction (HER) activity over the corresponding homogeneous controls. This result demonstrates the role of hierarchically assembled multifunctional sites in artificial photosynthesis. Indeed, a number of MOFs have recently been studied for photocatalytic HER,¹⁻³ a key half reaction for total water splitting that provides a potential solution to renewable energy production and mitigating the negative impact of rapid fossil fuel consumption.⁴⁻⁵ The incorporation of both photosensitizers (PSs) and catalytic sites into MOF structures not only facilitates multi-electron transfer to drive photocatalytic HER but also stabilizes the PSs and catalysts via site isolation.⁶⁻⁷

However, MOF particles tend to scatter light and have low light penetration efficiency. The strict symmetry requirement of MOF building blocks constrains the ability to fine-tune their compositions for further optimization of photocatalytic activities.⁸⁻⁹ The restricted diffusion of active reaction components through MOF channels further compromises the photocatalytic efficiency.¹⁰ To address these issues, metal-organic layers (MOLs) have been developed as a new class of two-dimensional materials for photocatalytic applications.¹¹⁻¹³

Earth-abundant, cheap and readily available Ce-based materials (e.g. CeO₂, CeCl₃) have recently been demonstrated as highly active photocatalysts for a variety of photocatalytic reactions, including proton reduction,¹⁴⁻¹⁸ water oxidation,¹⁹⁻²⁰ and organic photoreactions.^{12, 21-25}

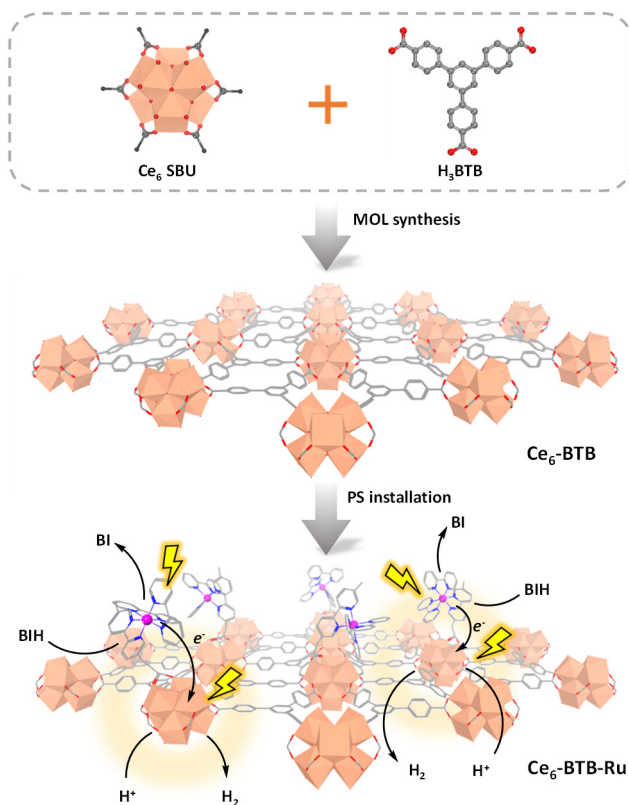


Figure 6-1. Schematic showing the synthesis of Ce₆-BTB and Ce₆-BTB-Ru MOFs and photocatalytic HER by Ce₆-BTB-Ru through dual photoexcitation. Ce, Ru, N and O atoms are shown in orange, pink, blue and red, respectively. Reprinted with permission from *Journal of the American Chemical Society*, **2020**, 142, 6866-6871. Copyright 2020 American Chemical Society.

In this chapter, we will discuss the design and synthesis of the first Ce-based MOF, Ce₆-BTB (BTB = 1,3,5-benzenetribenzoate), and its post-synthetic functionalization with photosensitizing [(MBA)Ir(ppy)₂]Cl or [(MBA)Ru(bpy)₂]Cl₂ capping ligands (MBA = 2-(5'-methyl-[2,2'-bipyridin]-5-yl)acetate, ppy = 2-phenylpyridine, bpy = 2,2'-bipyridine) to afford Ce₆-BTB-Ir or Ce₆-BTB-Ru, respectively, for photocatalytic HER. The low-lying 4f orbitals of Ce^{IV} centers in the MOFs readily accept electrons from photoreduced Ir- and Ru-PSs to generate Ce^{III}

species,²⁶⁻²⁷ which are then photoexcited to the Ce^{III*} excited states via the spin-allowed $(4f)^1 \rightarrow (5d)^1$ manifold.²⁸ The Ce^{III*} species reduce nearby protons for hydrogen production. The proximity of PSs and Ce_6 SBUs in the MOLs facilitates electron transfers and dual photoexcitation to drive photocatalytic HER (**Figure 6-1**).

6.2 Results and Discussion

6.2.1 Synthesis and Characterization of Ce_6 -BTB MOL

$(NH_4)_2Ce(NO_3)_6$ (117 mg) or Ce_6 cluster (82 mg) was dissolved in H_2O (0.4 mL) at 80 °C by vigorous stirring and followed by the dropwise addition of a 1,3,5-benzenetribenzoate acid (H_3BTB , 31.3 mg) solution in DMF (1.2 mL) and formic acid (50 μ L). The mixture was stirred at 80 °C for 15 minutes and then cooled to room temperature. The mixture was reheated to 80 °C and kept at that temperature for 15 minutes to afford Ce_6 -BTB as a bright yellow solid (**Figure 6-2**). The resultant Ce_6 -BTB MOL was centrifuged and washed with DMF three times, then dispersed in DMF for further use.

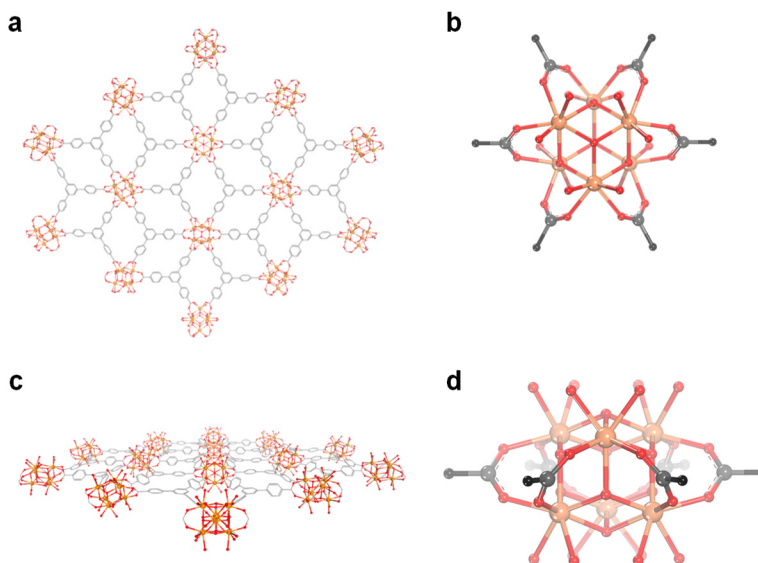


Figure 6-2. Views of Ce_6 -BTB (a) and Ce_6 SBU (b) along the vertical direction. Views of Ce_6 -BTB (c) Ce_6 SBU (d) along the lateral direction. Reprinted with permission from *Journal of the American Chemical Society*, 2020, 142, 6866-6871. Copyright 2020 American Chemical Society.

Power X-ray diffraction (PXRD) analysis showed that the as-synthesized Ce₆-BTB material adopted the same structure as the reported Hf₆-BTB MOL (**Figure 6-3**).²⁹

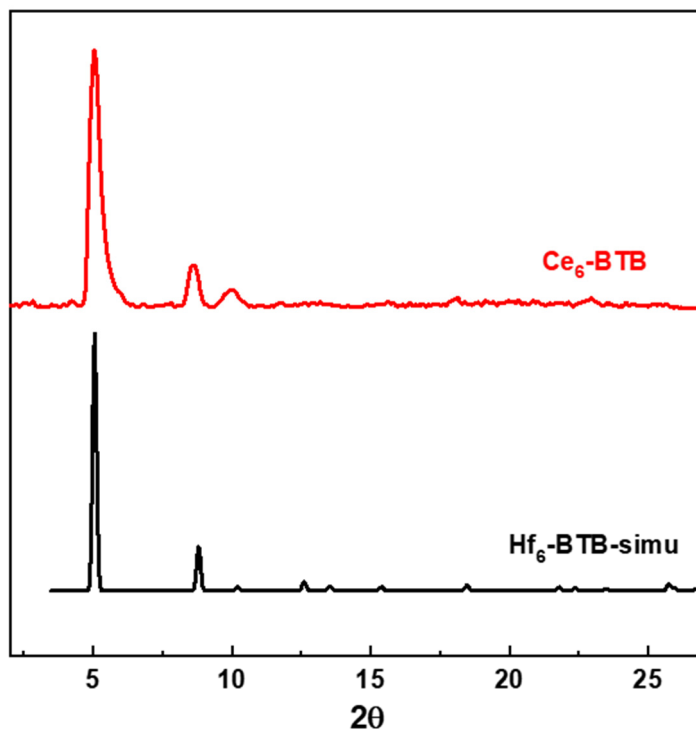


Figure 6-3. PXRD pattern of Ce₆-BTB MOL in comparison to the simulated pattern of Hf₆-BTB MOL.

To determine the formula of Ce₆-BTB, 2 mg Ce₆-BTB was dried under vacuum and then digested in 50 μL D₃PO₄. The mixture was sonicated for 10 min, followed by the addition of 500 μL DMSO-*d*₆ and 50 μL D₂O, and analyzed by ¹H NMR. No formate peak was observed when compared to those of BTB ligands, indicating H₂O/OH⁻ capping groups on the Ce₆ SBUs (**Figure 6-4**). The formula of Ce₆-BTB was thus determined to be Ce₆(μ₃-O)₄(μ₃-OH)₄(μ-OH)₆(μ-H₂O)₆(BTB)₂.

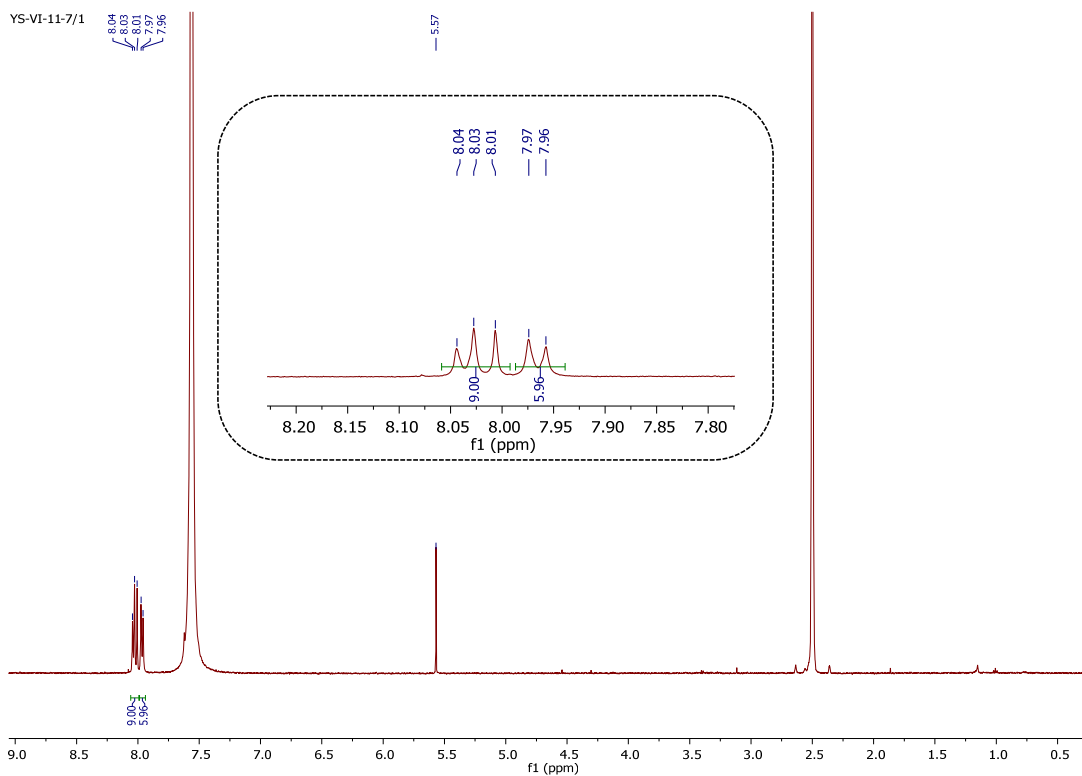


Figure 6-4. ^1H NMR spectra of digested $\text{Ce}_6\text{-BTB}$. Reprinted with permission from *Journal of the American Chemical Society*, **2020**, 142, 6866-6871. Copyright 2020 American Chemical Society.

This formula was supported by thermogravimetric analysis (TGA) (**Figure 6-5**). The first weight loss (23.9%) in the 25 to 210 °C temperature range corresponds to the removal of adsorbed solvents in the MOL. The second weight loss (51.0%) in the 210-600 °C temperature range corresponds to decomposition of the MOL to metal oxides, consistent with a calculated weight loss of 50.9% based on the conversion of $\text{Ce}_6(\mu_3\text{-O})_4(\mu_3\text{-OH})_4(\mu\text{-OH})_6(\mu\text{-H}_2\text{O})_6(\text{BTB})_2$ to 6CeO_2 .

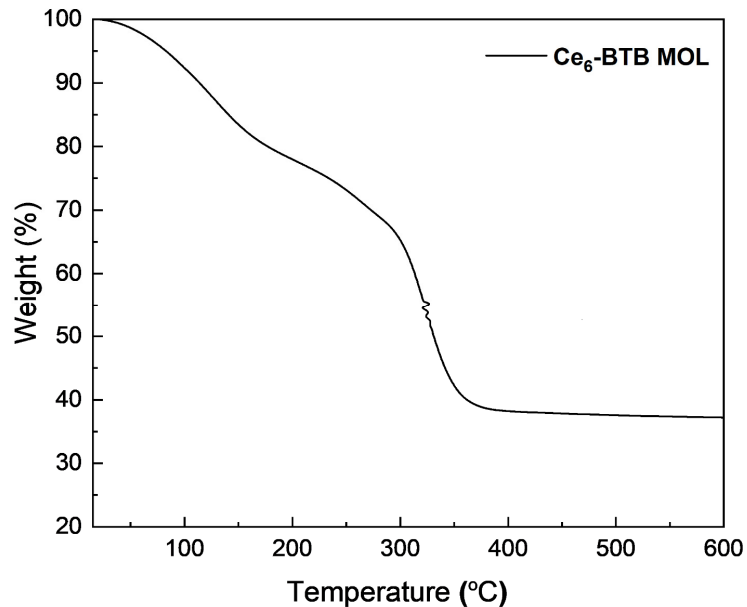


Figure 6-5. TGA curve of freshly prepared Ce₆-BTB in the 25 - 600 °C range. Reprinted with permission from *Journal of the American Chemical Society*, **2020**, 142, 6866-6871. Copyright 2020 American Chemical Society.

Transmission electron microscopy (TEM) imaging showed Ce₆-BTB as ultrathin nanoplates of ~500 nm in diameter (**Figure 6-6a**). High-resolution TEM (HRTEM) imaging confirmed the topological structure of Ce₆-BTB MOL with lattice points corresponding to Ce₆ SBUs and the fast Fourier transform (FFT) revealed a six-fold symmetry that is consistent with the projection of Ce₆-BTB down the vertical direction (**Figure 6-6b**). The distance between two adjacent spots on the HRTEM was measured to be ~2.0 nm, matching the distance between adjacent Ce₆ SBUs.

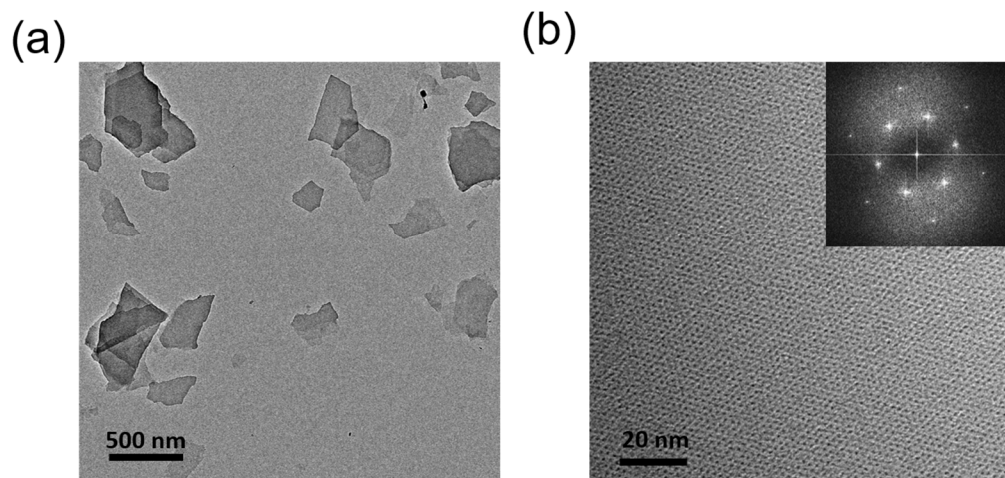


Figure 6-6. TEM (a) and HRTEM (b) of Ce₆-BTB. Reprinted with permission from *Journal of the American Chemical Society*, **2020**, 142, 6866-6871. Copyright 2020 American Chemical Society.

The monolayer nature of Ce₆-BTB was confirmed by atomic force microscopy (AFM) imaging (**Figure 6-7**). Nanoplates of Ce₆-BTB exhibited a thickness of ~1.2 nm, which is similar to that of Hf₆-BTB MOL and consistent to the modeled height of Ce₆ SBUs (**Figure 6-8**).

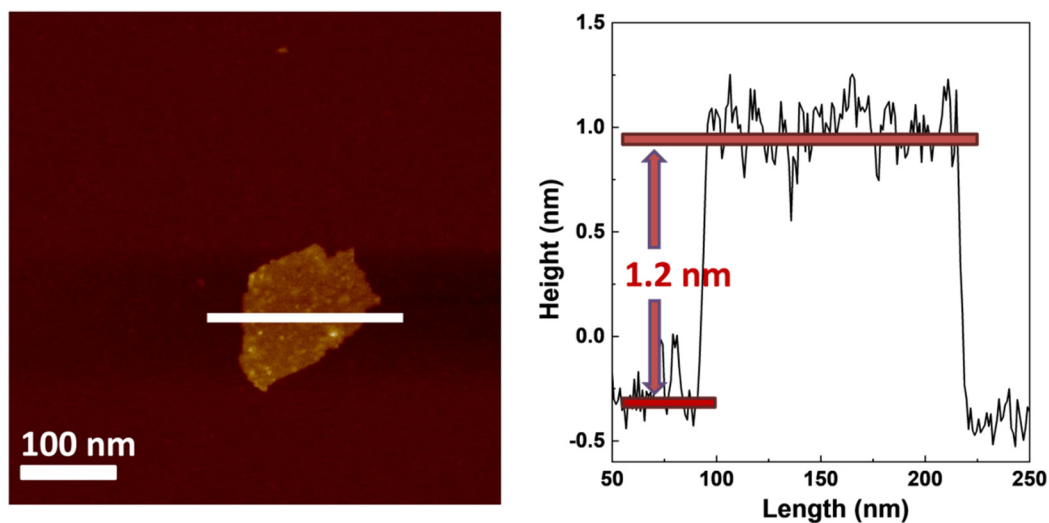


Figure 6-7. AFM topography and height profile of Ce₆-BTB. Reprinted with permission from *Journal of the American Chemical Society*, **2020**, 142, 6866-6871. Copyright 2020 American Chemical Society.

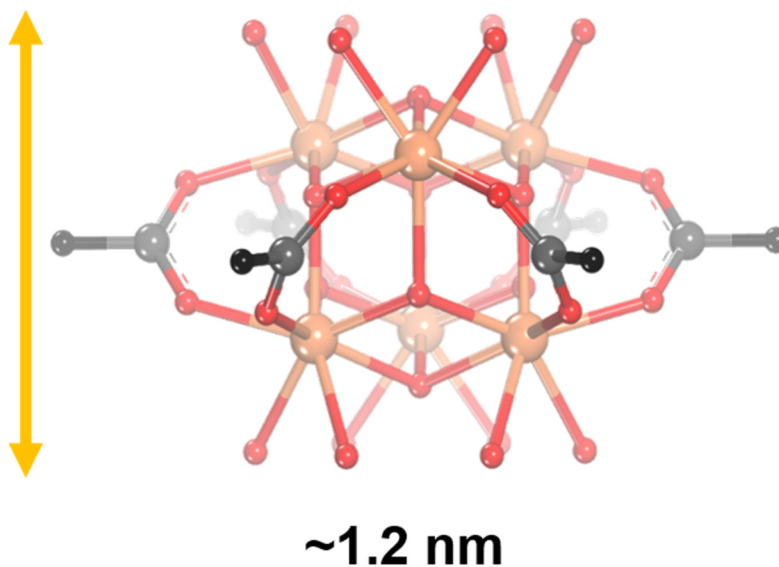


Figure 6-8. Schematic showing a Ce₆ SBU with an estimated height of ~1.2 nm. Reprinted with permission from *Journal of the American Chemical Society*, **2020**, 142, 6866-6871. Copyright 2020 American Chemical Society.

6.2.2 Synthesis and Characterization of Ce₆-BTB-Ir and Ce₆-BTB-Ru

The photosensitizing capping ligands [(HMBA)Ir(ppy)₂]Cl and [(HMBA)Ru(bpy)₂]Cl₂ were synthesized from the reaction between MeMBA (Methyl 2-(5'-methyl-[2,2'-bipyridin]-5-yl)acetate) and [Ir(ppy)₂Cl]₂ or Ru(bpy)₂Cl₂, respectively, followed by mild hydrolysis of the ester groups.

Ce₆-BTB-Ru was synthesized by heating a mixture of Ce₆-BTB and (HMBA)Ru(bpy)₂]Cl₂ in DMF at 60 °C overnight. The light red precipitate was collected by centrifugation and washed with DMF three times and acetonitrile three times. The ratio between Ce and Ru was determined to be ~12:1 by ICP-MS, corresponding to one [(HMBA)Ru(bpy)₂]Cl₂ for every two Ce₆ SBUs.

Ce₆-BTB-Ir was similarly synthesized by treating Ce₆-BTB suspension and [(HMBA)Ir(ppy)₂]Cl at 60 °C. The orange precipitate was collected by centrifugation and washed

with DMF three times and acetonitrile three times. The ratio between Ce and Ir was determined to be ~12:1 by ICP-MS, corresponding to one [(HMBA)Ir(ppy)₂]Cl on every two Ce₆ SBUs.

The empirical formulae of Ce₆-BTB-Ir and Ce₆-BTB-Ru are thus approximated as Ce₆(μ₃-O)₄(μ₃-OH)₄(μ-OH)_{5.5}(μ-H₂O)_{5.5}(BTB)₂[(MBA)Ir(ppy)₂Cl]_{0.5} and Ce₆(μ₃-O)₄(μ₃-OH)₄(μ-OH)_{5.5}(μ-H₂O)_{5.5}(BTB)₂[(MBA)Ru(bpy)₂Cl₂]_{0.5}, respectively. These formulae were supported by thermogravimetric analysis results which showed residual weights of 45.5% (expected 47.1%) and 45.4% (expected 45.9%) for Ce₆-BTB-Ir and Ce₆-BTB-Ru, respectively.

In the TGA of Ce₆-BTB-Ir, the first weight loss (20.7%) in the 25 to 240 °C temperature range corresponded to the removal of adsorbed solvents in the MOL. The second weight loss (54.5%) in the 240-600 °C temperature range corresponded to decomposition of the MOL to metal oxides, consistent with a calculated weight loss of 52.9% based on the conversion of Ce₆(μ₃-O)₄(μ₃-OH)₄(μ-OH)_{5.5}(μ-H₂O)_{5.5}(BTB)₂[(MBA)Ir(ppy)₂Cl]_{0.5} to 6CeO₂ and 0.5 IrO₂ (**Figure 6-9**).

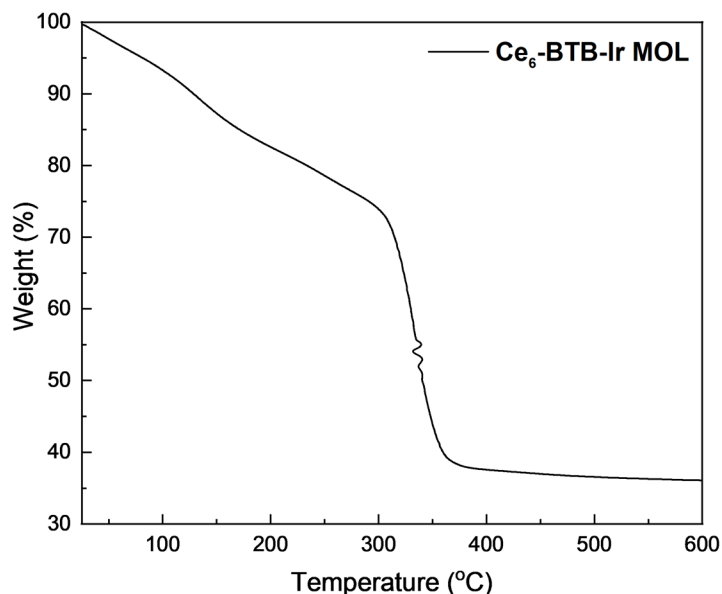


Figure 6-9. TGA curve of freshly prepared Ce₆-BTB-Ir in the 25 - 600 °C range. Reprinted with permission from *Journal of the American Chemical Society*, **2020**, 142, 6866-6871. Copyright 2020 American Chemical Society.

In the TGA of Ce₆-BTB-Ru, the first weight loss (16.8%) in the 25 to 210 °C temperature range corresponds to the removal of adsorbed solvents in the MOL. The second weight loss (54.6%) in the 210-600 °C temperature range corresponds to decomposition of the MOL to metal oxides, consistent with a calculated weight loss of 54.1% based on the conversion of Ce₆(μ₃-O)₄(μ₃-OH)₄(μ-OH)_{5.5}(μ-H₂O)_{5.5}(BTB)₂[(MBA)Ru(bpy)₂Cl₂]_{0.5} to 6CeO₂ and 0.5 RuO₂.

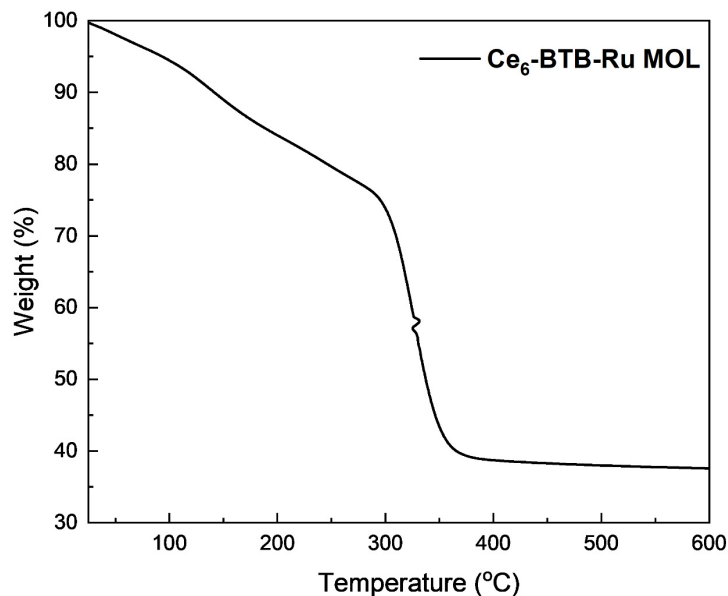


Figure 6-10. TGA curve of freshly prepared Ce₆-BTB-Ru in the 25 - 600 °C range. Reprinted with permission from *Journal of the American Chemical Society*, **2020**, 142, 6866-6871. Copyright 2020 American Chemical Society.

TEM and HRTEM images showed that Ce₆-BTB-Ir (**Figure 6-11**) and Ce₆-BTB-Ru (**Figure 6-12**) exhibited similar sizes and morphologies to Ce₆-BTB.

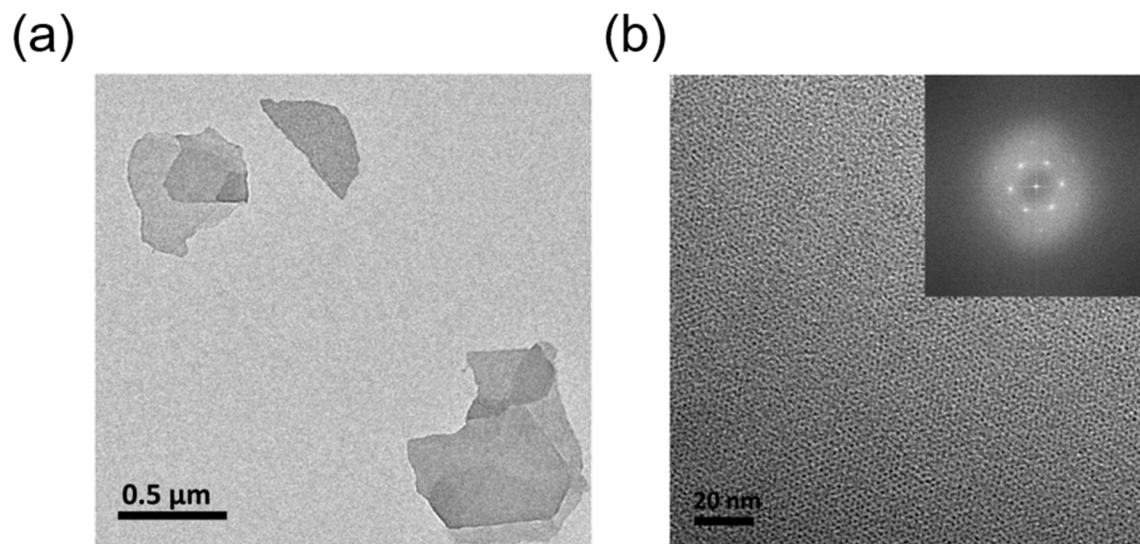


Figure 6-11. TEM (a) and HRTEM images (b) of Ce₆-BTB-Ir. Reprinted with permission from *Journal of the American Chemical Society*, **2020**, 142, 6866-6871. Copyright 2020 American Chemical Society.

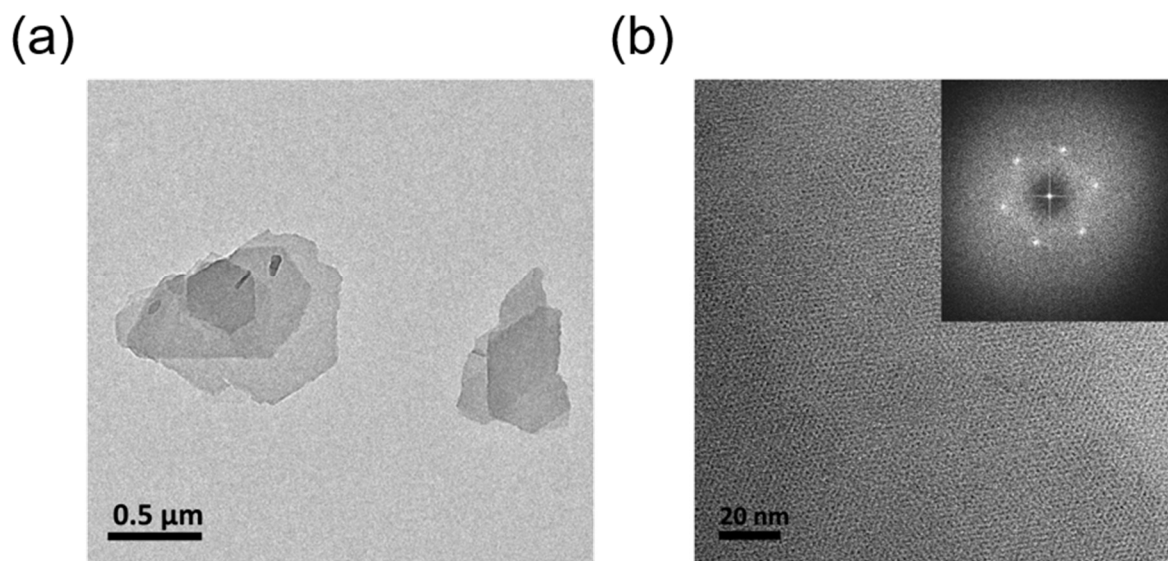


Figure 6-12. TEM (a) and HRTEM images (b) of Ce₆-BTB-Ru. Reprinted with permission from *Journal of the American Chemical Society*, **2020**, 142, 6866-6871. Copyright 2020 American Chemical Society.

Furthermore, PXRD patterns showed both Ce₆-BTB-Ir and Ce₆-BTB-Ru maintained the same crystalline structure as Ce₆-BTB (**Figure 6-13**).

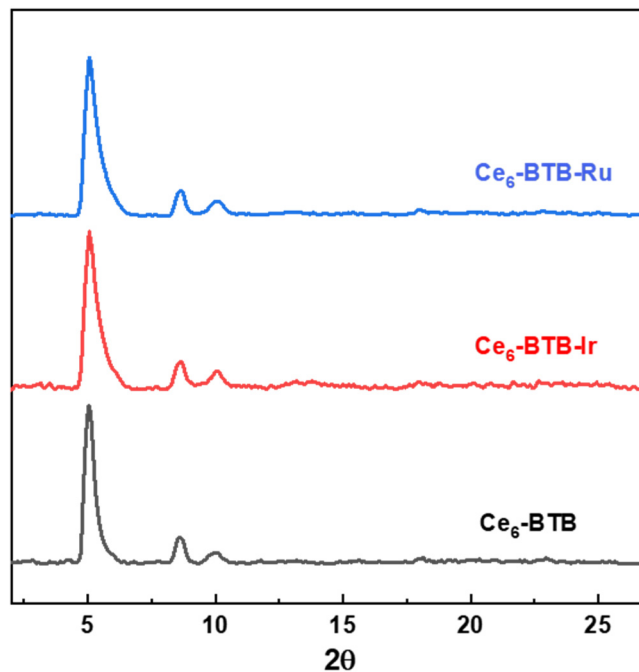


Figure 6-13. PXRD patterns of Ce₆-BTB-Ir and Ce₆-BTB-Ru in comparison to Ce₆-BTB pattern.

6.2.3 Photocatalytic Hydrogen Evolution Reaction

Photocatalytic HER was carried out in an external illumination type reaction vessel with a magnetic stirrer. Samples were prepared in 4.5 mL septum-sealed glass vials. Each sample was made up to a volume of 2.05 mL with 2.0 mL MeCN and 0.05 mL AcOH as proton source, 64 mg BIH (0.3 mmol) as sacrificial agent. Samples contained Ce₆-BTB-Ru or Ce₆-BTB-Ir (0.01 μmol based on Ru or Ir). Sample vials were capped and deoxygenated by bubbling nitrogen through for 20 min to ensure complete air removal. The solution was irradiated with a 13.9 W 350 – 700 nm solid state light source. After the hydrogen evolution reaction, the gas in the headspace of the vial was analyzed by GC to determine the amount of hydrogen generated. The turnover number (TON) [defined as n(1/2H₂)] reached 1357 for Ce₆-BTB-Ir and 484 for Ce₆-BTB-Ru after photoirradiation with a 13.9 W 350–700 nm solid-state plasma light source for 72 h (**Figure 6-14**). In comparison, the homogeneous mixtures of [Ce₆(μ₃-O)₄(μ₃-OH)₄(NH₃CH₂COO)₈(NO₃)₄(H₂O)₆]Cl₈•8H₂O (Ce₆

cluster) and photosensitizing ligands $[(\text{MeMBA})\text{Ir}(\text{ppy})_2]\text{Cl}$ or $[(\text{MeMBA})\text{Ru}(\text{bpy})_2]\text{Cl}_2$ afforded much lower TONs of 156 and 52, respectively. The photocatalytic HER activities of the Ce_6 -BTB-Ir and Ce_6 -BTB-Ru MOFs are thus 8.7 and 9.3 times higher than those of their homogeneous controls, indicating the important role of hierarchical assembly $[(\text{HMBA})\text{Ir}(\text{ppy})_2]^+$ or $[(\text{HMBA})\text{Ru}(\text{bpy})_2]^{2+}$ PSs and catalytic Ce_6 SBUs in facilitating electron transfer to drive photocatalytic HER.

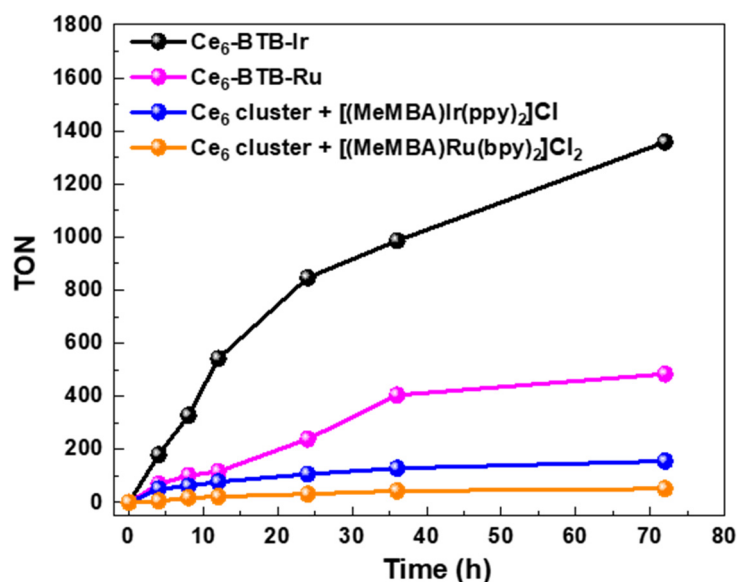


Figure 6-14. Time-dependent HER TONs of Ce_6 -BTB-Ir and Ce_6 -BTB-Ru along with homogenous controls. Reprinted with permission from *Journal of the American Chemical Society*, **2020**, 142, 6866-6871. Copyright 2020 American Chemical Society.

After photocatalytic HER, both Ce_6 -BTB-Ir and Ce_6 -BTB-Ru maintained their PXRD patterns (**Figure 6-15**) with $< 3\%$ leaching of Ce into the solution, indicating their structural stability under reaction conditions.

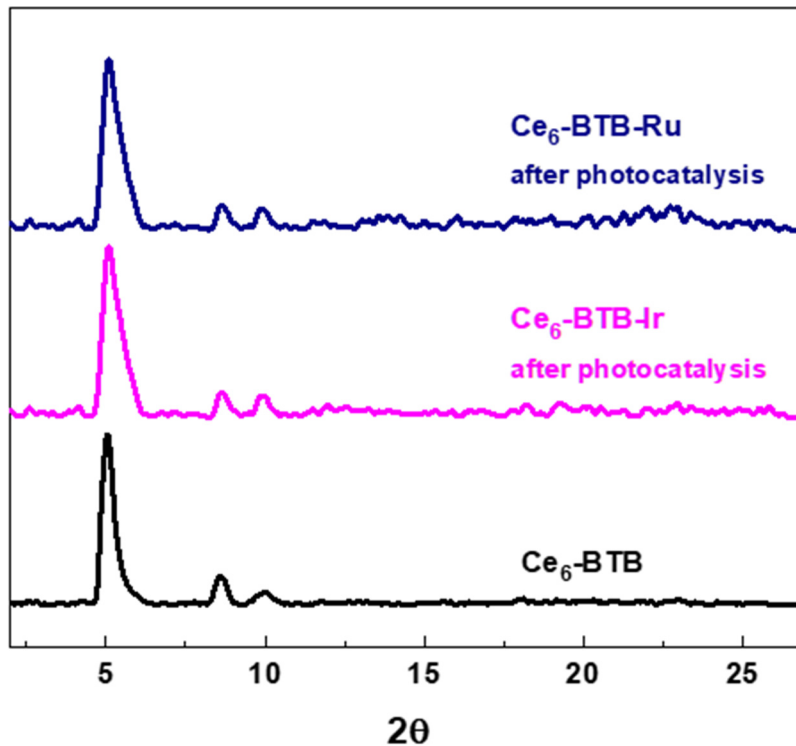


Figure 6-15. PXRD pattern of Ce₆-BTB-Ir (after reaction), and Ce₆-BTB-Ru (after reaction) in comparison to the Ce₆-BTB pattern. Reprinted with permission from *Journal of the American Chemical Society*, **2020**, 142, 6866-6871. Copyright 2020 American Chemical Society.

6.2.4 Photophysical Studies

We then performed UV-vis study of Ce₆-BTB-Ir and Ce₆-BTB-Ru. The UV-Vis spectra indicated that both [(MeMBA)Ir(ppy)₂]Cl and [(MeMBA)Ru(bpy)₂]Cl₂ and were successfully introduced into the corresponding MOL (**Figure 6-16**).

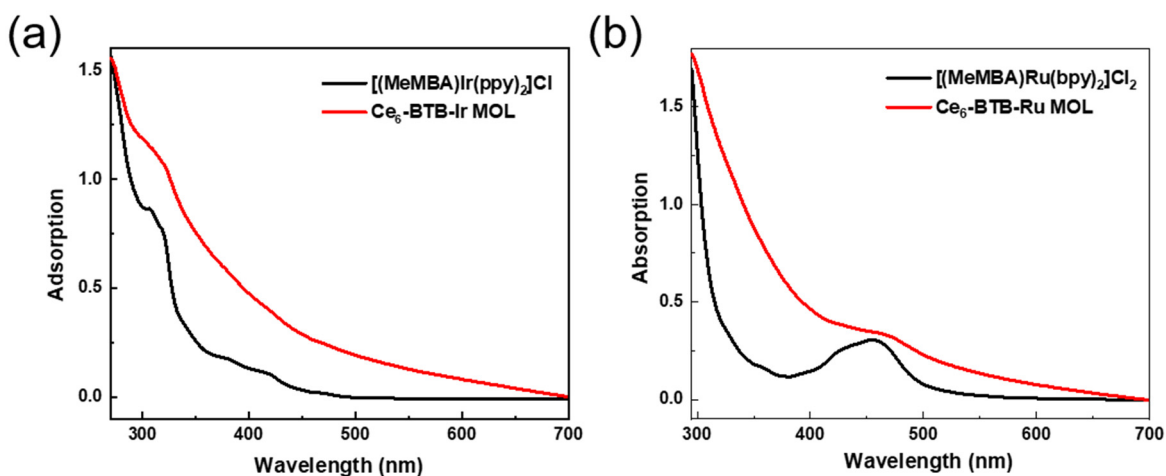


Figure 6-16. UV-vis spectra of (a) Ce₆-BTB-Ru and (b) Ce₆-BTB-Ir in comparison to their homogeneous photosensitizing ligands in DMF with a concentration of 20 μM based on Ir/Ru. Reprinted with permission from *Journal of the American Chemical Society*, **2020**, 142, 6866-6871. Copyright 2020 American Chemical Society.

We next examined whether the excited PS was reductively quenched by BIH or oxidatively quenched by Ce₆ SBUs to initiate photocatalytic HER. Luminescence spectroscopy showed that the emissions of both Ce₆-BTB-Ir and Ce₆-BTB-Ru were efficiently quenched by BIH in MeCN (**Figure 6-17**).

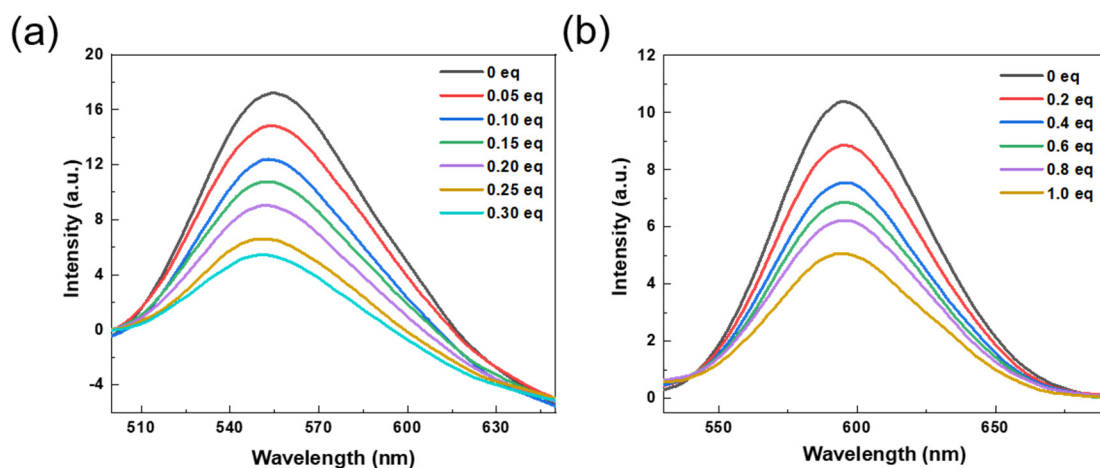


Figure 6-17. Emission spectra of Ce₆-BTB-Ru (a) and Ce₆-BTB-Ir (b) after the addition of different equivalents of BIH with 365 or 450 nm excitation, respectively. Reprinted with permission from *Journal of the American Chemical Society*, **2020**, 142, 6866-6871. Copyright 2020 American Chemical Society.

To quantitatively assess the quenching process, we determined luminescence intensities of homogeneous PSs [(MeMBA)Ir(ppy)₂]Cl and [(MeMBA)Ru(bpy)₂]Cl₂ in the presence of BIH and Ce₆ cluster in MeCN. As shown in **Figure 6-18**, and **Figure 6-19**, the luminescence of [(MeMBA)Ir(ppy)₂]Cl and [(MeMBA)Ru(bpy)₂]Cl₂ was efficiently quenched by BIH but not by Ce₆ cluster.

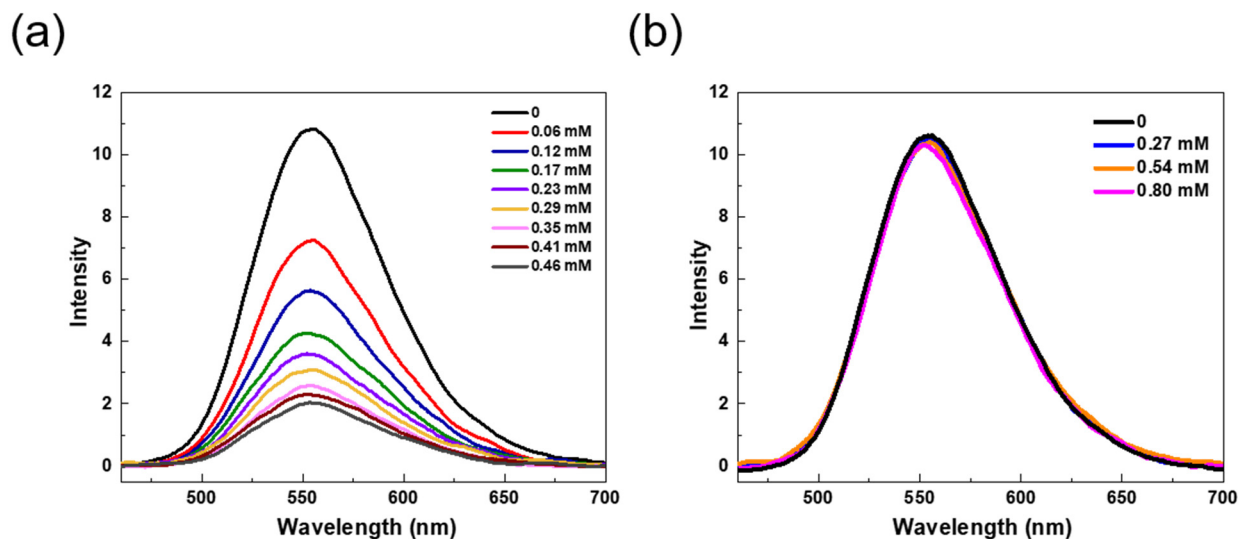


Figure 6-18. Emission Spectra of [(MeMBA)Ir(ppy)₂]Cl (30 μM) after addition of different amounts of BIH (a) and different amounts Ce₆ cluster (b) in 2 ml of MeCN under 365 nm excitation. Reprinted with permission from *Journal of the American Chemical Society*, **2020**, 142, 6866-6871. Copyright 2020 American Chemical Society.

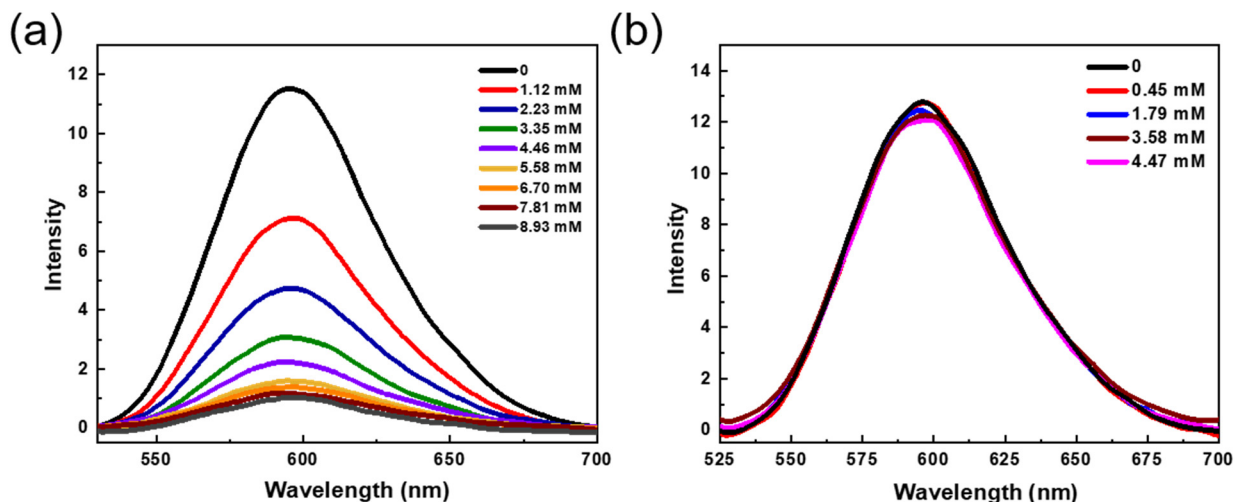


Figure 6-19. Emission Spectra of $[(\text{MeMBA})\text{Ru}(\text{bpy})_2]\text{Cl}_2$ ($30 \mu\text{M}$) after addition of different amounts of BIH (a) and different amounts Ce_6 cluster (b) in 2 ml of MeCN under 450 nm excitation. Reprinted with permission from *Journal of the American Chemical Society*, **2020**, 142, 6866-6871. Copyright 2020 American Chemical Society.

The luminescence quenching of $[(\text{MeMBA})\text{Ir}(\text{ppy})_2]\text{Cl}$ and $[(\text{MeMBA})\text{Ru}(\text{bpy})_2]\text{Cl}_2$ by BIH was fitted to the Stern-Völmer equation to afford K_{SV} values of 8.91 mM^{-1} and 1.06 mM^{-1} , respectively, indicating more efficient quenching for Ce_6 -BTB-Ir (**Figure 6-20**). These results suggest that photocatalytic HER in Ce_6 -BTB-M (M=Ru or Ir) initiates via electron transfer from BIH to the excited Ir-PS* or Ru-PS*, and the reduced $[\text{Ir-PS}]^-$ or $[\text{Ru-PS}]^-$ further transfer electron to the Ce_6 SBU to drive HER.

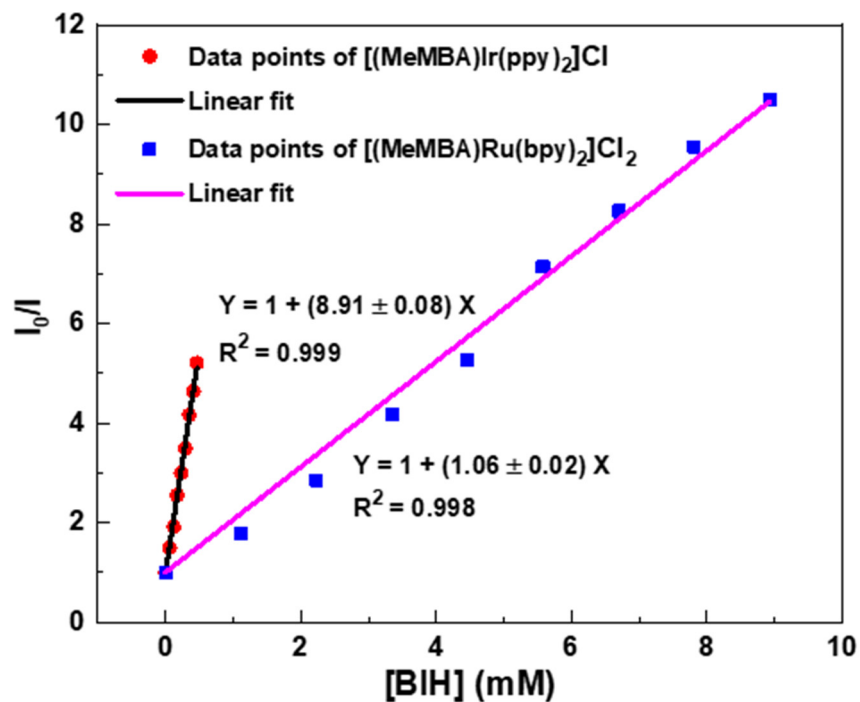


Figure 6-20. Plots of I_0/I of $[(\text{MeMBA})\text{Ir}(\text{ppy})_2]\text{Cl}$ and $[(\text{MeMBA})\text{Ru}(\text{bpy})_2]\text{Cl}_2$ as a function of BIH concentration (mM). Reprinted with permission from *Journal of the American Chemical Society*, 2020, 142, 6866-6871. Copyright 2020 American Chemical Society.

By comparison to $\text{Ce}^{\text{III}}\text{Cl}_3$ and $(\text{NH}_4)_2[\text{Ce}^{\text{IV}}(\text{NO}_3)_6]$ standards, X-ray absorption near-edge spectroscopy (XANES) analyses of $\text{Ce}_6\text{-BTB-Ir}$ and $\text{Ce}_6\text{-BTB-Ru}$ indicated the existence of Ce^{III} after photoirradiation (**Figure 6-21**), with increased intensity for the first peak at around 5726 eV.

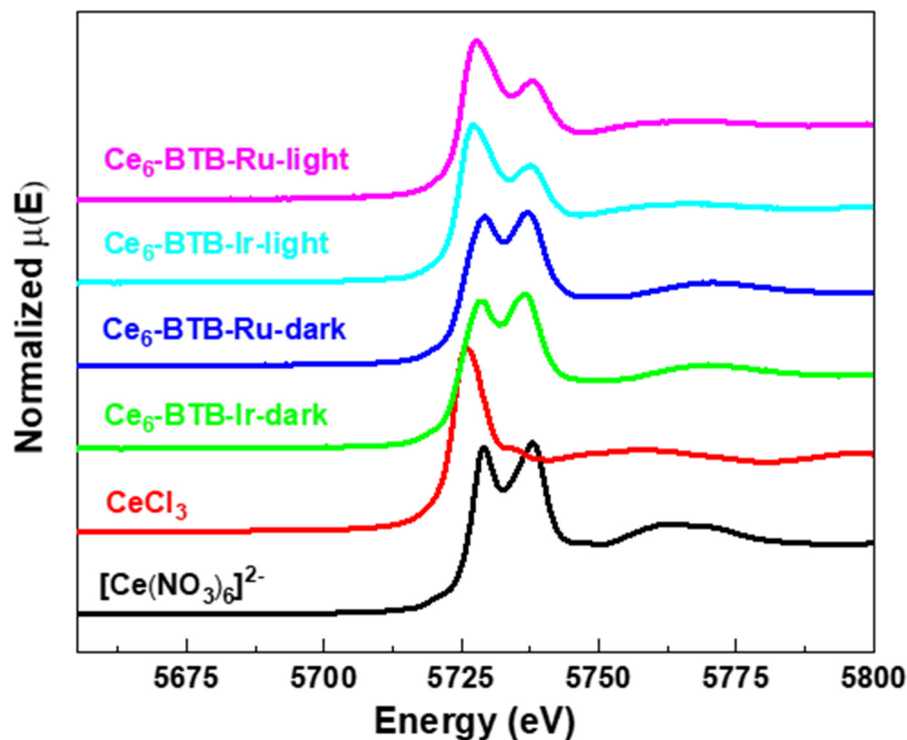


Figure 6-21. XANES spectra of Ce₆-BTB-Ir and Ce₆-BTB-Ru before and after photoirradiation. Reprinted with permission from *Journal of the American Chemical Society*, **2020**, 142, 6866-6871. Copyright 2020 American Chemical Society.

We performed linear combination fitting of the XANES spectra to quantify the amount of Ce^{III} in the MOLs after photoirradiation. As shown in **Figure 6-22a**, **Figure 6-22b**, both Ce₆-BTB-Ir and Ce₆-BTB-Ru contained ~50% Ce^{III} after photoirradiation. We propose that the Ce₆ SBU with attached PS can be fully reduced to Ce^{III} after photoirradiation in the presence of BIH. The presence of 50% Ce^{III} indicates that half of the Ce₆ SBUs in Ce₆-BTB-Ru and Ce₆-BTB-Ir have been modified with Ru- or Ir-PSs, which matches well with the empirical formula of both Ce₆-BTB-Ir and Ce₆-BTB-Ru.

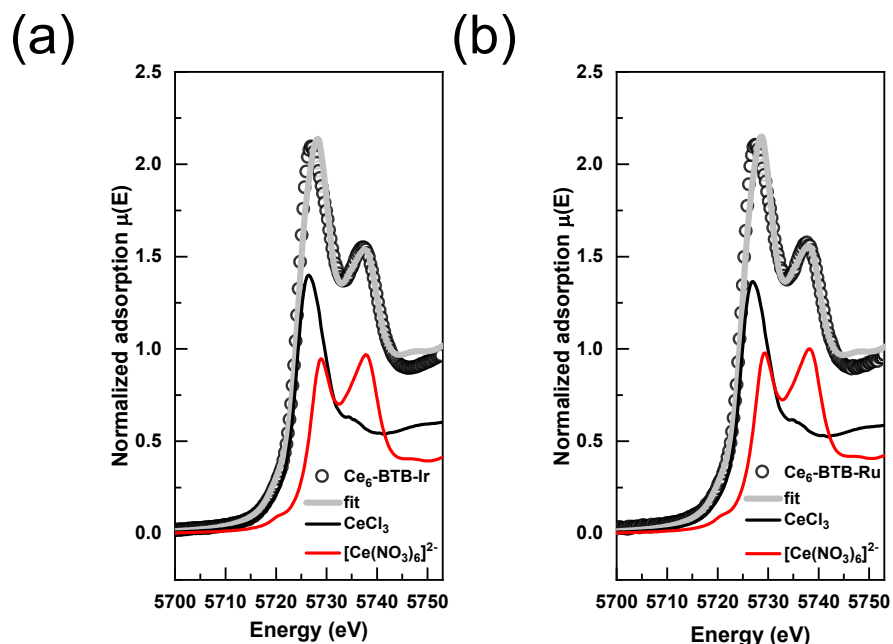


Figure 6-22. XANES fitting of (a) Ce₆-BTB-Ir and (b) Ce₆-BTB-Ru. Reprinted with permission from *Journal of the American Chemical Society*, **2020**, 142, 6866-6871. Copyright 2020 American Chemical Society.

6.2.5 Electrochemical Studies

In order to gain more insights into the HER at the Ce₆ SBU, we carried out cyclic voltammogram (CV) studies on Ce₆ cluster and Ce₆-BTB MOL. Under identical condition as HER, Ce₆ cluster showed an irreversible reduction peak with an onset potential of -1.17 V vs NHE (**Figure 6-23**). A similar CV feature was also observed for Ce₆-BTB MOL, suggesting hydrogen production commences upon the injection of one electron.

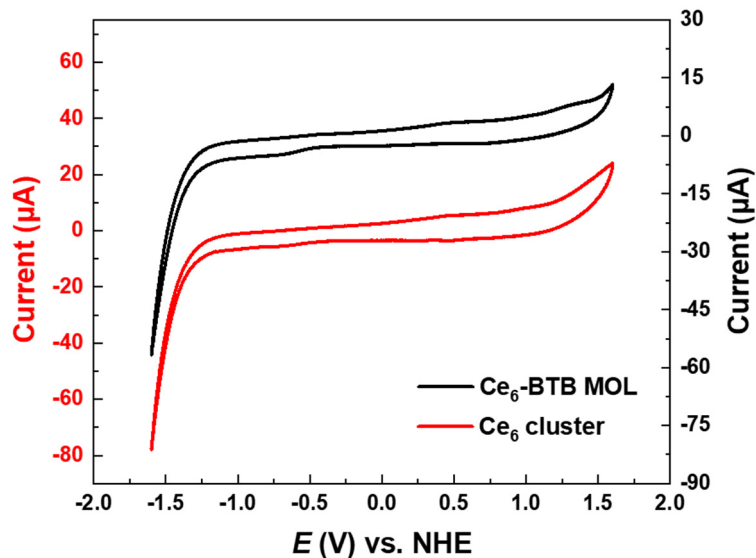


Figure 6-23. CVs of 5 mM Ce_6 cluster and 0.5 mg $\text{Ce}_6\text{-BTB MOL}$ coated on electrode surface under photocatalytic HER condition (20 mL 0.1 M TBAH/ CH_3CN solution with 0.5 ml AcOH. TBAH = Tetrabutylammonium hexafluorophosphate). Reprinted with permission from *Journal of the American Chemical Society*, **2020**, 142, 6866-6871. Copyright 2020 American Chemical Society.

Furthermore, CV scans of $[(\text{MeMBA})\text{Ir}(\text{ppy})_2]\text{Cl}$ (**Figure 6-24**) and $[(\text{MeMBA})\text{Ru}(\text{bpy})_2]\text{Cl}_2$ (**Figure 6-25**) displayed the first reduction peaks at -1.01 V and -0.93 V, respectively.

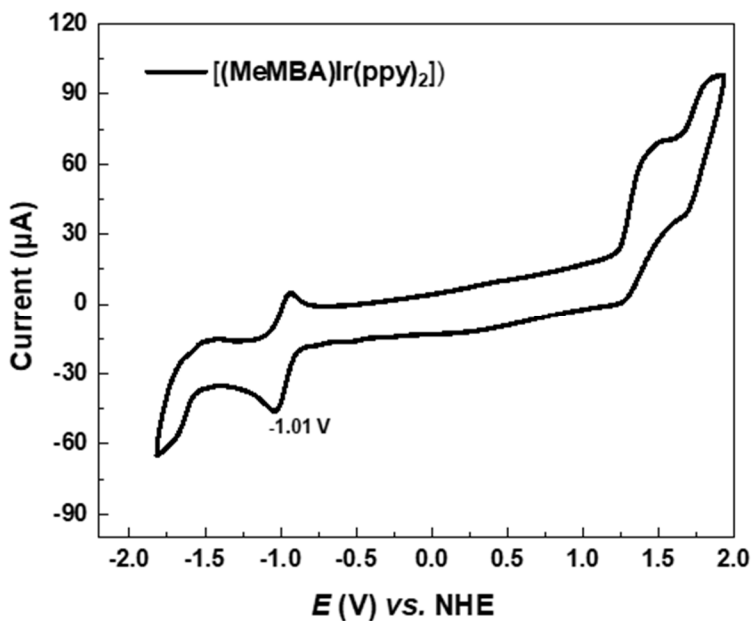


Figure 6-24. CVs of $[(\text{MeMBA})\text{Ir}(\text{ppy})_2]\text{Cl}$ in 0.1 M TBAH/MeCN (TBAH = Tetrabutylammonium hexafluorophosphate). Potential sweep rate was 100 mV/s. Reprinted with permission from *Journal of the American Chemical Society*, **2020**, 142, 6866-6871. Copyright 2020 American Chemical Society.

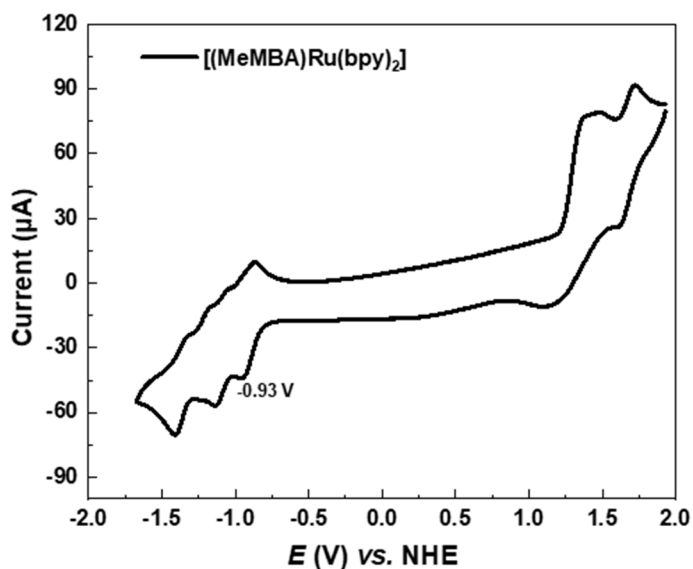


Figure 6-25. CVs of $[(\text{MeMBA})\text{Ru}(\text{bpy})_2]\text{Cl}_2$ in 0.1 M TBAH/MeCN (TBAH = Tetrabutylammonium hexafluorophosphate). Potential sweep rate was 100 mV/s. Reprinted with permission from *Journal of the American Chemical Society*, **2020**, 142, 6866-6871. Copyright 2020 American Chemical Society.

These energies are not enough to drive Ce₆ SBU-catalyzed HER (1.17 eV). Instead, we propose that further photoexcitation of Ce^{III} is needed to catalyze HER under photocatalytic conditions. Ce^{III} can be photoexcited to generate Ce^{III*} species through 4f→5d transitions²³ to drive photocatalytic HER.^{15, 17} In order to estimate the excited-state reduction potential ($E_{1/2}^*$), we followed the Rehm-Weller formalism:³⁰⁻³¹

$$E_{1/2}^* = E_{1/2} - E_{0,0} + \omega$$

where $E_{1/2}$ is the ground-state reduction potential; $E_{0,0}$ is the energy difference between zeroth vibrational states of the ground and electronic excited states and can be approximated as the emission energy of Ce^{III*}. The work function ω is usually a small contribution and is omitted here. Based on the reduction potential of Ce₆ cluster (**Figure 6-26**) and luminescence spectra of previously reported Ce^{III}₆-MOF-808 (**Figure 6-27**),³² we estimated the $E_{1/2}^*$ to be -2.63 eV. This value is negative enough to drive HER (Figure 4a).

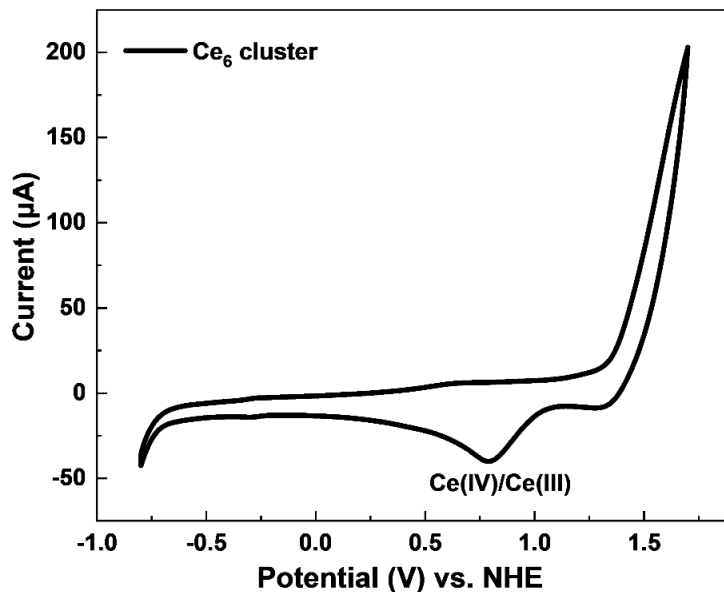


Figure 6-26. CV of Ce₆ cluster in 0.1 M TBAH/MeCN (TBAH = Tetrabutylammonium hexafluorophosphate). Potential sweep rate was 100 mV/s. Reprinted with permission from *Journal of the American Chemical Society*, **2020**, 142, 6866-6871. Copyright 2020 American Chemical Society.

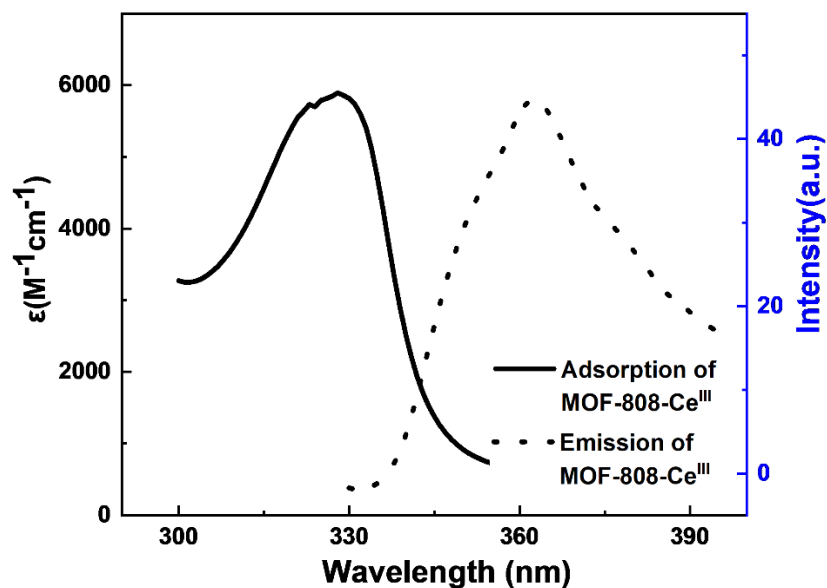


Figure 6-27. Absorption (solid line) and emission (dashed line) spectra of a Ce^{III} -MOF-808 suspension in MeCN. Reprinted with permission from *Journal of the American Chemical Society*, **2020**, 142, 6866-6871. Copyright 2020 American Chemical Society.

We performed several control experiments to support the dual photoexcitation pathway. As shown in **Figure 6-28**, when irradiated with a 450 nm light source for 24 h, Ce_6 -BTB-Ru MOL gave a low HER activity with a TON of 11 under ~ 450 nm irradiation owing to the inability to excite Ce^{III} to $\text{Ce}^{\text{III}*}$ at 450 nm. On the other hand, irradiation of Ce_6 -BTB MOL with the 350–700 nm solid-state plasma light source for 24 h afforded a low HER activity with a TON of 16, which shows the requirement of PSs to reduce Ce^{IV} to Ce^{III} in the photoreduction step. In contrast, Ce_6 -BTB-Ru showed a much higher HER activity with a TON of 239 under 350–700 nm solid-state plasma light source irradiation for 24 h.

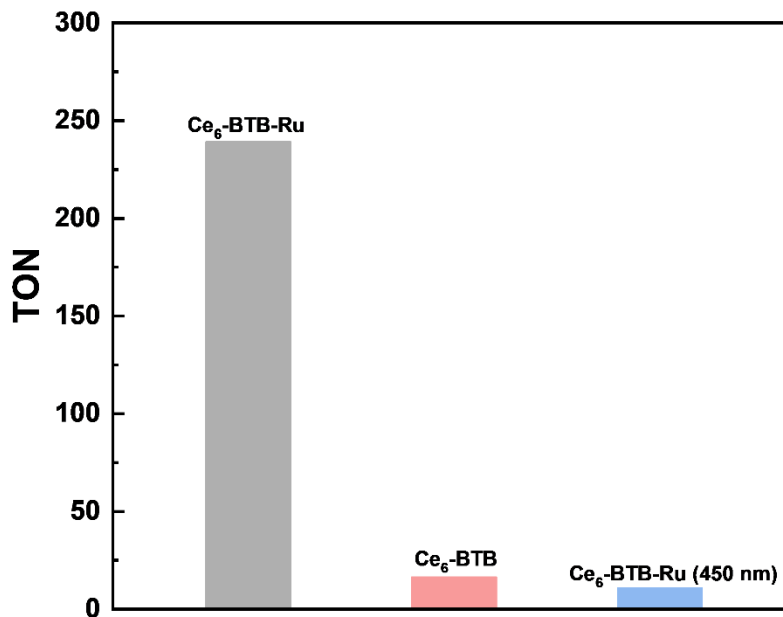


Figure 6-28. Photocatalytic activities of Ce₆-BTB-Ru under 450 nm irradiation and Ce₆-BTB and Ce₆-BTB-Ru under 350 – 700 nm irradiation for 24h. Reprinted with permission from *Journal of the American Chemical Society*, **2020**, 142, 6866-6871. Copyright 2020 American Chemical Society.

6.2.6 Proposed Reaction Mechanism

On the basis of photophysical and electrochemical results, we propose the photocatalytic HER cycle for Ce₆-BTB-Ru (**Figure 6-29**). Under photoirradiation, the [(MBA)Ru(bpy)₂]²⁺ (Ru-PS) is excited to the [(MBA)Ru(bpy)₂]^{2+*} (Ru-PS*) excited state, which is reduced by BIH to generate the photoreduced PS [(MBA)Ru(bpy)₂]⁺ ([Ru-PS]⁻). Photoreduced [Ru-PS]⁻ further transfers electron to the Ce₆ SBU to afford Ce^{III} species, followed by a second photoexcitation of Ce^{III} to generate Ce^{III*} species through a 4f → 5d transition. The Ce^{III*} species promoted the HER to release H₂ and was oxidized back to Ce^{IV}.

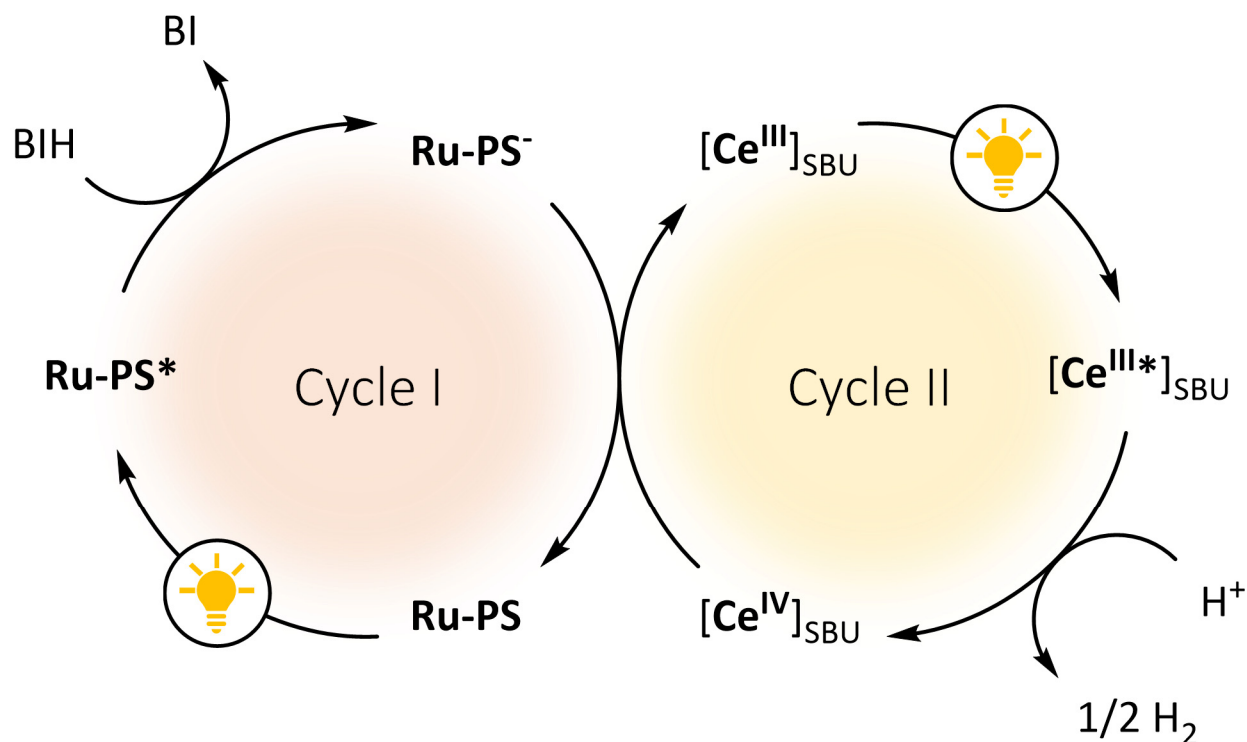


Figure 6-29. Proposed photocatalytic cycle for the hydrogen production catalyzed by Ce₆-BTB-Ru through a dual photoexcitation pathway. Reprinted with permission from *Journal of the American Chemical Society*, 2020, 142, 6866-6871. Copyright 2020 American Chemical Society.

With the well-defined structure of catalytic centers in the MOL, we further studied the photocatalytic HER mechanism and proposed a catalytic HER cycle on the Ce₆ SBUs. As shown in **Figure 6-30a**, after photoreduction by the anchored Ru or Ir PS, the Ce^{III} of the SBUs is subsequently photoexcited. The photoexcited Ce^{III*} species, which feature potent reductive potential, transfers an electron to the nearby proton to generate hydrogen radical. Such a Ce^{IV}⋯H[•] species can accept another electron from a photoreduced photosensitizer to generate a Ce^{IV}-hydride intermediate. Protonation of Ce^{IV}-hydride produces hydrogen and regenerates the Ce^{IV}-based catalyst. To support the proposed mechanism, we introduced TEMPO (TEMPO = 2,2,6,6-tetramethyl-1-piperidinyloxy) as a radical scavenger to photocatalytic HER systems. Under identical reaction conditions, addition of 1 equiv. of TEMPO (w.r.t BIH) nearly completely shut

down the photocatalytic HER process with the TON dropping from 230 to 5 in 24 h using Ce₆-BTB-Ru as the photocatalyst. This result shows radical quenching intercepts the HER process by preventing the generation of the key Ce^{IV}-hydride intermediate from the Ce^{IV}···H[•] species for H₂ production (**Figure 6-30b**).

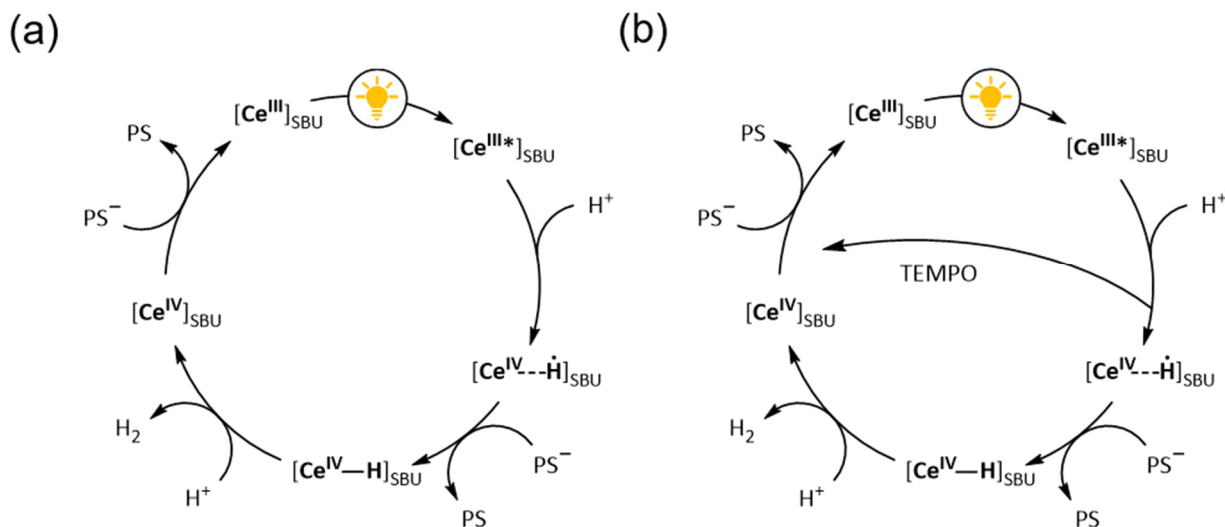


Figure 6-30. (a) Proposed photocatalytic HER pathway on the Ce site. (b) Shut down of photocatalytic HER on the Ce site with TEMPO as a radical scavenger. Reprinted with permission from *Journal of the American Chemical Society*, 2020, 142, 6866-6871. Copyright 2020 American Chemical Society.

6.3 Conclusion

In this chapter, we discussed the synthesis of the first Ce-based MOL and post-synthetically functionalized Ce₆-BTB with the photosensitizing capping ligands. The proximity of PSs to the catalytic Ce₆ SBUs facilitates electron transfer upon photoexcitation, leading to 8.7- to 9.3-fold enhancement in HER activity over their homogeneous controls. Photophysical and electrochemical studies revealed a dual photoexcitation pathway whereby the photoreduced PS convert Ce^{IV} to Ce^{III} which is further photoexcited to Ce^{III*} for HER. This work shows the potential of using multifunctional MOLs to uncover new photochemical processes relevant to artificial photosynthesis.

6.4 Experimental

6.4.1 Material and Methods

All the reactions and manipulations were carried out under N₂ with the use of a glovebox or Schlenk technique, unless otherwise indicated. Tetrahydrofuran and toluene were dried by passing through a neutral alumina column under N₂. Benzene, *d*₆-benzene, and *n*-octane were distilled over CaH₂.

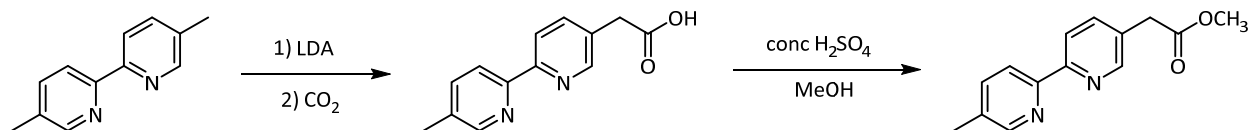
Powder X-ray diffraction (PXRD) data was collected on a Bruker D8 Venture diffractometer using Cu K α radiation source ($\lambda = 1.54178 \text{ \AA}$). N₂ sorption experiments were performed on a Micrometrics TriStar II 3020 instrument. Thermogravimetric analysis (TGA) was performed in air using a Shimadzu TGA-50 equipped with a platinum pan and heated at a rate of 1.5 °C per min. Transmission electron microscopy (TEM) images were taken on a TECNAI F30 HRTEM. Atomic force microscopy (AFM) images were taken on a Bruker V /Multimode 8 instrument. ICP-MS data was obtained with an Agilent 7700x ICP-MS and analyzed using ICP-MS MassHunter version B01.03. Samples were diluted in a 2% HNO₃ matrix and analyzed with a ¹⁵⁹Tb internal standard against a 12-point standard curve over the range from 0.1 ppb to 500 ppb. The correlation was >0.9997 for all analyses of interest. Data collection was performed in Spectrum Mode with five replicates per sample and 100 sweeps per replicate. Cyclic voltammograms (CVs) were recorded on a CHI420 electrochemistry workstation with regular 3 electrode systems. Measurements were recorded using a glassy carbon disk working electrode (S = 0.07 cm²) and a platinum wire as the counter electrode. The Ag/AgCl/1 M KCl electrode was used as the reference electrode in all experiments. ¹H and ¹³C NMR spectra were recorded on a Bruker NMR 500 DRX spectrometer at 500 MHz, referenced to the proton resonance resulting from incomplete deuteration of CDCl₃ (δ 7.26), C₆D₆ (δ 7.16), CD₃OD (3.31) or DMSO-*d*₆

(δ 2.50). The following abbreviations are used herein: s: singlet, d: doublet, t: triplet, q: quartet, m: multiplet, br: broad, app: apparent. Amounts of H₂ generated in the photocatalytic experiments were determined by gas chromatography (GC) using an SRI 8610C Gas Chromatograph with the nitrogen carrier gas and a TCD detector.

6.4.2 Synthesis of [(HMBA)Ir(ppy)₂]Cl and [(HMBA)Ru(bpy)₂]Cl₂

Synthesis of MeMBA Methyl 2-(5'-methyl-[2,2'-bipyridin]-5-yl)acetate (MeMBA) was synthesized in two steps from 5,5'-dimethyl-2,2'-bipyridine according to a modified literature method. In a pre-dried round flask, di-isopropylamine (0.8 mL, 6.5 mmol) was dissolved in THF (3 mL) and cooled to -78 °C before the dropwise addition of n-BuLi (3.5 mL 5.6 mmol). The resulting solution was stirred for 30 mins at -78 °C before the quick addition of a solution of 5,5'-dimethyl-2,2'-bipyridine (1.0 g, 5.5 mmol) in THF (12 mL) and the resultant mixture was stirred for 2 h at this temperature. Dry CO₂ was then bubbled through at the same temperature for 1 h and the mixture was warmed to ambient temperature with CO₂ still being bubbled through. Ether (100 mL) was added to the resulting semisolid white mass, and the mixture was extracted with 1 M NaOH aqueous solution (20 mL \times 3). The alkaline layer was acidified to pH 1 with concentrated HCl and then extracted with ether (20 mL \times 3). The acidic solution was buffered to pH 5 with sodium acetate. After removing the solvent, the crude product was directly used for the next step without purification.

Scheme 6-1. Schematic representation of the synthesis of MeMBA. Reprinted with permission from *Journal of the American Chemical Society*, **2020**, 142, 6866-6871. Copyright 2020 American Chemical Society.



To a methanol solution (40 mL) containing the above crude product was added conc. H₂SO₄ (1.0 mL) dropwise, and the solution was stirred at reflux for 24 hours. After being cooled to room temperature, the solution was neutralized with saturated NaHCO₃ aqueous solution and then extracted with DCM several times. The combined organic layer was washed with water and saturated NaCl and dried over anhydrous sodium sulfate. After removing the solvent, the crude product was subjected to column chromatography (SiO₂, CH₂Cl₂/MeOH/TEA, 100:5:1) to give the pure product MeMBA as an off-white solid (930 mg, 70% in two steps). ¹H NMR (500 MHz, Chloroform-*d*) δ 8.56 (s, 1H), 8.50 (s, 1H), 8.35 (d, *J* = 8.2 Hz, 1H), 8.28 (d, *J* = 8.1 Hz, 1H), 7.75 (d, *J* = 8.1 Hz, 1H), 7.63 (d, *J* = 8.1 Hz, 1H), 3.71 (d, *J* = 1.4 Hz, 3H), 3.70 – 3.67 (m, 2H), 2.39 (s, 3H) (**Figure 6-31**). ¹³C NMR (126 MHz, Chloroform-*d*) δ 171.12, 154.89, 153.07, 149.63, 149.37, 137.88, 137.79, 133.60, 129.55, 120.73, 120.71, 52.32, 38.18, 18.38 (**Figure 6-32**). HR-MS (ESI, positive mode): *m/z* calc'd for C₁₄H₁₅N₂O₂ [M+H]⁺: 243.1034, found 243.1153.

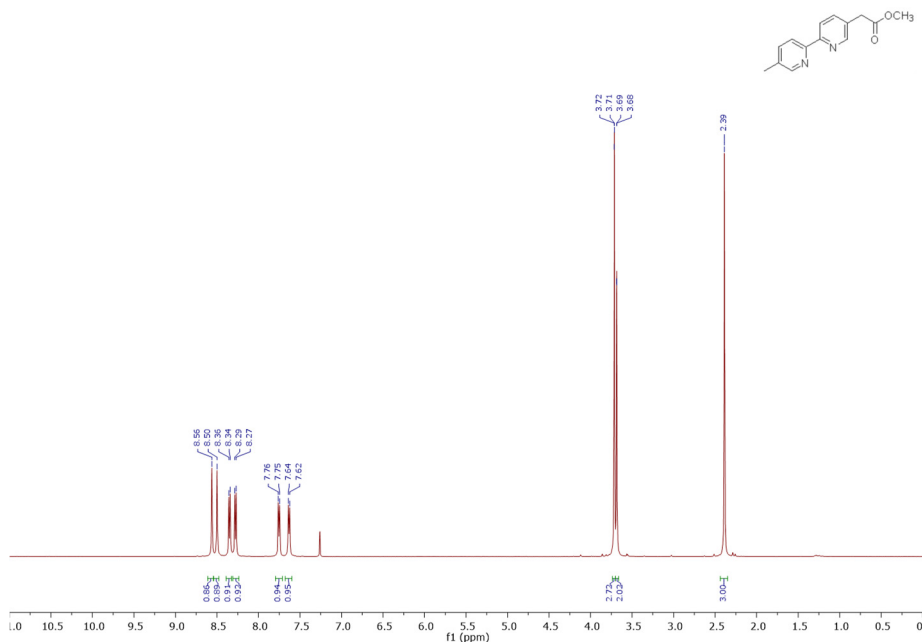


Figure 6-31. ¹H NMR spectrum of MeMBA (500 MHz) in CDCl₃. Reprinted with permission from *Journal of the American Chemical Society*, **2020**, 142, 6866-6871. Copyright 2020 American Chemical Society.

^{13}C NMR (126 MHz, Chloroform- d) δ 171.12, 154.89, 153.07, 149.63, 149.37, 137.88, 137.79, 133.60, 129.55, 120.73, 120.71, 52.32, 38.18, 18.38.

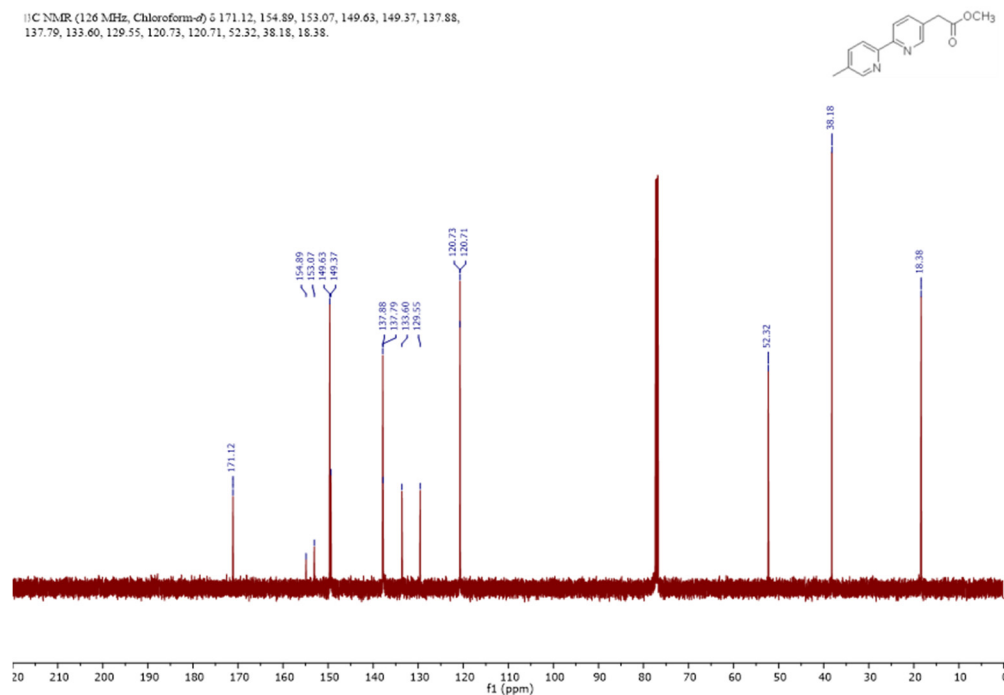


Figure 6-32. ^{13}C NMR spectrum of MeMBA (500 MHz) in CDCl_3 . Reprinted with permission from *Journal of the American Chemical Society*, **2020**, 142, 6866-6871. Copyright 2020 American Chemical Society.

Synthesis of [(HMBA)Ir(ppy) $_2$]Cl [Ir(ppy) $_2$ Cl] $_2$ (553 mg, 0.51 mmol), MeMBA (250 mg, 1.03 mmol), methanol (18 mL) and chloroform (18 mL) were added to a 100 mL thick-walled Pyrex tube. The tube was sealed and heated at 110 $^\circ\text{C}$ for 2 days. After cooling to ambient temperature, the solvent was removed under reduced pressure and the crude product was purified by column chromatography (SiO_2 , $\text{CHCl}_3/\text{MeOH}$, 10:1 to 5:1) to yield the product [(MeMBA)Ir(ppy) $_2$]Cl as a light yellow solid (770 mg, 96%). ^1H NMR (500 MHz, Chloroform- d) δ 9.47 (d, $J = 8.4$ Hz, 1H), 9.40 (d, $J = 8.4$ Hz, 1H), 8.16 (dd, $J = 8.4, 2.1$ Hz, 1H), 8.03 (dd, $J = 8.4, 2.1$ Hz, 1H), 7.91 (d, $J = 8.1$ Hz, 2H), 7.77 (td, $J = 7.8, 1.5$ Hz, 2H), 7.71 (d, $J = 2.0$ Hz, 1H), 7.68 – 7.65 (m, 2H), 7.62 (d, $J = 2.0$ Hz, 1H), 7.46 (ddd, $J = 17.2, 5.8, 1.5$ Hz, 2H), 7.06 – 6.98 (m, 4H), 6.90 (td, $J = 7.3, 1.3$ Hz, 2H), 6.31 – 6.25 (m, 2H), 3.62 (s, 3H), 3.53 (d, $J = 4.1$ Hz, 2H), 2.23 (s, 3H) (**Figure 6-33**). ^{13}C NMR (126 MHz, Chloroform- d) δ 169.73, 167.91, 167.84, 155.04,

153.40, 150.47, 150.44, 149.98, 149.72, 148.52, 148.43, 143.39, 143.38, 141.13, 140.77, 138.59, 138.02, 137.98, 134.17, 131.67, 131.61, 130.84, 130.80, 126.60, 126.39, 124.76, 123.28, 123.22, 122.60, 122.57, 119.61, 52.51, 37.83, 18.78 (**Figure 6-34**). HR-MS (ESI, positive mode): m/z calc'd for $C_{36}H_{30}N_4O_2Ir [M-Cl]^+$: 743.1998, found 743.2003.

Scheme 6-2. Schematic representation of the synthesis of [(HMBA)Ir(ppy)₂]Cl.

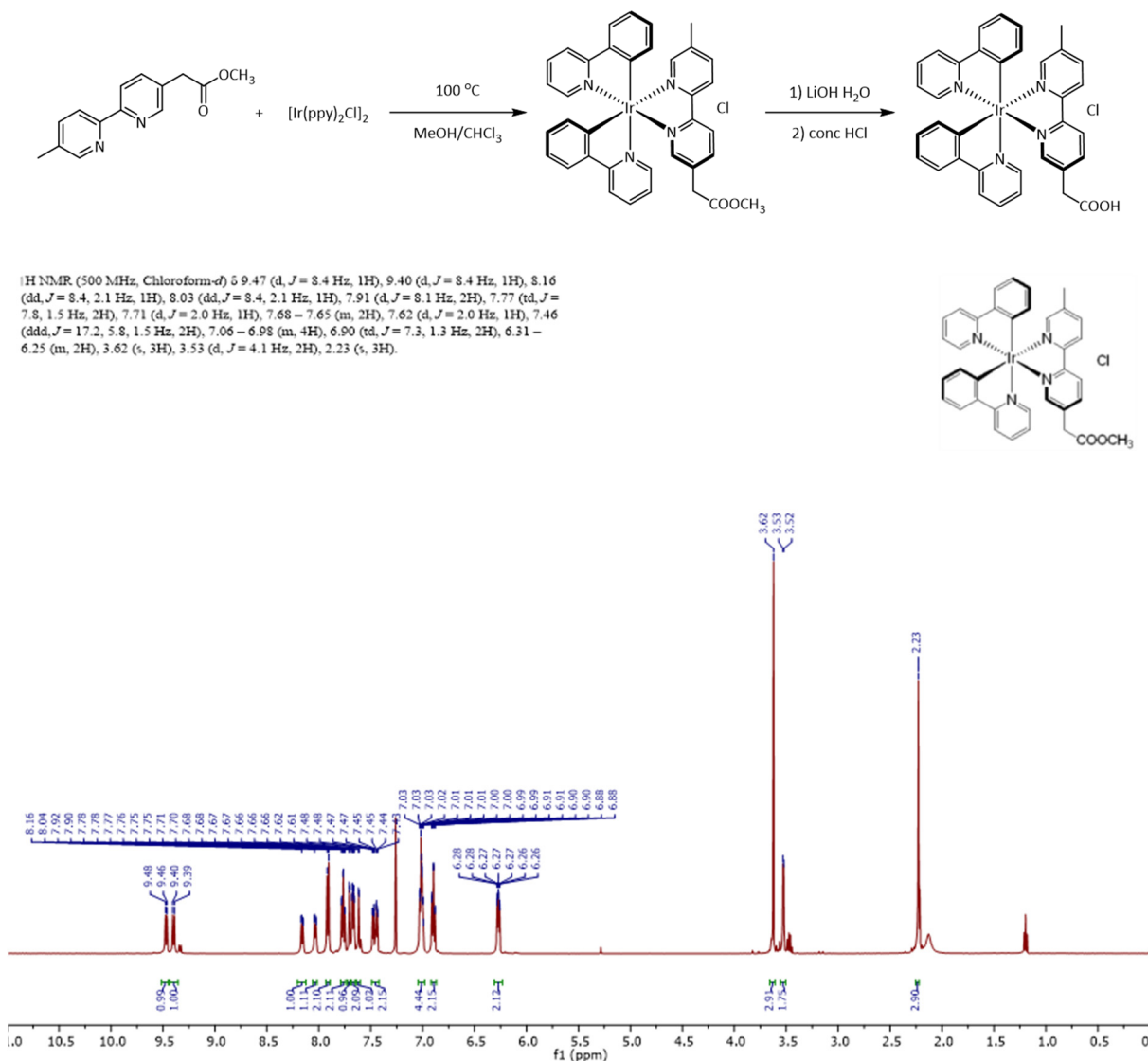


Figure 6-33. ¹H NMR spectrum of [(MeMBA)Ir(ppy)₂]Cl (500 MHz) in CDCl₃. Reprinted with permission from *Journal of the American Chemical Society*, **2020**, 142, 6866-6871. Copyright 2020 American Chemical Society.

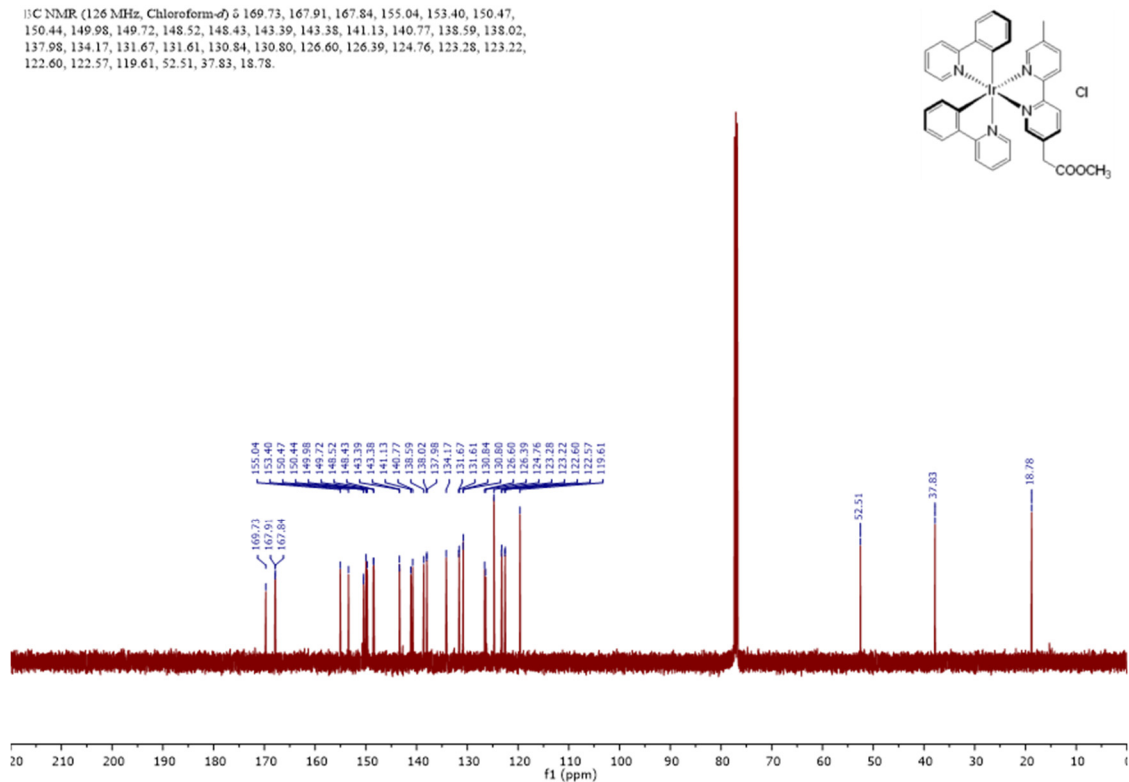


Figure 6-34. ^{13}C NMR spectrum of $[(\text{MeMBA})\text{Ir}(\text{ppy})_2]\text{Cl}$ (500 MHz) in CDCl_3 . Reprinted with permission from *Journal of the American Chemical Society*, **2020**, 142, 6866-6871. Copyright 2020 American Chemical Society.

$[(\text{MeMBA})\text{Ir}(\text{ppy})_2]\text{Cl}$ (100 mg, 0.13 mmol) was suspended in THF (13 mL) in a 50 mL flask. An aqueous solution of LiOH (17 mg LiOH \cdot H $_2$ O in 6 mL deionized water) was added dropwise to the solution while stirring. The solution was stirred at ambient temperature to reaction completion as monitored by TLC. After MeOH was removed under reduced pressure, the solution was acidified with concentrated HCl. The precipitated solid was filtered, washed with deionized water, and ether, and finally dried under vacuum to afford $[(\text{HMBA})\text{Ir}(\text{ppy})_2]\text{Cl}$ as a fine yellow powder (93 mg, 95%). ^1H NMR (500 MHz, DMSO- d_6) δ 12.63 (s, 1H), 8.78 (d, $J = 8.4$ Hz, 1H), 8.74 (d, $J = 8.3$ Hz, 1H), 8.30 – 8.22 (m, 2H), 8.14 (dd, $J = 8.4, 2.1$ Hz, 1H), 8.12 – 8.09 (m, 1H), 7.96 – 7.87 (m, 4H), 7.77 (d, $J = 1.9$ Hz, 1H), 7.63 – 7.56 (m, 3H), 7.16 (dddd, $J = 7.4, 5.9, 3.0, 1.4$ Hz, 2H), 7.05 – 6.96 (m, 2H), 6.90 (dtd, $J = 14.6, 7.4, 1.4$ Hz, 2H), 6.17 (ddd, $J = 15.2, 7.6,$

1.2 Hz, 2H), 3.61 (s, 2H), 2.20 (s, 3H) (**Figure 6-35**). HR-MS (ESI, positive mode): m/z calc'd for $C_{35}H_{28}N_4O_2Ir [M-Cl]^+$: 729.1842, found 729.1854.

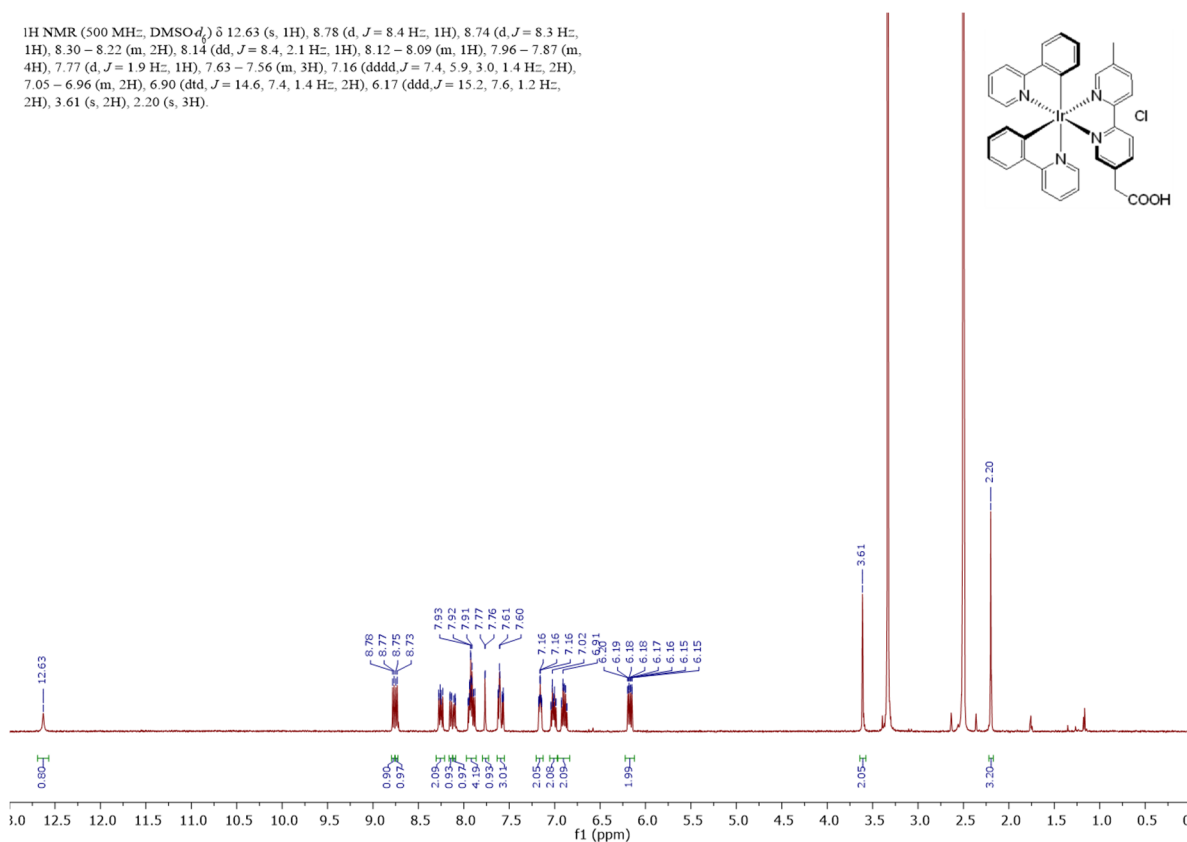
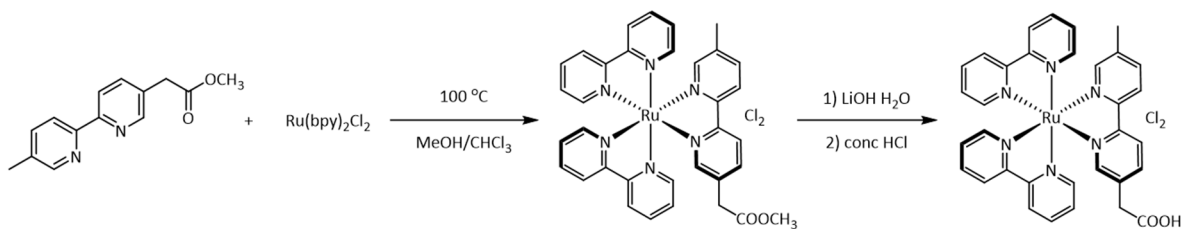


Figure 6-35. ¹H NMR spectrum of [(HMBA)Ir(ppy)₂]Cl (500 MHz) in DMSO-*d*₆. Reprinted with permission from *Journal of the American Chemical Society*, **2020**, 142, 6866-6871. Copyright 2020 American Chemical Society.

Synthesis of [(HMBA)Ru(bpy)₂]Cl₂ Ru(bpy)₂Cl₂ (484 mg, 1.0 mmol), MeMBA (242 mg, 1.0 mmol), methanol (18 mL) and chloroform (18 mL) were subjected to a 100 mL thick-walled Pyrex tube. The tube was sealed and heated at 100 °C for 1 days under N₂ atmosphere. After cooling to ambient temperature, the solvent was removed under reduced pressure and the crude product was carefully poured into a large amount of ether. After filtration and drying under vacuum, dark red solid of [(MeMBA)Ru(bpy)₂]Cl₂ was obtained in 91% yield. ¹H NMR (500 MHz, Methanol-*d*₄) δ 8.74 (dd, *J* = 8.5, 3.4 Hz, 4H), 8.60 (dd, *J* = 10.5, 8.4 Hz, 2H), 8.19 – 8.10 (m, 4H),

8.02 (dd, $J = 8.4, 1.9$ Hz, 1H), 7.97 (dd, $J = 8.3, 1.9$ Hz, 1H), 7.87 – 7.79 (m, 4H), 7.74 (d, $J = 1.9$ Hz, 1H), 7.59 (d, $J = 1.9$ Hz, 1H), 7.55 – 7.46 (m, 4H), 3.70 (d, $J = 1.7$ Hz, 2H), 3.62 (s, 3H), 2.26 (s, 3H) (**Figure 6-36**). ^{13}C NMR (126 MHz, Methanol- d_4) δ 172.01, 158.64, 158.57, 157.09, 155.80, 153.09, 152.68, 152.63, 152.52, 152.22, 140.33, 140.26, 140.00, 139.19, 139.18, 139.17, 136.07, 128.91, 128.90, 125.70, 125.68, 125.65, 125.63, 125.01, 124.61, 52.79, 37.70, 18.45 (**Figure 6-37**). HR-MS (ESI, positive mode): m/z calc'd for $\text{C}_{34}\text{H}_{30}\text{N}_6\text{O}_2\text{Ru} [\text{M}-2\text{Cl}]^{2+}$: 328.0737, found 328.0747.

Scheme 6-3. Schematic representation of the synthesis of $[(\text{HMBA})\text{Ru}(\text{bpy})]\text{Cl}_2$.



^1H NMR (500 MHz, Methanol- d_4) δ 8.74 (dd, $J = 8.5, 3.4$ Hz, 4H), 8.60 (dd, $J = 10.5, 8.4$ Hz, 2H), 8.19 – 8.10 (m, 4H), 8.02 (dd, $J = 8.4, 1.9$ Hz, 1H), 7.97 (dd, $J = 8.3, 1.9$ Hz, 1H), 7.87 – 7.79 (m, 4H), 7.74 (d, $J = 1.9$ Hz, 1H), 7.59 (d, $J = 1.9$ Hz, 1H), 7.55 – 7.46 (m, 4H), 3.70 (d, $J = 1.7$ Hz, 2H), 3.62 (s, 3H), 2.26 (s, 3H).

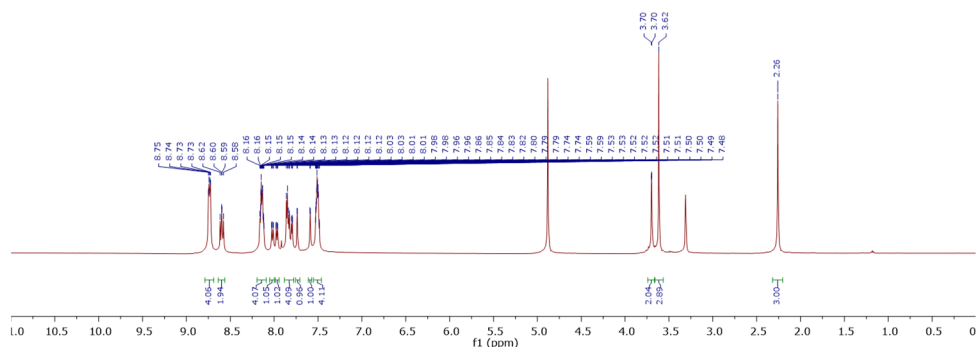
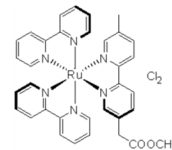


Figure 6-36. ^1H NMR spectrum of $[(\text{MeMBA})\text{Ru}(\text{bpy})_2]\text{Cl}_2$ (500 MHz) in CD_3OD . Reprinted with permission from *Journal of the American Chemical Society*, **2020**, 142, 6866-6871. Copyright 2020 American Chemical Society.

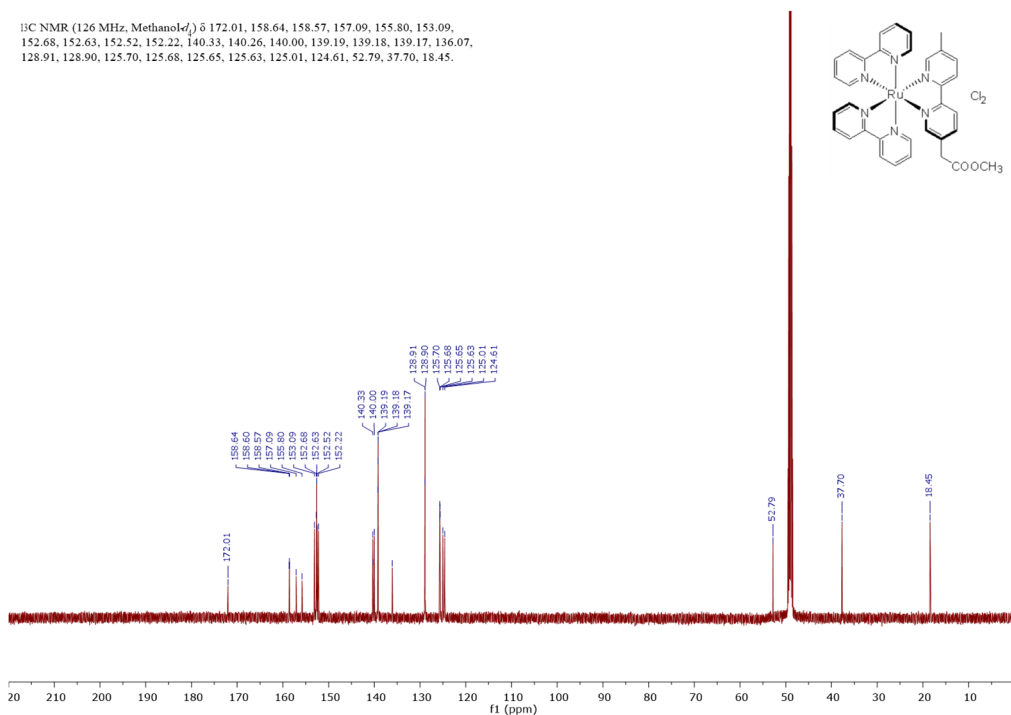


Figure 6-37. ¹³C NMR spectrum of [(MeMBA)Ru(bpy)₂]Cl₂ (500 MHz) in CD₃OD. Reprinted with permission from *Journal of the American Chemical Society*, **2020**, 142, 6866-6871. Copyright 2020 American Chemical Society.

[(MeMBA)Ru(bpy)₂]Cl₂ (120 mg, 0.16 mmol) was suspended in THF (15 mL) in a 50 mL flask. An aqueous solution of LiOH (21 mg LiOH•H₂O in 6 mL deionized water) was added dropwise to the solution with stirring. The solution was stirred at ambient temperature to reaction completion as monitored by TLC. After MeOH was removed under reduced pressure, the solution was acidified by concentrated HCl. The precipitated solid was filtered, washed with deionized water, and ether, and finally dried under vacuum to afford [(HMBA)Ru(bpy)₂]Cl₂ as a dark red powder (102 mg, 87%). ¹H NMR (500 MHz, DMSO-*d*₆) δ 8.91 (tt, *J* = 12.8, 6.5 Hz, 6H), 8.48 (dd, *J* = 8.5, 1.8 Hz, 1H), 8.26 – 8.16 (m, 4H), 8.06 (d, *J* = 8.3 Hz, 1H), 7.94 (d, *J* = 1.8 Hz, 1H), 7.83 (d, *J* = 5.6 Hz, 1H), 7.75 (dd, *J* = 14.3, 5.6 Hz, 3H), 7.63 – 7.54 (m, 4H), 7.53 – 7.49 (m, 1H), 3.41 (s, 2H), 2.24 (s, 3H). HR-MS (ESI, positive mode): *m/z* calc'd for C₃₃H₂₈ClN₆O₂Ru [M-Cl]⁺: 677.1006, found 677.1057.

¹H NMR (500 MHz, DMSO-*d*₆) δ 8.91 (tt, *J* = 12.8, 6.5 Hz, 6H), 8.48 (dd, *J* = 8.5, 1.8 Hz, 1H), 8.26 – 8.16 (m, 4H), 8.06 (d, *J* = 8.3 Hz, 1H), 7.94 (d, *J* = 1.8 Hz, 1H), 7.83 (d, *J* = 5.6 Hz, 1H), 7.75 (dd, *J* = 14.3, 5.6 Hz, 3H), 7.63 – 7.54 (m, 4H), 7.53 – 7.49 (m, 1H), 3.41 (s, 2H), 2.24 (s, 3H).

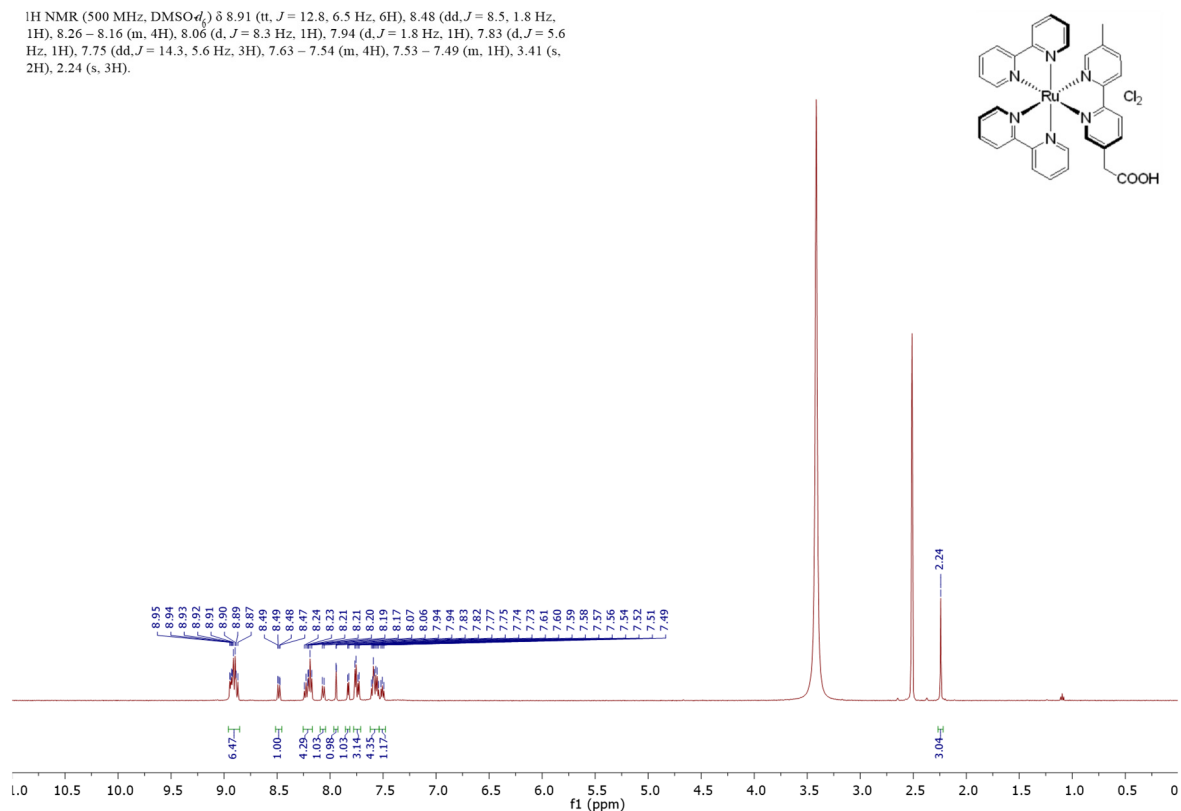


Figure 6-38. ¹H NMR spectrum of [(HMBA)Ru(bpy)₂]Cl₂ (500 MHz) in DMSO-*d*₆. Reprinted with permission from *Journal of the American Chemical Society*, **2020**, 142, 6866-6871. Copyright 2020 American Chemical Society.

6.4.3 X-ray Absorption Spectroscopy

X-ray absorption data were collected at Beamline 10-BM-A, B at the Advanced Photon Source (APS) at Argonne National Laboratory. Spectra were collected at the Ce L₃-edge (5723 eV) in transmission mode. The X-ray beam was monochromatized by a Si (111) monochromator and detuned by 50% to reduce the contribution of higher-order harmonics below the level of noise. A metallic chromium foil standard was used as a reference for energy calibration and was measured simultaneously with experimental samples. The incident beam intensity (*I*₀), transmitted beam intensity (*I*_t), and reference (*I*_r) were measured by 20 cm ionization chambers with gas compositions of 29% N₂ and 71% He, 90% N₂ and 10% Ar, and 100% N₂, respectively. Data were collected over six regions: -250 to -30 eV (10 eV step size, dwell time of 0.25 s), -30 to -12 eV (5

eV step size, dwell time of 0.5 s), -12 to 30 eV (1.1 eV step size, dwell time of 1 s), 30 eV to 6 Å⁻¹, (0.05 Å⁻¹ step size, dwell time of 2 s), 6 Å⁻¹ to 12 Å⁻¹, (0.05 Å⁻¹ step size, dwell time of 2 s), 12 Å⁻¹ to 15 Å⁻¹, (0.05 Å⁻¹ step size, dwell time of 4 s). Multiple X-ray absorption spectra were collected at room temperature for each sample. Samples were ground and mixed with polyethyleneglycol (PEG) and packed in a 6-shooter sample holder to achieve adequate absorption length.

Data was processed using the Athena and Artemis programs of the IFEFFIT package based on FEFF 6. Prior to merging, spectra were calibrated against the reference spectra and aligned to the first peak in the smoothed first derivative of the absorption spectrum, the background noise was removed, and the spectra were processed to obtain a normalized unit edge step.

XANES analysis of Ce oxidation states of Ce₆-BTB-Ru and Ce₆-BTB-Ir before and after photoirradiation carried out by comparing to the standard edge features of both CeCl₃ and (NH₄)₂Ce(NO₃)₆.

6.4.4 Fitting of Luminescence Quenching

[(MeMBA)Ir(ppy)₂]Cl by BIH The reductive quenching mechanism was supported by fitting the data of luminescence quenching of [(MeMBA)Ir(ppy)₂]Cl by BIH to the Stern-Volmer equation,

$$\frac{I_0}{I} = 1 + K_{SV}C_{BIH}$$

where K_{SV} is the Stern-Völmer constant, and I_0/I is the ratio of luminescence intensity in the absence and presence of BIH. I_0/I showed a good linear relationship with respect to the concentration of BIH (C_{BIH}) with $R^2 = 0.999$ and $K_{SV} = 8.91 \text{ mM}^{-1}$.

[(MeMBA)Ru(bpy)₂]Cl₂ by BIH The reductive quenching mechanism was supported by fitting the data of luminescence quenching of [(MeMBA)Ru(bpy)₂]Cl₂ by BIH to the Stern-Volmer equation,

$$\frac{I_0}{I} = 1 + K_{SV}C_{BIH}$$

where K_{SV} is the Stern-Völmer constant, and I_0/I is the ratio of luminescence intensity in the absence and presence of BIH. I_0/I showed a good linear relationship with respect to the concentration of BIH (C_{BIH}) with $R^2 = 0.998$ and $K_{SV} = 1.06 \text{ mM}^{-1}$.

6.5. References

- (1) Fateeva, A.; Chater, P. A.; Ireland, C. P.; Tahir, A. A.; Khimyak, Y. Z.; Wiper, P. V.; Darwent, J. R.; Rosseinsky, M. J., A Water-Stable Porphyrin-Based Metal–Organic Framework Active for Visible-Light Photocatalysis. *Angewandte Chemie International Edition* **2012**, *51* (30), 7440-7444.
- (2) Zhang, T.; Lin, W., Metal–organic frameworks for artificial photosynthesis and photocatalysis. *Chemical Society Reviews* **2014**, *43* (16), 5982-5993.
- (3) Zhu, B.; Zou, R.; Xu, Q., Metal–Organic Framework Based Catalysts for Hydrogen Evolution. *Advanced Energy Materials* **2018**, *8* (24), 1801193.
- (4) Lewis, N. S.; Nocera, D. G., Powering the planet: Chemical challenges in solar energy utilization. *Proceedings of the National Academy of Sciences* **2006**, *103* (43), 15729.
- (5) Sun, Z.; Zheng, H.; Li, J.; Du, P., Extraordinarily efficient photocatalytic hydrogen evolution in water using semiconductor nanorods integrated with crystalline Ni₂P cocatalysts. *Energy & Environmental Science* **2015**, *8* (9), 2668-2676.
- (6) Pullen, S.; Fei, H.; Orthaber, A.; Cohen, S. M.; Ott, S., Enhanced Photochemical Hydrogen Production by a Molecular Diiron Catalyst Incorporated into a Metal–Organic Framework. *Journal of the American Chemical Society* **2013**, *135* (45), 16997-17003.
- (7) Zhang, Z.-M.; Zhang, T.; Wang, C.; Lin, Z.; Long, L.-S.; Lin, W., Photosensitizing Metal–Organic Framework Enabling Visible-Light-Driven Proton Reduction by a Wells–Dawson-Type Polyoxometalate. *Journal of the American Chemical Society* **2015**, *137* (9), 3197-3200.
- (8) Hermes, S.; Witte, T.; Hikov, T.; Zacher, D.; Bahnmüller, S.; Langstein, G.; Huber, K.; Fischer, R. A., Trapping Metal–Organic Framework Nanocrystals: An in-Situ Time-Resolved Light Scattering Study on the Crystal Growth of MOF-5 in Solution. *Journal of the American Chemical Society* **2007**, *129* (17), 5324-5325.

- (9) Wang, T. C.; Doty, F. P.; Benin, A. I.; Sugar, J. D.; York, W. L.; Reinheimer, E. W.; Stavila, V.; Allendorf, M. D., Get the light out: nanoscaling MOFs for luminescence sensing and optical applications. *Chemical Communications* **2019**, *55* (32), 4647-4650.
- (10) Cao, L.; Lin, Z.; Shi, W.; Wang, Z.; Zhang, C.; Hu, X.; Wang, C.; Lin, W., Exciton Migration and Amplified Quenching on Two-Dimensional Metal–Organic Layers. *Journal of the American Chemical Society* **2017**, *139* (20), 7020-7029.
- (11) Luo, B.; Liu, G.; Wang, L., Recent advances in 2D materials for photocatalysis. *Nanoscale* **2016**, *8* (13), 6904-6920.
- (12) Zhao, M.; Huang, Y.; Peng, Y.; Huang, Z.; Ma, Q.; Zhang, H., Two-dimensional metal–organic framework nanosheets: synthesis and applications. *Chemical Society Reviews* **2018**, *47* (16), 6267-6295.
- (13) Wang, Y.; Feng, L.; Pang, J.; Li, J.; Huang, N.; Day, G. S.; Cheng, L.; Drake, H. F.; Wang, Y.; Lollar, C.; Qin, J.; Gu, Z.; Lu, T.; Yuan, S.; Zhou, H.-C., Photosensitizer-Anchored 2D MOF Nanosheets as Highly Stable and Accessible Catalysts toward Artemisinin Production. *Advanced Science* **2019**, *6* (11), 1802059.
- (14) Heidt, L. J.; Smith, M. E., Quantum yields of the photochemical reduction of ceric ions by water and evidence for the dimerization of ceric ions. *Journal of the American Chemical Society* **1948**, *70* (7), 2476-2481.
- (15) Heidt, L. J.; McMillan, A. F., Influence of perchloric acid and cerous perchlorate upon the photochemical oxidation of cerous to ceric perchlorate in dilute aqueous perchloric acid. *Journal of the American Chemical Society* **1954**, *76* (8), 2135-2139.
- (16) Kadowaki, H.; Saito, N.; Nishiyama, H.; Inoue, Y., RuO₂-loaded Sr²⁺-doped CeO₂ with d₀ electronic configuration as a new photocatalyst for overall water splitting. *Chemistry Letters* **2007**, *36* (3), 440-441.
- (17) Lu, X.; Zhai, T.; Cui, H.; Shi, J.; Xie, S.; Huang, Y.; Liang, C.; Tong, Y., Redox cycles promoting photocatalytic hydrogen evolution of CeO₂ nanorods. *Journal of Materials Chemistry* **2011**, *21* (15), 5569-5572.
- (18) Li, W.; Xie, S.; Li, M.; Ouyang, X.; Cui, G.; Lu, X.; Tong, Y., CdS/CeO_x heterostructured nanowires for photocatalytic hydrogen production. *Journal of Materials Chemistry A* **2013**, *1* (13), 4190-4193.
- (19) Primo, A.; Marino, T.; Corma, A.; Molinari, R.; García, H., Efficient Visible-Light Photocatalytic Water Splitting by Minute Amounts of Gold Supported on Nanoparticulate CeO₂ Obtained by a Biopolymer Templating Method. *Journal of the American Chemical Society* **2011**, *133* (18), 6930-6933.
- (20) Montini, T.; Melchionna, M.; Monai, M.; Fornasiero, P., Fundamentals and Catalytic Applications of CeO₂-Based Materials. *Chemical Reviews* **2016**, *116* (10), 5987-6041.

- (21) Yin, H.; Carroll, P. J.; Anna, J. M.; Schelter, E. J., Luminescent Ce(III) Complexes as Stoichiometric and Catalytic Photoreductants for Halogen Atom Abstraction Reactions. *Journal of the American Chemical Society* **2015**, *137* (29), 9234-9237.
- (22) Hu, A.; Guo, J.-J.; Pan, H.; Tang, H.; Gao, Z.; Zuo, Z., δ -Selective Functionalization of Alkanols Enabled by Visible-Light-Induced Ligand-to-Metal Charge Transfer. *Journal of the American Chemical Society* **2018**, *140* (5), 1612-1616.
- (23) Qiao, Y.; Schelter, E. J., Lanthanide Photocatalysis. *Accounts of Chemical Research* **2018**, *51* (11), 2926-2936.
- (24) Qiao, Y.; Yang, Q.; Schelter, E. J., Photoinduced Miyaura Borylation by a Rare-Earth-Metal Photoreductant: The Hexachloroacetate(III) Anion. *Angewandte Chemie* **2018**, *130* (34), 11165-11169.
- (25) Zhang, K.; Chang, L.; An, Q.; Wang, X.; Zuo, Z., Dehydroxymethylation of Alcohols Enabled by Cerium Photocatalysis. *Journal of the American Chemical Society* **2019**, *141* (26), 10556-10564.
- (26) Esch, F.; Fabris, S.; Zhou, L.; Montini, T.; Africh, C.; Fornasiero, P.; Comelli, G.; Rosei, R., Electron Localization Determines Defect Formation on Ceria Substrates. *Science* **2005**, *309* (5735), 752.
- (27) Wu, X.-P.; Gagliardi, L.; Truhlar, D. G., Cerium Metal–Organic Framework for Photocatalysis. *Journal of the American Chemical Society* **2018**, *140* (25), 7904-7912.
- (28) Yin, H.; Jin, Y.; Hertzog, J. E.; Mullane, K. C.; Carroll, P. J.; Manor, B. C.; Anna, J. M.; Schelter, E. J., The Hexachloroacetate(III) Anion: A Potent, Benchtop Stable, and Readily Available Ultraviolet A Photosensitizer for Aryl Chlorides. *Journal of the American Chemical Society* **2016**, *138* (50), 16266-16273.
- (29) Lin, Z.; Thacker, N. C.; Sawano, T.; Drake, T.; Ji, P.; Lan, G.; Cao, L.; Liu, S.; Wang, C.; Lin, W., Metal–organic layers stabilize earth-abundant metal–terpyridine diradical complexes for catalytic C–H activation. *Chemical Science* **2018**, *9* (1), 143-151.
- (30) Rehm, D.; Weller, A., Kinetics of Fluorescence Quenching by Electron and H-Atom Transfer. *Israel Journal of Chemistry* **1970**, *8* (2), 259-271.
- (31) Cker, J. W.; Stephenson, C. R. J., Shining Light on Photoredox Catalysis: Theory and Synthetic Applications. *The Journal of Organic Chemistry* **2012**, *77* (4), 1617-1622.
- (32) Ji, P.; Sawano, T.; Lin, Z.; Urban, A.; Boures, D.; Lin, W., Cerium-Hydride Secondary Building Units in a Porous Metal–Organic Framework for Catalytic Hydroboration and Hydrophosphination. *Journal of the American Chemical Society* **2016**, *138* (45), 14860-14863.